Electrogenerated Mesoporous Silica Thin Films : Thickness Control and Electroanalytical Applications

Taisiia Sikolenko

Ecole Doctorale C2MP (Chimie – Mécanique – Matériaux - Physique)

Thèse

présentée pour l'obtention du titre de

DOCTEUR DE l'UNIVERSITE DE LORRAINE

Mention : « Chimie »

par Taisiia SIKOLENKO

Films Minces de Silice Mésoporeuse Electrogénérée : Contrôle de l'épaisseur et Applications Analytiques

Soutenue publiquement le 16 décembre 2020

Membres du jury :

Rapporteurs :	Dr. Christine MOUSTY	Directrice de Recherche – Institut de Chimie de Clermont-Ferrand, Université Clermont Auvergne
	Dr. Fethi BEDIOUI	Directeur de Recherche – Institute of Chemistry for Life and Health Sciences (i-CLeHS), Chimie ParisTech
Examinateurs :	Pr. Christophe RAPIN	Professeur – Institut Jean Lamour, Université de Lorraine
Directeur de thèse :	Dr. Alain WALCARIUS	Directeur de Recherche – LCPME, Université de Lorraine
Membre invitée	Dr. Sophie LEGEAI	Maitre de Conférences – Institut Jean Lamour, Université de Lorraine
Co-encadrante Membre invitée :	Dr. Christelle DESPAS	Maitre de Conférences – LCPME, Université de Lorraine

Laboratoire de Chimie Physique et Microbiologie pour les Matériaux et l'Environnement (LCPME)
UMR 7564, CNRS / Université de Lorraine
405, rue de Vandoeuvre 54600 Villers-lès-Nancy France

Doctoral School C2MP (Chimie – Mécanique – Matériaux - Physique)

Thesis

Presented for the title of

DOCTOR OF CHEMISTRY FROM THE UNIVERSITY OF LORRAINE

Speciality : « Chemistry »

by Taisiia SIKOLENKO

Electrogenerated Mesoporous Silica Thin Films: Thickness Control and Electroanalytical Applications

Public defence on 16th December 2020

Members of jury :

Reviewers :	Dr. Christine MOUSTY	Research Director – Institute of Chemistry of Clermont-Ferrand, Université Clermont Auvergne
	Dr. Fethi BEDIOUI	Research Director – Institute of Chemistry for Life and Health Sciences (i-CLeHS), Chimie ParisTech
Examiners :	Pr. Christophe RAPIN	Professor – Institute Jean Lamour, Université de Lorraine
Supervisor :	Dr. Alain WALCARIUS	Research Director – LCPME, Université de Lorraine
Invited member	Dr. Sophie LEGEAI	Lecturer – Institute Jean Lamour, Université de Lorraine
Co-supervisor Invited member :	Dr. Christelle DESPAS	Lecturer – LCPME, Université de Lorraine

Laboratoire de Chimie Physique et Microbiologie pour les Matériaux et l'Environnement (LCPME)
UMR 7564, CNRS / Université de Lorraine
405, rue de Vandoeuvre 54600 Villers-lès-Nancy France

When life leaves us blind,
Love keeps us kind.

Acknowledgements

First of all, I would like to express my sincerest gratitude to my supervisors, **Alain Walcarius** and **Christelle Despas,** for guiding me through this project and for sharing your experience with me. I enjoyed our discussions and I believe that your advices will help me in my professional life wherever I will end up. Even though **Neus Vilà** was not officially my supervisor, she contributed significantly to this project and to my development as a scientist, for what I am very thankful.

I would like to thank the members of my thesis committee, **Dr. Christine Mousty**, **Prof. Christophe Rapin**, **Dr. Fethi Bedioui**, and **Dr. Sophie Legeai**, for their critical evaluations of my research work and for their suggestions during the defense.

I appreciate the involvement of all **LCPME team members**, particularly **Grégoire Herzog**, **Liang Liu**, **Marc Hébrant, Michel Perdicakis** and **Mathieu Etienne**, who shared their thoughts and suggestions throughout the project. I would like to thank **Claire Genois**, with whom I have shared the office for these three years, for her kindness and help in the laboratory. Furthermore, I would like to acknowledge **Aurélien Renard** for XPS measurements, **Jaafar Ghanbaja** and **Sylvie Migot** for TEM images and trainings, **Jérôme Grausem** for help with spectroscopy, and **Mélanie Emo** for GISAXS measurements.

No work could have been done without a technical support of **Marie Rambeau** and **Pascal Kissienne**, as well as without **Gérard Paquot** and **Jean-Paul Moulin**, who were designing and creating the devices necessary for the experimental work. I will always remember the workshop as an especially welcoming place, and I am grateful for heartwarming talks and laughs we had, despite my broken French. A special appreciation is devoted to **Christelle Charbaut** and **Marie Tercier**, for being patient and helpful with the administrative issues.

The international team I joined in the end of 2017 has already had a lot of PhD students, who were very kind and open-minded, who were guiding us, the freshers, in the laboratory and outside it, showing us the new city and all the local secrets they knew to make our life in Nancy easier. **Cheryl Karman**, **Christelle Ghazaly**, **Elena Yunda, Maciej Mierzwa**, **Martha Collins**, **Samuel Ahoulou** and **Tauqir Nasir**, thank you all for your constant support while being colleagues and even after your graduation. Since we were a lot in our year as well, I wish to acknowledge my peer-PhD colleagues, **Deomila Basnig**, **Guofeng Lu, Himanshu Maheshwari**, **Jianren Wang**,

Joanna Rogińska, **Laura Didierjean, Ning Dang** and **Wahid Ullah**, for scientific discussions and heart-to-heart conversations, for litters of coffee consumed together and for all celebrations and fun we had. In these three years, I was also lucky to meet postdocs, interns, and students from all over the world, who are all wonderful people, and I am happy that we had this opportunity to cross paths in Nancy.

I would like to thank **Ilona Saraieva**, **Marvin Middelhoff** and **Shantanu Misra** for being an important part of my PhD life outside the lab and for making it integral and colorful. You became my family here, and I can say with certainty that I was lucky to find friends for a lifetime. I am especially grateful to **Ilona** for sharing so many great moments together, for her exceptional diplomacy and endless understanding, which helped us to become perfect partners in crime. I would also like to acknowledge **Carlo Nainer**, **Dasha Panicheva**, **Maxim Proskurin** and many other shiny people I met in Nancy, for making my life brighter.

During the work on PhD project, I was constantly supported by my Ukrainian friends **Dmitry Danylchuk, Elina Kovalenko**, **Inna Khutorianska, Oksana Reznichenko**, **Oleksandra Prokopenko** and **Olesia Slobodyan**. Wherever you were, close or far, you encouraged me and cheered for me all the time. This kind of friendship is a secret superpower that helps to go through a lot of difficulties in life and I am very thankful to have you as my friends.

I want to express my deepest gratitude to **my family**, who always had faith in me and who taught me to be strong and dream big. My **mom** and **dad**, you were those who inspired me for this three-year adventure, you always pushed me towards my limits knowing that I will appreciate a result after all invested efforts. And, surely, you were right. My **brother**, thank you being so supportive and calming when I needed it. Last but not least, I want to thank my **grandparents** for their kindness and wisdom they shared with me.

And of course, I would like to acknowledge **Université de Lorraine** and **Ecole Doctorale C2MP** for the opportunity I was given to perform the research in LCPME and to discover new horizons of scientific life.

Thank you all for being the pieces of the puzzle, that helped me to put this thesis together.

Contents

Résumé 1
Introduction 11
Chapter 1 13
Literature review 13
1.1 Introduction 13
1.1.1 Sol-gel process 14
1.1.2 Mesoporous silica 16
1.1.3 Mesoporous silica thin films 20
1.2 Main approaches for electrode modification 23
1.2.1 Electrode modification by mesoporous silica films 24
1.2.2 Mesoporous silica films with vertically oriented pores for electrochemical application 27
1.2.3 Functionalisation of vertically oriented mesoporous silica films 31
1.2.4 Practical application of vertically oriented mesoporous silica films 32
1.3 Our research project 36
Chapter 2 37
Experimental part 37
2.1 Instrumental techniques 37
2.1.1 Electrochemistry 37
2.1.2 Spectroscopy 42
2.1.3 Microscopy 45
2.1.4 Profilometry 48
2.2 Protocol for synthesis of (3-azopropyl)triethoxysilane (AzPTES) 49
2.3 Mesoporous silica film preparation by electrochemically-assisted self-assembly 50
2.3.1 Sol preparation and film deposition 50
2.3.2 Surfactant extraction 51

2.3.3 Click reaction to prepare modified films 51
2.4 Electrochemical characterisation of mesoporous silica films 53
2.4.1 Characterisation with conventional probes 53
2.4.2 Characterisation with haemoglobin 55
2.5 Protocol for etching experiments 56
Chapter 3 57
Tuning the thinness of well-organised mesoporous silica film 57
3.1 Introduction 57
3.2 Investigating the deposition time parameter for obtaining the thinnest flawless films 62
3.3 Wet etching approach to control the thickness of mesoporous silica film 69
3.3.1 Control experiments 70
3.3.2 Effect of mesoporous silica film nature 76
3.3.3 Effect of the NH_4F concentration 88
3.3.4 The effect of the etching agent 91
3.4 Conclusions 94
Chapter 4 95
Development of system based on $Ru(bpy)_3^{2+}$ modified mesoporous silica thin film for glyphosate detection by electrochemiluminescence 95
4.1. Introduction 95
4.1.1 General information about $Ru(bpy)_3^{2+}$ as electrochemiluminescence reactant 95
4.1.2 Immobilisation of $Ru(bpy)_3^{2+}$ onto solid matrix 101
4.1.3 Glyphosate and its detection 105
4.2 Glyphosate detection by ECL – $Ru(bpy)_3^{2+}$ complex system: solution approach 109
4.2.1 ITO working electrode 109
4.2.2 ITO working electrode modified by mesoporous silica film 112
4.3 Impregnation of $Ru(bpy)_3^{2+}$ complex onto silica film surface 119
4.3.1 Electrode preparation 119

4.3.2 Characterisation of mesoporous silica films with physically adsorbed $Ru(bpy)_3^{2+}$ complex 119

4.3.3 Electrochemical response in presence of glyphosate 122

4.4 Covalent immobilisation of $Ru(bpy)_2(bpy')^{2+}$ onto mesoporous silica film surface 123

4.4.1 $Ru(bpy)_2(bpy')^{2+}$ complex preparation 124

4.4.2 Huisgen "click" reaction 127

4.4.3 Characterisation of $Ru(bpy)_2(bpy)$'-modified mesoporous silica films 129

4.4.4 Electrochemical response in presence of glyphosate 134

4.5 Analytical aspect of electrochemical detection of glyphosate 136

4.6 ECL measurements: challenges and complications in course of the project 138

4.7 Conclusions 140

General conclusion and perspectives 142

Appendix 1: Chemicals 146

Appendix 2: Determination of ammonium fluoride concentration 148

Appendix 3: Surfactant extraction from mesopores during etching 150

Appendix 4: Effect of pH on glyphosate detection using $Ru(bpy)_3^{2+}$ glyphosate co-reactant system on ITO electrode 152

Appendix 5: NMR characterisation 154

Bibliography 156

Abstract 180

Résumé abrégé 181

Résumé

La modification d'électrodes par des films de silice mésoporeuse ouvre des perspectives intéressantes dans le développement de capteurs électrochimiques en promettant de répondre aux besoins de détection spécifique de substances, d'un abaissement des limites de quantification et d'une mise en œuvre sur site. En particulier, la combinaison de la méthode électrochimique EASA (electrochemically-assisted self-assembly, [1]) avec le procédé sol-gel en présence de tensioactifs (ici le bromure de cétyltriméthylammonium, CTAB) permet d'obtenir des films fins et réguliers de silice mésoporeuse, de structure hexagonale et dont l'originalité repose sur une orientation des pores perpendiculaire à la surface du support. Ces caractéristiques singulières contribuent à des transports de matière rapides et indispensables aux applications type capteurs. La modification chimique de la surface de silice mésoporeuse est essentielle pour personnaliser l'électrode afin d'améliorer encore ses performances pour la détection électrochimique. Par conséquent, la modification de la couche de silice mésoporeuse est au centre de ce travail.

Malgré l'orientation verticale des pores, le transport de matière à travers la couche de silice déposée peut tout de même être affecté. En effet, dans les conditions de fonctionnement qui impliquent normalement un pH supérieur à 3, les groupements silanol de surface (≡Si-OH) subissent une déprotonation. La surface du film de silice se charge donc négativement. D'un côté, cela permet d'introduire des fonctionnalités intéressantes pour le développement de capteur (sélectivité, préconcentration) mais d'un autre côté, la détection des espèces anioniques devient difficile voire impossible en raison des répulsions de charges. Cependant, conserver la possibilité de recouvrir les électrodes avec des films de silice mésostructurée reste intéressant même non fonctionnalisée au regard de la propriété de tamis moléculaire de ces films apportant ainsi la possibilité d'une détection basée sur la sélectivité de taille et une limitation dans l'encrassement de l'électrode. La première partie de la thèse s'est intéressée à la diminution de l'épaisseur de film de silice mésostructurée obtenu par la méthode EASA dans le but de modifier une électrode d'ITO (oxyde d'indium-étain) avec la couche la plus fine possible. L'objectif est de préserver les bénéfices apportés par le matériau (diffusion facilitée des analytes, sélection de taille) tout en minimisant ses effets les plus négatifs (répulsion de charge) (*Figure 1*). Le contrôle de l'épaisseur peut être réalisé

lors de l'étape de synthèse en contrôlant la composition du sol [2] ou le temps de déposition, ou post-synthèse.

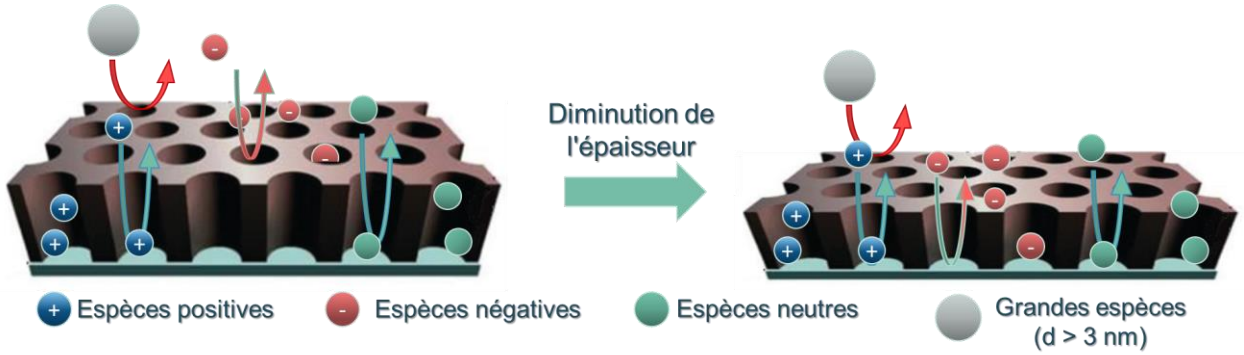

Figure 1 – Effet de l'épaisseur du film de silice mésostructurée possédant des pores parallèles à la surface du support sur la diffusion d'analytes

Tout d'abord, l'effet de la durée d'application du potentiel de déposition (-1,3V/Ag) a été étudiée pour une composition de sol reconnue pour permettre l'obtention d'un film de silice parfaitement mésostructuré ([Si] = 100 mM, [CTAB] = 32 mM en milieu eau-EtOH (50 :50 v:v)). La perméabilité des films préparés a été évaluée par voltampérométrie cyclique à l'aide de sondes électrochimiques positive et neutre, respectivement $Ru(NH_3)_6^{3+}$et $Fc(MeOH)_2$, en maintenant le tensioactif, CTAB, à l'intérieur des pores de la silice. L'obtention d'un film sans défaut à la surface de l'électrode conduit à l'absence d'un signal électrochimique de la sonde positive et un déplacement en potentiel de celui de la sonde neutre. Ceci est observé avec un film obtenu en 10 secondes et plus (*Figure 2A*). Des analyses par spectroscopie de photoélectrons X (XPS) confirme la couverture complète de l'électrode dans ces mêmes conditions opératoires. La microscopie électronique en transmission (MET) et des mesures par diffusion de rayons X aux petits angles en incidence rasante (GISAXS) démontrent la parfaite structuration du film de silice obtenu avec la présence d'une organisation hexagonale de la porosité et une orientation verticale des canaux cylindriques par rapport au support (*Figure 2B*). L'épaisseur de ces films est de 80 ± 9 nm (potentiel de -1,3V/Ag appliqué pendant 10 s). Par la méthode EASA et pour notre composition de sol choisie, il n'est donc pas possible d'obtenir un recouvrement homogène de l'électrode avec films de silice mésostructurée de moins de 80 nm d'épais.

(A) (B)

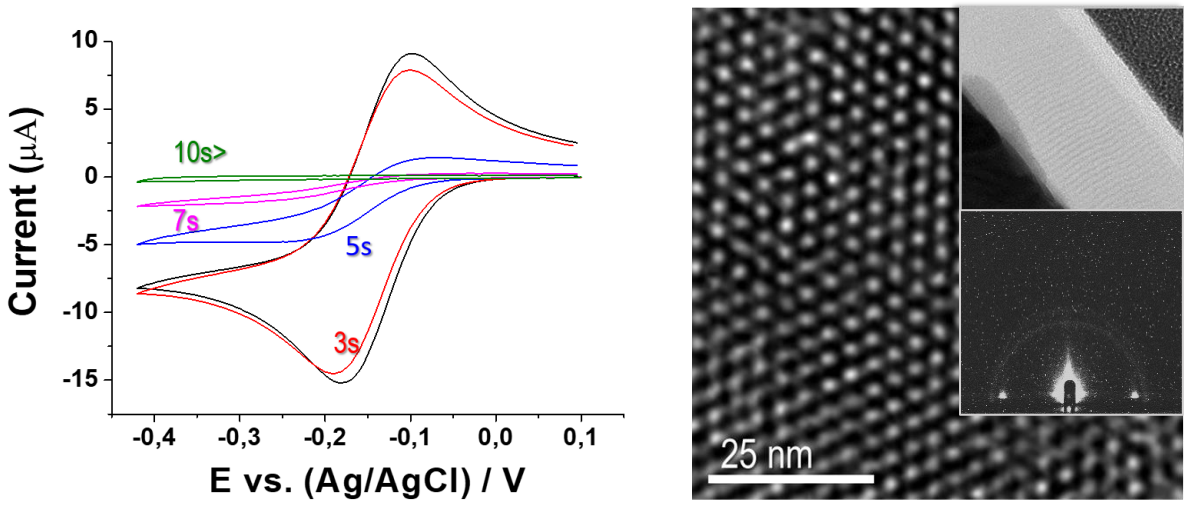

Figure 2 – (A) Analyse par voltampérométrie cyclique de la perméabilité des films de silice préparés avec différents temps de déposition. Sonde électrochimique : $Ru(NH_3)_6^{3+}$ 0,5mM en milieu $NaNO_3$ 0,1M - vitesse de balayage 50 mV/s et (B) Images MET présentant une vue du dessus (image principale) et une coupe transversale (image en haut à droite) d'un film de silice obtenu avec un temps de dépôt de 10 secondes, et l'image GISAXS correspondante (image en bas à droite)

Un traitement post-synthèse est nécessaire pour obtenir des couches plus fines. Sur la base d'une étude bibliographique, l'approche retenue a consisté à dissoudre le film de silice en utilisant des solutions aqueuses de fluorure d'ammonium, NH_4F, cité comme réactif « doux » [3]. L'effet de maintenir ou pas l'agent structurant (CTA^+) dans les pores sur la cinétique et l'homogénéité de dissolution a été étudié ainsi que l'influence de son mode d'extraction (calcination ou par voie chimique (HCl 0,1 M – EtOH)). Les mesures d'épaisseur à l'aide d'un profilomètre à stylet ont permis de suivre la progression de la réaction de dissolution. La réponse électrochimique de la sonde ruthénium, $Ru(NH_3)_6^{3+}$ et de l'hémoglobine possédant une taille supérieure au diamètre des pores et l'analyse de surface par XPS nous ont permis de rendre compte l'apparition ou pas de défauts dans le film de silice. Quant aux mesures GISAXS et la microscopie MET, elles ont été mises en œuvre pour suivre l'effet de la réaction chimique sur la structuration du matériau.

La *Figure 3* décrit l'évolution de l'épaisseur du film en fonction du temps lorsque l'agent structurant, le tensioactif, est conservé au sein de la silice (courbe noire - gCTAB) ou a été préalablement extrait par calcination (courbe bleue- gCALC) ou voie chimique (courbe rouge - gEXTR). Le film le plus fin est obtenu en faisant réagir des échantillons sans extraction du CTA^+.

L'ensemble des résultats d'analyse montre également clairement que le maintien du tensioactif dans les pores de la silice permet une dissolution plus rapide et le maintien d'une organisation structurelle du matériau pour de plus faibles épaisseurs, c'est-à-dire 28 ± 9 nm (pour gCTAB). Lorsque le traitement est mené sur des films de silice pour lesquels le tensioactif a été extrait par voie humide ou par calcination, l'épaisseur la plus petite atteinte sans créer de défaut ou de changement d'organisation dans le film est seulement de 57 ± 11 nm. Le CTA^+ présent au sein des pores permet d'améliorer la mouillabilité de la solution et de favoriser le transport et l'accumulation des ions fluorure par l'excès de charges positives qu'il génère par son accumulation le long des parois de la silice. La réaction de dissolution s'en trouve, à la fois, accélérée et mieux contrôlée, soit 1,1 nm/min pour les échantillons gCTAB à comparer avec 0,6 nm/min pour ceux extraits avec une solution NH_4F 0,05 M.

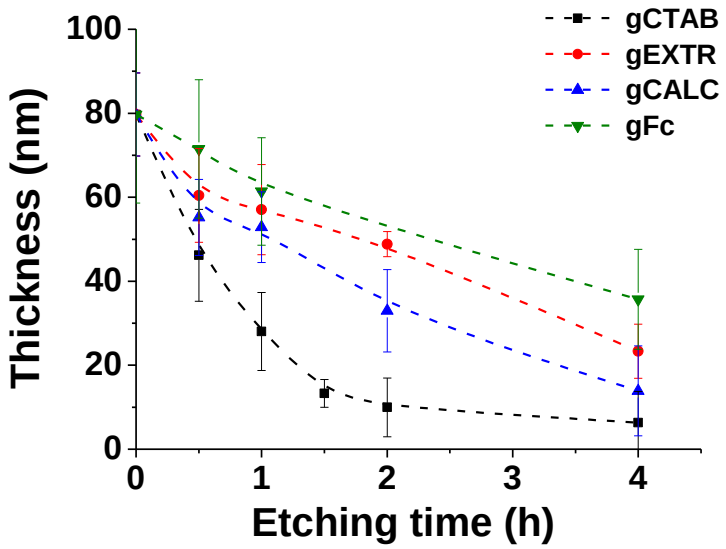

Figure 3 – Evolution de l'épaisseur normalisée des films (mesurée par profilométrie) en fonction du temps de contact avec une solution de NH_4F 0,05 M

Le greffage de groupements électroactifs à l'intérieur des pores de la silice permet également de rendre compte de la dissolution du film de silice en contact avec la solution aqueuse de NH_4F [4]. L'éthylnylferrocène est greffé post-synthèse par chimie « click » sur les films de silice portant des groupements azoture introduits par co-condensation au cours de la synthèse. La dissolution du film conduit à une perte de matière et donc à une diminution du nombre de groupement électroactif

pour une même surface d'électrode modifiée considérée. Par conséquent, la réponse électrochimique doit décroître en augmentant le temps de contact du film avec la solution de NH_4F. La *Figure 4* confirme la dissolution du film et démontre de la bonne adéquation entre le signal électrochimique du ferrocène et l'épaisseur mesurée.

(A) (B)

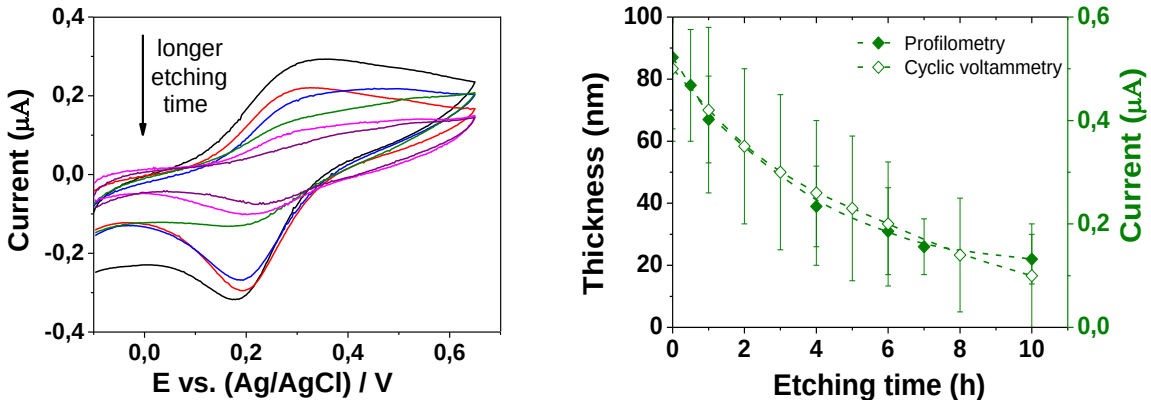

Figure 4 – (A) Évolution du signal électrochimique d'une électrode d'ITO recouverte d'un film de silice mésoporeuse fonctionnalisée par des groupements ferrocène et enregistré dans $NaNO_3$ 0,1M (vitesse de balayage 5 mV/s) et (B) correspondance entre la variation de l'épaisseur et l'évolution du courant de pic d'oxydation du Fc observée au cours de la réaction avec NH_4F 0,05 M

Dans la deuxième partie de l'étude, les films de silice mésoporeuse ont été fonctionnalisés par un complexe organométallique de ruthénium(II) dans le but d'essayer de développer une plateforme d'électrochimiluminescence (ECL) pour la détection du glyphosate, un herbicide organophosphoré faisant l'objet d'un programme de surveillance. L'originalité de l'approche est le choix d'immobiliser de manière covalente un complexe ruthénium(II) tris(bipyridine), $Ru(bpy)_2(bpy)'^{2+}$, au sein du film de silice mésoporeuse dans le but d'obtenir des capteurs utilisables *ex situ* comme *in situ*, sans nécessité d'ajouter le complexe organométallique dans l'échantillon à analyser. L'approche par chimie « click » a été privilégiée et réalisée sur un film de silice modifiée par des groupements azoture préparé par co-condensation (*Figure 5*). Le complexe de ruthénium tris(bipyridine) avec un substitut alcyne terminal présenté sur la *Figure 5* n'étant pas disponible à la vente, il a été tout d'abord synthétisé [5].

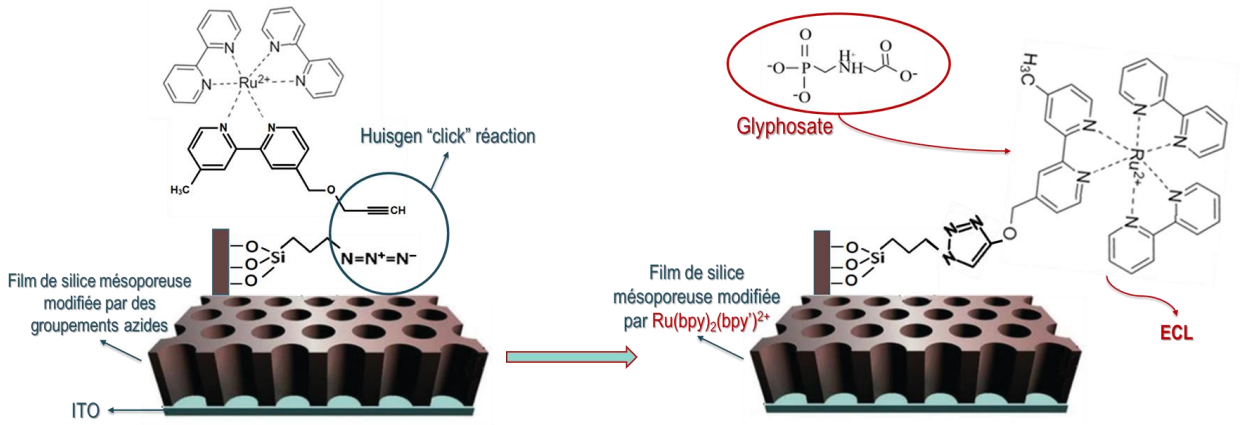

Figure 5 – Greffage du complexe $Ru(bpy)_2(bpy)^{2+}$ par la chimie « click » pour la détection du glyphosate par électrochimiluminescences

Les analyses spectroscopiques infrarouge et UV-visible démontrent que le complexe de ruthénium a bien été fixé à la surface de la silice de manière covalente, confirmée par la présence de la bande d'élongation $\nu_{C=C}$ de la bipyridine à 1595 cm^{-1} sur le spectre infrarouge (*Figure 6A*) et de la bande d'adsorption dans le visible du complexe à 445 nm, causée par le transfert de charge métal-ligand (MLCT) (*Figure 6B*).

(A) (B)

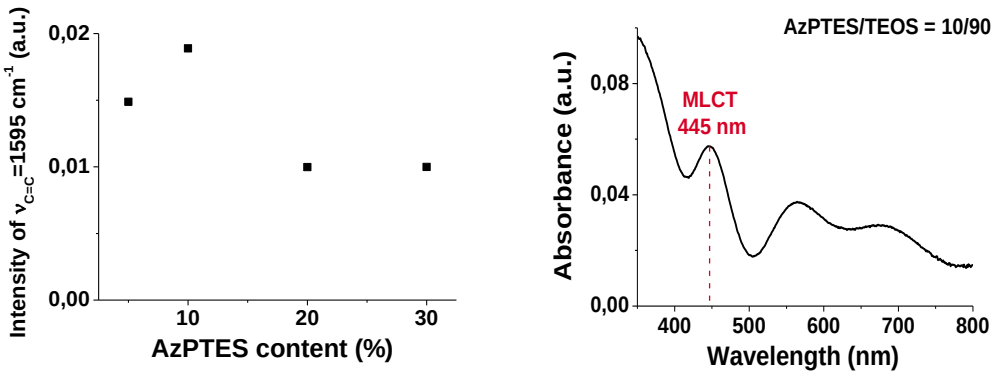

Figure 6 – (A) Suivi par spectrométrie infrarouge de l'intensité de la bande d'élongation vC=C de la bipyridine pour les films greffés en fonction des différentes teneurs d'AzPTES introduites dans le sol et (B) spectre UV/vis d'un film greffé (rapport AzPTES/TEOS : 10/90) après réaction de clic avec $Ru(bpy)_2(bpy')^{2+}$

Par électrochimie, on observe que son activité rédox est maintenue dans le milieu confiné constitué par les pores du matériau et que l'on obtient une meilleure stabilité de la réponse (*Figure 7A*) en comparaison avec celle issue d'une imprégnation (*Figure 7B*). Nos premiers essais montrent que la quantité maximale de complexe pouvant être introduite dans le film est obtenue lorsque le film de silice est préparé à partir d'un rapport 10 : 90 de (3-azidopropyl)triéthoxysilane (AzPTES) : tétraéthoxysilane (TEOS) (*Figure 6A*).

(A) (B)

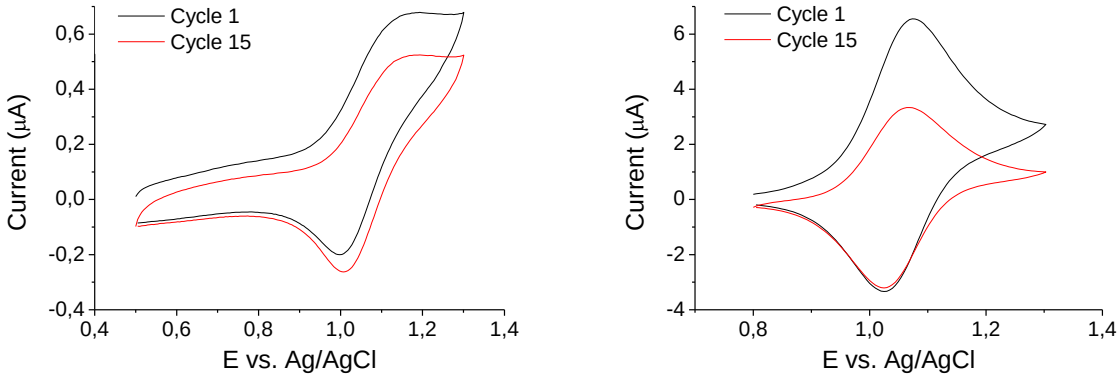

Figure 7 – Voltampérogrammes cycliques enregistrés dans une solution de NaNO3 0,1 M en utilisant une électrode (A) greffée $Ru(bpy)_2(bpy')$ (rapport AzPTES/TEOS : 10/90) et (B) préalablement imprégnée avec le complexe $Ru(bpy)_3^{2+}$. (Conditions : vitesse de balayage de 50 mV/s, 15 balayages consécutifs)

Possédant un groupement amine secondaire puisque dérivé de la glycine, le glyphosate (Glyp) peut jouer le rôle de coréactif dans des réactions de chimiluninescence induite par électrochimie. En particulier, il va permettre de porter le luminophore, qui est ici le complexe ruthénium(II) tris(bipyridine), à l'état excité suivant un mécanisme réactionnel décrit ci-dessous [8] :

$$Ru(bpy)_3^{2+} \rightarrow Ru(bpy)_3^{3+} + e^-$$

$$Ru(bpy)_3^{3+} + Glyp \rightarrow Ru(bpy)_3^{2+} + Glyp^{\bullet+}$$

$$Glyp^{\bullet+} \rightarrow Glyp(-H)^{\bullet} + H^+$$

$$Ru(bpy)_3^{3+} + Glyp(-H)^{\bullet} \rightarrow Ru(bpy)_3^{2+*} + produits$$

$$Ru(bpy)_3^{2+*} \rightarrow Ru(bpy)_3^{2+} + h\upsilon$$

Les signaux électrochimiques enregistrés par voltampérométrie cyclique à pH 7 pour les systèmes respectifs ITO/$Ru(bpy)_3^{2+}$/Glyp et ITO modifié par un film de silice/$Ru(bpy)_3^{2+}$/Glyp sont cohérents avec ce mécanisme proposé (*Figure 8*). Le système rédox Ru(III)/Ru(II) est réversible. En présence du pesticide, le courant d'oxydation du complexe de ruthénium(II) augmente proportionnellement à la quantité introduite de dérivé aminé alors que l'on observe la disparition de courant de réduction du composé de ruthénium (III) lié à la réaction spontanée du ruthénium(III) produit à l'électrode avec le glyphosate.

(A) (B)

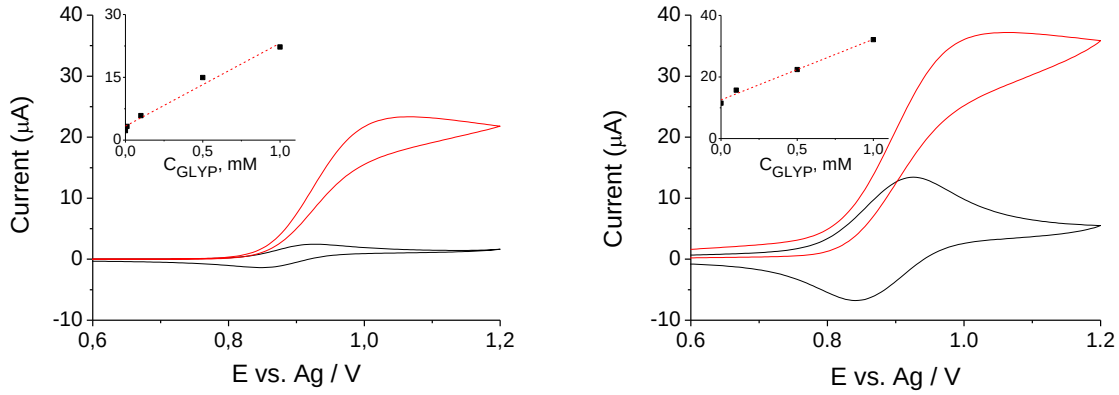

Figure 8 – Signal électrochimique d'une solution aqueuse de $Ru(bpy)_3^{2+}$ 0,1 mM enregistré sur une électrode (A) ITO et (B) ITO recouverte d'un film de silice mésoporeuse en absence (ligne noire) ou en présence de glyphosate 1 mM (ligne rouge) avec les courbes de calibration correspondantes (1^{er} scan, vitesse de balayage 50 mV/s, milieu tampon phosphate 50 mM à pH 7)

La *Figure 9* décrit la réponse d'une électrode d'ITO modifiée par un film de silice greffé avec le complexe de ruthénium tris(bipyridine). On peut y observer une modification du signal électrochimique lorsque l'on ajoute du glyphosate en solution.

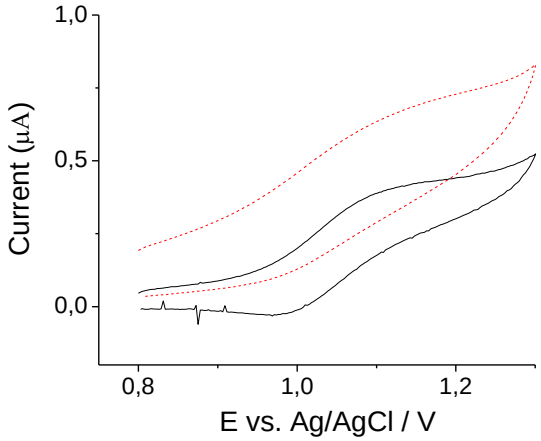

Figure 9 – Signal électrochimique enregistré sur une électrode d'ITO recouverte d'un film de silice mésoporeuse greffée $Ru(bpy)_2(bpy)'^{2+}$ en absence (ligne noire) et en présence de 4 µM (pointillés rouges) (1er scan, vitesse de balayage 20 mV/s, tampon phosphate 50 mM, pH 7)

L'effet sur la réponse est cependant moins marqué que celle pour les systèmes où le complexe $Ru(bpy)_3^{2+}$ est libre en solution. L'immobilisation du luminophore n'empêche donc pas le processus de détection du glyphosate.

Bibliographie

[1] A. Walcarius, E. Sibottier, M. Etienne, J. Ghanbaja, Electrochemically assisted self-assembly of mesoporous silica thin films, Nat. Mater. 6 (2007) 602–608. https://doi.org/10.1038/nmat1951.

[2] A. Goux, M. Etienne, E. Aubert, C. Lecomte, J. Ghanbaja, A. Walcarius, Oriented mesoporous silica films obtained by Electro-Assisted Self-Assembly (EASA), Chem. Mater. 21 (2009) 731–741. https://doi.org/10.1021/cm8029664.

[3] M. Kobayashi, K. Susuki, T. Otani, S. Enomoto, H. Otsuji, Y. Kuroda, H. Wada, A. Shimojima, T. Homma, K. Kuroda, Thickness control of 3-dimensional mesoporous silica ultrathin films by wet-etching, Nanoscale. 9 (2017) 8321–8329. https://doi.org/10.1039/c7nr01560g.

[4] T. Sikolenko, C. Despas, N. Vilà, A. Walcarius, Thickness control in electrogenerated

mesoporous silica films by wet etching and electrochemical monitoring of the process, Electrochem. Commun. 100 (2019) 11–15. https://doi.org/10.1016/j.elecom.2019.01.013.

[5] A. Walcarius, R. Nasraoui, Z. Wang, F. Qu, V. Urbanova, M. Etienne, M. Göllü, A.S. Demir, J. Gajdzik, R. Hempelmann, Factors affecting the electrochemical regeneration of NADH by (2,2'-bipyridyl) (pentamethylcyclopentadienyl)-rhodium complexes: Impact on their immobilization onto electrode surfaces, Bioelectrochemistry. 82 (2011) 46–54. https://doi.org/10.1016/j.bioelechem.2011.05.002.

Introduction

Design and development of new electrochemical sensors is a constant challenge. Using the electrode coatings is one of the ways to improve their performance. Silica coatings are of big interest due to their hard network, variety of forms in which they can exist (e.g. powders, nanoparticles, films), satisfactory stability in aqueous and organic media. An additional advantage of silica is its rich chemistry, which allows to introduce organic functional groups during material preparation by co-condensation or after synthesis by post-synthetic grafting of silica through reactive surface silanol groups (Si-OH).

A new approach presented by Mobil Oil Corporation in 1992 triggered a development of mesoporous silica with narrow pore size distribution called M41S family [4]. It was based on sol-gel synthesis combined with soft templating by surfactant micelles. Owing to a uniform pore diameter and diversity of pore morphologies along with high surface area, rigidity of the network and non-inert silica surface it was possible to apply this material for molecular sieving and selective adsorption of organic and inorganic species [5]. In a short time, the application of these systems became beneficial for electroanalysis in form of coatings. The main trends of the electrode modification included the use of mesoporous particles, membranes and films based on silica materials [6]. The exceptional selectivity was reached due to functionalisation of silica, which led to the increased affinity of grafted groups towards the analyte (such as the interactions between heavy metals and thiol functions [7]). Moreover, the mass transport was improved because of the well-organised and controlled porosity, although it was still hindered as a result of unfavourable pore morphology.

In the early 2000s, the development of the Electro-Assisted Self-Assembly (EASA method) for the deposition of mesoporous structured silica films with vertical pore orientation [1] have further extended and revived the interest of silica as electrode modifier [8]. Even though vertical pore alignment showed that this is a promising material to be used in electrochemical sensing, some mass transport restrictions still exist due to non-inert surface of silica. It occurs because in the range of pH where silica materials are normally used (pH from 2 to 8), surface silanol groups are existing in deprotonated form, what creates an excess of negative charge over the film surface.

After a general review on mesoporous silica materials, their specific properties and applications in the field of electrochemistry for the electrode modification, the second chapter describes techniques and experimental procedures, which were used in this study. **Chapter III** focuses on the first objective of this thesis that is to reduce the film thickness in order to minimise the influence of coating while keeping the advantage of the silica film (e.g. even with the reduced thickness, mesoporous silica film acts as a size-excluded membrane for molecules that are larger than pore diameter). A specific attention will be paid to maintaining a well-defined hexagonal mesostructure of the deposit. The film thickness reduction is presented based on the decrease of deposition time, which in case of EASA is determined by time of potential application to sol containing silica precursor. For the further film thinning, wet etching approach by soft etching agent (NH_4F) is proposed. Thickness decrease was studied with respect to the film nature (in presence of soft template or without it) and etching agent and its concentration. Film functionalisation with redox active species (e.g. ferrocene) was performed by post-grafting of azide-modified silica films with ethynyl ferrocene following Huisgen 1,3-cycloaddition (also called "click" reaction). Study is supported by thickness measurements made by profilometry, electrochemical characterisation with electroactive probes, spectroscopy (XPS, GISAXS) and microscopy (SEM, TEM) surface characterisation.

Chapter IV introduces a practical application of functionalised mesoporous silica films for electrochemiluminescence (ECL) sensing of glyphosate. As the ECL reactant and film modifier $Ru(bpy)_3^{2+}$ was selected because of its electroactivity and ability to produce luminescence even in aqueous media in presence of oxygen. It also allows obtaining enhanced electrochemical and ECL response in presence of glyphosate, making the detection of the herbicide possible. In view of rich surface chemistry of silica, the incorporation of the organometallic ruthenium(II) complex onto mesoporous films was performed in two ways, respectively by physical adsorption (based on charge interaction between electroactive $Ru(bpy)_3^{2+}$ species and negative silica surface) and chemical functionalisation. The latter pathway was achieved by the introduction of azide functions on the silica walls (co-condensation route) followed by Huisgen 1,3-cycloaddition with terminated alkyne derivative of $Ru(bpy)_3^{2+}$. The effect of the herbicide addition on electrochemical signal was investigated in order to conclude on the possibility to detect glyphosate using functionalised mesoporous silica films. **General conclusions and perspectives** are finalising the manuscript.

Chapter 1

Literature review

1.1 Introduction

Silicon dioxide is one of the most commonly studied inorganic oxides [9]. Silicon is the second main component of the Earth crust in the form of minerals (mainly SiO_2). In the large scale, silicon oxide is used in production of concrete, glass and ceramics. Other than this, crystalline (i.e. quartz) and amorphous silicon dioxide found even wider application in microelectronics and integrated circuit technologies as insulator [9], in medical field for drug delivery and as a highly effective sorbents [10], in food production as separation and adsorption agent [11]. Such a wide application of silica in different fields is explained by its properties. Depending on the form, silica-based materials exhibit a good stability on air and satisfactory stability in aqueous and organic media. Surface chemistry allows modification of material, whereas a low toxicity of oxide was a reason to extend its use for pharmaceutical and medical purposes. An ability of silica to form porous structures is of significant importance and worth to be specifically highlighted. During the past half of the century a number of porous inorganic materials (including those based on silica) were in the middle of interest of scientific community. An attention was driven to them due to a high surface area, open structure, tuneable pore shape and size. Owing to these features, both crystalline and amorphous porous materials of different nature (zeolites, silica molecular sieves, metal oxides) nowadays are widely applied as adsorbents and ion exchangers, catalysts and energy materials.
In case of porous silica, chemically non-inert surface, which can be functionalised, is an absolute advantage [12,13]. Application of pure silica materials is normally based on their porous properties, large surface area and hardness of matrix. This is why, the main process here is based on phenomenon of adsorption. Introduction of particular chemical functions expands the areas of utilisation by improving selectivity of interaction between silica surface and targeted molecules. The main role of silica in this case is to act as a hard support for reactive species that are arranged over its surface. Modification of surface is mainly performed either by co-condensation on preparation step [14] or by grafting after synthesis of silica support.

The idea behind the first method is a one-pot synthesis. It is performed by addition of precursors in sol, which are acting like a source of silica building blocks for a network creation. One of them

is organosilane (R-Si-(OR')$_3$) with required functional group (so-called co-reactant or co-precursor). Chemicals are added in reaction media in the same time to undergo hydrolysis and further condensation. Obtained in this way silica gels exhibit homogeneous incorporation of functional groups in the outer walls of matrix [14].

The second approach requires organosilanes with common formula R_n-Si-X_{4-n} (where R is an organic group and X is a hydrolysable ligand). Typically, monosylated organosilanes with n=1 are used to functionalise silica support with R-species [14]. Generally, the homogeneity of functional group distribution is not excellent. Grafting of porous silica materials is even less successful as it can lead to pore blocking [15].

Another approach includes immobilisation through attracting electrostatic forces between surface silanol groups and species of cationic nature. In this way, apart from the evident adsorption of inorganic cations (e.g. Ca^{2+} [16]), organic compounds such as dyes [17] can be also immobilised. To perform this modification, silica is immersed in solution with dissolved modifier, which is accumulated inside pores. Even though this method seems to be less time-consuming and easier to be carried out, it is still more preferable to use covalent modification because of the strong chemical bond, which should prevent leaching of grafted species [14].

It is evident, that more pores lead to larger specific surface area. Consequently, more active centres are present on silica, resulting in more efficient sorption-desorption process and higher number of functional groups in case of modification. Nevertheless, in order to have a uniform performance over all surface of mesoporous material it is necessary for it to have homogeneous distribution of pores. According to IUPAC classification, micropores are possessing pore diameter smaller than 2.0 nm, for mesopores the value is in the range of 2.0 to 50.0 nm, and microporous materials have pore size exceeding 50.0 nm [18]. In turn, geometry of pores is defined as cylindrical, slit-shaped, conical and ink-bottled [19].

1.1.1 Sol-gel process

The sol-gel process is a frequently used approach for synthesis of silica-based materials. Two major steps (illustrated with *Eq. 1.1-1.4*, adjusted from [18]) include i) hydrolysis of silica precursor (*Eq. 1.1 and Eq. 1.2*) and ii) its following condensation (*Eq. 1.3-1.4*). Usually, tetraethyl orthosilicate (TEOS) or tetramethyl orthosilicate (TMOS) are used as main precursors in case if

the aim is obtaining a silica material. The degree of hydrolysis depends on amount of water, catalyst (acid or base) and time [20], leading to completely (all OR groups transformed to OH, presented on *Eq. 1.1*) or partially (some of the OR groups are replaced with OH, illustrated on *Eq. 1.2*) hydrolysed precursor. Then, hydrolysed molecules are acting as building blocks to assemble the silica network during the condensation step (*Eq. 1.3-1.4*).

Eq. 1.1

Eq. 1.2

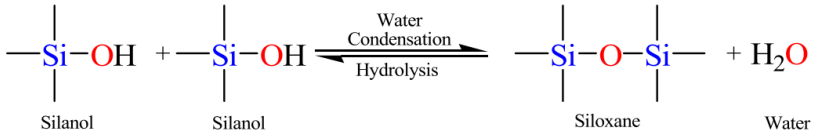

Eq. 1.3

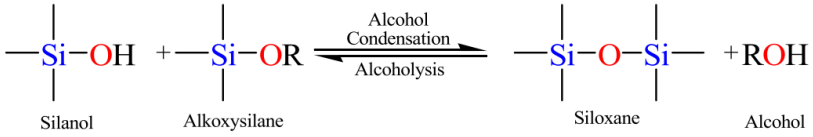

Eq. 1.4

The state of the hydrolysed precursor and the final structure of silica polymer strongly depends on the nature of the catalyst [4]. Thus, under the effect of H^+, silica forms linear chains, which are partially cross-linked. They are also able to form new branches, resulting in gelation. At high pH levels the hydrolysis occurs faster. It is followed by formation of more branched clusters, which in turn cross-link during gelation.

On *Figure 1* the diagram with rates of hydrolysis (marked as H) and condensation (marked as C) of silica is presented depending on pH of sol. Generally, minimum hydrolysis rate is observed around pH 7. Higher acidity/basicity of solution increases rate of hydrolysis (see line H on *Figure 1*). On the other hand, pH < 3 provides lower rates of condensation with respect to hydrolysis (line

C on *Figure 1*). Alkaline media causes much faster condensation reaching maximum around pH 7-8 [23] (*Figure 1*).

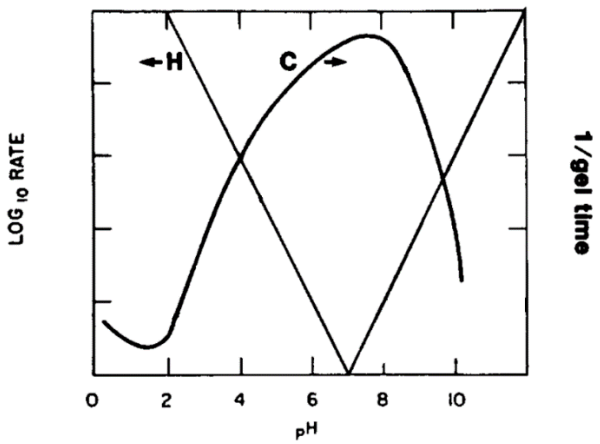

Figure 1 – Schematic representation of the pH dependences of the hydrolysis (H) and condensation (C) rates (adjusted from [23])

1.1.2 Mesoporous silica

Highly ordered mesoporous silica materials possess a regular structure with a unique pore size and shape despite being amorphous at atomic level. After discovery of specific class of porous materials called MCM (Mobil Composition of Matter) in 1992 [4], the interest in porous materials based on silica increased significantly, what is illustrated by a number of publications on this topic since 1996 on *Figure 2*.

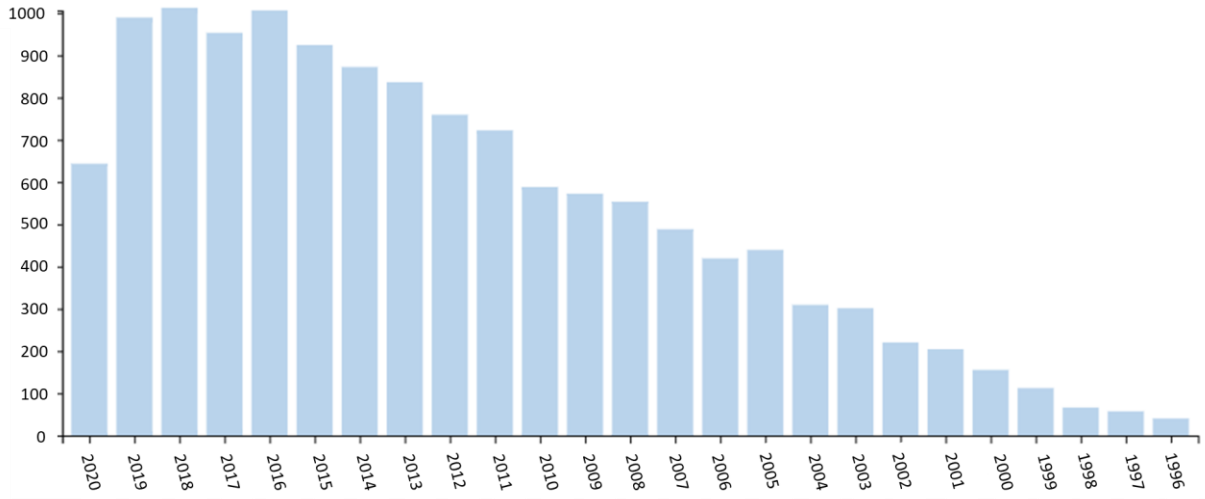

Figure 2 – A number of publications entitled “mesoporous silica” starting from 1996 according to Web of Science

The simplest way to introduce pores is by changing the conditions of sol-gel preparation of silica. Initially, sol-gel process by its nature implies H_2O (*Eq. 1.3*) and alcohol (*Eq. 1.4*) release after the Si-O-Si bond creation [20]. These small molecules remain in silica network, creating pores.

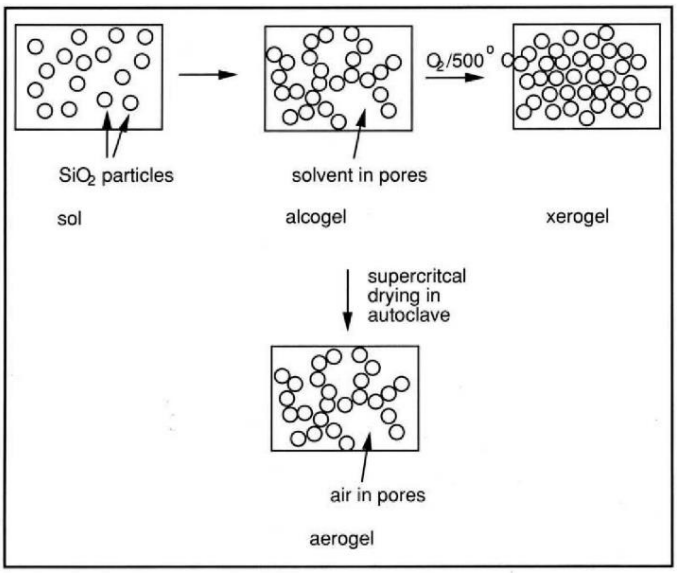

Figure 3 – Transition from sol to xerogel and aerogel while drying [21]

During the aging step, liquid stays inside gel and cross-linking continues with formation of alcogel (*Figure 3*). Depending on drying conditions, pores with different morphology and size can be formed as a result of liquid removal from a solid matrix [20,21]. If solvent extraction is performed at relatively high temperatures (500°C) xerogel will be formed, when the use of autoclave results in aerogel. Aerogels possess low density with larger porosity in contrast to xerogels, which are much denser. Other parameters, which can be varied to affect the pore size, are catalysts, pH of sol and alcohol/TEOS and water/TEOS ratio [24]. Larger pores can be obtained by adding ammonia catalyst (alkaline pH), whereas the use of HCl (acidic pH) leads to smaller pores with diameter around 4 nm maximum. Introduction of HF or NH_4F catalysts allows obtaining porous system with pore size in the wide range of 4-100 nm. Increasing the water/TEOS molar ratio from 2 to 6 causes the rise of porosity ten times. Contrary to this, higher content of ethanol has the reducing effect on pore diameter.

Despite the pore formation, the system obtained in this way is highly disordered and has a wide pore size distribution what was an issue since many potential applications (among which it is fair to name electrochemistry) demand a uniform structuration [18]. Although zeolites and zeolite-related molecular sieves were offering pore size from 4 to 12 Å in diameter with the possibility to

additionally introduce mesopores [25], there was still a need to break past the pore-size constraint (< 15 Å). As for silica-based porous materials the narrow pore distribution was unreachable by modification of synthesis conditions. Therefore, design of mesoporous materials required new approaches. In the early 1990s, a new method for obtaining mesoporous molecular sieves with a regular pore structure was described in the work of Kresge [4]. The study was based on a combination of sol-gel and template synthesis, which introduced to the world new organic-inorganic hybrid materials called M41S family. They possessed extremely high surface area (> 700 m^2g^{-1}) with tuneable pore size in the range of 15 to 100 Å [26].

Liquid crystal templating was proposed as a mechanism for the pore formation like in case of synthesis of other molecular sieves [27]. According to it, assemblies of molecules rather than individual molecules are taking part in pore formation and are acting as structure directing agents for the mesophase formation. Anionic, cationic and neutral surfactants and triblock copolymers [28] can be chosen due to their ability to organize hexagonal, lamellar or cubic structures above the Critical Micelle Concentration (CMC) [29,30]. In parallel to self-organisation of the template into a form of lyotropic liquid-crystalline phase, the condensation of the silica precursor occurs, followed by the assembly of mesostructured composite around template. Two main mechanisms can be involved with respect to surfactant concentration [31].

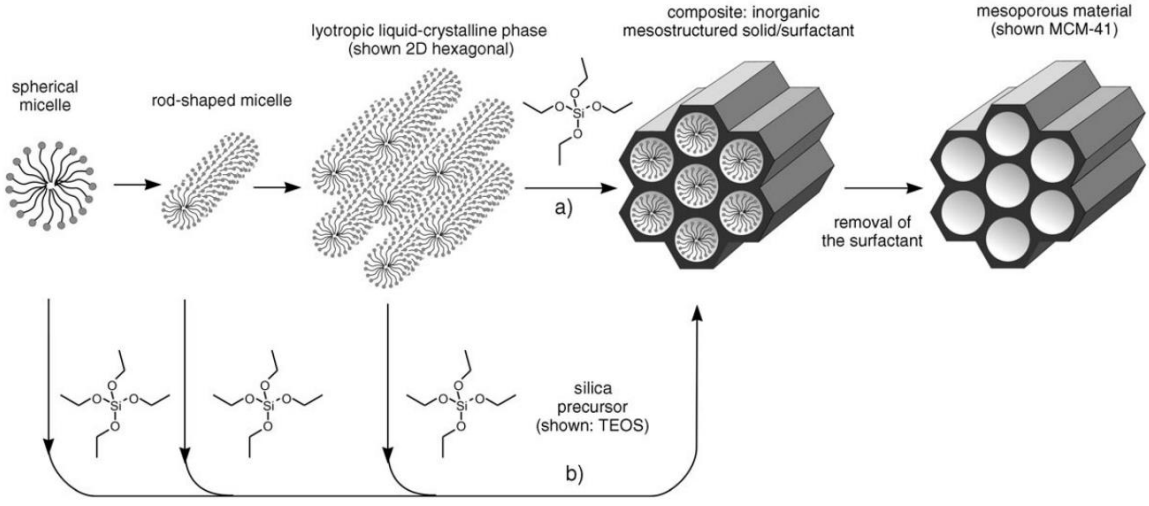

Figure 4 – Formation of mesoporous materials by structure directing agents: a) true liquid-crystal template mechanism, b) cooperative liquid-crystal template mechanism [31]

At high concentrations, a lyotropic liquid-crystalline phase is created on its own without silica precursor, which is added later [32] (*path a, Figure 4*). The use of lower surfactant concentrations

also leads to formation of the same phase, but along with inorganic precursor self-assembly in the meantime [33] (*path b, Figure 4*).

Materials with hexagonal (MCM-41), cubic (MCM-48) or layered (MCM-50) structures can be obtained as it is depicted on *Figure 5* by varying the reactant stoichiometry, the nature of surfactant and its concentration [18].

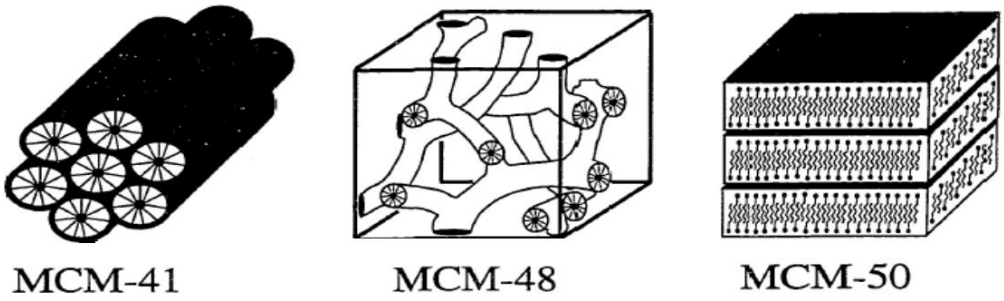

Figure 5 - Schematic diagram of the M41S materials: MCM-41 (hexagonal), MCM-48 (cubic) and MCM-50 (layered) [18]

Along with tuning the pore structure, it was shown that different morphologies can be obtained for porous silica. In particular, synthesis in static conditions leads to rope-shaped forms, when under the controlled agitation gyroid-type structures were prevailing [34,35]. Increase of the time of preparation also lead to transition from rope-based shapes to gyroids [36] or to worm-shaped structures [35]. Morphological changes were explained by re-organisation of secondary building units [36]. By electrospinning deposition with low spinning voltage (15-25 kV) mesoporous particles with poorly defined shape were formed, whereas higher one (25-30 kV) caused rope formation [37]. Synthesis by modified Stöber method in presence of tetraethoxysilane, cationic surfactant and ammonia catalyst along with alcohol (ethanol or isopropanol) resulted in formation of homogeneous spherical particles [38,39], which can be also doped with transition metals [40].

1.1.3 Mesoporous silica thin films

One of interesting type of morphology is film. The big interest to it is given due to their multiple applications in optical, electronic and sensing devices, in separation and hosting [41,42], to which powder samples are not accessible [43].

The first notions about sol-gel deposited silica films on support appeared in 1996 [44–46]. An approach of growing the film from acidic solution containing silica precursor and alkyltrimethylammonium chloride as surfactant template was used by Aksay et al. on graphite, mica and silica support [44]. Authors showed that synthesised films have the same alignment as mica and graphite substrates, but film growth at silica/water interphase triggered a random orientation. The same way of depositing films of 0.2 – 1.0 μm thick was also used by Yang et al. on mica surface [46]. For all described cases, the pore size was typically defined by chosen surfactant and the time of synthesis was defined from hours to weeks. Ogawa [45] presented an utilisation of a spin-coating technique to deposit film on glass substrate from solution of the same composition. For this purpose, liquid was placed on the rotating support which distributes solution homogeneously around the surface (via centrifugal force) with subsequent evaporation of the solvent. As reported, obtained coating is 2 μm thick and possesses hexagonal mesostructure. These described films exhibited pore orientation parallel to the electrode substrate. Dip coating was also used to obtain porous silica films with wide pore distribution and pore diameter from 1.5 to 3.1 nm depending on time of aging [47]. An idea behind this method of deposition is in dipping a substrate for inside the solution with precursor and surfactant for the certain time with following slow vertical lifting of it back on air. The faster substrate is pulled out, the thicker the deposit is obtained. Finally, the liquid is evaporated and silica network undergoes a cross-linking.

Later, Brinker [30] introduced an Evaporation-Induced Self-Assembly (EISA) approach for generation of highly ordered mesostructured thin films. Most of the drawbacks of the firstly proposed methods, such as time-consuming deposition procedure, scale limit, and poorly-defined thin film morphology, which was closer to powders, were overcome. The key requirement for EISA is presence of volatile solvent (normally ethanol), which can be easily evaporated. EISA film deposition includes four main steps presented on example of dip coating film deposition technique illustrated on *Figure 6* [48]:

1. *Preparation of homogeneous sol* (hydro-alcoholic media) with silica precursor for solid network creation around soft template (introduced in low concentration) *and its hydrolysis*. Condensation of silica is optimally slowed down by keeping low pH (*Figure 1*).
2. *Evaporation of solvent,* which causes an increase of surfactant concentration. Evaporation continues reaching the concentration of surfactant at which the transition from individual molecules to molecular assemblies starts (CMC). In case of dip coating, this process occurs much faster pace while pulling out the film from solution due to volatile nature of solvent.
3. Evaporation is complete and *the film mesostructure is tuned* by adjusting relative humidity (RH). At higher rates of RH more water molecules are present in silica matrix. In this way an increase of water content causes a transition of mesostructure from disordered (RH 20%) to 2D-hexagonal (RH 40%) and cubic (RH > 40%) [49].
4. *Condensation of inorganic network* and final stabilisation of hybrid mesostructure to increase porosity by template extraction. Condensation of silica network successfully occurs from 130^{o}C for 48 h in air for functionalised films (with no degradation of organic groups [50]) up to 800^{o}C (for unmodified mesoporous silica film with cubic orientation [51]).

Apart from dip coating film deposition [52–54], spin coating [30,45,55,56] technique was also used to obtain thin layers. Following EISA approach with liquid-crystalline templating based mechanism it is possible to obtain thin films with worm-like, 2D hexagonal, 3D hexagonal and cubic mesostructure [30]. Tuning of mesostructure is carried out by adjusting surfactant/silica molar ratio and RH value. As an example, CTAB/Si ratio below 0.10 at RH = 40% results in disordered material. Changing the ratio from 0.10 to 0.12 leads to changing from 3D hexagonal to cubic mesostructure. Increasing this proportion to 0.18 causes transition to 2D hexagonal organisation.

There are also reports about aerosol EISA deposition [57] and ink-jet printing [58]. For both methods a hydro-alcoholic solution containing dissolved silica precursor with surfactant at concentration smaller than CMC is used. Aerosol deposition requires a specific setup with a gas flow to carry aerosol particles. On their way through chambers they are dried, heated and collected on a support in hexagonal mesostructure [57]. Ink-jet printing deposits ink-like solution on surface and an evaporation of ethanol triggers EISA process following the steps 1-4 on *Figure 6*. This

method was found to be useful for production of mesoporous films of cubic orientation with width from micrometers to millimeters [58].

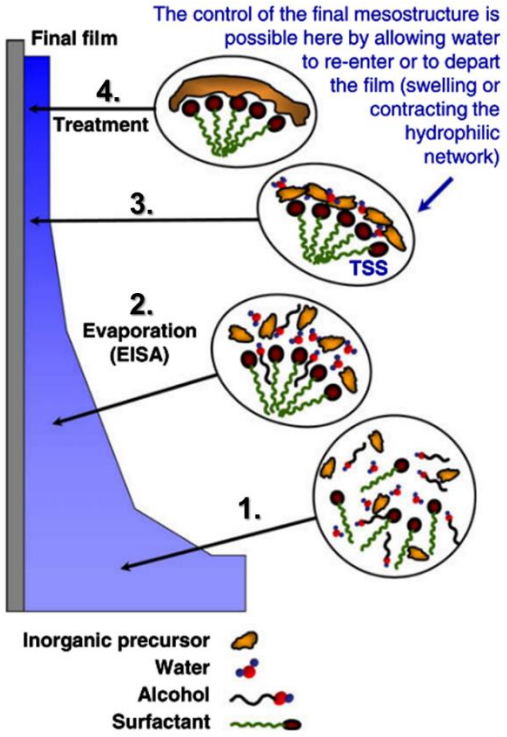

Figure 6 - Mesostructured thin film formed by dip coating (adjusted from [48,59])

The thickness control for sol-gel films can be regulated by concentration of sol [52]. As it was demonstrated for coatings obtained by spin-coating, 27-times dilution decreases film thickness by almost 30 times (from 1310 to 40 nm) [55]. Higher spinning rate is also known to affect film thickness by its reduction [60]. Deposition by dip-coating technique provided with 70 – 500 nm thick mesoporous coatings [54]. Films with thickness lower than 300 nm lack the long-distant hexagonal order. Those that are thick (1 μm) tend to disorganisation [55] and crack formation during the calcination step, limiting maximum reachable thickness [60]. Most of the operated mesoporous silica films were possessing thickness of around 300 nm [49,51,56].

1.2 Main approaches for electrode modification

Among numerous potential applications of mesoporous silica films listed above, special attention is drawn to their electrochemical use. Due to their porous morphology, chemical and thermal stability, and the ability to be modified they are a good choice for being used as electrode coatings. Starting from the very beginning, it is important to highlight the main purposes of the electrode modification [61]. This procedure is performed in order to:

- Lower the activation energy of the electron transfer selectively for chosen probes;
- Regulate mass transport of species particularly based on charge or size exclusion;
- Selectively and reversibly accumulate the analyte inside coating via physical or chemical bonds;
- Improve the long-term stability and durability of the electrode.

According to classification introduced by Bard [62], electrode modification can be performed by:

1. *Irreversible adsorption of species.* Modification is typically conducted on metal electrodes due to strong attraction between metal and modifier. As an example, platinum electrode can be modified by As, Bi and Se [63,64] and using sulphur-containing species is more common for mercury or gold substrates [62].
2. *Covalent attachment of a monolayer*, which can require surface pre-treatment to form surface groups. In case of gold electrodes, a monolayer can be formed through diazonium salts [65] or cystamine [66]. For glassy carbon intermediate a layer which is used for further modification can be obtained by amines or arylacetates, aryl diazonium cations [67] or by 4-aminobenzoic acid [68].
3. *Langmuir-Blodgett (LB) monolayer formation*, reached by transferring of a surface-active compounds on a substrate from the liquid/air interface [69–71].
4. *Deposition of polymers* which have i) multiple electroactive sites (i.e. poly(vinylferrocene) [72]), ii) groups to attach electroactive species to polymer matrix, iii) sites with ion-exchange properties (i.e. Nafion [73]), iv) electronically conductive properties [74], v) biological origin (i.e. enzymes [75] or other proteins), vi) capability to form blocking polymers from given monomers.
5. *Deposition of* metal oxide *films*, clays and zeolites, *other complex coatings* [62].

Apart from the chemical nature of coating, thickness (that typically varies from nanometres to thousand nanometres) and morphology of the film are two other factors that can influence the performance of the electrode and therefore they must be controlled [61].

1.2.1 Electrode modification by mesoporous silica films

Surface modification of electrodes by mesoporous silica thin films gives wide spectrum of advantages in terms of application. The use of mesoporous silica systems was studied for anti-corrosion coatings for Zn [76]. Thicker films were protecting metal surface from degradation much better and it shows that this approach can help to increase the durability of metal electrodes. For the analytical application comparison between bulk and porous silica coatings demonstrates that porous analogues provide much easier access of analysed species and, hence, improved the mass transport [77].

Owing to these properties and to feasibility of homogeneous modification by one-pot co-condensation mesoporous silica expanded the areas of film usage for detection of various analytes like gases (including humidity sensors and sensors for alcohol detection), heavy metals and organic molecules. Mesoporous films modified by β-cyclodextrin were used for benzene detection using quartz crystal microbalances [78], unmodified films showed sensitivity to relative humidity from 30 to 70% based on conductivity changes as a result of water adsorption [79] and to alcohols by current variation after potential application [80]. Modification of mesoporous silica surface by co-condensation with triethoxysilyl-propyl-5-mercapto-1-methyl-tetrazole allowed accumulation of Hg(II) at low values and its following analysis by anodic stripping square wave voltammetry [81]. The limits of Hg(II) detection by using this electrode is 2 nM. Targeted preconcentration of mercury ions was also provided by 3-mercaptopropyltrimethoxysilane-functionalised silica film [82]. Furthermore, it was shown that templating by organic molecules instead of surfactant (i.e. dopamine) can improve the recognition of this particular analyte when using sol-gel silica film [83]. In all cases, films were deposited by spin-coating [78,81–83] or dip-coating technique [79,80].

Moreover, immobilisation of proteins such as cytochrome c [84] and haemoglobin [85] triggered a development of biosensors for reduction of oxygen [86] or hydrogen peroxide [84–86] same as oxidation of ascorbic acid [84]. In the case of cytochrome c, the use of block copolymer was enough to provide amine-functionalised silica film with suitable diameter of pores to accommodate

protein by impregnation without losing its electrochemical activity [84]. Immobilisation of haemoglobin required larger pores, hence more complicated system based on silica particles with bimodal pore distribution and chitosan was used [85]. Films were obtained by placing and drying a drop of suspension containing bimodal silica particles, chitosan and haemoglobin on the glassy carbon electrode. Composite materials based on mesoporous silica films were also studied extensively. Incorporation of nanoparticles inside silica matrix makes material with high surface area a perfect choice for catalytic systems. It was demonstrated on example of Au-modified mesosystem for glucose oxidation, where due to gold nanoparticles oxidation of analyte became possible [87]. Under the optimised conditions, limit of detection of glucose was estimated to be 0.1 mM.

In terms of electrochemical performance, presence of mesoporous silica film is known to affect the cyclic voltammetry signal of redox probes. There are two main reasons to this. The first is related to nature of silica matrix, which is not completely inert [13]. All over its surface there are silanol groups, which are charged differently according to pH of solution. The transition of a silanol group from highly acidic pH to alkaline can be described as following: $-Si-OH_2^+ \rightarrow -Si-OH \rightarrow -Si-O^-$. Although this process does not occur equally to all surface groups due to their different environment, prevailing charge determines the film behaviour. Too high and too low pH lead to silica dissolution, therefore these conditions are typically avoided [88]).

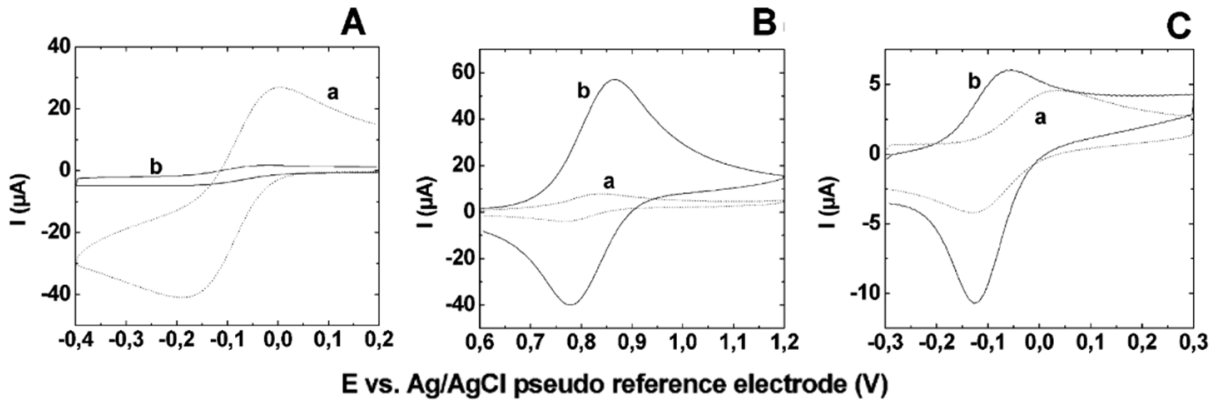

Figure 7 – Cyclic voltammetric curves recorded in 0.05 M hydrogen phthalate solutions (pH 4.1) containing (A) 0.5 mM $Fe(CN)_6^{3-}$, (B) 50 μM $Ru(bpy)_3^{2+}$ and (C) 50 μM FcMeOH at a bare ITO electrode (dotted lines) and an ITO electrode covered by surfactant-extracted mesoporous silica thin films with cubic symmetry (plain lines) (adjusted from [89])

Mostly, the detection is performed in media with pH close to neutral, therefore negative charge of silica surface is expected. The effect of probe charge on CV response was studied for EISA deposited films with cubic symmetry and CTAB used as a template [89]. For negative, positive and neutral probes $Fe(CN)_6^{3-}$, $Ru(NH_3)_6^{3+}$ and ferrocene methanol (FcMeOH) respectively were chosen by authors. Prior to electrochemical tests, surfactant was extracted by calcination to open mesopores.

Indeed, at the working pH (pH =4), negative charge of silica surface caused by deprotonation of the silanol groups that lead to $Si\text{-}O^-$ formation prevents the diffusion of $Fe(CN)_6^{3-}$ (*Figure 7A)*. Therefore, film acts as a permselective barrier against anionic species. On contrary, positively charged redox probe diffuses and tends to accumulate inside silica pores giving higher electrochemical signal because of the electrostatic interactions, what was shown on example of $Ru(bpy)_3^{2+}$ on *Figure 7B.* Neutral species (like FcMeOH) can be detected on the electrode as well as positive probe due to their diffusion with an additional aspect. Oxidation of FcMeOH leads to formation of ferrocinium $FcMeOH^+$, which accumulates on silica surface because of the gained positive charge increasing cathodic peak current as it is illustrated on *Figure 7C*).

The second source, which has an influence on CV signal, is morphology of mesoporous silica film. This parameter affects diffusion of species through coating. In this way, the mass transport of analysed molecules from solution to the electrode surface can be deteriorated, resulting in signal reduction if less molecules can reach the electrode. The effect of mesoporous deposit structure was investigated on films obtained by EISA with dip-coating deposition [89]. During film preparation relative humidity was controlled from 40 to 70% in order to form 2D and 3D hexagonal or cubic mesophases. Surfactant was removed by calcination before recording electrochemical signal from $Ru(bpy)_3^{2+}$, which was chosen to study permeability. It was demonstrated that among deposited coatings the fastest mass transport rate was reached for cubic structure [59,89].

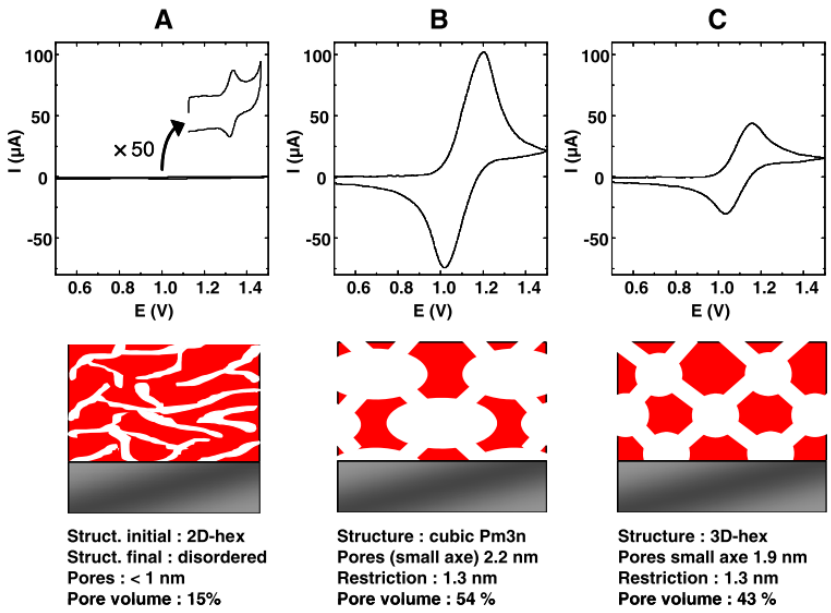

Figure 8 - Cyclic voltammograms recorded in a solution containing 0.5 mM $Ru(bpy)_3^{2+}$ (in 0.05 M hydrogen phthalate solutions at pH 4.1) using ITO electrodes covered by mesoporous silica thin films with (A) 2D-hexagonal, (B) cubic, and (C) 3D hexagonal symmetry [59]

This suggestion is based on the largest current CV peak intensity obtained with $Ru(bpy)_3^{2+}$ probe (*Figure 8B*). Similarly, the mass transport was evaluated for mesoporous films with 2D and 3D hexagonal structure (*Figure 8 A and C* respectively*)*. Electrochemical results suggest that 2D hexagonal system is the least adaptable for diffusion of reactive species.

1.2.2 Mesoporous silica films with vertically oriented pores for electrochemical application

The fact that conductive electrode surface was covered by non-conductive film may have a negative impact on electrochemical response in solution [59]. A presence of mesoporous film hindered the mass transport of analysed species to the electrode surface because the coating was acting as an obstacle due to the charge of the material surface, the pore shape and orientation. In spite of these limitations, mesoporous films stay interesting because of the provided access for guest species of organic and inorganic nature and preconcentration behaviour which increases sensitivity of electrochemical detection [59]. Since the pore size was an easily tuneable parameter [90,91], the main complications which were noticed were related to morphology and orientation of pores [92]. This is why it was suggested that perpendicular arrangement of channels would be more favourable for mesoporous silica films use as electrode coatings.

Silica films with perpendicular pore orientation were obtained by application of a high magnetic field [93,94]. The vertical film organisation from acidic aqueous solution containing TEOS silica precursor and template (be it CTAB, Brij 56 or P123 triblock copolymer) takes place owing to the influence of magnetic field on rod-shaped self-assembled surfactants which possess magnetic anisotropy. Pore diameter was determined by the chain length of used template. The disadvantage of this method is a necessity to have a specific apparatus for the film generation.

Another presented approach used block copolymer to form porous template by spin-coating with subsequent deposition of TEOS precursor in humidified supercritical CO_2 [95]. This method did not find a wide application: in addition to two-step procedure, which implies pre-deposition of copolymer, pores of formed silica material are not perfectly homogeneous.

An interesting method of deposition of mesoporous platinum films using potential-controlled assembly of surfactant coupled with an electrodeposition process was reported back in 2003 [96]. It was successfully shown that at certain potential two parallel processes can occur: organisation of surfactant-inorganic matrix and reduction of metal ions, leading to generation of porous film. In this light, classical potentiostats can be used for the film deposition in one step.

Stöber film deposition

Stöber method is another way to deposit continuous mesoporous silica thin films (MSFs) with 2D-ordered hexagonal mesostructure parallel to support. It was presented by Teng and Zhao [97] with suggested mechanism of the film growth illustrated on *Figure 9*.

This procedure includes immersion of the electrode substrate in hydro-alcohol solution, which contains silica precursor (TEOS), template (CTAB) and ammonia. It was assumed that the assembly of the film starts from the support by adsorption of self-assembled CTAB spherical micelles, unlike for EISA method where rod-shaped micelles are acting as template. Then, negatively charged hydrolysed silica precursor arranges around cationic template to form a deposit.

The specific role of ammonia in this sol is to catalyse the transition from spherical to cylindrical micelles. Further it drives the formation of cylindrical pores, which are vertically oriented to the substrate. Resultant film possesses high surface area typical for mesoporous materials (calculated

value 834 m^2g^{-1}) and narrow pore size distribution determined by chosen surfactant (i.e. 2.3 nm for CTAB).

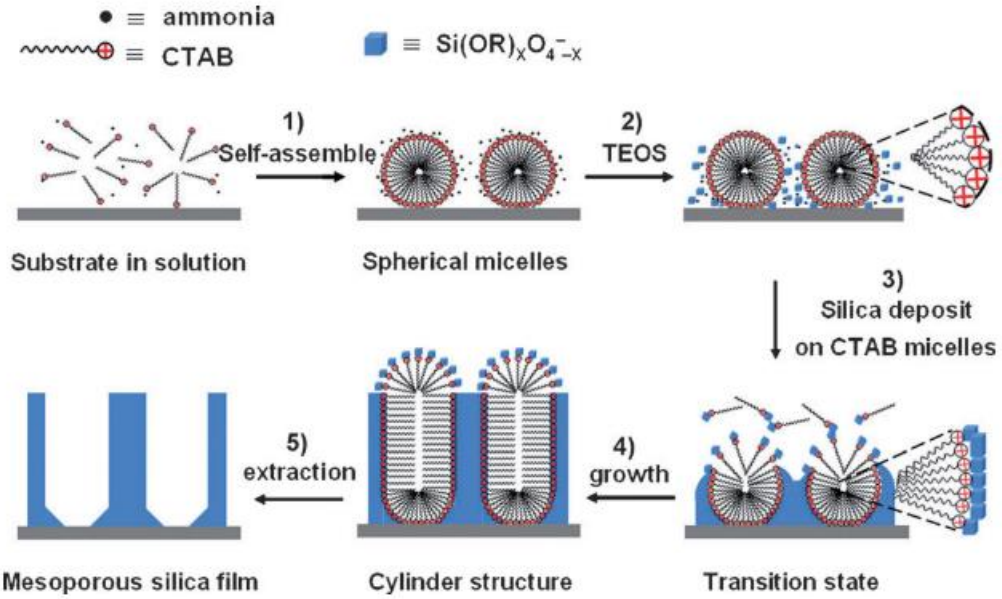

Figure 9 - Formation process of ordered mesoporous silica films with perpendicular mesochannels by the Stöber-solution spontaneous growth procedure [97]

Recent modification of Stöber deposition approach demonstrated that addition of the oily phase (such as decane [98] or cyclohexane [99]) to TEOS – CTAB – EtOH ammonium solution leads to formation of mesoporous silica films with larger pores. The pore extension became possible because of the interaction between cationic surfactant and added organic component. Basically, oil molecules like decane are accumulating inside hydrophobic phase of CTA^+ micelles, increasing their size. In turn, it results in formation of mesoporous silica material with pore range from 2.8 to 11.8 nm in diameter, which can be adjusted by quantity of added organic solvent (cyclohexane, [99]).

Electro-assisted self-assembly (EASA) film deposition

Inspired by publication of Sucky et al. [96], Walcarius et al. introduced to the world an EASA (Electro-Assisted Self-Assembly) method [1] to obtain MSFs with pores perpendicularly oriented to the support using a combination of sol gel process and electrochemical deposition.

A typical sol for the EASA film preparation is based on the water-ethanol solution, hydrolysed under acidic pH silica precursor and surfactant in concentration higher than CMC (*Figure 10, A*). Cationic surfactants are preferential to be used as a template and arguments for this will be given

further. Unlike for EISA film deposition, solution composition additionally includes a supportive electrolyte (usually $NaNO_3$), which provides enough conductivity for electrodeposition. A film generation itself is initiated by the application of the defined potential, which depends on the electrode nature.

Under the reductive potential, two parallel processes occur. The first one is the reduction of water, which releases hydroxide anions (OH^-) in the pre-electrode area, increasing the pH locally approximately to 9 (see it on *Figure 10*, *B1*). Due to the alkaline pH, the rate of silica condensation drastically increases near the electrode [23]. The second process is self-organisation of surfactant micelles on the electrode, which drives the film growth (*Figure 10*, *B2*). Since for the film deposition negative potential is applied to the electrode, its surface is charged negatively. Therefore, having specifically cationic surfactant in solution in the form of pre-assembled micelles ($C_{surfactant}$ > CMC) triggers a self-organisation on the electrode because of the favourable charge interaction. Further arrangement of silica precursor around soft template happens due to electrostatic attraction between positive micelles of surfactant and negative charge of hydrolysed silica, leading to vertical film growth (*Figure 10*, *B2-D*).

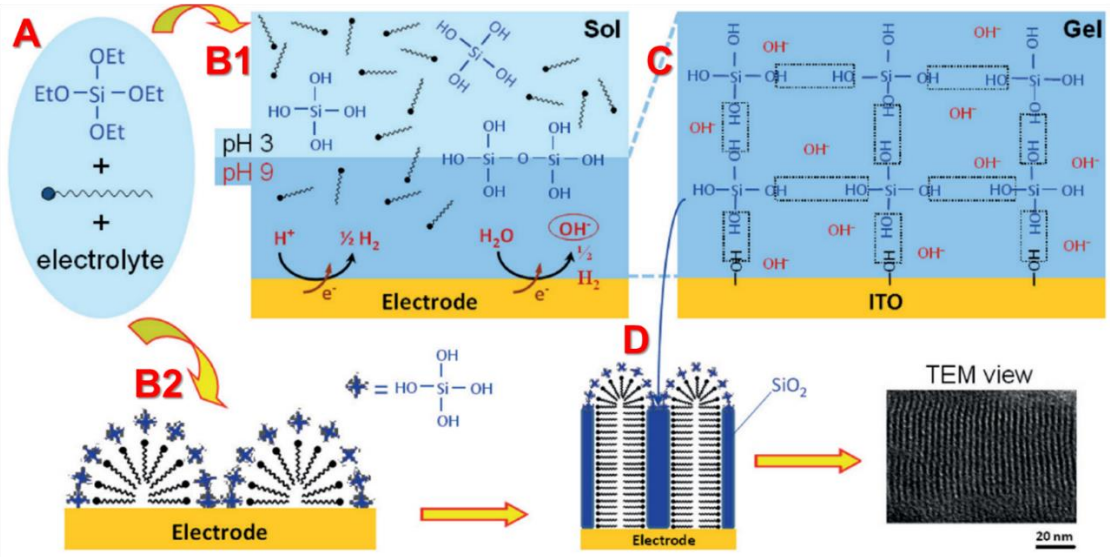

Figure 10 - Schematic representation of the Electro-Assisted Self-Assembly (EASA) method used to generate ordered and vertically-aligned sol-gel-derived mesoporous silica thin films
A – sol preparation, B1 – generation of OH^- catalyst, B2 – self-assembly of cationic surfactant, C – condensation of silica precursor, D – schematic and TEM cross-view of film with vertical pore orientation (adjusted from [100])

The diameter of mesochannels can be regulated by changing the surfactant. The longer aliphatic chain forms pores of bigger diameter. Lattice parameter was tuned from 3.8 to 4.6 nm using surfactants with number of Carbon from C_{14} to C_{18} [2].

1.2.3 Functionalisation of vertically oriented mesoporous silica films

Homogeneous distribution of functional groups on silica surface is reached by co-condensation. It implies the addition of co-precursor with selected functional group to sol solution with main precursor (usually TEOS or TMOS) before the film deposition be it electrodeposition by EASA or film formation by Stöber-related methods.

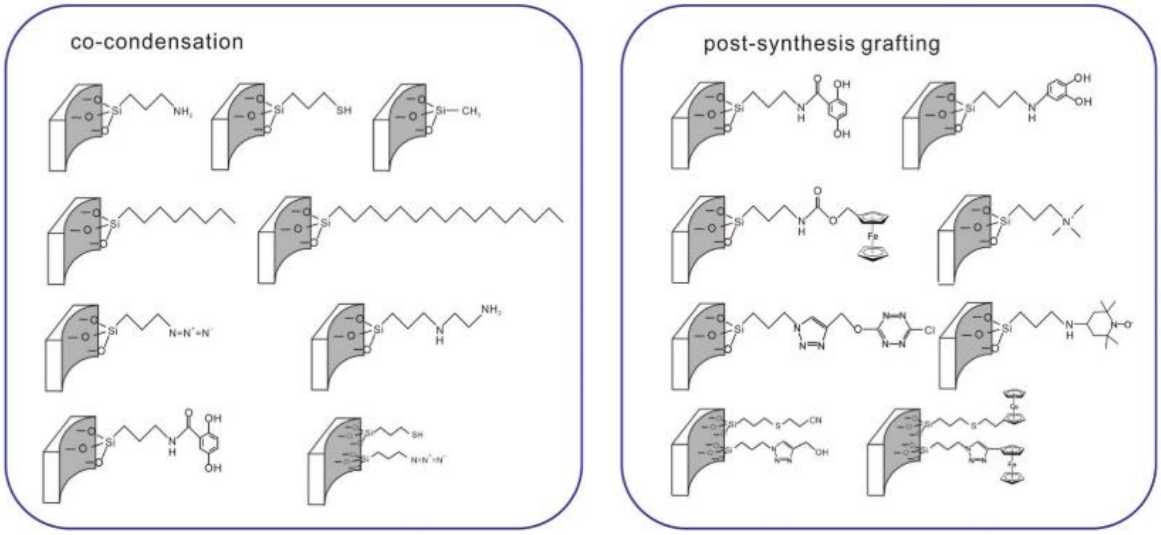

Figure 11 - Various organo-functional groups for the functionalisation of silica mesochannels walls by co-condensation and post-synthesis grafting routes [101]

To keep the hexagonal mesostructure of silica films, not more than a particular amount of chosen organosilane must be added:

- amine ($-NH_2$): 10% [102];
- methyl ($-CH_3$): 60% [104];
- thiol (-SH): 10% [106];
- azide ($-N_3$): 40% [107];
- ethylenediamine ($-NH-(CH_2)_2-NH_2$): 8% [103];
- hexadecyl ($-C_{18}H_{37}$): 5% [105];
- octyl ($-C_8H_{17}$): 20% [105].

If the ratio between TEOS and co-precursor is higher than the one which is given above, the structure of films becomes disordered and non-porous.

Specific interest is given to thiol and azide-functionalised films since they can provide the further post-functionalisation due to their reactivity. In particular, the reaction of 1,3-cycloaddition in presence of copper(I) catalyst that occurs between azide functions and alkynes demonstrated a good efficiency for film grafting. Using this approach, ethynylferrocene [108,109] and propargyl derivative of tetrazine [110] were covalently bonded inside pores. More details about this reaction is presented in **Section 2.2.4**. An example of amine-catalysed thiol-ene click coupling was shown on bifunctional silica film functionalised by azide and thiol groups by prior co-condensation [111]. Two sequential click reactions were conducted by $-N_3$ and -SH functions to obtain grafted cobaltocenium and ferrocene moieties.

Using post-synthetic grafting (*Figure 11*) it was possible to introduce ammonium [112], hydroquinone [113] and ferrocene moieties [114]. Generally, this type of reaction requires prior drying of silica surface to remove physically adsorbed water so that the rates of reaction will not be affected by hydrolysis of silane. Modification with R' species occurs in dry organic solvents following the reaction between silanol groups of silica surface -SiOH and trialkoxy- sites of chosen silane R'-$Si(OR)_3$.

Co-condensation and post-grafting are classical approaches for modification of silica surface. Nevertheless, the first is more widely used for functionalisation of vertically oriented mesoporous films. The reason behind it is inhomogeneous modification of channels by post-grafting approach. It can lead to more grafted surface on the top of the channels and less grafted in the bottom [101].

1.2.4 Practical application of vertically oriented mesoporous silica films

Owing to specific pore morphology and orientation, and feasibility to functionalise films with vertical pore alignment, multiple ways of their utilisation were discovered [8]. Oriented mesoporous silica films can be used in four main conditions: with surfactant inside pores, as semi-permeable membranes after support removal, after its extraction, and after functionalisation.

The use of surfactant-containing films on the electrode support is presented on *Figure 12A*. Due to their anti-biofouling capacity, small pore size, lipophilicity, charge selectivity and preconcentration abilities they can be used for detection of small molecules in complex systems (i.e. chloramphenicol in human blood [115]). Another study [116] showed their utility for trace nitroaromatic explosives as well as for pesticide detection. Incorporated surfactant in described

cases assists in preconcentration of analysed species increasing the sensitivity of voltammetric detection.

After the support removal film was used as a membrane (*Figure 12B*) for selective transport of species (specifically shown for metoprotol [117]) between two liquid phases promoted by electrochemically-induced transfer. Films obtained by oil-induced Stöber deposition exhibited an excellent performance in separation of nanosized gold nanoparticles and proteins [99].

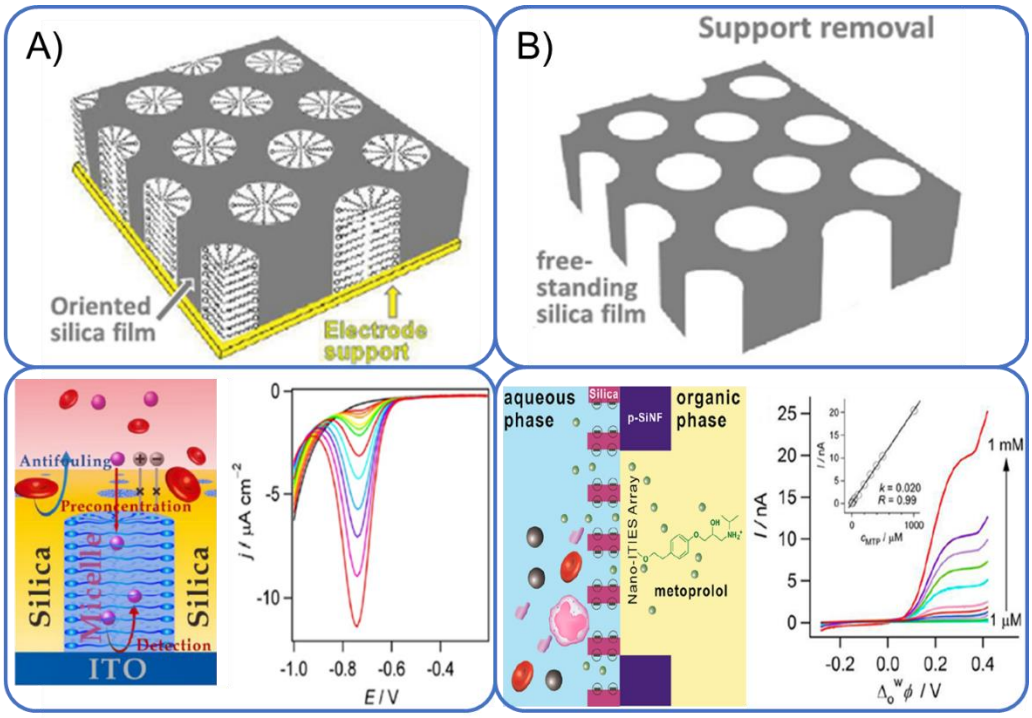

Figure 12 – Application of silica films (A) with soft template inside pores and (B) as semi-permeable membrane (adjusted from [8])

Films after surfactant extraction can be applied as size-exclusion molecular sieves [118] (*Figure 13A*). Due to the fixed pore size, molecules, which have larger diameter than that of silica pores, cannot diffuse through coating. The permeability of species was controlled by cyclic voltammetry signal that was present if analysed molecule was small enough to penetrate through channels. When the redox probe was larger than silica pore, no electrochemical signal was detected. Another possible application is as matrix for pre-concentration of cations showed on example of paraquat [119]. It was demonstrated that due to accumulation of positively charged analyte in mesoporous silica film the sensitivity of pesticide detection was increasing almost by 30 times compared to bare glassy carbon electrode. Large surface area of film also allowed an incorporation of

$Ru(bpy)_3^{2+}$ luminophore because of the electrostatic interactions for sensing of amines. This approach demonstrated 107-folded increase of the electrochemiluminescence signal compared to that on bare ITO electrode [120].

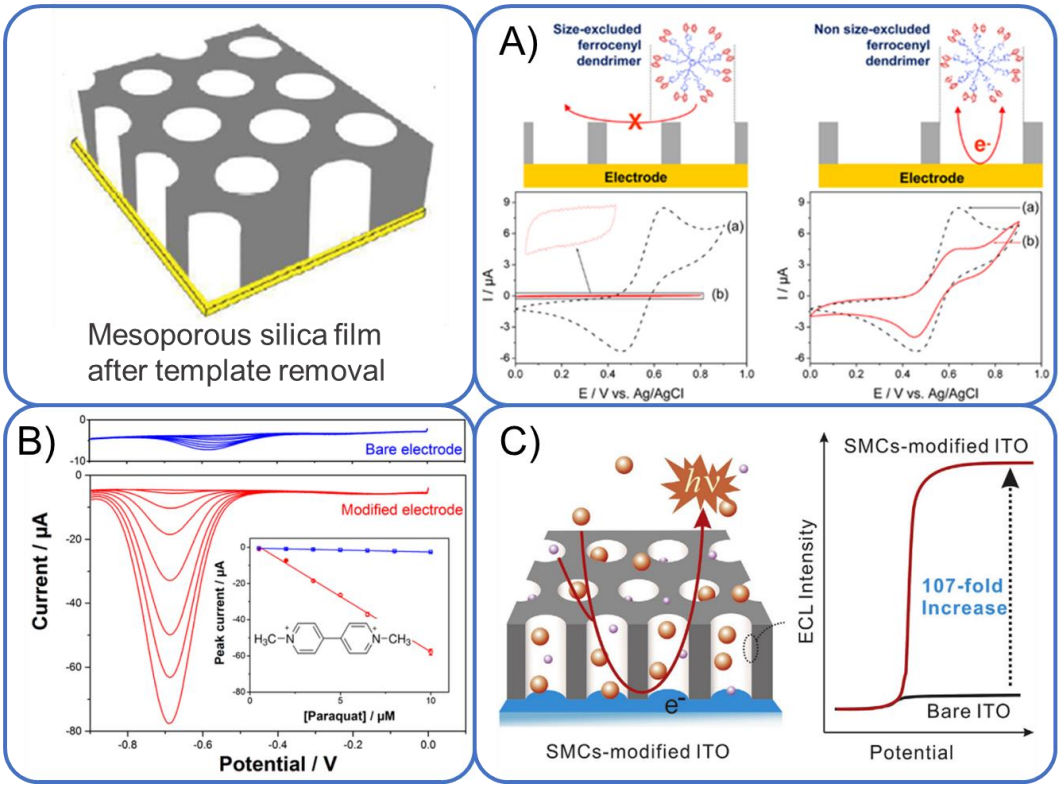

Figure 13 – Application of silica films after soft template removal as (A) size-exclusion molecular sieves, (B) as matrix for pre-concentration and (C) incorporation of luminophores (adjusted from [8])

Examples of functionalised mesoporous silica film application are illustrated on *Figure 14*. Introduction of functional groups finds an application in electrocatalysis and positively affects the sensitivity in detection of analyte. Particularly, polyaniline-nanowire system in couple with mesoporous film (*Figure 14A*) was applied for electrocatalysis of ascorbic acid [121]. Non-redox anions that cannot diffuse through negatively charged silica film could be finally indirectly detected using ferrocene functionalised mesoporous films by flow-injection analysis [109] (*Figure 14B*). A long sequence of film modification, which included post-synthesis grafting with active epoxy groups, allowed further covalent immobilisation of capture DNA probe via primary amine group of its nucleic acid [122]. This electrode was then used to detect target DNA in presence of which hybridisation with grafted species occurs. As pores become blocked by large molecules, no redox peak of $Fe(CN)_6^{3-}$ is observed because it cannot diffuse through channels to Au electrode

(*Figure 14C*). Authors are claiming that using this method nanomolar levels of DNA can be detected. Recent publications report also about a detection of hydrogen peroxide by iron-triazole modified films [123]. Additionally, ferrocene functionalised mesoporous electrode coating can be applied for analysis of cysteine [124].

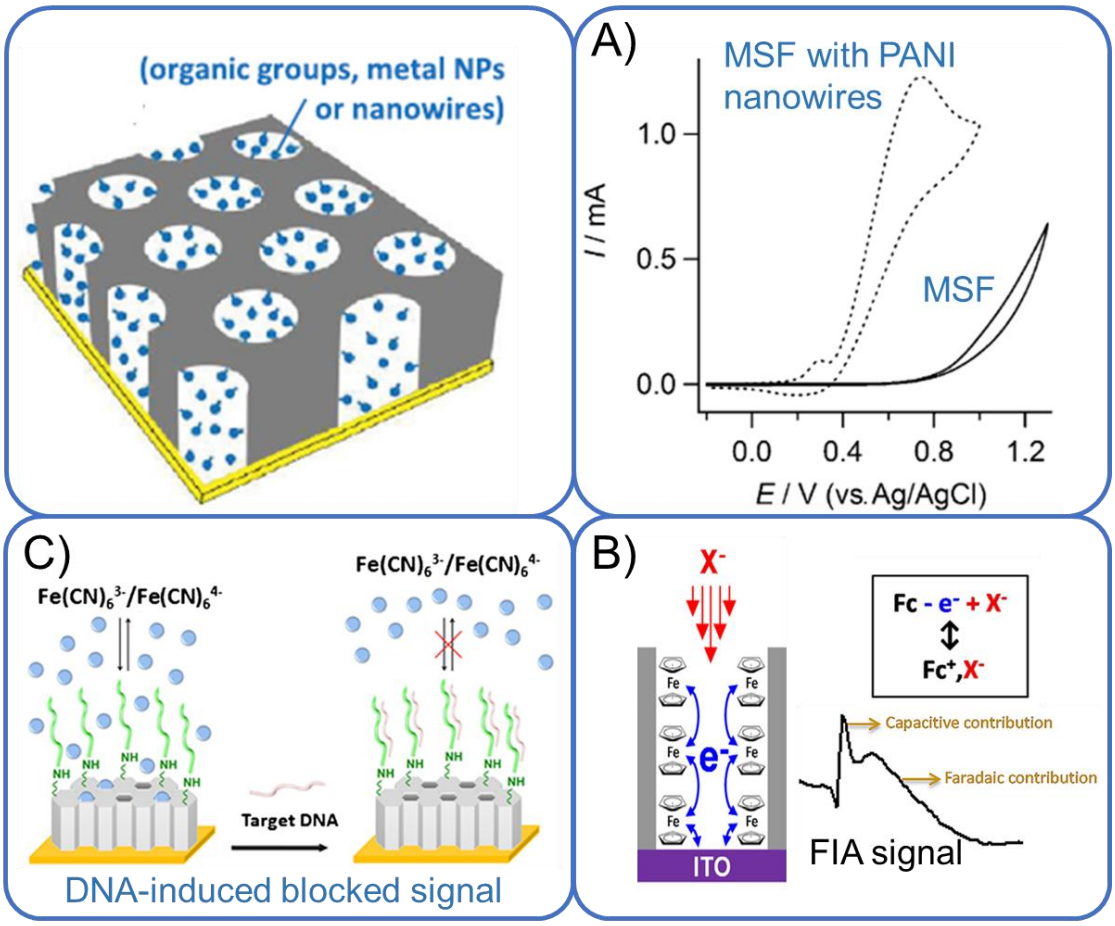

Figure 14 – Application of functionalised silica films with (A) polyaniline (PANI) nanowire, (B) ferrocene electroactive moieties and (C) incorporation of luminophores (adjusted from [8])

1.3 Our research project

As it was shown, mesoporous silica materials are nowadays of big interest due to their variety of pore structures, accessibility of shapes which they can take after being synthesised, diversity of surface chemistry along with stability of hard matrix (in pH range from 2 to 8) and, hence, applicability in wide spectrum of domains. The use of mesoporous silica in form of continuous film is one of the promising directions, which is rapidly developing, especially in the field of electrochemistry for the electrode modification. However, in order to use these electrode coatings, it is necessary to provide a good mass transport, which will not be interfered by deposited layer. Vertical orientation of mesopores was proved to be a beneficial morphology for this purpose. By now, several approaches for synthesis of mesoporous silica film with perpendicular orientation of channels were reported. All of them resulted in material with vertically standing pores that showed a potential to be used in electroanalytical analysis. Electrodeposition by EASA method seems a flexible and fast way to obtain uniform films with long-range hexagonal order on surfaces and to bring an interesting reactivity to the electrode. However, the non-inert silica material can interfere the electroanalysis. The objective of this work is to decrease the thickness of the silica film to reduce its influence, but at the same time to maintain its good organisation to continue benefiting its chemical properties. In the first part, we determined the minimal thickness of well-organised mesoporous silica films, which were obtained by EASA from a sol containing 100 mM silica precursor. To obtain thinner coatings, we investigated the wet etching with soft reactant, i.e. NH_4F. We studied the effect of the nature of the starting film, in particular the effect of the surfactant kept inside the silica pore or not, the nature and the concentration of the etchant. Finally, we were interested in performing a glyphosate detection by combining the silica film formation onto ITO electrode, its surface modification and thickness management.

Chapter 2

Experimental part

2.1 Instrumental techniques

2.1.1 Electrochemistry

Chronoamperometry

Chronoamperometry is a time-dependant technique during which a square-wave potential is applied to the working electrode (*Figure 15*). Current response is then detected over a time under potentiostatic control [1]. Chronoamperometry can be performed by single or double potential step. The first approach allows an electron transfer process to undergo up to its completion (*Eq. 2.1*), when the second is a reversal technique, which includes the re-oxidation of the previously generated species (*Eq. 2.2*). Consequently, on *Figure 15* the single potential step chronoamperometry is depicted for time $t < \tau$ and double potential step process is the one for $t > \tau$. For a diffusion-controlled process occurring at a planar electrode the recorded current is proportional to the concentration of redox species in solution. It undergoes a decrease with longer time of potential application. It is fair for both anodic and cathodic currents depending on the reaction which takes place at the electrode. A specific attention must be paid to the representation of cyclic voltammogram: the values of currents for American community are $i_a < 0$ and $i_c > 0$, (as it is on *Figure 15*), whereas the rest stick to IUPAC standard with the opposite current values ($i_a > 0$ and $i_c < 0$).

$$Ox + ne^- \rightarrow Red \quad (Eq.\ 2.1)$$

$$Red - ne^- \rightarrow Ox \quad (Eq.\ 2.2)$$

This technique is normally used to identify mechanisms of redox reactions in diffusion-controlled processes. Nevertheless, the formation of new species at the electrode surface can be also used for the local catalysis in pre-electrode area. In this light, mesoporous silica films deposition was carried out in the chronoamperometry mode. While potential application (–1.3 V/Ag, ITO), reduction of H^+ takes place from acidic hydroalcoholic solution (*Eq. 2.3*) along with the generation of OH^- catalyst occurs at the electrode surface (*Eq. 2.4)*:

$$H^+ + e^- \rightarrow \tfrac{1}{2}\, H_2 \quad (Eq.\ 2.3)$$

$$H_2O + e^- \rightarrow \mathbf{OH^-} + \tfrac{1}{2}\, H_2 \quad (Eq.\ 2.4)$$

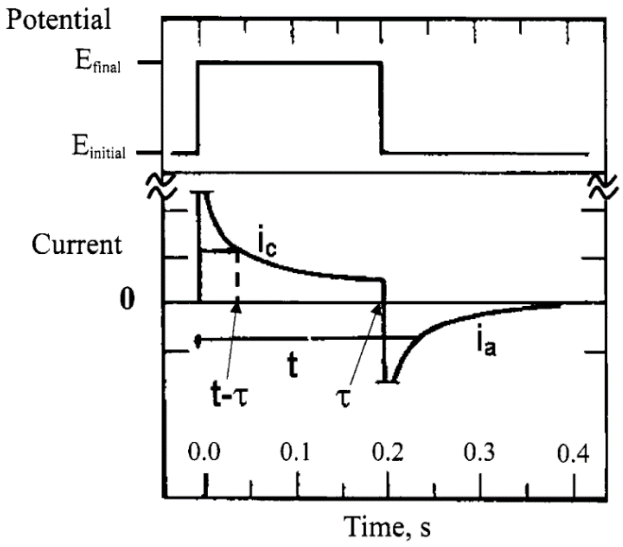

Figure 15 – Chronoamperometric double potential step experiment for the process: Ox + ne^- ⇆ Red; inversion time τ = 0.2 s. The top part shows the perturbation of the potential applied to the working electrode with time [125]

Potentiostat μAutolab provided with GPES software was used to generate films. An adapted three-electrode setup (illustrated on *Figure 16*) with ITO working (WE), stainless-steal counter (CE) and silver pseudo-reference electrodes was used for deposition of MSFs. Films with 10 or 14 mm of diameter can be deposited by adapting the top part of the cell.

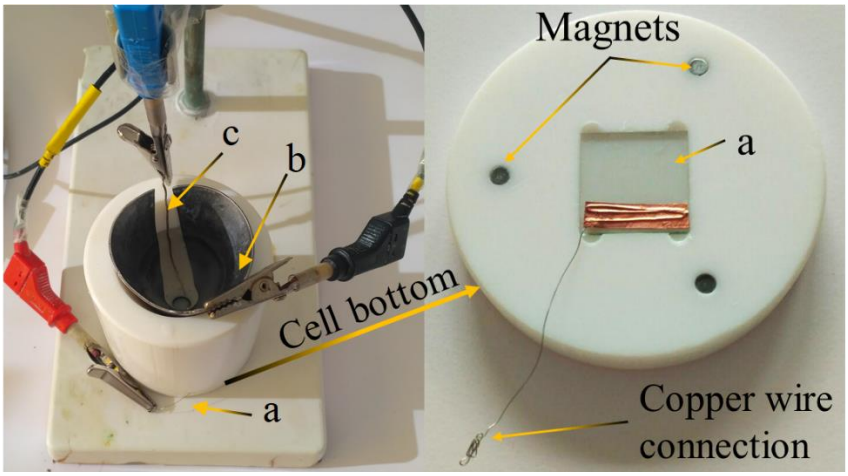

Figure 16 – Photo of the homemade three-electrodes cell for silica film deposition a) ITO plate as working electrode, b) stainless steel (counter electrode) and c) Ag wire as pseudo reference electrode

Cyclic voltammetry

Cyclic voltammetry (CV) is one of the most popular electrochemical techniques. It is based on variation of potential applied to the working electrode, which is immersed in solution. As a result, the change of current is recorded under stationary conditions to keep preferable diffusive mass transport.

Since the potential is changed linearly in time, CV belongs to linear potential sweep chronoamperometric methods. The measurement is carried out from an initial potential E_i (*Figure 17a*), where no current flows in the system ($i = 0$, no redox reaction takes place). The linear change of potential at constant scan rate (marked as v) performed to final value E_f results in a forward peak. After reaching E_f, a reversed scan is recorded under the same conditions of potential sweeping and the measurement stops at E_i. In case of presence of redox species in solution, current starts flowing in a system giving rise to a specific curve called cyclic voltammogram (illustrated on *Figure 17*). With respect to the redox reaction occurring, current can be anodic (represents an oxidation, forward peak on *Figure 17a*) or cathodic (refers to reduction of species, reversed peak on *Figure 17a*).

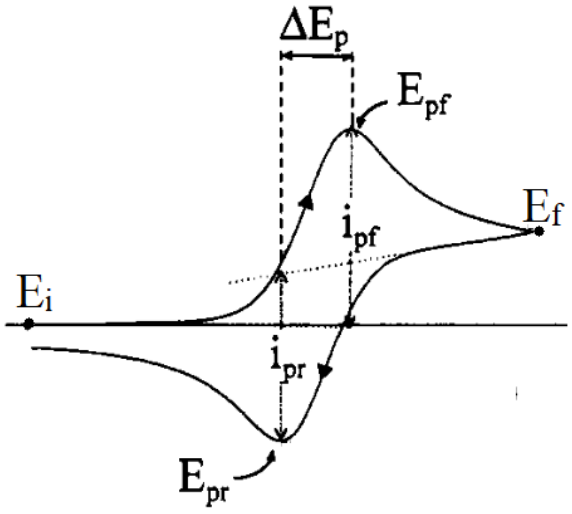

Figure 17 – General shape and basic parameters for a cyclic voltammogram: E_{pf} = potential of the forward peak, E_{pr} = potential of the return peak; range of scanning from E_i = initial to E_f = final potentials; i_{pf} = current of the forward peak with respect to its baseline; i_{pr} = current of the return peak with respect to its baseline; ΔE_p = peak-to-peak separation (modified from [125])

Randles-Sevcik equation (*Eq. 2.5*) expresses the relation between peak current and such parameters as diffusion coefficient, concentration of redox probe and potential scan rate:

$$i_p = 2.69\ 10^5 n^{3/2} A D^{1/2} \nu^{1/2} C \ (Eq.\ 2.5)$$

where:

i_p – peak current (A)

n – number of electrons which take part in electrochemical reaction

A – area of the electrode (m^2)

D – diffusion coefficient of redox probe ($m^2\ s^{-1}$)

C – concentration of redox probe (mol m^{-3})

ν – potential scan rate (V s^{-1})

CV allows to extract information about redox system based on three main parameters: potential at which the electrochemical reaction occurs, value of current recorded as a result of electron transfer of redox species and the shape of CV curve. In terms of electrochemical process itself, it can be characterised as reversible, irreversible or quasireversible. Three typical cyclic voltammograms related to these cases are illustrated on *Figure 18*.

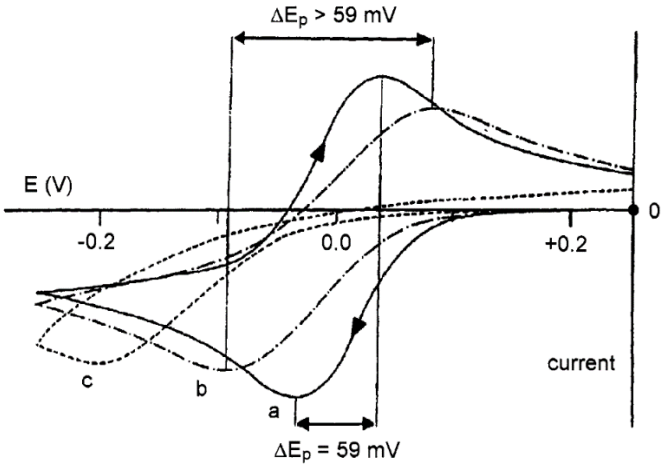

Figure 18 – Typical cyclic voltammetric profile of a) a reversible b) quasireversible c) an irreversible system at 25°C [125]

Reaction is electrochemically reversible when the rate of mass transport is lower than the rate of the electron transfer. It is achievable by maintaining following criteria: (i) the potential of forward peak Ep_f is independent of the scan rate, (ii) the peak-to-peak separation ΔE_p at 25°C is equal to

59/n mV (calculated from *Eq. 2.5*), (iii) a ratio between the current of the forward peak and square root of the scan rate ($i_{pf}/v^{1/2}$) stays unchangeable and (iv) the ratio between currents of forward and reverse peaks is constant and equal to 1. A typical curve for a reversible system has a shape as the one illustrated on *Figure 17, curve a*.

Irreversible process results in much lower electron transfer in comparison to the mass transport. As a result, a larger peak-to-peak separation is observed (even up to the moment, when the reverse peak is not detectable as it is illustrated for curve *c* on *Figure 17, curve c*. For such systems, the peak potential shifts with the scan rate, the current function $i_{pf}/v^{1/2}$ stays the same and no constant current ratio i_{pf}/i_{pr} is observed. For quasireversible process the rates of mass transport and electron transfer are relatively equal. These systems are behaving in between reversible and irreversible processes. As a result, typically the peak-to-peak separation is more than 59 mV/s (a case of a curve *b* on *Figure 17, curve b*). At higher scan rates forward peak potential shifts causing larger ΔE_p. Additionally, the current of a forward peak rises as a function of $v^{1/2}$ (not necessarily linearly).

Cyclic voltammetry is a very useful technique for the preliminary determination of the redox species and their electrochemical behaviour. It gives quantitative and qualitative information about electroactive components in solution and allows to study their stability in solution. Therefore, it was chosen as one of the main techniques for the further research.

Characterisation of the deposited silica films, of their chemical modification and the feasibility of electrochemical detection of analytes were performed in cyclic voltammetry mode either on EMStat 2 PalmSens (PSTrace software) or on μAutolab (GPES software). The classical three-electrode system with stainless-steel counter electrode (CE) and Ag/AgCl reference electrode (RE) (or Ag wire as a pseudo-reference electrode) was applied in a home-made cell *Figure 19*. In case of recording a response from mesoporous silica film covered ITO electrode, only a part of it stays in contact with solution, what is defined by the o-ring with diameter 5 mm.

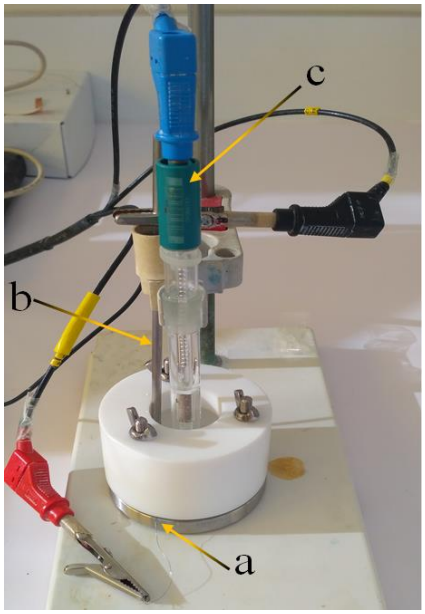

Figure 19 – Setup for the electrochemical characterisation of mesoporous silica films deposited onto ITO plate with positions for a) ITO WE, b) stainless steel CE and c) Ag/AgCl RE

2.1.2 Spectroscopy

Fourier Transform Infrared spectroscopy (FTIR)

The infrared (IR) spectroscopy as analytical technique is used to identify the functional groups. Instrumental setup includes the source of light, interferometer and detector (*Figure 20*). Fourier transformation is used to convert obtained raw data (interferogram) into IR spectrum. Qualitative analysis is conducted mostly in the mid-infrared region (from 4000 cm^{-1} to 400 cm^{-1}), where adsorption of such emitted IR light causes changes in vibrational energy state of many functional groups, giving characteristic signals [126].

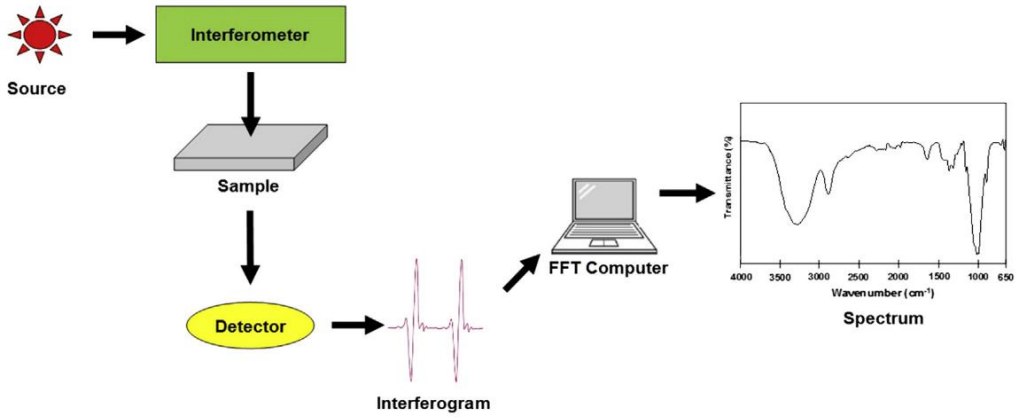

Figure 20 – Basic component in Fourier Transform Infrared spectrometer [127]

Nicolet 8700 spectrometer equipped with a diffuse reflectance accessory was used to characterise the surface of MSFs functionalised with organic functional groups. Spectrum of unmodified ITO plate was recorded as a background before collecting spectra from modified films. No sample preparation was required.

X-Ray photoelectron Spectroscopy (XPS)

X-Ray photoelectron Spectroscopy (XPS) is a standard surface characterisation technique. It requires an X-Ray source of light with constant excitation energy during the experiment and high vacuum. After contact of photons with sample, an emission of excited electrons from the core levels (such as *s, p* and *d*) occurs. Each electron has its own binding energy, which defines a kinetic energy with which they are passing through electron analyser to be further detected (*Figure 21*). Obtained plot is represented as the number of electrons at a specific binding energy. Since each type of element has a unique distribution of core levels, each registered peak corresponds to a particular element, providing semi-qualitative data about elemental composition of upper layer (in the range of nanometres) of solid samples. Additionally, XPS delivers the information about quantity of elements which are present.

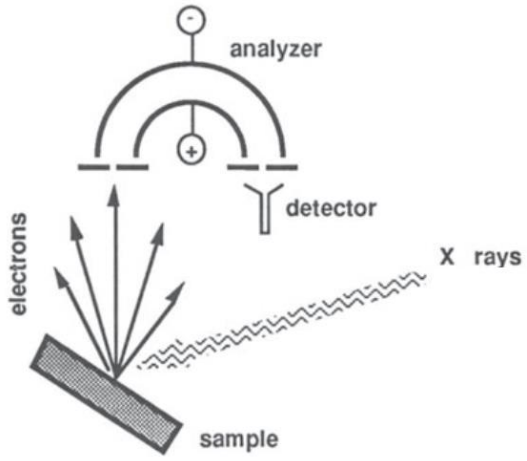

Figure 21 – Simplified sketch of the basic setup of a photoelectron spectrometer for XPS (adjusted from [128])

Characterisation of samples was conducted to determine the elemental composition of sample's surfaces. The presence of silica deposit and its homogeneity were monitored by changings of the main components of ITO substrate (In and Sn) with KRATOS Axis Ultra X-ray photoelectron

spectrometer (Kratos Analytical, Manchester, UK) equipped with a monochromatic Al Kα X-ray source ($h\nu$ = 1486.6 eV) operated at 150 W). Except diminishing of the ITO plate size to fit in sample holder (cut with glass cutter to have dimensions of 10 mm × 10 mm), no specific sample preparation was required.

UV/vis spectroscopy

UV/vis spectroscopy is widely used for species which can adsorb ultraviolet and visible light. Electronic transitions involving *n*, σ and π orbitals are typical for chromophores – compounds, which due to their bonds (and therefore functional groups) adsorb ultraviolet and visible light (as an example, C=C, C=O, C=N, N=N can be highlighted as one of the most important bonds). Transitions caused by *d*-electrons of metal ions (like Cu^{2+} and Co^{2+}) give rise to light adsorption as well, although the resulting *d-d* transitions are relatively weak. For complex compounds, charge transfer between metal and ligand is more important as it produces large absorbance and can be used for more sensitive analysis.

The simplest instrument presented as a block diagram on *Figure 22* includes a source of light, monochromator or interferometer (for the wavelength selection) and detector. Switching between H_2/D_2 and Tungsten lamp allows recording absorbance/transmission spectra in the range of 160-380 nm to 800 nm (the end of visible spectra) [129].

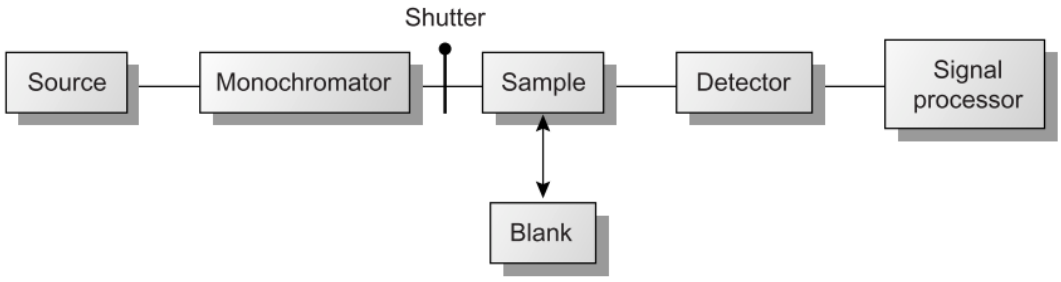

Figure 22 – Block diagram for a single-beam fixed-wavelength spectrophotometer [129]

This technique was used to verify the presence of the (tris)bipyridine ruthenium (II) complex in silica films. It was completed with Cary 60 UV/vis spectrometer in absorbance mode. As a reference, spectrum of ITO plate faced with ITO side to a source of light was firstly recorded. MSF-modified ITO samples containing $Ru(bpy)_3^{2+}$ complex were positioned the same way to be

characterised afterwards with subtraction of ITO baseline. Presence of MSF does not have an impact on obtained spectra because silica does not absorb the light in the analysed region.

Grazing-incidence small-angle X-Ray scattering (GISAXS)

GISAXS is a non-destructive method which allows to identify the morphological properties of the thin layers in particular. The idea of method lays in reflection of the incident (vector k_i) X-ray beam, which grazes the sample under a very small angle a_i, with following recording of scattering (vector k_r) coming from sample. It gives the specific patterns (detector plane q) with respect to material structure (*Figure 23*).

Experiments were carried out on MSF samples to verify and confirm the organisation of a pore structure, especially during the etching process. The apparatus "SAXSess mc2" (Anton Paar) was used with GISAXS equipped accessory "VarioStageXY" (X-ray tube from PANalytical, λ Cu, Kα=0.1542 nm) set to 0.25° incident angle).

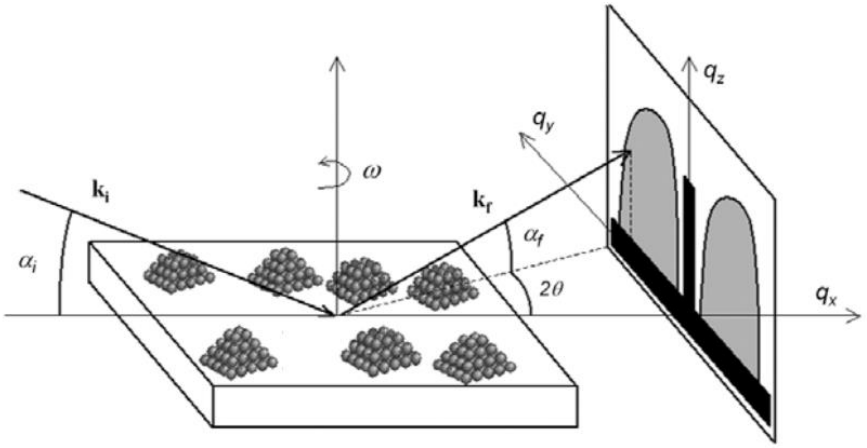

Figure 23 – GISAXS geometry (adjusted from [130])

2.1.3 Microscopy

Optical microscopy

Optical microscope is one of the simplest techniques used for the visual analysis of sample surface. It uses visible light and system of lenses to magnify the image of the object [131].

Optical microscopy observations of MSF top surface were conducted by Nikon Eclipse microscope equipped with Nikon LHS-H100P-2 (12V; 100W) and Halogen lamp and lenses with 5x, 10x, 20x, 50x, and 100x magnifications.

Scanning electron microscopy (SEM)

Scanning Electron Microscopy (SEM) is a microscopy technique which uses focused electron beam to scan the surface of sample placed in the vacuum chamber in order to retrieve a topographical and compositional information [132]. Electrons with an energy from hundreds of volts to 35-40 keV are emitted by an electron gun and delivered through the column with pair of scanning coils by lens system, which also controls the beam current and diameter (*Figure 24*). More commonly, low-energy (<50 eV) secondary electrons are collected, amplified and obtained signal is simultaneously displayed on monitor. Surface-beam interaction depends on the electron energy and atomic number of the material components.

Top-view film images were taken using JEOL JCM-6000 microscope at 10 kV acceleration.

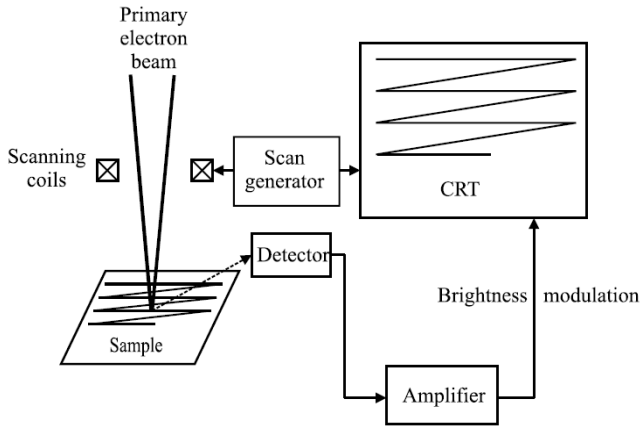

Figure 24 – Scheme showing the principle of SEM [132]

Transmittance electron microscopy (TEM)

Transmittance Electron Microscopy (TEM) is a powerful microscopy technique which uses transmitted through sample electron beam to create an image [133]. Electrons emitted by the electron gun are accelerated away from the source in high vacuum and focused by magnetic condenser lens into a beam, which then reaches and traverses a specimen (*Figure 25*). Passed

through sample beam can be then focused on the back focal plane to result in diffraction pattern. Obtained electron image and diffraction pattern are giving structural information of analysed material.

TEM characterisation was performed for mesoporous silica films in order to confirm or disprove the presence of hexagonal structuration and vertical channels after mechanical preparation. MSF was cut and removed from the ITO support. Pieces were carefully deposited on the carbon-coated copper grid to picture top and cross-sectional views of samples. Either Philips CM200 microscope or JEOL ARM F200 FEG microscope at an acceleration voltage of 200 kV were used.

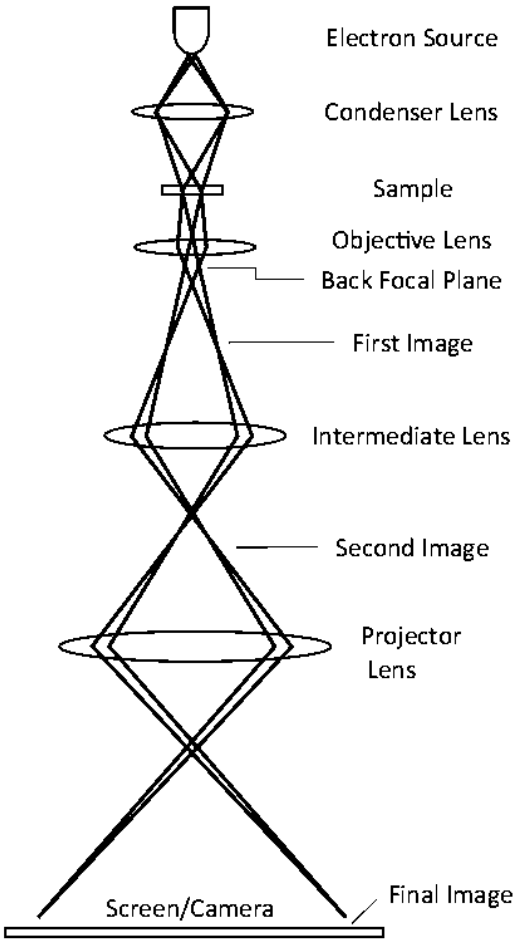

Figure 25 – Geometric optics of a basic TEM for imagining (adjusted from [133])

2.1.4 Profilometry

To determine efficiency of wet etching treatment on silica film, measurements of thickness of the film thickness are essential. Profilometry is a method that was favoured. This technique allows to obtain topographical data from the surface and to determine the thickness of deposits after scratching its surface. It is based on a direct contact between a tip and an analysed sample. During the measurement, the tip touches the surface while moving horizontally along its surface. Following the profile of the sample by the X-axis, the tip undergoes the simultaneous displacements in perpendicular Y-axis direction, resulting in the scanned profile.

To determine the thickness, it requires a partial destruction of sample by scratching it to the surface of the substrate. *Figure 26* depicts the preparation of the sample. The scratch was made with metallic stick (tweezers) 1 mm in diameter (resulting in scratch width around 0.5 mm) until reaching the support on which film was deposited in order to create a baseline. A good progress was controlled by optical microscope. The thickness measurements were carried out using contact stylus profilometer (Bruker's DektakXT®). The stylus radius was determined by the tip equal to 2 μm, that sweeps the sample from left to right for 3 mm distance measurement with the pressure force of 3 mg.

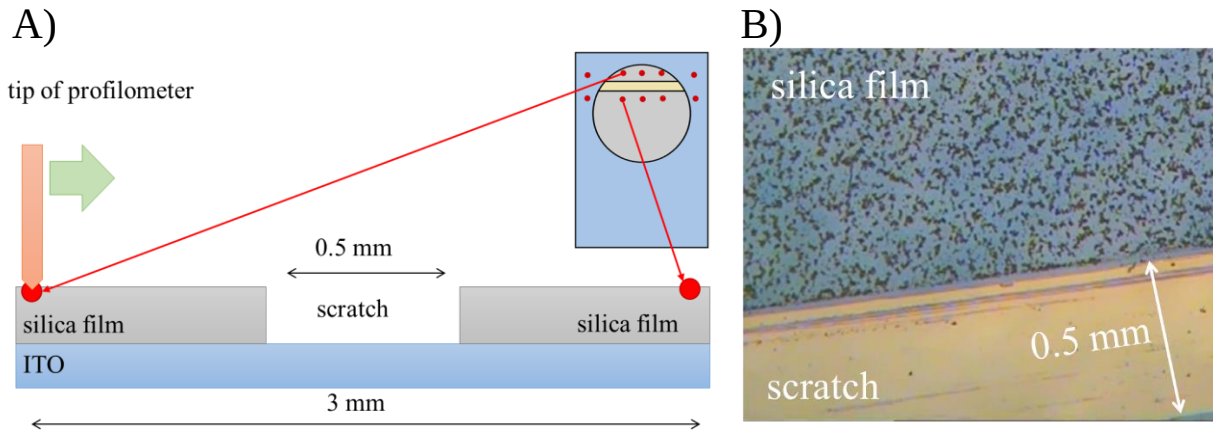

Figure 26 – (A) Scheme of the film thickness measurement with marked positions of start and finish of sweeping (red dots) and (B) optical microscope top image of the film at the scratch zone

Three measurements for each sample were performed to calculate the average silica film thickness before and after etching procedure (red dots, *Figure 26A*). It was noticed, that the ITO support possesses not a perfectly flat surface, which affects the film profile as well (see the recorded profile (red line) on *Figure 27A*). By collecting the profile of corresponding ITO plate at the same distance from the scratch as for the film profile recording, a correction was made in order to obtain a regular

and comparable baseline that determines the surface of the ITO support (height equal to 0) (*Figure 27B*). So, all variations in terms of height can be interpreted as a thickness modification. The example of typical profiles collected before and after the mathematical treatment is shown on *Figure 27*.

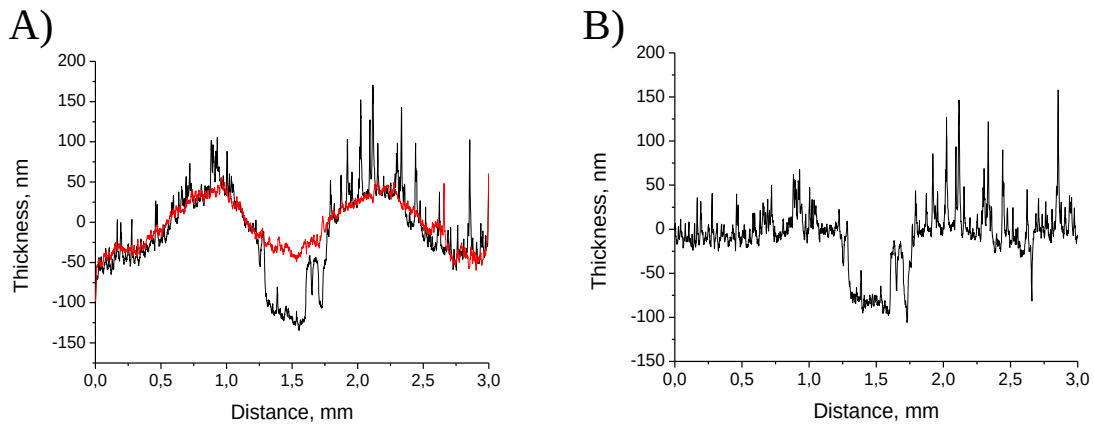

Figure 27 – Baseline correction of the profiles: (A) ITO (red line) and film (black line) profiles before and (B) after the substitution of ITO baseline

The peaks which exist on the right side of the profile, correspond to the small aggregates of silica formed on the film surface during their deposition. Their presence was also observed on the optical microscope image on *Figure 26B*. They appear as small beads, generation of which is explained in **Section 3.2**.

2.2 Protocol for synthesis of (3-azopropyl)triethoxysilane (AzPTES)

For preparation of the films with azide functional groups, it was necessary to synthetise the corresponding silane. (3-azopropyl)triethoxysilane (AzPTES) that is not commercially available was prepared from the modified protocol reported by Vilà *et al*. [107]. In 50 ml of acetonitrile, NBu_4Br (tetrabutylammonium bromide) (0,644 g, 2 mmol), NaN_3 (sodium azide) (1.08 g, 16.6 mmol) and (3-chloropropyl)triethoxysilane (ClPTES, 2.0 g, 8.3 mmol) were added while stirring. The mixture was being stirred while refluxing for 24 hours. The product cleaning firstly included the evaporation of solvent under the vacuum pressure using rotor evaporator. After, 50 ml of cyclohexane was added to the flask and insoluble residue was filtered through a paper filter. The solution of AzPTES in organic solvent was finally distilled under vacuum pressure. The product was characterised and its purity was controlled by proton nuclear magnetic resonance (1H-NMR) spectroscopy in deuterated chloroform $CDCl_3$. Characteristic peaks were observed at δ 3.75

(multiplet, 3H), 3.20 (triplet, 2H), 1.65 (multiplet, 4H), 1.16 (triplet, 9H), 0.61 (triplet, 2H) (*Figure 28*).

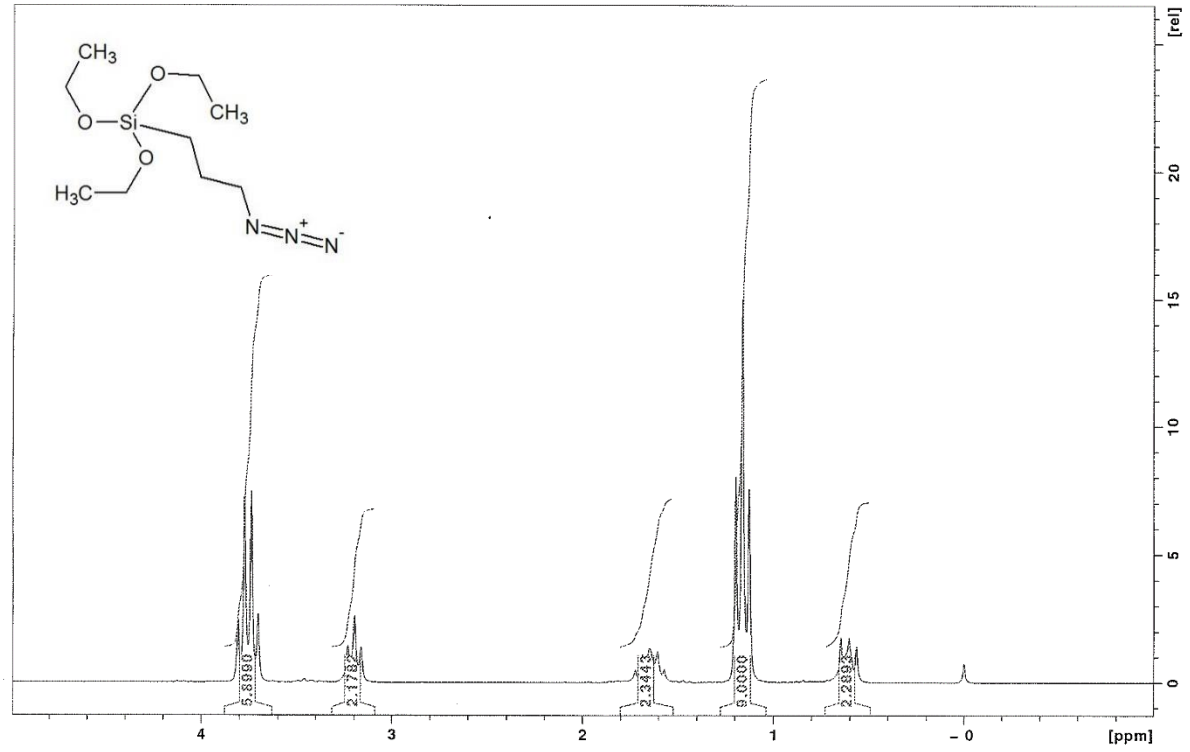

Figure 28 – 1H-NMR spectrum of AzPTES recorded in $CDCl_3$ (400MHz);
Inset – AzPTES structural formula

2.3 Mesoporous silica film preparation by electrochemically-assisted self-assembly

2.3.1 Sol preparation and film deposition

A typical sol for mesoporous silica film preparation was based on water-ethanol solution (1:1 v/v ratio) with 0.1 M $NaNO_3$, which increases the conductivity of sol, essential for the application of electrochemistry. Such solution was adjusted to pH 3 by addition of 1 M HCl. Silica precursor was hydrolysed for 2 to 2 hours 15 minutes at the ambient temperature under stirring and then was used to deposit films. Homemade Teflon cells were designed for film deposition (*Figure 16*). The ITO electrode was placed in the bottom (a), stainless steel conical- or cylindrical-shaped counter (b) and Ag wire pseudo-reference electrode (c) were placed in the cell to complete a three-electrode. The dimension of the obtained MSF is defined by the surface of ITO plate in contact with the sol, typically a circle with 10 or 14 mm diameter. A cathodic potential of –1.3 V was applied to ITO electrode during the determined time to deposit MSF. Sol solution was then immediately removed

from the cell, and the electrode was then rinsed with ethanol and water. Finally, ITO plates were put in the oven at 130^{o}C overnight to ensure the proper cross-linking of silica network.

Unmodified films were prepared by selecting tetraethoxysilane (TEOS) as silica precursor with a concentration typically equal to 100 mM. At these conditions, the concentration of chosen surfactant (cetyltrimethylammonium bromide, CTAB) was kept at 32 mM. The constant ratio of $C_{CTAB}/C_{Silica\ precursor}$ = 0.32 is chosen according to previously optimised conditions to keep control over the hexagonal mesostructure, because the changing of it lead to poorly organised or non-ordered films [2].

To obtain functionalised silica films, a mixture of silica precursors (TEOS and silane with desired functional group) was used respecting a sum of total precursor concentration equivalent to 100 mM with different ratio of components (95 to 70% for TEOS and 5 to 30% for modified silane respectively).

2.3.2 Surfactant extraction

The removal of the surfactant template is an important step as it empties the silica pores and provides the unobstructed access of the analysed species to the electrode surface. The procedure was performed by solvent extraction or calcination (only when non-functionalised silica precursors are used for synthesis). For the solvent removal of CTA^{+}, films were immersed in the 0.1 M HCl solution prepared in ethanol [134]. After 15 minutes under stirring, samples were rinsed with ethanol and dried on air. Calcination was carried out by placing the samples in the oven, which was programmed for heating to 450^{o}C for 2 hours in the air atmosphere (3.6^{o}C/min), followed by a 2 hours isotherm at 450^{o}C [2] before slow cooling.

2.3.3 Click reaction to prepare modified films

Azides are widely used in organic chemistry due to their high reactivity. Coupled with their stability toward H_2O, O_2 and the majority of organic solvents, it makes them ideal candidates for Cu^{I}-catalysed azide-alkyne click (CuAAC) chemistry purposes leading to 1,2,3-triazole formation. The regioselectivity of reaction towards 1,5-isomere is controlled by addition of copper (I) catalyst, which assists in 1,4-cycloaddition [135,136]. CuAAC reaction is easily performable even at room

temperature and due to this it found applications in organic synthesis, in synthesis of dendrimers, in polymer modification and surface functionalisation [137].

Introduction of azide-containing organosilanes (such as (3-azidopropyl)triethoxysilane, AzPTES, see its synthesis in **Section 2.2**) in sol for MSF preparation results in modified films with freely accessible N_3- groups, which can be further functionalised by click reaction with alkyne-terminated molecules [107]. A special interest is drawn to MSF modification by redox-, chromophore- and luminophore-containing species because of their potential applications in electrochemical and spectroscopic sensing.

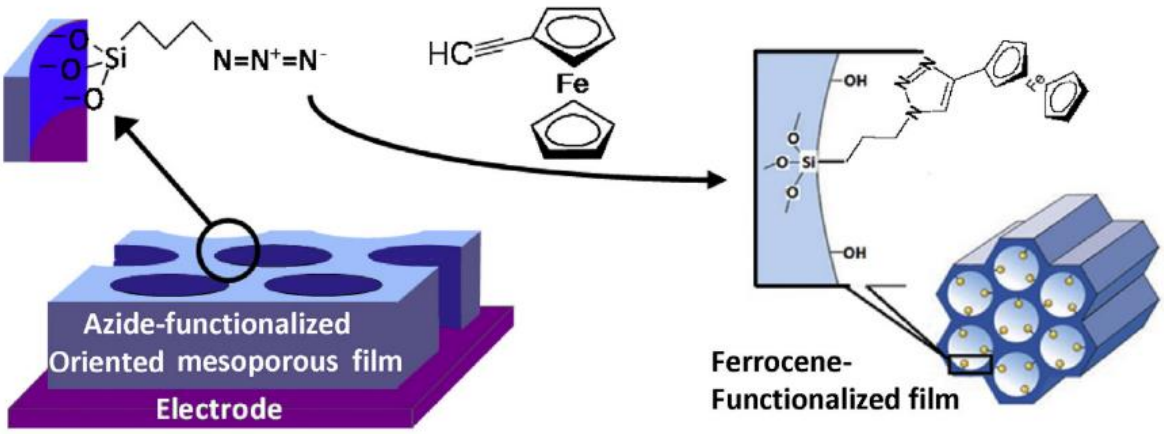

Figure 29 – Schematic illustration of ferrocene post-derivatisation of azide-functionalised films by 'click chemistry' [108]

Huisgen click reaction is conducted from the azide-modified films after the surfactant extraction by the liquid phase approach. Post-derivatisation grafting of by ethynyl ferrocene is illustrated on *Figure 29*. Formation of 1,2,3-triazole ensures the covalent bonding of ferrocene species.

The procedure for incorporation of ferrocene (Fc) and $Ru(bpy)_2(bpy')$- groups was carried out the same way for both kinds. The aqueous fraction with Cu(I) catalyst and organic part with alkyne derivative of chosen complex were prepared separately. Firstly, Cu (II) acetate (or nitrate) and ascorbic acid were dissolved and mixed to result in Cu(I) *in situ*, since it is not stable in aqueous phase [138]. In parallel, the ethynyl-containing modifier (HC≡C–R) was solvated in N,N-dimethylformamide (DMF). The amounts of added reagents are compiled in *Table 1*. Both aqueous and organic phases were then combined resulting in solution of interest in which MSFs were

immersed. The reaction is conducted in the protected from light vessel during 18-24 h and 36 h respectively for ferrocene (commercially available ethynyl ferrocene was used) and (tris)bipyridine ruthenium (II) (not available commercially, its synthesis is described **Section 4.4.1**) derivates. Samples were then rinsed with ethanol following by their immersion in 0.05 M sodium diethyldithiocarbamate (NaDDTC) ethanol solution for 30 minutes to remove the copper catalyst. Modified electrodes were finally rinsed with ethanol and water before their drying on air.

Table 1 – Composition of solution for Huisgen click reaction (given for 20 ml solution)

	Fc-modified		$Ru(bpy)_2(bpy)$'-modified	
Cu (II)	0.8 mmol [a)]	3.0 mg [a)]	1.0 mmol [b)]	4.8 mg [b)]
Ascorbic acid	2.1 mmol	7.5 mg	2.5 mmol	8.8 mg
Ethynyl ferrocene	2.4 mmol	10.0 mg	-	-
$Ru(bpy)_2(bpy)'(PF_6)_2$	-	-	1.0 mmol	20.0 ml
H_2O	-	8.0 ml	-	10.0 ml
DMF	-	12.0 ml	-	10.0 ml

[a)] Cu (II) acetate [b)] Cu (II) nitrate

2.4 Electrochemical characterisation of mesoporous silica films

2.4.1 Characterisation with conventional probes

The electrochemical characterisation was performed by cyclic voltammetry technique using 0.5 mM $Ru(NH_3)_6Cl_3$ as a positive, 0.5 mM $Fc(MeOH)_2$ as a neutral and 0.5 mM $Fe(CN)_6^{3-}$ as a negative probes in 0.1 M $NaNO_3$ aqueous solution. Typical CV curves obtained on perfect unmodified films or azide-functionalised MSF before and after surfactant extraction, are depicted on *Figure 30*. Presence of N_3 functional groups in confined silica channels before surfactant extraction does not affect the redox signal because the pores are blocked. Therefore, the same response from unmodified and azide-modified films is recorded.

For a defectless well-organised mesoporous silica film, no CV response is seen while characterisation with $Ru(NH_3)_6^{3+}$ (grey line on *Figure 30A*). Because of the excess of positive

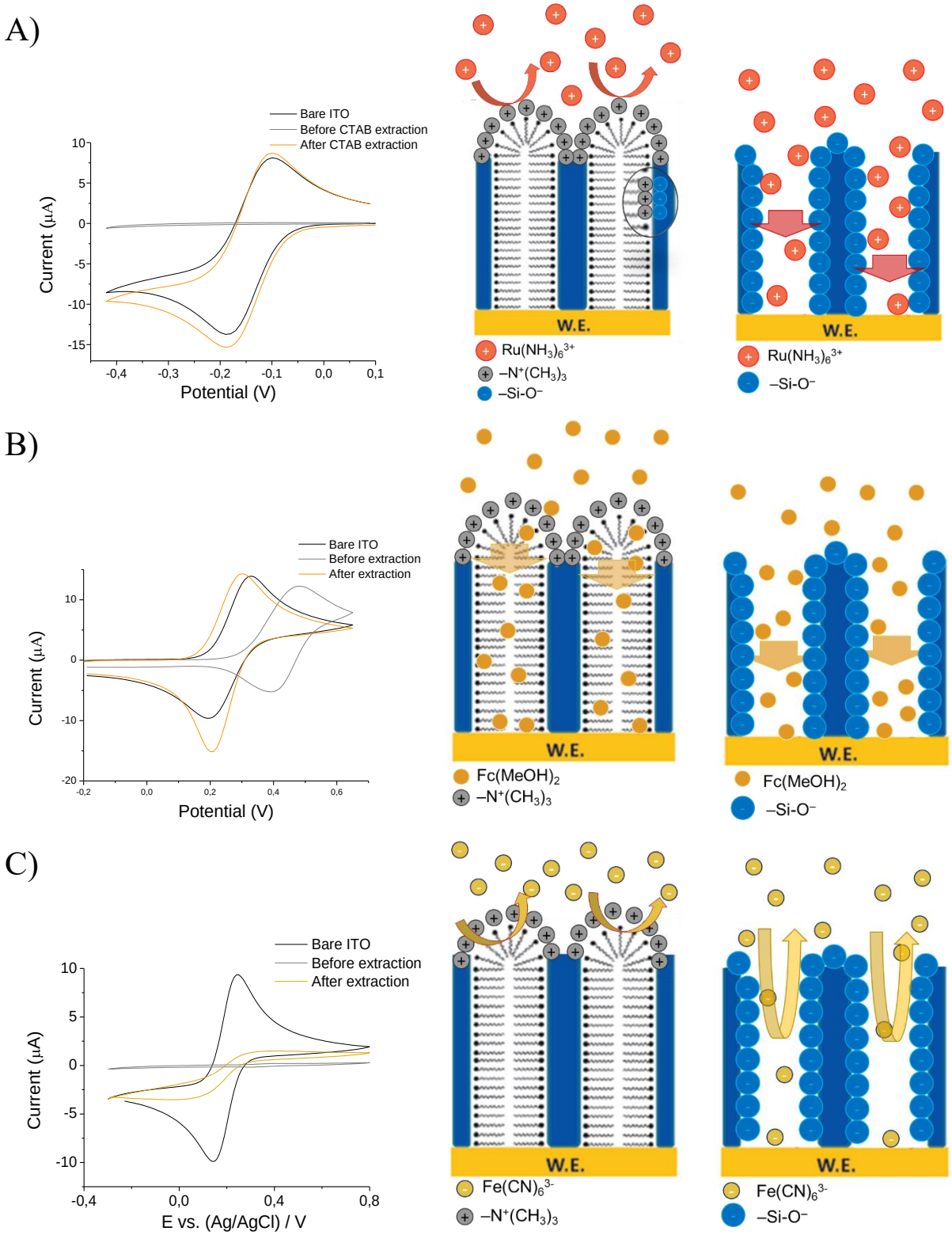

Figure 30 – Typical CV curves obtained in 0.5 mM (A) $Ru(NH_3)_6^{3+}$ and (B) $Fc(MeOH)_2$ and (C) $Fe(CN)_6^{3-}$ aqueous solution (0.1 M $NaNO_3$) using bare ITO (black line), ITO electrode covered with MSF before (grey line) and after (yellow line) soft template extraction (50 mV/s scan rate)

charge created by CTA^+ micelles (marked in grey color), no $Ru(NH_3)_6^{3+}$ can pass through the surfactant barrier due to the electrostatic repelling. After surfactant extraction (see the yellow dotted line on *Figure 30A*), the redox signal from $Ru(NH_3)_6^{3+}$ is recovered showing the possible diffusion of the molecules through film. Signals with a higher current intensity are observed compared to that recorded on bare ITO electrode as a result of probe accumulation on negatively charged silica walls.

The characterisation with neutral probe gives rise to shift of the current peaks towards higher potentials when the template is maintained inside the pores and a reduction of the peak intensity when comparing with bare ITO (grey line on *Figure 30B*). The observed changes are caused by the possibility of $Fc(MeOH)_2$ to be solubilised in the liquid-crystalline phase of surfactant, what allows it to be detected at the surface covered with unextracted MSF, though in the smaller quantities because of the mass transport limitations. With the removal of CTA^+, the mass transport issues do not affect the oxidation of $Fc(MeOH)_2$ anymore and cathodic peak intensity increases due to accumulation of positively charged Fc^+ on silica film as in case of $Ru(NH_3)_6^{3+}$ probe [1]. In addition, recovered electrochemical signal located at the same potential as on bare ITO.

When using the negative probe, no signal is observed in presence of soft template in pores (*Figure 30C*). It happens because the charge of the probe does not allow it to penetrate to hydrophobic liquid-crystalline phase and to pass it to reach electrode surface. Nevertheless, a signal is recovered after the soft template extraction, yet not of the same intensity as of bare ITO due to interactions between $Fe(CN)_6^{3-}$ and negatively charged silica walls.

2.4.2 Characterisation with haemoglobin

Haemoglobin (Hb) was considered to evaluate the presence or not of some defect on the structure after etching. Due to its relatively large diameter of 5-6 nm [139] and electroactivity [140] it can give an idea about minor defects created during etching of the films with and without soft template in pores.

Aqueous solution of Hb (5 µM) in the phosphate buffer solution (PBS, 0.1 M pH 5) was prepared after the grinding of Hb in the mortar. The grinded product was quantitatively transferred in the measuring flask containing a small amount of PBS, dissolved using the ultrasonication and filled to the mark by PBS. The solution of Hb was firstly bubbled with N_2 for 30 minutes in order to

eliminate oxygen (even 15-20 minutes were found to be enough [141,142], but in order to ensure that no oxygen reduction takes place, bubbling time was extended). Hereinafter, probe solution was placed in the cell for electrochemical characterisation and was purged for another 10 minutes. CV analysis was always proceeded by preventing oxygen ingress in the system.

2.5 Protocol for etching experiments

Etching was applied for the samples with 14 mm diameter of silica films by drop etching method, inspired by publication of Kobayashi *et al.* [3].

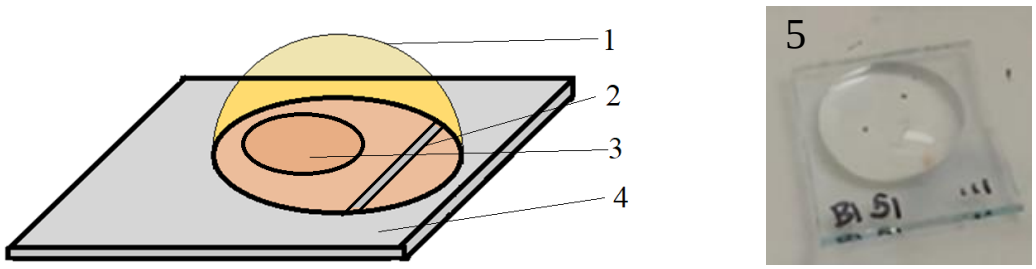

Figure 31 – Scheme of the film while etching process (1 – the drop of the etching agent, 2 – the scratch for thickness measurements, 3 – place for the electrochemical characterisation, 4 –ITO surface, 5 – photo of sample while etching)

The scratch for film thickness measurement by profilometry was done either prior to etching (Preparation 1) or after it (Preparation 2). Following Preparation 1, the thickness before and after etching was measured independently for each sample. Preparation 2 required the determination of the average thickness of the batch, which was assigned to be a starting thickness for each film related to this group. Unscratched films from this batch were etched and only afterwards, a scratch was done to determine individually film thickness after treatment.

In order to cover all film surface by etchant, 200 µl etching solution was placed on the top of the film (*Figure 31, 1*). The determination of concentration of the most commonly used etching solution is presented in **Appendix 2**. The use of larger volumes did not allow keeping drop on the film and it was spreading for the ITO surface. Samples were covered with a Petri dish and were kept during the reaction time at controlled room temperature (21°C). After the reaction time was over, the etchant was carefully removed by rinsing a sample with distilled water and finally by finishing with ethanol for a more rapid dry.

Chapter 3

Tuning the thinness of well-organised mesoporous silica film

3.1 Introduction

The Evaporation-Induced Self-Assembly [30,53] process became a breakthrough in the mesoporous material synthesis. Apart from the formation of mesoporous silica materials with defined pore distribution and size, which was already known before on the family for MCM materials [26], this method allowed to obtain continuous mesoporous silica thin films. Materials obtained by EISA deposition were showing a prospect of success in electrochemical sensing, but the unsuitable pore morphology (mainly because of mesopore channels were oriented parallel to the film surface which was creating mass transport issues) was the major factor which did not allow this method to be used wider [59]. With the discovery of Electrochemically-Assisted Self-Assembly (EASA) [101] and Stöber [97] methods for mesoporous thin film deposition the arrangement of cylindrical pores was changed from parallel to perpendicular to the underlying support. In comparison to films obtained by EISA method, vertical pore orientation facilitates the mass transport through channels to electrode, making material attractive for use not only in electrochemical field. Additionally, particular pore organisation possesses a fully accessible high specific surface area, which is easy to be functionalised with organic groups, pores can be used for hosting adsorbed species with potential application in catalysis or in biochemical domain [100]. These properties show that mesoporous silica film is a coating with a very promising future.

Although the vertical pore orientation overcame the major mass transport issues regarding the pore morphology, functionalisation of the pore surface can still disrupt the diffusion of species because of the pore space filling with grafted modifier. By cyclic voltammetry, the diminution of the peak intensity from $Ru(NH_3)_6^{3+}$ probe was observed for on electrode modified by azide-functionalised films synthetised with a variation of the azide precursor content in starting sol from 10 to 40 % [107].

Another difficulty which may affect the analysis is charge interaction with silica material itself. While working with silica in aqueous solutions, normally the pH range of 2 to 8 is kept to ensure that no drastic degradation of surface occurs [88], which gives rise to the negatively charged

surface with Si-O^- terminated groups [143]. Even though the excessive negative charge of silica walls provides an advantageous preconcentration of species of cationic nature [6], the detection of negatively charged ones is still troubled. Electrostatic repelling between negatively charged silica surface and a negative probe does not work towards the analyte diffusion through channels, leading to a consequent suppression of voltammetric current like in case of $Fe(CN)_6^{3-}$ probe [2].
MSFs are remaining frequently used due to their numerous advantages despite the described mass and charge issues. By decreasing the film thickness, it can be expected that the mass transport issues caused by the charge interactions may be reduced. A combination of opened cylindrical pores and shorter distance, which redox probe overcomes to reach the electrode in case of thinner silica film, could contribute to more species to pass through charged silica walls causing an increase of electrochemical signal. One of the goals of this work is to diminish the effect of the film thickness on the electrochemical performance of electrodes modified by EASA generated MSFs.

In general, two main pathways can be used in order to get thinner films: bottom-up or top-down approaches. The first one allows to decrease the film thickness directly during its synthesis by adjusting particular parameters in deposition procedure used to obtain film [144], such as the reactant concentration and temperature in chemical vapour deposition method [145] or the speed of support withdrawal from precursor solution while using dip-coating [42,146]. Basically, the deposition of the film in this case is stopped before reaching the great thicknesses. Conversely, the top-down approach requires an additional step after film deposition in order to reduce its thickness. This process, which is also used to remove the top layer of material, is defined as **etching** (*Figure 32*). It became of demand when the microelectromechanical systems (MEMS) and the fabrication of integrated circuits started to develop rapidly. Physical or chemical approaches are possible [147].

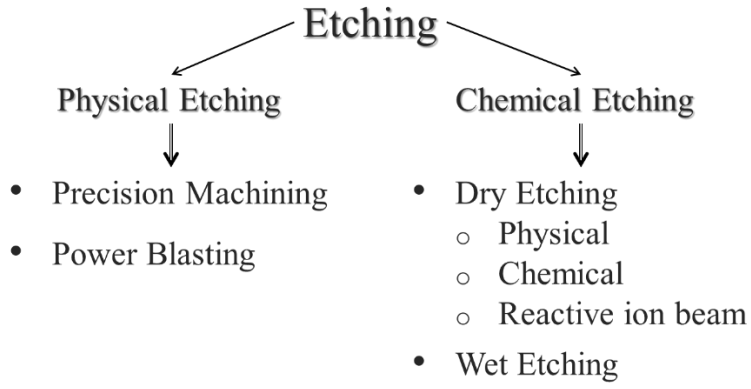

Figure 32 – Etching approaches (according to [147])

Precision machining and powder blasting belong to **physical etching**. The physical removal of the material is carried out by the direct contact between the rotated hard tool and material in the first case, while the second one uses multiple small abrasive particles.

Chemical etching nowadays is performed by dry and wet processes. **Dry etching** is carried out using gases or plasma as etchants. Three subcategories based on the nature of interaction between the attacking particles and etched material are distinguished [148]. The first one is physical dry etching, where no chemical reaction takes place. An ion/electron/photon beam with high kinetic energy is used to attack mechanically the surface (sputtering). The second subtype is chemical dry etching (or vapor phase etching), which results in a chemical reaction between gases and surface. For silica-containing materials, commonly utilised agents are tetrafluoromethane (CF_4), sulphur hexafluoride (SF_6), nitrogen trifluoride (NF_3), chlorine (Cl_2) or fluorine (F_2) gases. The last one is the combination of two previously mentioned, named physical-chemical etching, also known as Reactive Ion Etching (RIE). Reactive cations generated by ionisation of gases are accelerated and are reacting chemically with the atoms of the material surface. **Wet etching** is a technique that requires the use of liquid reagent (etchant) to remove material. Each type of material requires its own etching solution. The main reactants are mineral acids (HF, HNO_3, H_3PO_4), bases (KOH, NaOH) and ammonium aqueous systems [149]. Wet chemical etching is carried out by the immersion of the substrate in reactant, by spraying [147] or by placing an etchant as a drop on material's surface [3].

Etching is characterised by the isotropic (uniform in any direction) or anisotropic (non-uniform in all directions) dissolution of material. Depending on the etching approach, on the chemical nature of material and etchant, one or another type prevails [147].

In our study, both bottom-up and top-down approaches were used to obtain the thinnest possible well-organised mesoporous silica films synthesised by EASA method. Unlike dry etching, wet etching does not demand specific equipment like vacuum chambers [150], therefore this approach was chosen for diminution of film thickness.

Silica dissolution: general information

Since the silica films are widely used as dielectric material [151], a big attention was paid to wet etching procedure to improve its efficiency towards controlling the dissolution rate, developing the selectivity of etching with respect to different coatings and decreasing the final roughness of etched surfaces [152–154].

Typically, silica dissolution in fluoride-based media is described by *Eq. 3.1* [155]. The reaction takes place in the acidic solutions and the simplified product of reaction is normally given as soluble in water H_2SiF_6.

$$SiO_2(s) + 6\ HF \rightarrow H_2SiF_6(aq) + 2\ H_2O \qquad (Eq.\ 3.1)$$

In the alkaline media under the influence of OH^- anions the dissolution processes occurs with formation of SiO_3H^- and SiO_3^{2-} (*Eq. 3.2 – 3.3* [155]):

$$SiO_2(s) + OH^- \rightarrow SiO_3H^- \ (Eq.\ 3.2)$$

$$SiO_3H^- + OH^- \leftrightarrow SiO_3^{2-} + H_2O \ (Eq.\ 3.3)$$

Behind the generally simplified reaction of SiO_2 dissolution, the more complex process stays, which includes three main steps [155–157]:

1. Diffusion of the liquid reactant to the surface of material;
2. Reaction between the etchant and surface;
3. Diffusion of the products of reaction from the surface.

Etching process occurs at the solid/liquid interface, meaning that in terms of material in general, specifically the condition of the surface (not the bulk volume) is playing a major role in its dissolution, as it was stated for silicon dioxide etching in aqueous fluoride media [158]. Additionally it was demonstrated on the example of fused silica and quartz, that the dissolution of the amorphous silica in HF/HCl solution was faster than for the crystalline material in around 2 times [159], what shows that structural factor also affects the process.

A lot of studies were performed on silica materials in order to find the effect of other parameters on the etching rate. Among the frequently discussed, it is worth highlighting nature and concentration of the etchant solution [158,160–164], presence of additives (acids [158,161,165], ammonium fluoride [166]), temperature kept during etching [160], its density and conditions of preparation [167–170]. As it was discussed by Kern [171], for the thermally grown (1000^{o}C) or densified SiO_2 films the etching rate in P-etch (aqueous etching solution based on HNO_3 and HF) is 2.0 Å/s, for radio frequency sputtered films 4 – 12 Å/s, for undensified films 6 – 20 Å/s, for electron-gun evaporated films 20 – 70 Å/s, the anodised films were etched with 18 – 228 Å/s rate. Porosity of material [157], surface defects [161] and roughness [172], presence of dopants, in particular in silica network [156,169] also were found to have an impact on the etching rate. Agitation though appeared to be a controversial parameter, since Spierings [161] and Monk [170] in their reviews are giving the opposite opinions supported by references of conducted researches. For the first publication, it is claimed, that the agitation does not affect the etching rate. Contrary, the second reference shows that diffusion of the products of silica dissolution from the surface and the supply of material with the fresh etchant are increasing the rate of reaction.

Historically, the ammonium fluoride solution, NH_4F, as an individual etching agent was used for etching silicon surface [173,174]. It was also widely used in mixture with HF, forming so-called buffered hydrogen fluoride (BHF) solution (also known as buffered oxide etch, BOE). The idea behind mixing two fluoride-containing reactants is to keep the F^- concentration constantly high and, therefore, to reach the stable etching rate. The existing equilibria in etching solution is affected by strong electrolyte NH_4F and favours the creation of HF_2^- reactive species [162,175]:

$$NH_4F \rightarrow NH_4^+ + F^- \quad (Eq.\ 3.4)$$

$$HF + F^- \rightarrow HF_2^- \quad (Eq.\ 3.5)$$

The impact of NH_4F content in BHF has shown to increase the etching rates (up to 10-12% [156]) due to HF_2^- formation, which is believed to be one of the most reactive species in such solution [160,175] partially due to its linear geometry [36]. Additionally, the presence of small fraction of dissociated HF provides the etching solution with H^+ ions, which are catalysing the reaction of silica dissolution [165]. As an example, for silica materials of different nature the etching rate varied from around 10 nm/min to 100 nm/min while etching in 25:1 HF and 5:1 BHF respectively [176]. At higher NH_4F contents the deceleration is typically observed (e.g. in presence of 2.5 mol/l HF etching rate decreased when $[NH_4F] > 5$ mol/l [175]) as a result of poor solubility of $(NH_4)_2SiF_6$ (*Eq. 3.6*), HF_2^- deactivation by NH_4^+ cations (*Eq. 3.7*) and lower H^+ concentration in solution [166,175]:

$$SiO_2 + 4HF + 2NH_4F \leftrightarrow 2NH_4^+ + SiF_6^{2-} + 2H_2O \quad (Eq.\ 3.6)$$

$$NH_4^+ + HF_2^- \rightarrow NH_4HF_2 \quad (Eq.\ 3.7)$$

Even though, it was claimed that NH_4F does not dissolve silica materials due to the fact that normally in its solution the dissociated F^- anions are prevailed [160,161], for mesoporous thin silica films it was not the case. Ijichi et al. reported the use of aqueous ammonium fluoride (0.1 M) to fabricate bimodal mesoporous silica films (80 and 170 nm thick) with caged and vertically-aligned mesopores [177]. Etching procedure was carried out for 1.5 – 2.0 hours, showing that the dissolution rates are slow and easily controlled. Due to the easier controlled etching process, NH_4F was chosen as an etching agent to proceed the thickness reduction by top-bottom approach for our MSFs.

3.2 Investigating the deposition time parameter for obtaining the thinnest flawless films

The EASA method has an advantage in modifying the conditions of sol preparation and deposition procedure in order to adjust the thickness of film. The thickness for a uniform and homogeneous MSF is determined by three main criteria:

1. The rate of silica precursor condensation, which itself depends on:
    a) the nature of silica precursor. The simplest sol for MSF preparation contains only one silica precursor and typically it is TEOS. However, with the addition of another type of silane, the condensation rate in sol slows down forming thinner deposits. In

particular, by introducing in 100 mM sol containing TEOS from 10 to 60% of methyltriethoxysilane the thickness of MSF is decreased from 68 to 11 nm (on the ITO electrode, with the constant deposition time equal to 20 s) [104]. It is explained by higher hydrophobicity and lower reactivity of methylated silane in comparison to TEOS [178];

b) the concentration of silica precursor in sol. For a same deposition time (30 s) and a constant CTAB/TEOS ratio equal to 0.32, the increase of concentration of TEOS in the starting sol leads to thick deposited films. Exceeding 125 mM of TEOS generates silica aggregates on the film surface [2].

2. The current density. Deposition in the galvanostatic mode allows to change the rate of the film growth, thus for 8 s electrolysis on ITO electrode at –0.74, –1.5 and –3 mA/cm^2 the film thickness is equal to 112, 152 and 272 nm respectively [2].
3. The time of application of negative potential. The application of –1.3 V potential to a copper substrate for 1, 3 and 5 s generates MSFs 39 ± 9, 89 ± 8 and 132 ± 16 nm thick [1]. Film deposition on the Pt tip electrode formes porous deposits of 20 to 50 nm as a result of changing the deposition time from 2 to 5 s [179]. Much thicker mesoporous coatings (up to 400 nm) can be also obtained by multistep layer deposition [180].

If the minimum value of film thickness is defined by the total blocking of the electrode surface by deposit, the maximum one is limited by the aggregate formation [2]. Conditions which are normally used to obtain defectless coatings, comprise the concentration of TEOS precursor in the range of 75 – 125 mM and the duration of time deposition from 10 to 20 seconds on the ITO substrate [2]. The thickness of MSF varies starting from 83 nm [104] to 264 nm [181] using the most common conditions of sol preparation (TEOS silica precursor, 100 mM) under the same applied voltage and deposition time (-1.3 V for 20 s), electrode substrate (ITO plates).

While talking about the minimum thickness, the flaw factor should not be ignored either. Therefore, working with sol containing 100 mM TEOS for MSF preparation on ITO surface by EASA method with application of -1.3 V negative potential requires the determination of the minimum deposition time that is necessary to cover completely the surface of the ITO by defect-free mesoporous silica film with hexagonally organised pores. Thus, the least possible thickness for such experimental conditions will be determined.

Different times of deposition have been investigated. *Figure 33* displays the electrochemical characterisation of the obtained films before the soft template extraction with $Ru(NH_3)_6Cl_3$. The positively charged probe cannot diffuse through the silica film when surfactant is maintained inside the pores both due to the induced hydrophobic core and the presence of an excess of positive charge brought by the ammonium group of CTA^+ at the silica walls. Electrochemical signal of ruthenium complex disappears for samples obtained with a deposition time more than 10 seconds. For shorter deposition times, detection of the CV response occurs due to freely accessible bare electrode surface that was left after the film generation. Two possible reasons to this are either ITO surface is not completely covered by the silica film and/or some cracks are present over the film. Moreover, increasing deposition times causes a gradual reduction of peak current intensity, showing that the surface of the electrode becomes more fully covered by silica film and that only smaller areas of bare electrode stay reachable by the probe. ITO surface is completely blocked by MSF (before the extraction of the template) when reduction potential is applied for more than 10 s.

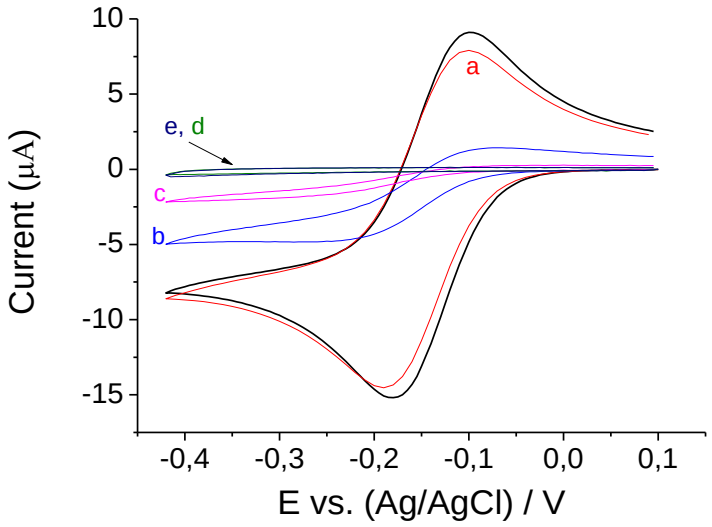

Figure 33 – Electrochemical characterisation of the films deposited during a) 3 (red), b) 5 (blue), c) 7 (pink), d) 10 (green) and e) 15 (dark blue) seconds with 0.5 mM $[Ru(NH_3)_6]Cl_3$ in 0.1 M $NaNO_3$ solution in comparison to bare ITO electrode (dashed black line) (50 mV/s scan rate, 1st cycle)

The electrochemical characterisation with neutral $Fc(MeOH)_2$ probe depicted on *Figure 34* was also used to check the deposits. This molecular family is known to be able to diffuse through liquid-crystal-like surfactant phase confined in mesochannels and react at the electrode surface to

give a redox signal shifted towards higher potential, consistent with a more difficult electron transfer in this medium.

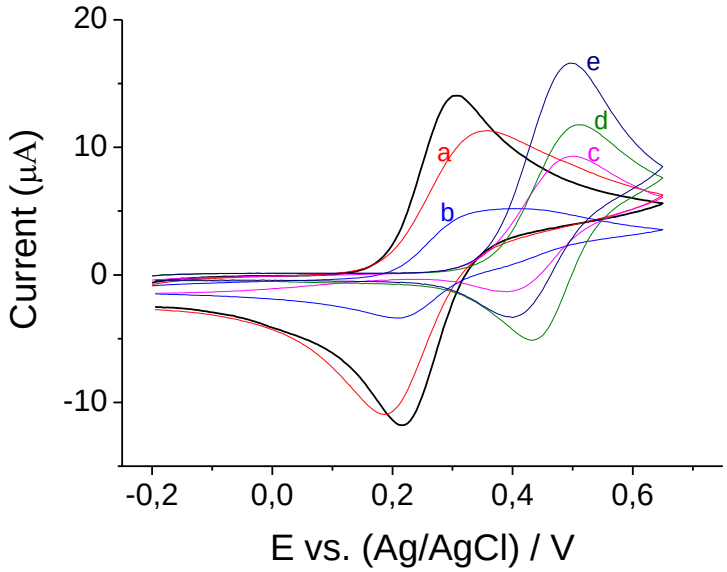

Figure 34 – Electrochemical characterisation of the films deposited during a) 3 (red), b) 5 (blue), c) 7 (pink), d) 10 (green) and e) 15 (dark blue) seconds with 0.5 mM $Fc(MeOH)_2$ in 0.1 M $NaNO_3$ solution in comparison to bare ITO electrode (dashed black line) (50 mV/s scan rate, 1st cycle)

Characterisation of MSF with $Fc(MeOH)_2$ has shown that in addition to expected peak shift, a variation of the current intensity was also observed. For films obtained with 3 and 5 seconds deposition time, CV results are consistent with a gradual blocking of the ITO surface by silica film without a full coverage of the electrode: the peak current decreases while staying in the same potential region than the signal onto bare ITO because of scattered film formation. When the layer is more considerable (increase of the deposition time, $t > 7$ s), the shift of the $Fc(MeOH)_2$ oxidation response is observed to a higher potential (+ 0.5 V) due to the influence of the surfactant medium on the redox process and, also, the increase of the peak intensity as a consequence of $Fc(MeOH)_2$ accumulation in the surfactant phase for thicker films. The peak current of the reverse scan of 7 to 15 s deposition time MSF (respectively 3.4, 6.6 and 4.4 µA) appears less intense than the forward scan (respectively 8.6, 11.1 and 15.9 µA) in accordance to the production of hydrophilic ferricenium cation. As it is not the case for 5 s deposition time MSF (the forward and reverse peak intensities are almost equivalent, Ip_a = 4.8 µA, Ip_c = –4.1 µA), it is another evidence that the electrode surface is covered by the MSF presenting some defects or cracks.

In parallel, XPS characterisation of the ITO plates before and after MSF deposition was made in four different zones to provide more information about uniformity of the silica layer. Characteristic peaks of two of the major components of ITO, In and Sn, and that of Si from silica matrix are used to estimate the covering degree of the electrode. *Table 2* reports the evolution of atomic concentrations of three considered elements in function of the MSF deposition time. Logically, longer deposition times give rise to signal reduction of ITO components to their absence with concurrent increase of Si content. Following this pattern, the breaking point was reached when no In or Sn of ITO were detected for sample obtained during 5 second potential application.

Table 2 - XPS characterisation and thickness determined by profilometry measurements of MSF deposited from 100 mM TEOS – 32mM CTAB sol on the ITO substrate in function of time deposition

	Atomic concentration, %			Film thickness, nm*
Surface element	In	Sn	Si	
ITO*	14.9 ± 1.2	2.3 ± 0.2	-	-
Film 3 seconds	9.3	1.5	9.8	cannot be determined
Film 5 seconds	Not detected	Not detected	18.3	23 ± 17
Film 7 seconds	-	-	-	42 ± 8
Film 10 seconds*	Not detected	Not detected	18.4 ± 0.6	80 ± 9
Film 15 seconds	Not detected	Not detected	18.3	111 ± 9

* values calculated from 3 measurements, each made in three different places

The fact that XPS analysis gives no evidences of bare ITO presence after 5 seconds deposition does not mean that the film covered the electrode homogeneously, because the CV characterisation with positive and neutral probes allowed to recover partially their redox signals using the equivalent MSF-covered ITO, showing that the film deposition was incomplete. Existing contradiction stemmed from two different methods lays in their fundamentals. The area of film engaged in the electrochemical testing is 20 mm^2 (which is defined by the o-ring of the cell for CV characterisation), while during the XPS analysis only few square micrometres of the surface area

are analysed [182]. It indicates the different scales of conducted analysis. Therefore, films deposited for 5 seconds are considered to be not homogeneous with respect to CV tests.

Combining the electrochemical and XPS data it was concluded that the deposited MSF totally covers the ITO electrode with a minimum time of deposition of 10 seconds. Whereas the answer on completeness of surface modification coverage was found, another important parameter of the structuration of the MSF required checking.

The organisation of films deposited during 10 seconds was verified by TEM and GISAXS. *Figure 35* shows TEM images of MSF. The top view of the deposit (*Figure 35A*) demonstrates that the hexagonal packing of mesopores is preserved throughout the wide area with no evident cracks and defects. In addition, cross-section view obtained with the help of Focused Ion Beam (FIB) in combination with TEM analysis confirms that material possesses cylindrical pores vertically oriented to electrode surface well-structured over the thickness (*Figure 35B*).

Figure 36 displays the GISAXS analysis of MSF deposited for 10 s. The integration of scattered spots on *Figure 36A* gives the 1D image (*Figure 36B*) with two significant peaks at q_y = 1.69 and 2.91 nm^{-1}. The ratio between their positions (2.91/1.69 = 1.72) is pointing on the hexagonal type of organisation of film [183]. The other peak at 1.96 nm^{-1} is attributed to amorphous silica aggregates (as well as observed halo) [184,185] that cover the surface of film and were observed by SEM (see the inset of *Figure 36A*).

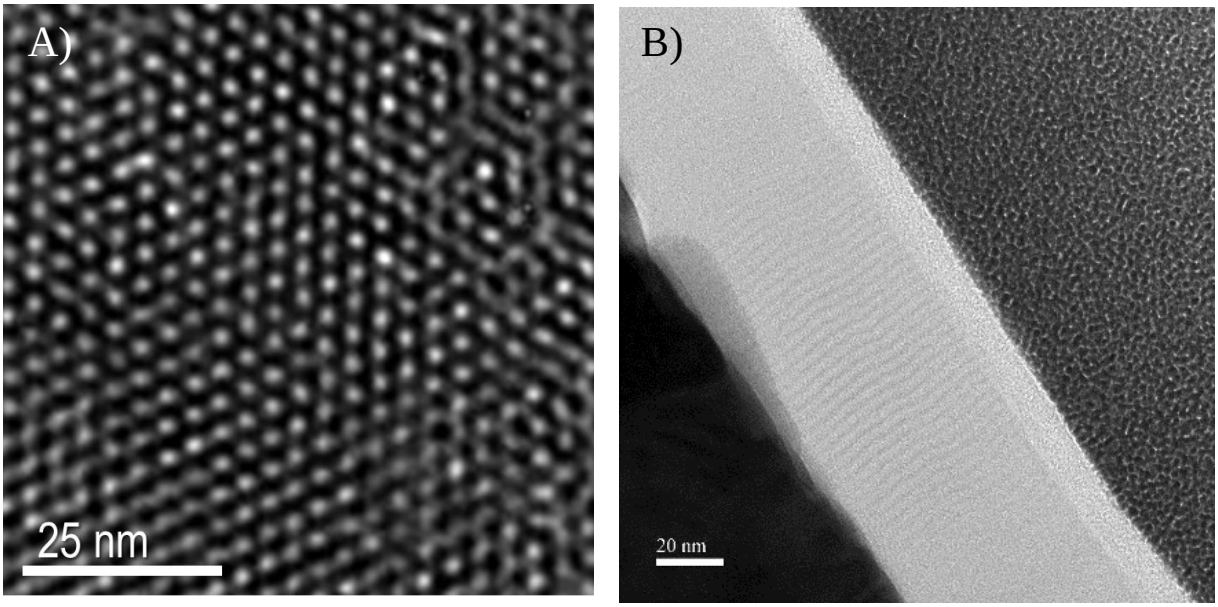

Figure 35 – TEM images of film deposited during 10 seconds from a pre-hydrolysed sol containing 100 mM TEOS and 32 mM CTAB: (A) top view and (B) cross section

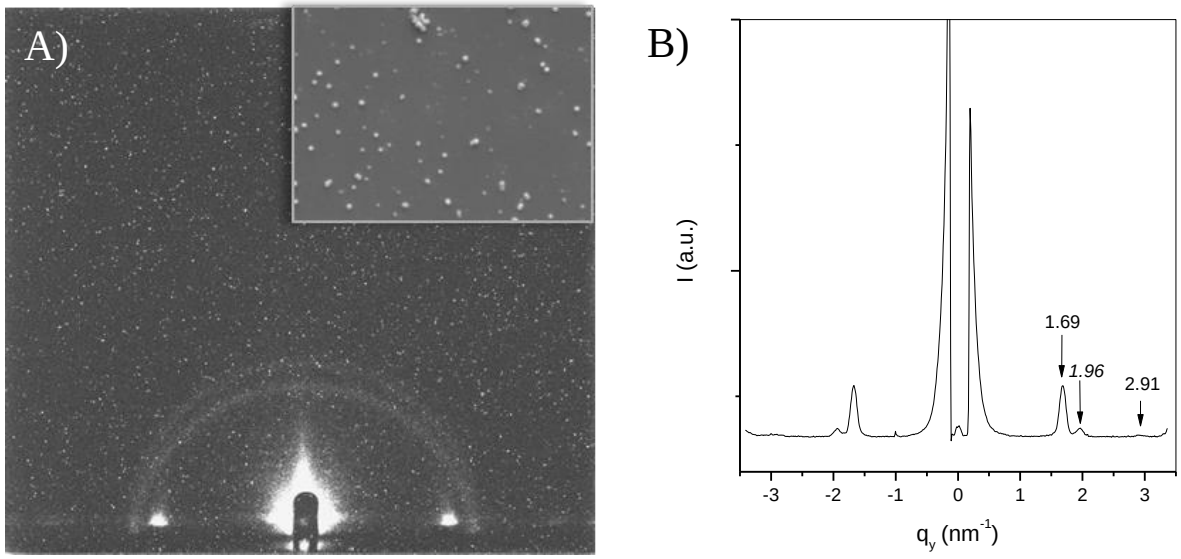

Figure 36 – GISAXS (A) pattern collected from film deposited during 10 seconds from a pre-hydrolysed sol containing 100 mM TEOS, 32mM CTAB (inset – SEM image of film's surface) and (B) its integration

Thickness of MSF films was additionally evaluated by profilometry. Results of conducted experiments are presented in *Table 2*. No data could be collected from films obtained after 3 seconds of deposition as samples were too thin, what made it impossible to create the proper scratch, which could serve as the baseline in profilometry measurements. Film deposition for 5

seconds and more causes a creation of layers with growing thickness from 23 ± 17 nm to 111 ± 9 nm (after 15 s deposition). Observed linear trend of increasing the film thickness with longer deposition times confirms data published in literature for EASA prepared samples [1,2]. The longer deposition times lead to the lower values of calculated standard deviations, which appear to be in a good accordance with thickness measurements earlier performed by profilometry, where the error bar varied generally from 5 to 10 nm for films around 100 nm thick [181].

Under the experimental conditions employed, the thinnest deposits with homogeneous surface coverage, which can be obtained by EASA method, have thickness of 80 ± 9 nm. Following experiments with unmodified films were performed with the samples possessing given above thickness.

3.3 Wet etching approach to control the thickness of mesoporous silica film

In order to reach the thinnest films with keeping the hexagonal organisation of channels, MSFs were exposed to the chemical treatment by aqueous ammonium fluoride solution, which is described as a soft etching agent.

The etching procedure can occur after the film deposition without any treatment of the silica film or after the extraction of the template. In this first case, the template is kept inside the silica pores, while in the second approach, the silica pores are freely accessible. It is interesting to study the effect of the presence or absence of template on the etching reaction (kinetic, effect on the silica film structure degradation). Samples were divided into four groups (*Figure 37*). The first group included samples with unextracted soft template left in pores after the film deposition (noted gCTAB), the second and third batches were represented by films where CTA^+ was extracted respectively by calcination (referred gCALC) and solvent extraction (named gEXTR). The last group consisted of ferrocene-modified silica films, which were obtained by co-condensation process in presence of (3-azopropyl)triethoxysilane (AzPTES) followed by the Huisgen cycloaddition after solvent extraction of the template (**Section 2.3.3**). The introduction of electroactive groups (ferrocene entities, Fc) should allow to follow the etching process electrochemically. The continuing decrease of Fc groups during the etching reaction should be coherent with the decrease of the recorded current.

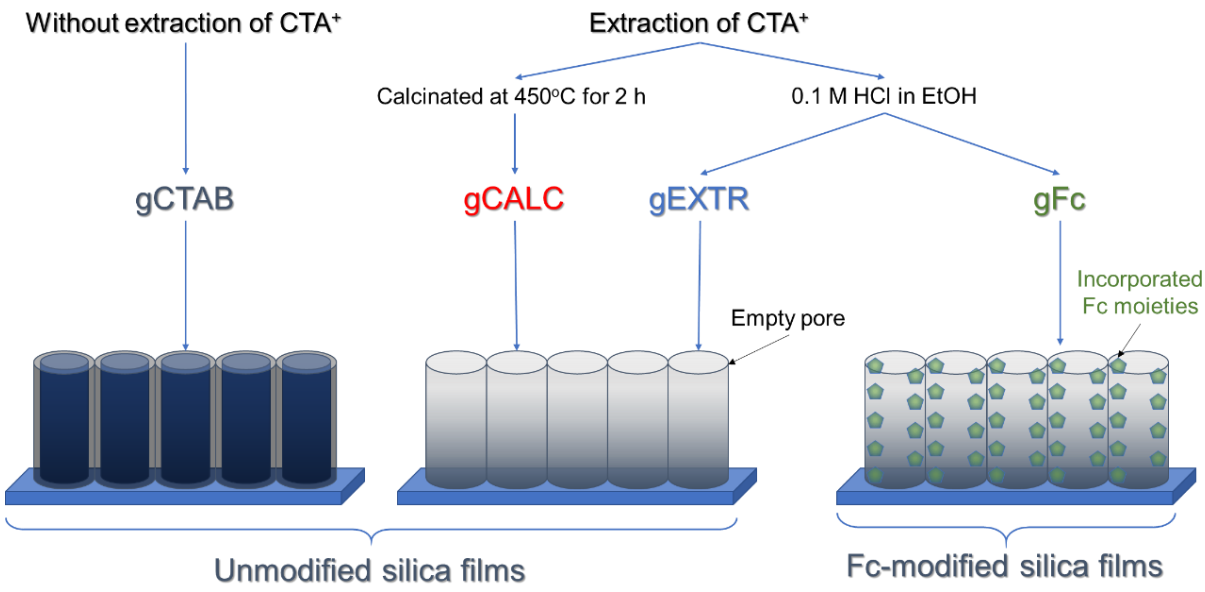

Figure 37 – Groups of the MSFs used for etching

3.3.1 Control experiments

No ITO etching

First, etching of ITO layer was investigated. A dissolution of the ITO surface layer can lead to random error on the thickness determination by profilometry technique. The control was made by putting bare ITO electrode in contact with 0.10 M NH_4F solution during 0.5 hour. *Figure 38A* depicts the evolution of the ITO surface profile before and after the reaction. No significant surface damage was noticed using profilometer when comparing the state of the ITO electrode before and after reaction. The almost overlaid cyclic voltammetry response of $Ru(NH_3)_6^{3+}$ on *Figure 38B* means that the surface area, which takes part in the electron transfer, stayed unchanged, what confirms the absence of dissolution. Therefore, the thickness values determined by profilometry reflect well those of silica films.

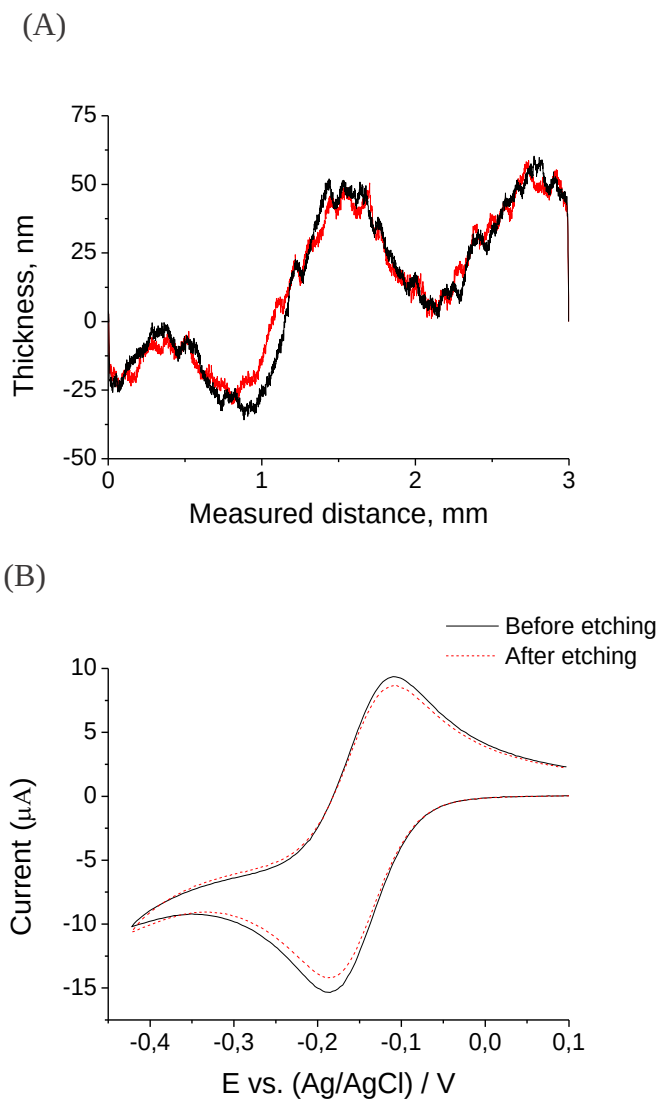

Figure 38 – (A) Profiles of ITO surface and (B) 0.5 mM $Ru(NH_3)_6Cl_3$ signal recorded before (black solid line) and after (red line) etching with 30 min 0.1 M NH_4F aqueous solution. (0.1 M $NaNO_3$, 50 mV/s scan rate)

Profilometry and CV measurements to follow etching process

The correlation between the profilometry measurements and the etching state in term of thickness was verified by using the gFc samples group. The presence of ferrocene functional groups attached on the internal silica walls of MSF is known to stay accessible and to give a reversible voltammetric response. This phenomena can be observed due to the electron hopping between the neighbouring Fc groups [107]. The CV peak current was found to be proportional to the quantity of grafted moieties [107,108]. Hence it was assumed, that in case of wet etching of Fc-modified

silica films, the thickness will be decreased leading to the loss of ferrocene entities and therefore, the electrochemical signal reduction (*Figure 39*).

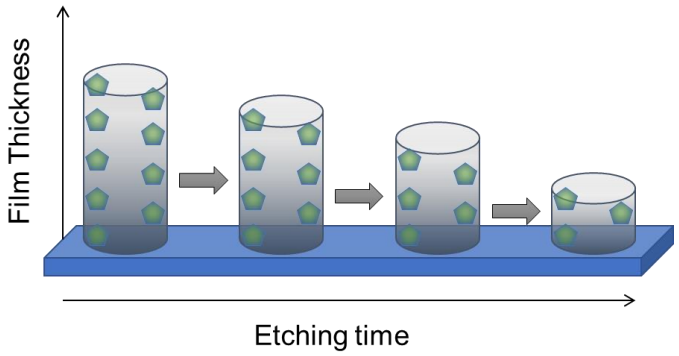

Figure 39 – The schematic representation of MSF thickness decrease during the wet etching of samples from gFc group

Electrochemical analysis was carried out at low scan rates (i.e. 5 mV/s) to allow the majority of the grafted electroactive groups take part in redox reaction [108]. Therefore, the peak current can be related to the thickness of the silica film. On *Figure 40*, the reduction of CV peak intensity while etching is depicted. The longer etching time results in the lower peak current. The decline is observed as the result of thickness decrease of modified MSF and fewer covalently bonded to silica channels Fc moieties inside pores after NH_4F treatment (*Figure 39*). The overlay of film thickness measured by stylus profilometry (in nm) and anodic peak intensities obtained from CV curves (in μA) as a function of etching time is presented on *Figure 41*. In this study, experiments were performed with 0.05 M NH_4F. The decrease of the CV signal recorded (anodic peak current) at low scan rate is in perfect agreement with the evolution of the thickness of MSF while wet etching.

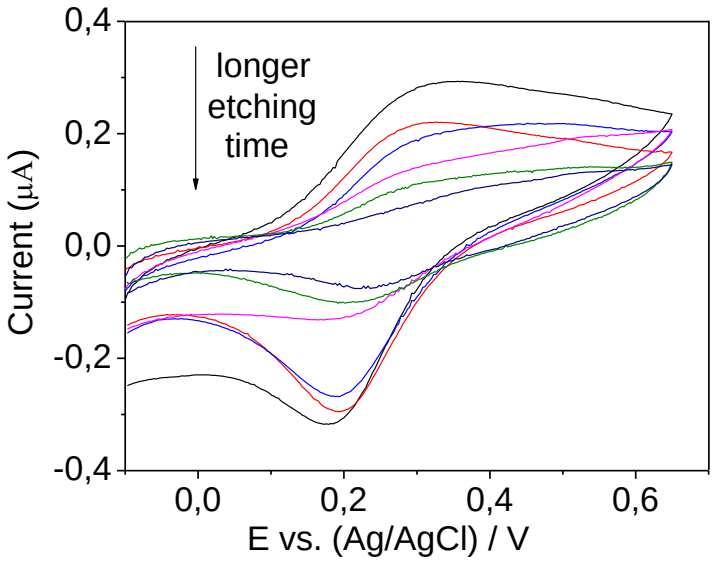

Figure 40 – The CV curves recorded in 0.1 M $NaNO_3$ (scan rate 5 mV/s) on ITO covered with ferrocene-modified MSF after etching with 0.05 M NH_4F for 0, 1, 2, 4, 7 and 10 hours

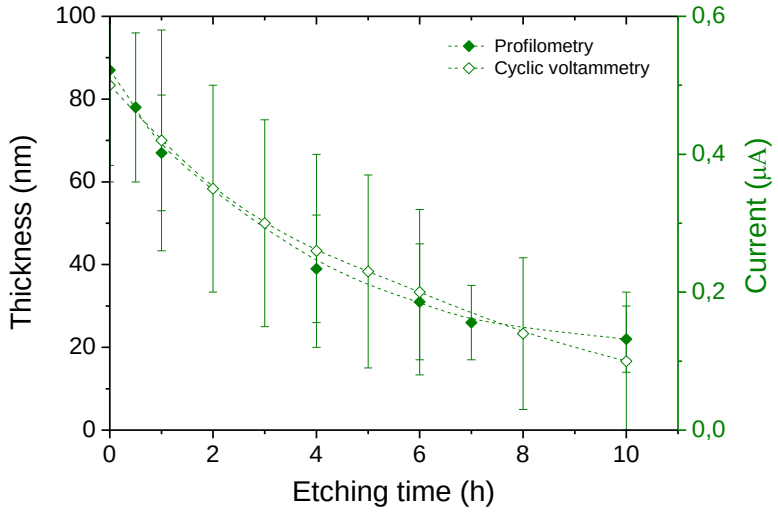

Figure 41 – Variation of film thickness from gFc group and evolution of the oxidation peak current while etching with 0.05 M NH_4F solution over increasing periods of time
(CVs were recorded in 0.1 M $NaNO_3$ with 5 mV/s scan rate)

Conditions for calcination

Bare ITO plates and ITO modified by MSF were exposed to 450°C (2 hours), 550°C (2 hours) and 600°C (1 hour) in order to test the conditions for template extraction by calcination.

The thermal treatment of MCM-41 silica around 800°C in presence of O_2 normally does not change the structuration of mesoporous material [186,187]. Such procedure results in modification of

surface silanol groups and densification of structure for sol-gel derived silica [188]. Treatment of thin films at 450°C does not affect ITO substrate and is known to be enough to extract organic template from vertically oriented pores [2]. At 500°C calcination of TiO_2 coated ITO was successfully performed [189], and treatment at 550°C was applied to extract the soft template from bimodal microporous-mesoporous silica film without losing its structuration [190]. Additionally to required surfactant removal by temperature treatment, keeping the mesoporous silica structure is another priority during this process. Hence, the chosen temperature range of 450 – 600°C seems to be appropriate for investigation of conditions for calcination.

GISAXS analysis of ITO covered with MSF after 450 and 550°C treatment resulted in two peaks typical for structured hexagonally packed material at $q_y = 1.72 \pm 1$ and 2.99 ± 1 nm^{-1} respectively (*Figure 42B* and *D*).

A peak at $q_y = 2.21$ nm^{-1} on *Figure 42D* corresponds to aggregates formed on the surface of films. After 1 hour of treatment at 600°C, no characteristic peaks for hexagonally oriented material are noticed on GISAXS image (*Figure 42F*), meaning that organisation of the film disappears. In parallel, profiles of MSF-covered ITO after high temperature treatment change their shape to dome-like (*Figure 42E*). Observed profile change and structural characterisation implies the idea of ITO or silica damage while calcination at high temperatures. A plate of ITO was treated at this temperature during the same time. Interestingly, linear to dome-shaped profile modification was noticed for the bare ITO treated at 600°C, when at lower tested temperatures no difference was noted (*Figure 42*, insets on *A*, *C*, and *E*). Based on the obtained results, it is suggested that deformation of ITO after being exposed to 600°C leads to the following damaging of the mesoporous structure of deposited film.

Therefore, soft conditions of calcination (2 hours at 450°C) were chosen in order to keep mesoporous silica film undamaged during the template extraction by thermal treatment.

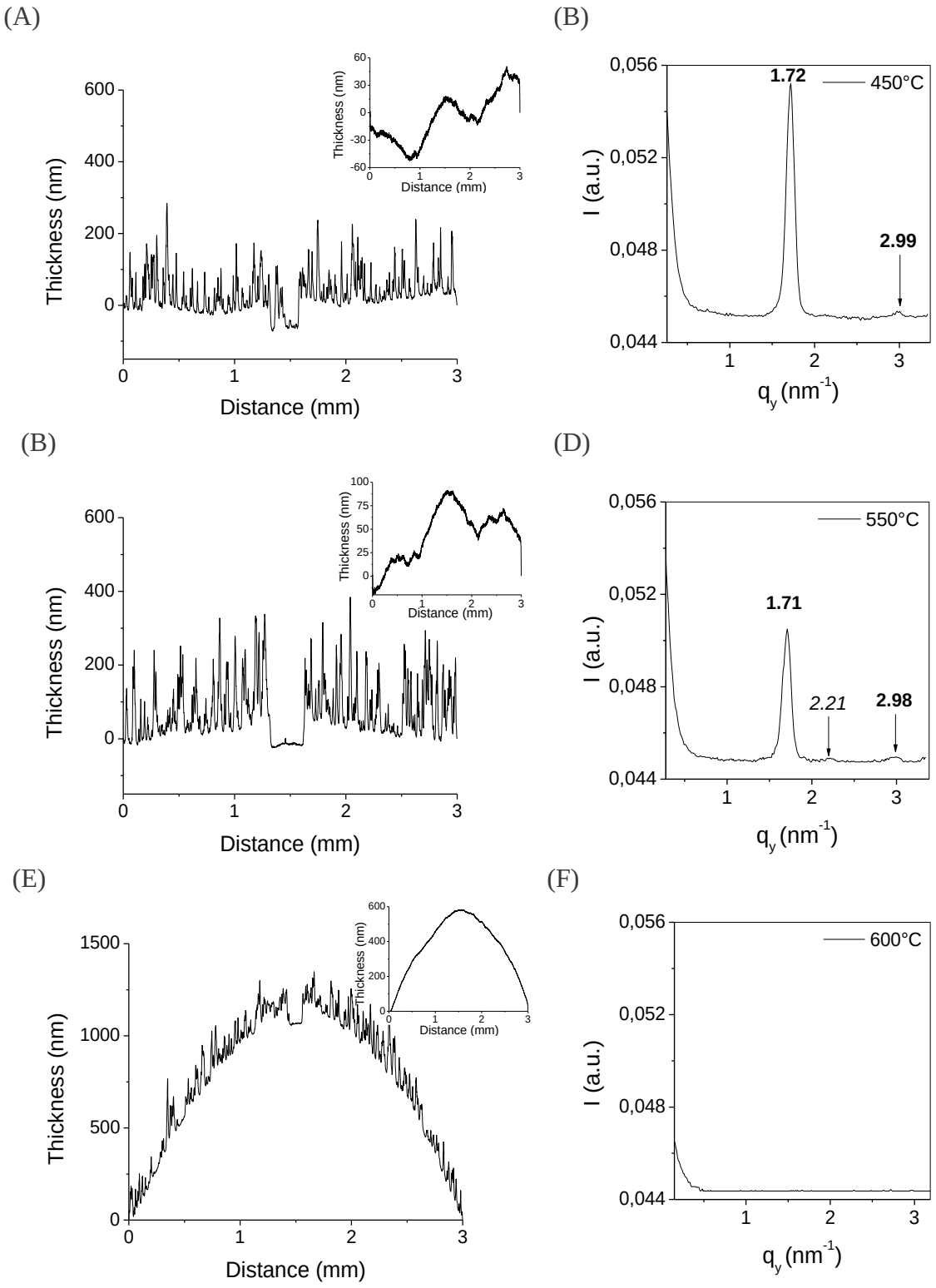

Figure 42 – Collected profiles and corresponding GISAXS patterns obtained after MSF-modified ITO calcination for CTA^+ removal at (A-B) 450ºC (2 hours), (C-D) 550ºC (2 hours), and (E-F) 600ºC (1 hour); Insets – related ITO profile after calcination

Effect of film scratching

In order to measure the thickness of mesoporous silica films, they were scratched before (*Preparation 1*) or after (*Preparation 2*) etching (**Section 2.5**). This manipulation partially destroys the film, and in case if it is done before etching, the presence of large defect can affect the etching rate and hence, the film thickness after treatment.

To verify the influence of sample preparation on final thickness, films with surfactant in pores (gCTAB) were etched with 0.05 M NH_4F for 1 hour following two described above ways of preparation. Statistical *t*-test for two means (two-tailed) was used to investigate if these two datasets can be treated as the same population. The Preparation 1 resulted in thickness 22.3 ± 9.1 nm (N = 6), whereas the Preparation 2 gave 38.8 ± 11.1 nm (N = 2). No statistical difference was observed between groups. Thus, both protocols can be used for the film preparation, where the scratch is made in the particular position according to *Figure 31*.

3.3.2 Effect of mesoporous silica film nature

Study of the etching rate

Etching was conducted on the different kinds of samples (i.e. unextracted and extracted template silica films) to see the influence of the surfactant presence and the way of its removal from the silica pores (liquid way or calcination). To conduct this study, etching was performed with 0.05 M NH_4F aqueous solution for different contact times. *Figure 43* depicts the evolution of the thickness measured by profilometry with respect to contact time with the etching reactant. As expected, whatever the group of the sample is, the increase of contact time with the NH_4F solution decreases, meaning that the silica film dissolution takes place. However, the general pattern for films with free silica channels is different from that of a film where surfactant was left inside the pores.

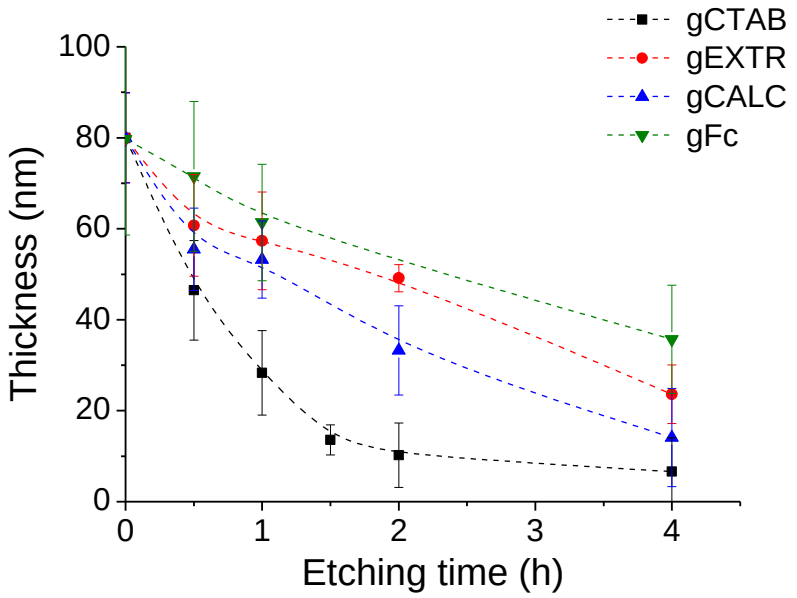

Figure 43 – Evolution of normalised thickness of films etched by 0.05 M NH_4F in function of reaction time: unextracted state (black line), extracted in 0.1 M HCl ethanol solution for 15 min (red line), calcined for 2 h at 450°C (blue line) and Fc-modified samples (green line).

Each curve presents two main steps: a more rapid etching step that occurs during the first hour of reaction and then a slower dissolution. The dissolution rate for extracted surfactant samples for the first 30 minutes is relatively slow and is equal to 0.6 nm/min comparing to films with CTA^+ staying inside the silica pores, which are dissolving twice as fast (1.1 nm/min). The change of thicknesses between gCTAB and gEXTR/gCALC batches starts being noticeable from 0.5 hours of etching. The obtained thickness around 10 nm for gCTAB samples etched for 4 hours is related to the aggregates left after etching on the ITO surface. They are not totally etched because of the large size comparing to thin mesostructured film.

The soft template extraction mode (solution way or calcination) does not seem to affect sufficiently the reactivity of the silica towards NH_4F. The evolution of the thickness in function of the reaction time for gEXTR and gCALC groups is quite similar. This same dissolution behaviour leads to the judgement that silica surface and its matrix possess similar properties towards NH_4F. In the same way, the presence of organic groups inside the silica pores does not impact the reaction kinetic what can be explained by the extraction of CTA^+ before the ferrocene grafting.

The temperature treatment is known to affect the nature of the silica material by densification of the network and hydrophobisation of the surface [191]. Thus, calcination reduces the reactivity of silica towards the etching agents [171]. Even though this effect was demonstrated for MSFs obtained by EISA-based dip-coating deposition after 2 hours exposure to 400^{o}C [192], it was not seen during etching of films generated by EASA, because materials are not quite the same (e.g. EISA films possess spherical pores, whereas those synthesised by EASA – cylindrical). Additionally, film surface recovers the regular hydrophilicity after staying at the ambient conditions before the contact with etchant [193]. Therefore, the extraction method does not affect the process of silica dissolution resulting in the comparable etching rate and profile evolution. Considering the aforesaid, gEXTR batch was chosen to represent MSF after the soft template extraction in the further experiments.

Keeping the surfactant inside silica pores leads to an increase of the dissolution rate, especially during the first hours. Different explanations can be proposed. The presence of CTA^+ that fills the pores leads to positive charge overload along the silica walls (see *Figure 33 e,d*). It contributes to the diffusion of anionic etching species. After the template removal and under the operated pH 5.5, silanol groups of the silica are deprotonated [13,194], hence pores are negatively charged. The diffusion of fluoride ions to surface and their adsorption on it becomes more difficult. In addition, the diffusion of the anionic dissolution products out of the pores is also difficult what can explain a lower etching rate [157,158]. On the other hand, Kikuyama *et al.* demonstrated that in presence of surfactant the wettability of the surface is improved leading to a possible and homogeneous etching [154]. Therefore, the variation observed between extracted and unextracted MSFs in the case of conducted experiments (*Figure 43*) is believed to be an outcome of pore state and in particular, the locally concentrated surfactant distributed over the pore surface.

The last type of films modified with ferrocene moieties have shown the similar decrease of their thickness after etching with NH_4F (*Figure 43*) but, in comparison to gEXTR and gCALC batches, the etching rate is somewhat slower. The incorporation of cyclopentadienyl parts of Fc leads to less hydrophilic characteristics of the material. The interaction between the etchant and the silica matrix becomes less favourable. Another restriction that appears with the modification of pores is their filling with introduced functional groups. This functionalisation leads to the mass transport

issues, what was shown on the example of azide-[107] and ferrocene-modified [108] films. The intensity of CV peak from the $Ru(NH_3)_6^{3+}$ probe is reduced for a film prepared with 10% AzPTES in the starting sol from and therefore in film. Under the operated conditions, gFc group of MSFs contains 20% of AzPTES and even larger mass transport limitations through channels are expected for fluoride etching species, reducing thereby quantity of etching fluoride species within the silica wall area. Presumably, less prominent hydrophilic properties of silica film surface coupled with the known mass transport restrictions in Fc-modified films, are causing the deceleration of silica dissolution rate of such samples in comparison to extracted gEXTR and gCALC samples.

Structural aspect of film etching

One important question for the analytical point of view is the need to preserve the film structure. TEM analysis was conducted on film samples after etching them for a determined time. Cyclic voltammetry was performed in parallel. As extracted films are permeable for the probes with the dimensions less than 3 nm (silica film pore diameter), the appearance of cracks during the etching process can be checked by selecting larger electroactive molecules. These probes cannot diffuse through the mesochannels to recover their redox signal. Previous papers demonstrated the exclusion of big molecules on flawless films in order to protect the electrode surface from fouling [195] or for molecular sieving by size-exclusion [118]. To see if some defects were produced during the etching reaction, electrochemical measurements with small conventional probe ($Ru(NH_3)_6^{3+}$ for gCTAB films) and larger one (haemoglobin (Hb) with a diameter around 5-6 nm [139]) were investigated.

For films without damage, the reduction of Fe (III) in Hb structure at the ITO surface according to *Eq. 3.8* is not possible due to its prevented diffusion across the silica film.

$$\text{Hb Fe(III)} + H^+ + e \rightarrow \text{Hb Fe(II)} \quad (\textit{Eq. 3.8}) \text{ [142,196]}$$

This statement is also true for the samples with soft template left in pores as well as for those that underwent the template extraction in solution or by calcination (see *Figure 44*).

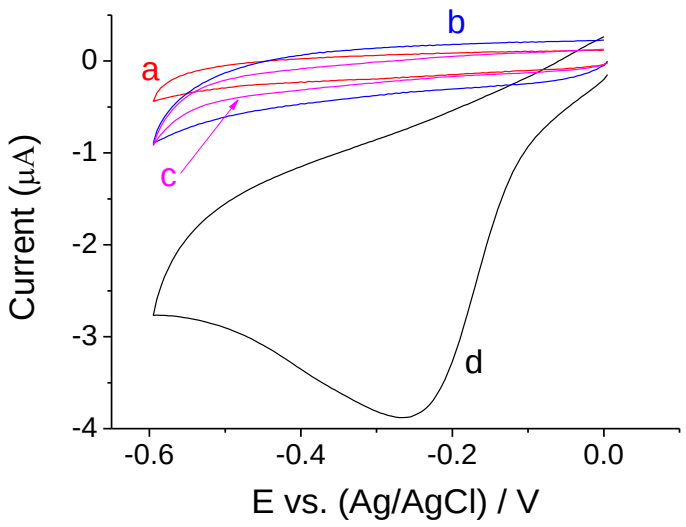

Figure 44 – The CV signal recorded in 5 μM Hb in phosphate buffer solution (PBS) (pH 5) on ITO covered with defectless MSF (a) before CTA^+ extraction (gCTAB, red line), (b) after solution CTA^+ extraction (gEXTR, blue line) and (c) calcination (gCALC, pink line) and (d) on bare ITO (black solid line)

Etching of template extracted films (gFc and gEXTR) shows a homogeneous etching up to 1 hour on the TEM top-view images (*Figure 45*). After 1 hour of contact with the solution, the organisation is maintained. However, on the gFc samples at a smaller scale more amorphous regions start to be created in the process of etching (*Figure 45B, 1h).* The cross sections display the presence of the vertically arrangement of the pores during etching up to 1 hour. With the increase of the contact time between silica sample and etchant, the edges of film become less sharp, what confirms the start of the structure loss (*Figure 45B, 4h*).

(A)

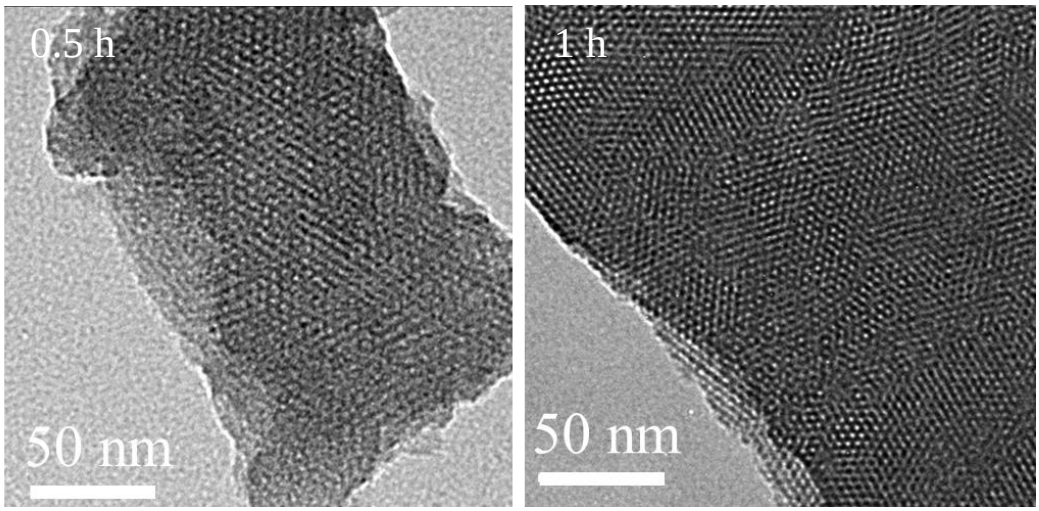

(B)

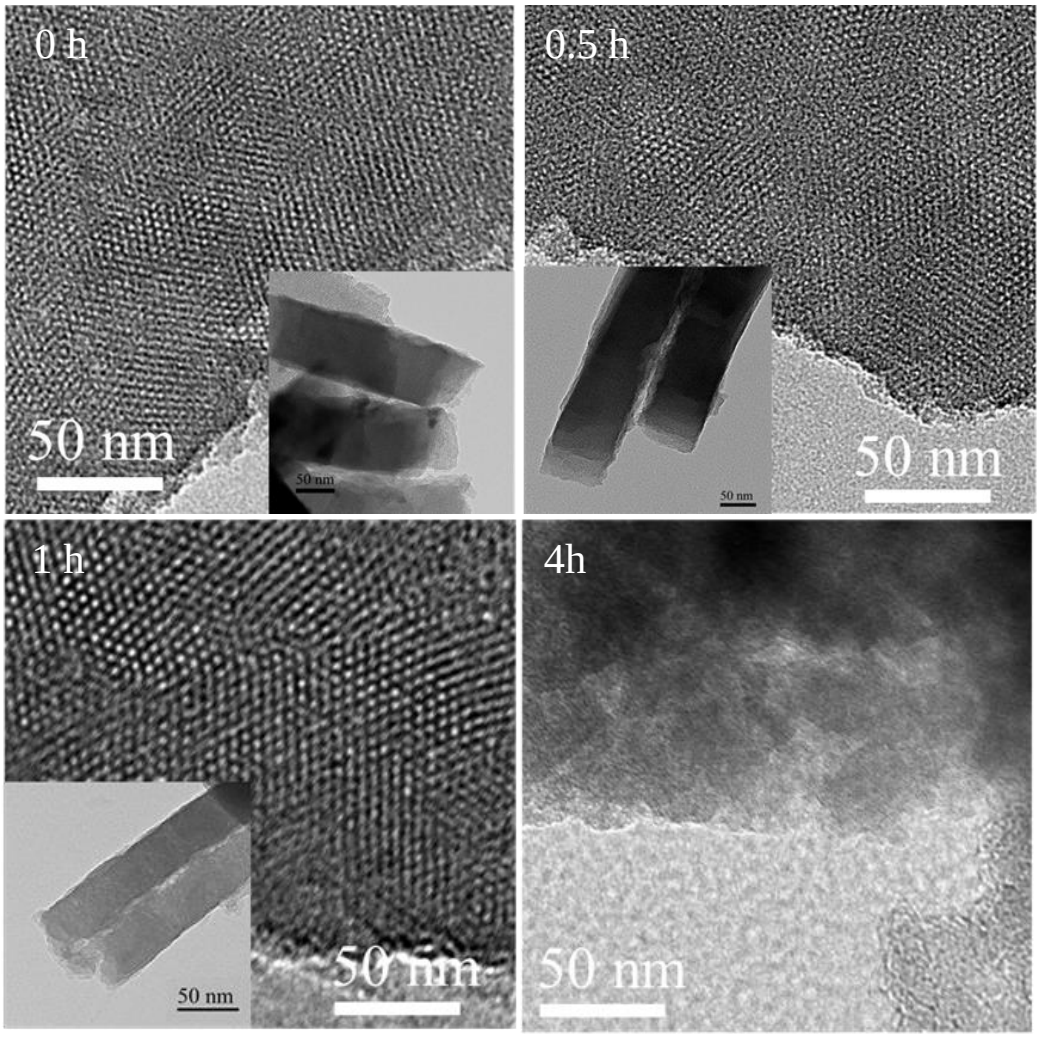

Figure 45 – TEM top view of (A) gEXTR and (B) extracted gFc mesoporous silica films before and after 0.5, 1 and 4 h etching times with 0.05 M NH_4F. Insets show the cross-section view

Electrochemical analysis performed with the Hb probe brings another evidence of the homogeneous etching of the extracted films. No prominent signal of Hb is detected up to 1 hour of reaction (*Figure 45A*). For longer reaction times, the clear signal of the reduction of Hb proves that more severe damage takes place during the etching and that is in good consistence with TEM observations. Some cracks are generated and they allow the diffusion of Hb.

(A)

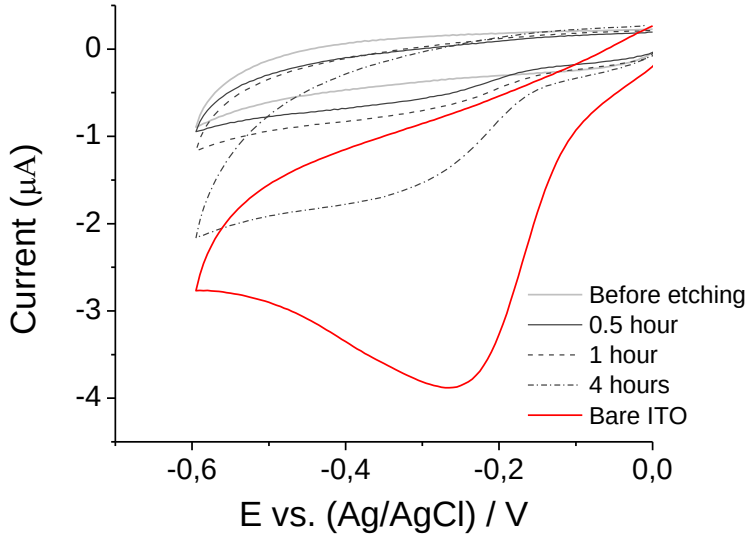

(B)

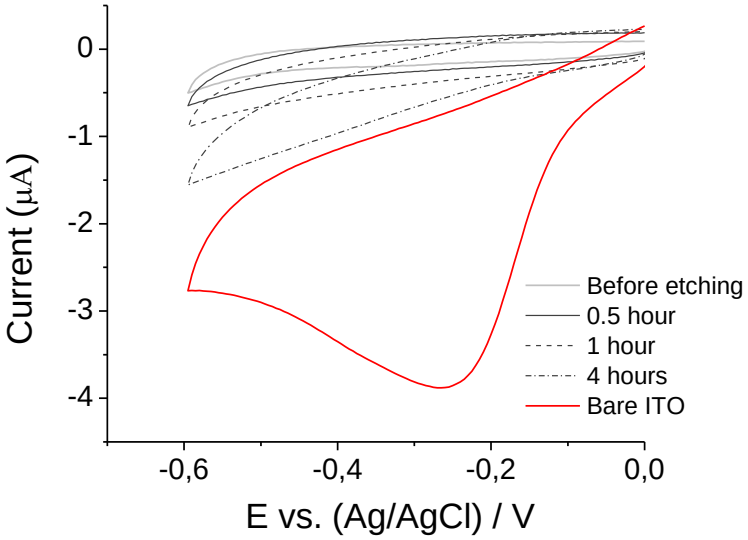

Figure 46 – Permeability of (A) gEXTR and (B) gCTAB MSF samples established by CV using 5 µM Hb deoxygenated solution in 0.1 M PBS (pH 5) before (grey bold line) and after etching with 0.05 M NH_4F for defined time (black lines). Comparison with the signal recorded on the bare ITO electrode (red line)

The silica deposit obtained by EASA method consists of the interconnected arrays as it was demonstrated on TEM image (*Figure 45A, 0h*) and the places of their joining are believed to be less protected from the etchant attack due to more surface area and non-stochiometric silicon dioxide ratio [155]. In addition, it is known that etching is inhomogeneous for the material with closed microcracks and defective surface like in case of silicate glass [161] and it causes the extra damage in these regions.

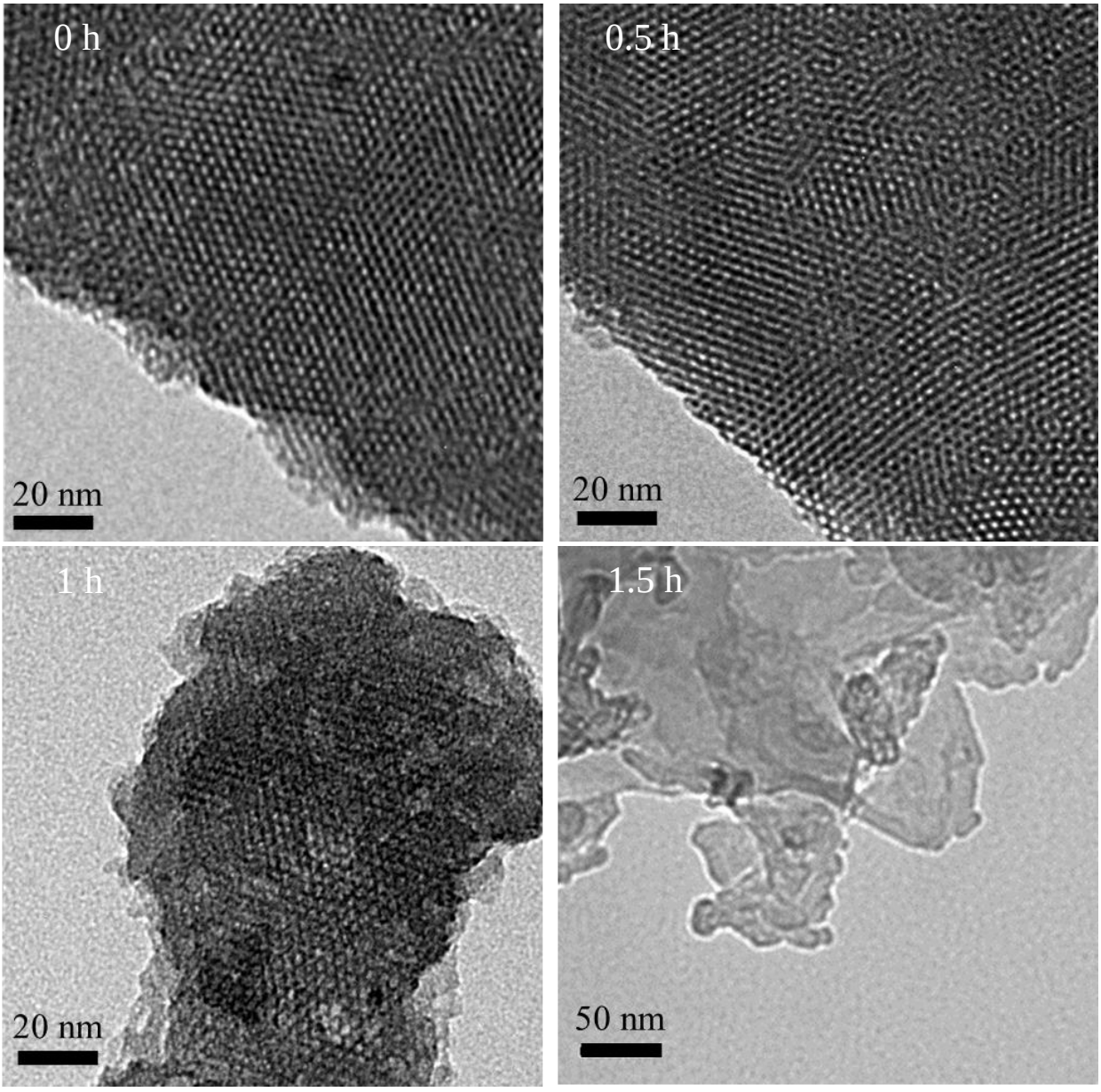

Figure 47 – TEM top view of gCTAB mesoporous silica films before and after 0.5, 1 and 1.5 h etching times with 0.05 M NH_4F

For the samples from gCTAB group with soft template kept inside the silica pores, the similar homogeneous etching was observed for short reaction times. Up to 1 hour exposure of NH_4F solution on film preserves the structure (see *Figure 47*). Nevertheless, the structure of the film starts to be somewhat affected after 1 hour contact, which was not the case of gEXTR films and even to a lesser extend for Fc modified MSF. The organisation of the silica film is not completely damaged, but also not entirely preserved compared to what was seen for gEXTR MSFs.

Electrochemical characterisation with Hb redox probe on *Figure 46B* shows the consistency with TEM images up to 1 hour of treatment. No signal from Hb is observed for 0.5 and 1 hour of etchant exposure, what points on the homogeneously etched film without large defects. However, the electrochemical characterisation of films after 4 hours of etching seems to be not in a good agreement with TEM analysis. Completely recovered Hb signal is expected on the ITO electrode after silica film dissolution, whereas the recorded curve does not show any signal of Hb. If the TEM image of the gFc MSF recorded after 4 hours of reaction displays some blurry regions of mesopores (*Figure 45B,* 4h) and can explain the possible diffusion of the probe molecule to the electrode surface, the TEM image of gCTAB films after 1.5 hours (*Figure 47*) shows a quite smooth film without a real porosity, preventing the Hb detection. The current peak intensity of $Ru(NH_3)_6^{3+}$ probe that was not recovered completely after 1.5 hours of etching also proves the presence of damaged film (*Figure 48*). Moreover, it is in accordance with TEM images (*Figure 47*, 1.5 h) and Hb characterisation (*Figure 46B*), as it shows that the film is still covering ITO surface.

The CTA^+ left inside the pores may act as a reinforcing agent to silica mesostructure. Therefore, while film dissolution, pore collapsing is delayed due to the additional wall support. Furthermore, it is also known that the addition of surfactant to etching solution prevents the formation of microroughness during the dissolution of silica-based materials, in particular for silica [154] and silicon [152,153]. The explanation of better etching performance lays in wettability of the surface, which increases in presence of surfactant. Having the CTA^+ micelles on the top of silica film could improve the discussed parameter, giving rise to more homogeneous dissolution of silica film without electrochemical detection of the evident flaws by Hb probe.

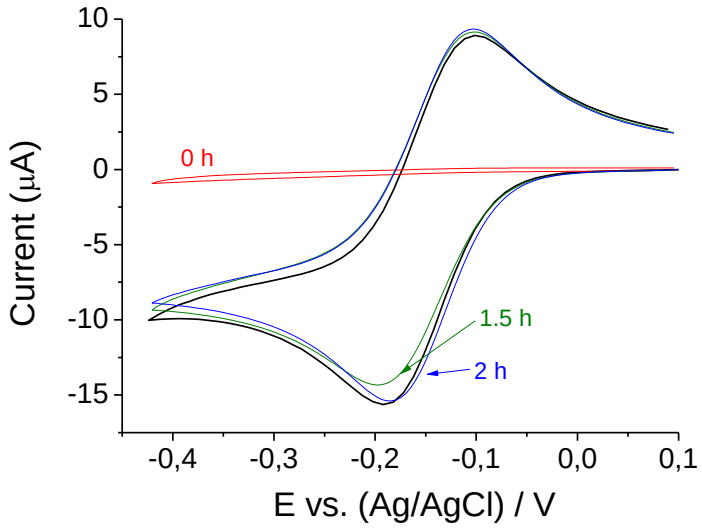

Figure 48 – Permeability of gCTAB MSF samples established by CV using 0.5mM $Ru(NH_3)_6^{3+}$ in 0.1 M $NaNO_3$ before (red line, 0 h) and after etching with 0.05 M NH_4F for 1.5 (green line) and 2 hours (blue line). Comparison with the signal recorded on the bare ITO electrode (bold black line)

1D GISAXS patterns are shown for gEXTR and gCTAB films respectively before and after etching (*Figure 49* and *Figure 50*). If the organisation of films is kept during the etching process, hexagonal orientation of cylindrical mesopores must lead to a diffraction ray centred on q_{max} = 1.69 [184], as observed on *Figure 49A* and *Figure 50A*).

After treatment with 0.05 M NH_4F solution during 0.5 hour, the main diffraction peak is still observed, with a lower intensity, a widening and a small shift (centred on q_{max} = 1.72 and 1.70, respectively for gEXTR and gCTAB). The second one at 2.91 nm^{-1} is not detectable (*Figure 49B*). It indicates that the pore diameter reduces during the treatment [197]. Particularly, changing of *d*-spacing occurs from 3.72 to 3.65 and 3.70 nm (calculated using equation $d = 2\pi / q_{max}$ [183]).

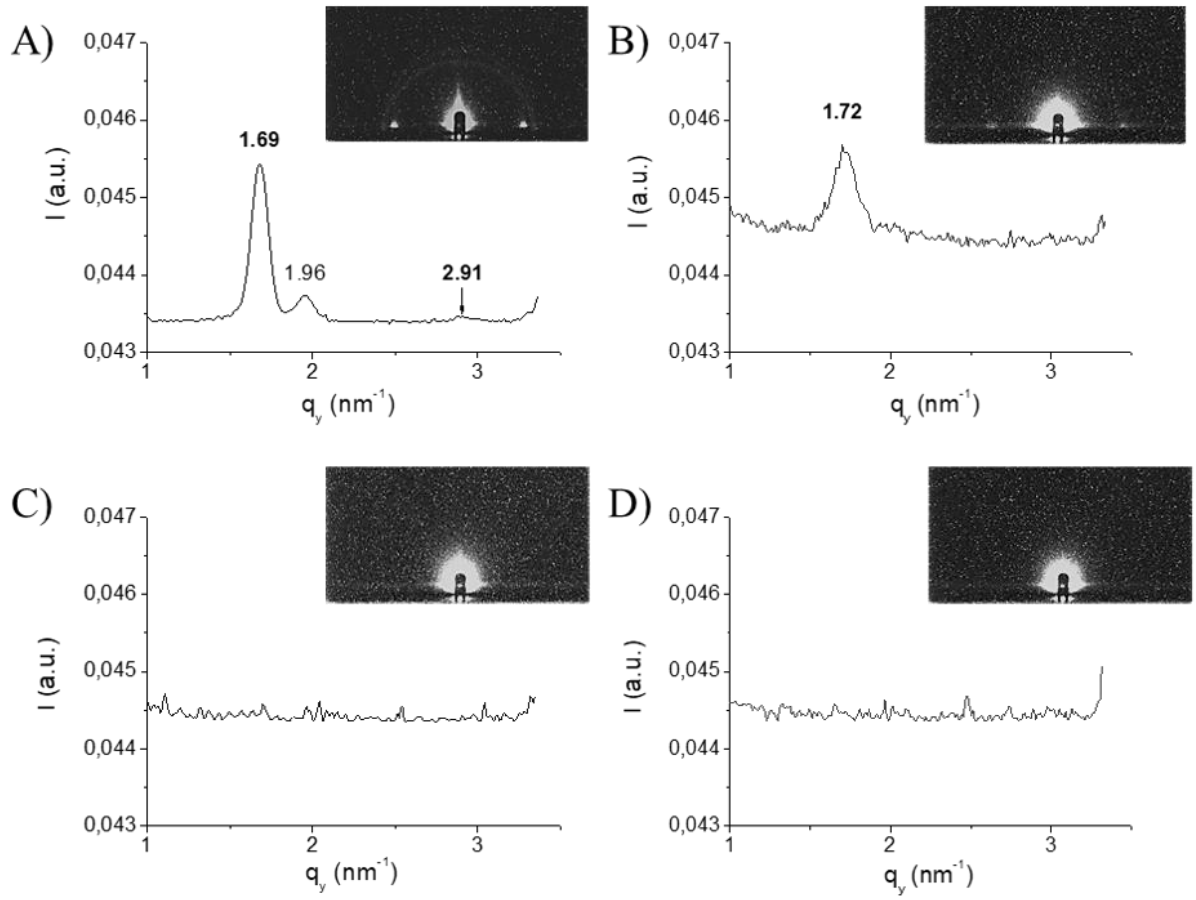

Figure 49 – GISAXS images of films before etching (A) and after etching without soft template (gEXTR) for 0.5 (B), 1 (C) and 4 (D) hours with 0.05M NH_4F
Insets – corresponding scattering (angle of measurement 0.25°)

Nevertheless, after 1 hour contact with gCTAB MSF, peaks that are typical for hexagonal orientation of material are not visible. This observation is supposedly related to the reduced thickness of the film and not to the issues of organisation, since TEM images and CV characterisation with Hb confirmed that films are staying structured and without big damages. Comparing the etching behaviour of gEXTR and gCTAB batches, the latter showed more rapid decrease of their thickness along with keeping the structure and the organisation of the silica film for longer time.

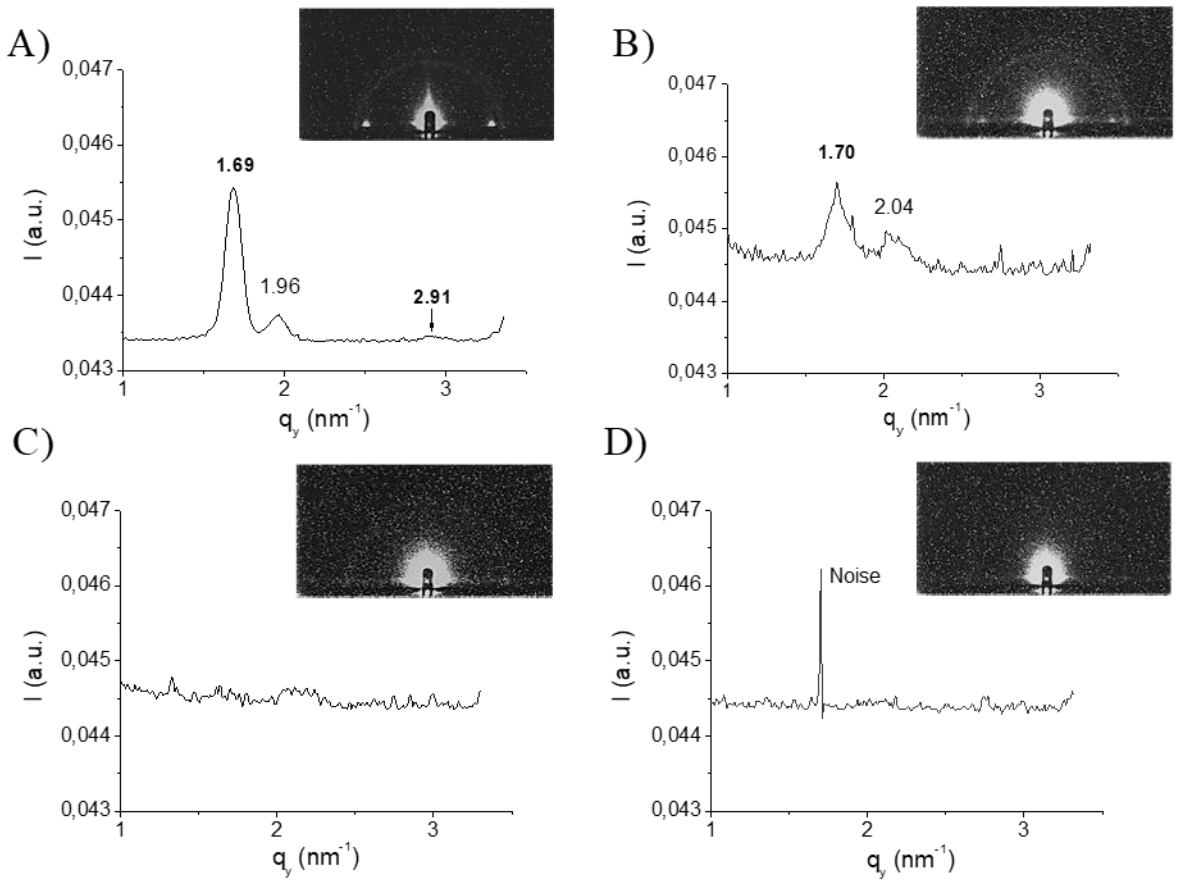

Figure 50 – GISAXS images of films before etching (A) and after etching with unextracted soft template (gCTAB) for 0.5 (B), 1 (C) and 4 (D) hours with 0.05M NH_4F
Insets – corresponding scattering (angle of measurement 0,25°)

Whatever the kind of MSF, the profilometry thickness measurement shows that the first region, which corresponds to the first hour of etching, depicts the linear evolution with homogeneous dissolution. The second phase of the wet etching process leads to the other tendency with slower etching rates, film damage and, finally, to collapse of mesostructure [3].

The measured thickness of well-organised gCTAB films is 28 ± 9 nm after being etched for 1 hour, while the minimal thickness for gEXTR group which can be reached for the undamaged mesoporous films by this approach is 57 ± 11 nm.

3.3.3 Effect of the NH_4F concentration

The impact of the NH_4F concentration was also studied. Although the effect of the etching agent concentration was mostly described for stronger reagents like HF or mixture of HF and NH_4F with or without the addition of acids [158,160,170], the common idea is that the increase of the fluoride-containing component leads to faster silica dissolution as the result of higher content of attacking species.

Wet etching of gCTAB and gEXTR films was conducted in 0.01 M and 0.1 M NH_4F solutions. *Figure 51* depicts a comparison of new data with those previously obtained (0.05 M NH_4F solution). The decline of thickness for extracted and unextracted films in case of etching with different NH_4F concentrations is logically observed for all tested conditions. Overall, the linear range of the thickness evolution while etching is much shorter with higher etchant concentration. Faster thickness reduction is always observed for gCTAB sample group and, as expected, the reaction rate is faster with the increase of the etchant concentration. With 0.10 M NH_4F, it is approximately 1.5 times faster than after its extraction with the etching rates 1.7 nm/min for extracted and 0.8 nm/min for unextracted films. The increase of etchant concentration to 0.10 M for etching of extracted films did not allow recording the instant film thickness reduction for the first 15 minutes supposedly due the hydrophilization of the silica surface that takes place at this step [142], although in the next 15 minutes the faster dissolution occurs. Moreover, 0.10 M NH_4F does not cause the complete dissolution of gEXTR samples in 2 hours (34 nm), unlike for unextracted MSFs.

Dissolution of unextracted films presented on *Figure 51A* demonstrates that dissolution is faster with more concentrated NH_4F. Comparison of results obtained with 0.01, 0.05 and 0.10 M NH_4F solutions for the first 30 minutes leads to 0.3, 1.1 and 1.7 nm/min etching rate, respectively. In 30 minutes, the thickness of the film was reduced from 80 to 71 nm after etching by 0.01 M NH_4F, while for 0.05 and 0.10 M solutions it was decreased to 47 and 29 nm respectively.

(A)

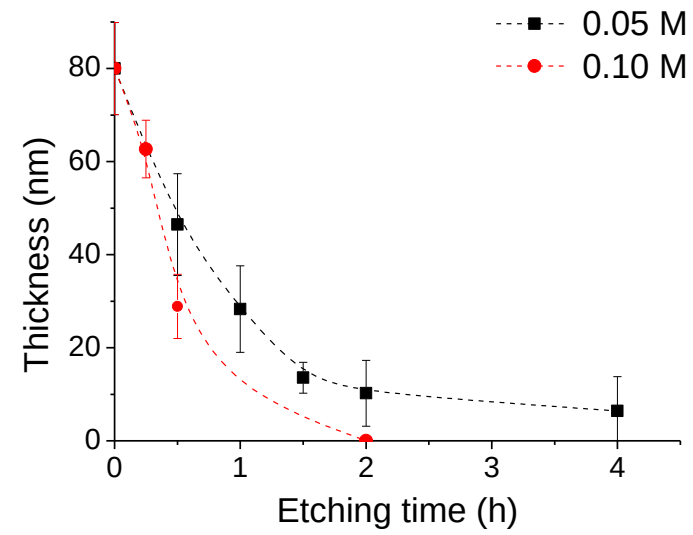

(B)

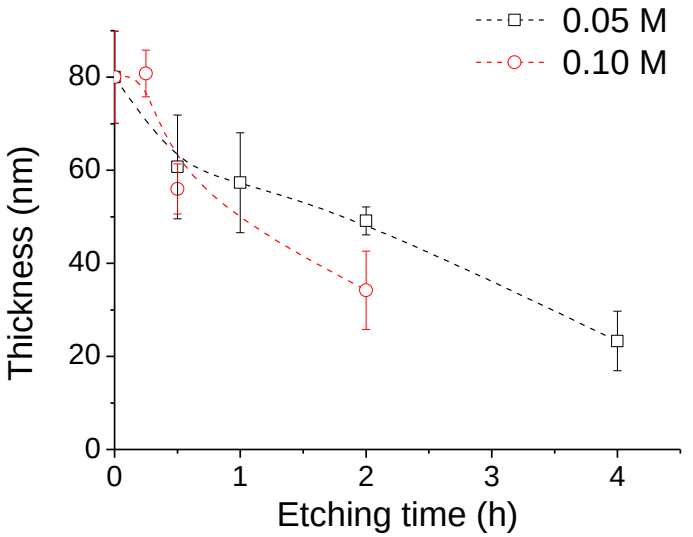

Figure 51 – The effect of the NH_4F concentration on the rate of etching of (A) gCTAB and (B) gEXTR groups

The elemental analysis obtained from XPS analysis for the samples which were etched by 0.01 M NH_4F solution for 10-30 minutes is given in *Table 3*. The shortest tested time (10 minutes) resulted in traces of In and Sn which were detected. With the longer etching times higher, the presence of the ITO components was found. The increase of In and Sn parts is gradual and show the dissolution of the silica film as the reaction time progresses (*Figure 51*).

Table 3 – XPS surface characterisation of ITO electrodes before and after MSF deposition and after etching of MSF with 0.01 M NH_4F aqueous solution during different periods of time (measurements performed on four zones)

	Atomic concentration, %					
	Si	In	Sn	O	C	N
Before etching						
Bare ITO	-	14.9 ± 1.2	2.3 ± 0.2	32.1 ± 1.7	50.6 ± 3.3	0.2 ± 0.3
MSF / gCTAB	18.3 ± 0.6	-	-	37.3 ± 1.0	43.2 ± 1.3	1.2 ± 0.2
After etching						
10 min	18.2 ± 1.3	0.1 ± 0.1	-	37.5 ± 2.6	42.8 ± 3.8	1.3 ± 0.2
20 min	21.1 ± 2.0	0.3 ± 0.2	0.1 ± 0.0	42.7 ± 4.9	35.0 ± 6.8	0.9 ± 0.3
30 min	16.6 ± 0.5	1.8 ± 1.1	0.3 ± 0.2	37.6 ± 2.0	42.8 ± 3.2	0.9 ± 0.3

After etching of gCTAB MSFs for 10 minutes with 0.05 M NH_4F solution some traces of In were noted (because of the more sensitive signal) that is in good agreement with a homogeneous etching reaction and the absence of real defect generation. The ITO components, which were detected after etching for a longer time, are confirming the release of the electrode substrate after treatment as a result of possible silica film damaging. It should be noted that the Nitrogen, which was also detected along with the other chemical elements, is related to the hydrophilic part of tertiary amine of CTA^+ that was kept inside pores during the conducted experiments. Another hypothesis that could be used to explain the appearance of In and Sn traces in XPS spectra as well as CV signal of $Ru(NH_3)_6^{3+}$ for films after etching is the surfactant extraction during etching under the influence of fluoride media. No strong evidences were found to support this theory (**Appendix 3**).

A structural characterisation by GISAXS was performed on sample etched with soft template for 30 minutes with 0.10 M NH_4F and result is shown on *Figure 52*. Interestingly, a characterisation peak at $q_y = 1.71$ was observed for this film after treatment along with a peak related to aggregates at $q_y = 2.18$. Appearance of a first one shows that hexagonal organisation of the film is quite maintained after etching by more concentrated etching solution with concurrent thickness reduction to 29 nm (measured by profilometry and normalised).

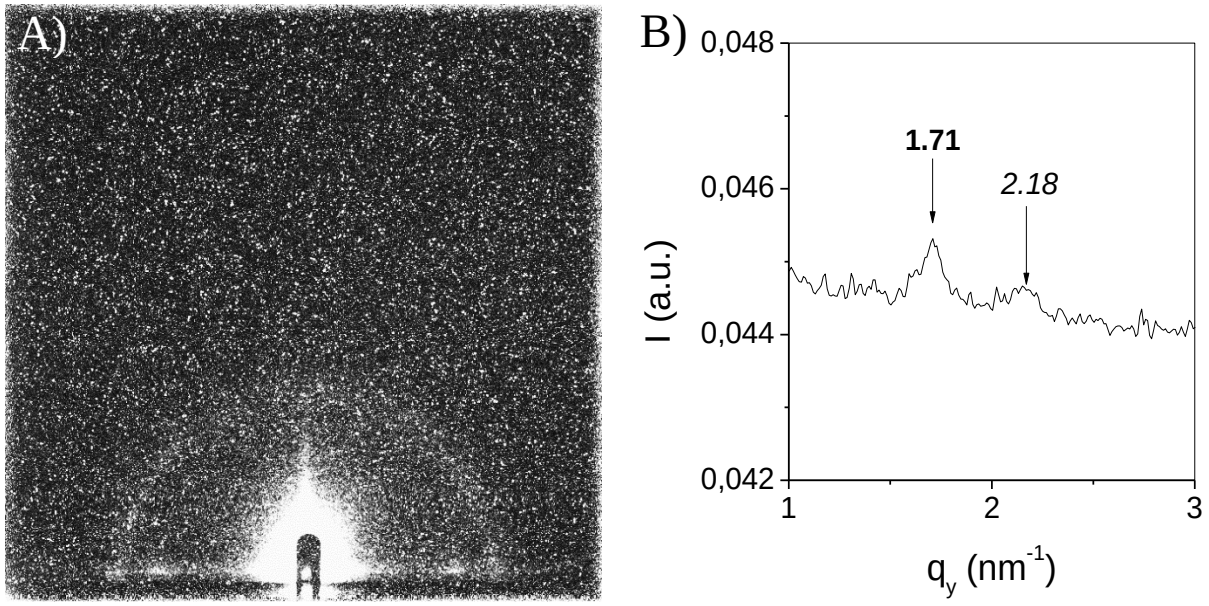

Figure 52 – (A) GISAXS pattern and (B) its integration recorded for gCTAB film after etching for 30 minutes in 0.10 M NH_4F solution

Apparently, more concentrated etching solution causes faster decrease of MSF thickness. Besides, wet etching gives rise to small defect formation over the gCTAB MSF surface, which was proved to occur using the electrochemical probing with $Ru(NH_3)_6^{3+}$ and by presence of In and Sn peaks in XPS spectra. The majority of obtained results showed that regardless the concentration of the etching agent and time of its exposure on film, the creation of minor flaws is inevitable.

3.3.4 The effect of the etching agent

The nature of the MSFs was shown to influence the etching procedure. Therefore, it was interesting to study films behaviour in function of other commonly referred etchants. Two main families of reactants were selected: alkaline- (hydroxides KOH and NaOH) and fluoride-based (HF, NH_4F, KF) aqueous solutions. The dissolution process is somewhat different in function of the nature of the etchant for a same initial concentration (0.05 M) and a same reaction time (30 minutes) (*Table 4*).

Table 4 – Thickness of MSF determined by profilometry in function of etching agents and the nature of the film for a reaction time of 30 minutes and etchant concentration of 0.05 M

Etching agent, 0.05 M	Thickness before etching, nm	Thickness after etching, nm	
		gCTAB	gEXTR
NH_4F	80 ± 9	46 ± 11	60 ± 11
KF		65 ± 12	79 ± 6
HF		ND	ND
KOH		47 ± 8	ND
NaOH		67 ± 9	ND

ND – Not Detectable

The etching reaction is complete with hydrofluoric acid whatever the group of the MSF (CTA^+ inside the silica pores or not). After half an hour, the silica film is totally dissolved and the dissolution seems to be very fast with the etching rate > 2.7 nm/min. According to model presented by Verhaverbeke for SiO_2 films obtained at 1000°C in dry O_2 and etched in fluoride solutions [163], calculated values for etching rate of MSFs are 0.02 (without taking into account H_2F_2 active species) and 0.12 nm/min (includes the presence of H_2F_2). Following Kikuyama model for thermal silica which depends on [HF^{2-}] concentration [175], the etching rate calculated for EASA synthesised films is 0.04 nm/min. Much faster experimental etch rate values for MSF are believed to be an outcome of film nature. Firstly, sol-gel originated films obtained by EASA undergo 130°C treatment during their preparation, when SiO_2 films obtained by thermal oxidation are exposed to 1000°C. It makes silica matrix denser and can explain slower etching rates presented in publication [167]. As another example of temperature effect, for sol-gel films annealed at 500°C the etching rate (in BHF solution) was shown to be around 0.8 nm/min, when after 1000°C treatment it decreased to 0.2 nm/min [168]. Secondly, the porosity is also a factor that can explain the difference on the behaviour [168].

By using fluoride salts (NH_4F and KF), MSFs remain on the surface of the electrode with a decreased thickness for gCTAB group. A difference between performances of two fluoride salts is observed. Final thickness after etching is about 46 nm and 65 nm, respectively after treatment with

NH_4F and KF. As for gEXTR MSFs, silica dissolution occurs while using NH_4F (thickness decreased from 80 nm to 60 nm), but not with KF (no change of film thickness).

Aydin et al. demonstrated differences of reactivity of NH_4^+ and K^+ in aqueous solution even though the similarities are observed in the size of the first solvation shell of two ions. An easier migration of NH_4^+ into nanopores or ion exchange membranes was concluded by authors due to the smaller solvation energy, which facilitates desolvation and diffusion [198]. In particular, the most valuable effect is caused by H^+ [57] (H^+ possesses the largest solvation energy among the single charged cations [199]), in presence of which the fastest etching rates are observed. Similar assumption about the role of cation in etching solution was made by Luo and Chidsey. After etching of silicon surface with Ar-sparged 9.3 M KF and NH_4F aqueous solutions it was found that dissolution was four times faster with NH_4F treatment [200].

Alkaline media (NaOH and KOH) affected the film in a different way both on i) the resulting thickness for same experimental conditions and ii) in function of the nature of the MSF. Films of gEXTR group are totally dissolved after 30 min irrespectively of the nature of alkaline reactant. No thickness could be determined by profilometry. It was reported that alkaline solution, e.g. 0.01 M NaOH, was successfully used to produce ultrathin mesoporous films by very rapid etching with the mesostructured kept [3]. The gCTAB group was partially dissolved and with a sufficient difference when comparing results with KOH (thickness decreased from 80 to 47 nm) and NaOH solution where only a slight variation was observed (67 nm after etching). In alkaline media silica dissolution is caused by Si-O bond polarisation and weakening due to deprotonation of silanol groups and creation $Si\text{-}O^-$ sites [201]. High negative charge leads to detachment of silicon atoms. For quartz it was shown that the process accelerates at pH higher than 8. Interestingly, the action of counter-ions (and additional cations introduced to alkaline etching solution) has a catalytic effect as well as for fluoride solutions [202,203]. The main role of cations in silica-based material dissolution by alkaline is believed to be the removal of anions from the surface. Therefore, this phenomenon can result in different etching rates obtained with NaOH and KOH solutions (*Table 4*). Going from Na^+ to K^+ the radius increases, resulting in the lower charge density and, therefore, smaller hydrated radius of potassium cation [204]. It should assist in faster removal of anions and facilitate the silica dissolution. According to obtained results for gCTAB films, the strength of etchants increases in the order $KOH \approx NH_4F < NaOH \approx KF << HF$.

3.4 Conclusions

EASA method allows deposition of MSFs on ITO electrodes with the homogeneous continuous and undamaged layer of minimum thickness 80 ± 9 nm from a sol containing 100 mM silica precursor (TEOS) in presence of 32 mM CTAB by applying -1.3 V potential. Obtaining thinner deposits is restricted to a minimal time deposition of 10 s because of the uncomplete covering for shorter preparation times, which was proved by presence of ITO by XPS and electrochemical analysis.

Wet etching approach can be used to reduce thickness of films. With respect to pore conditions, etching rate differs. Whatever the tested etchant or its concentration is, faster film dissolution occurs for samples with unextracted soft template (gCTAB sample). HF solution is not recommendable due to fast film dissolution and difficulty to adjust wet etching procedure. With 0.05 M NH_4F solution, the rate of 1.1 nm/min, etching of extracted films (gEXTR group) happens almost two times slower (0.6 nm/min). It is suggested, that the difference is observed due to the combination of increased wettability of unextracted films and their excessive positive charge on the top, which attracts more anionic etching species.

Soft etching agents like NH_4F are more preferable because of the slower etching rates and, therefore, more controllable process. Thin films that keep their well-organised structure were obtained with 0.05 M NH_4F aqueous solution up to 1 hour of treatment. The presence of surfactant inside pores allows to prepare the thinnest well-organised films 28 ± 9 nm. On contrary, for films with free pores the smaller thickness without damaging the structure is only about 57 ± 11 nm. Longer etching times lead to destruction of film structure.

Chapter 4

Development of system based on $Ru(bpy)_3^{2+}$ modified mesoporous silica thin film for glyphosate detection by electrochemiluminescence

4.1. Introduction

4.1.1 General information about $Ru(bpy)_3^{2+}$ as electrochemiluminescence reactant

Since the publication of Burstall [205] reported about the synthesis of a new orange $Ru(bpy)_3^{2+}$ compound back in 1936 (*Figure 53 inset*), the properties of the complex and its derivatives were extensively studied by electrochemistry [206–208] and spectroscopy [209–211]. Having the ruthenium in the centre of coordination sphere allows to oxidise complex following the reaction (*Eq. 4.1*):

$$Ru(bpy)_3^{2+} \rightarrow Ru(bpy)_3^{3+} + e^- \quad (Eq.\ 4.1)$$

(Orange) (Green)

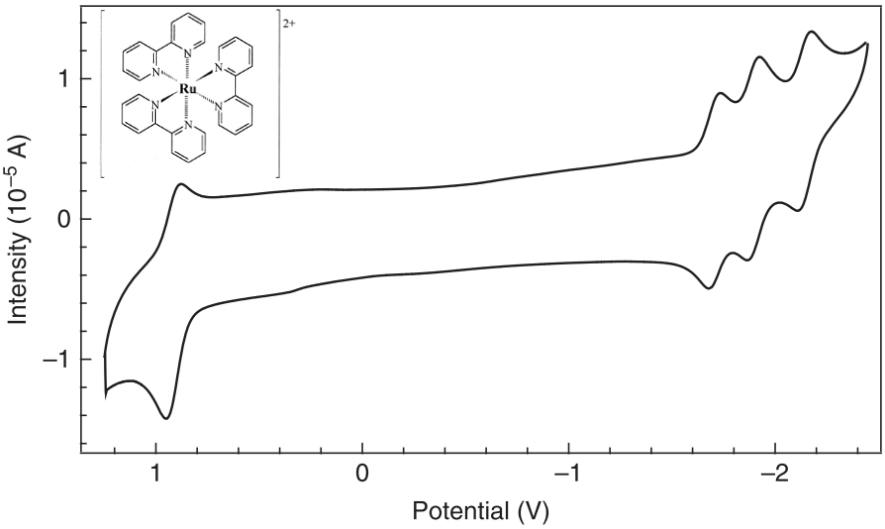

Figure 53 – Cyclic voltammogram of $[Ru(bpy)_3](PF_6)_2$ in CH_3CN solution, using 0.1 M tetrabutylammonium hexafluorophosphate as supporting electrolyte (potentials are referenced to the Fc/Fc^+ couple that was added as an internal standard) [212]

The reduction process involves three electron transfers observed in the range of – 1.5 to – 1.3 V depicted on *Figure 53*. They correspond to reduction of each of three bipyridine ligands and can be described by following equations [212]:

$$[Ru(bpy)_3]^{2+} + e^- \rightarrow [Ru(bpy^{\cdot -})(bpy)_2]^+ \text{ (}Eq.\ 4.2\text{)}$$

$$[Ru(bpy^{\cdot -})(bpy)_2]^+ + e^- \rightarrow [Ru(bpy)(bpy^{\cdot -})_2] \text{ (}Eq.\ 4.3\text{)}$$

$$[Ru(bpy)(bpy^{\cdot -})_2] + e^- \rightarrow [Ru(bpy^{\cdot -})_3]^- \text{ (}Eq.\ 4.4\text{)}$$

Along with the loss of the electron, the colour of the compound in solution changes from orange-red to green (*Eq. 4.1*). Coloration, which can be observed, appears as a result of electronic charge transfers of different nature (*Figure 54A*). With the report of Paris and Brandt in 1959 [213] another important property was discovered, namely luminescence of the complex caused by metal-to-ligand charge transfer (MLCT).

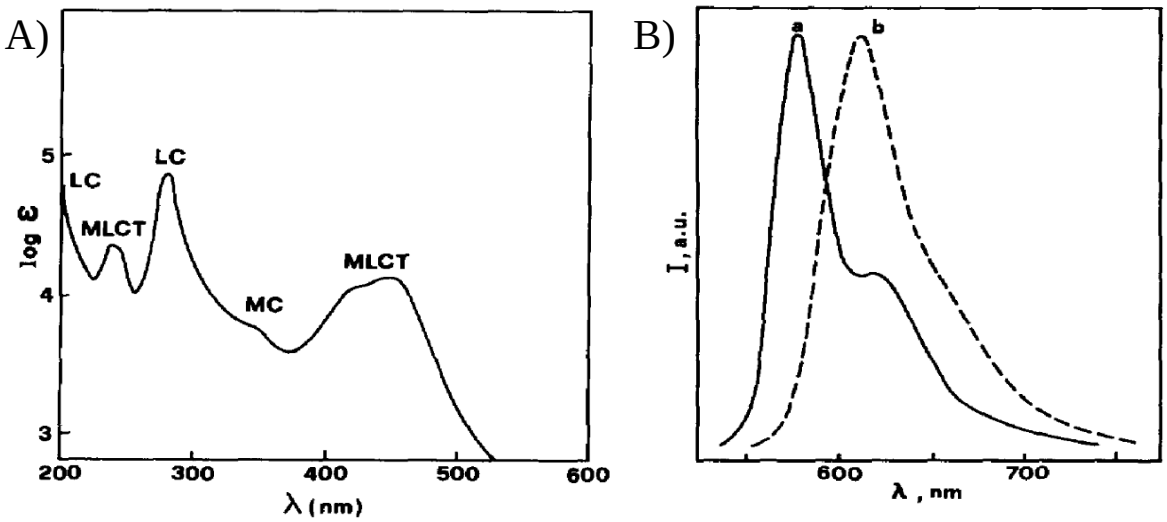

Figure 54 – A) Absorption spectrum of $Ru(bpy)_3^{2+}$ in aqueous solution at room temperature (LC – ligand-centred, MC – metal-centred, MLCT – metal-ligand charge transfers) and B) emission spectrum of $Ru(bpy)_3^{2+}$* in alcoholic solution (*a* – at 77 K and *b* – at room temperature) [214]

Overall, ligand centred (LC) π- π* transitions can be seen at λ = 185, 208 and 285 nm, the weak shoulders at 323 and 345 nm along with the twin peaks at 238 and 250 nm are corresponding to metal-centred (MC) *d*-*d** transitions [209]. The broad intense peak at 452 nm was attributed to metal-ligand charge transfers (MLCT) after the evidences provided by Classen and Crosby [215, 216].

Another specific property of $Ru(bpy)_3^{2+}$ complex and its derivatives is generation of a light emission from the excited state called luminescence. Typical emission spectra in alcoholic solution

at 77 K and at the room temperature are illustrated on *Figure 54B*. Excited state of the molecule can be reached by different sources such as chemical reaction or external light irradiation of suitable wavelength, what leads to chemiluminescence or photoluminescence respectively.

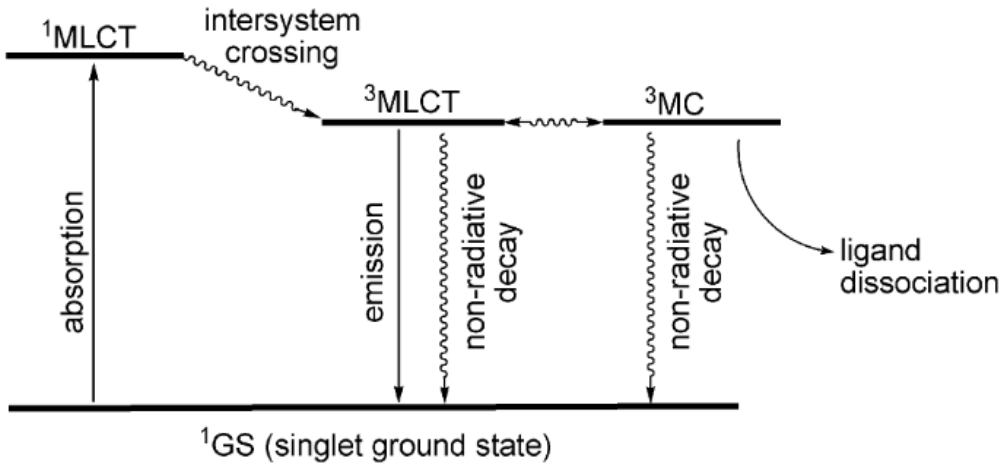

Figure 55 – A simplified Jablonski diagram for Ru(II) polypyridine complexes (^{1} – singlet and ^{3} – triplet states) [217]

In case of photoluminescence, the energy which was adsorbed in the visible region causes the electron transfer from a ground state of the highest occupied molecular orbital of metal to lowest unoccupied molecular orbital of ligand. The following inter-system crossing results in the light emission (about 600 nm, *Figure 54B*), coming from the electron transfer from triplet excited state down to the singlet ground state [217], what is schematically represented on Jablonski diagram for Ru(II) complexes on *Figure 55*. The presence of reductants like 1,6-diaminopyrene [13] and oxalate anions [218, 219] causes the chemiluminescence, which has the same steps of excitation and emission.

Electrochemical and spectroscopic properties resulted in the utilisation of $Ru(bpy)_3^{2+}$ complex and its derivatives for electrochemiluminescence (ECL), firstly described in acetonitrile media in 1972 [220]. In these experimental conditions, observed emission was generated by alternative and rapid changing the electrode potential, which created locally a mixture of $Ru(bpy)_3^{3+}$ and $Ru(bpy)_3^{+}$ (*Eq. 4.5* and *Eq. 4.6*). As a result, an interaction between them led to the excited state species, $Ru(bpy)_3^{2+*}$ (*Eq. 4.7*). Its decay to the ground state was accompanied by a light emission at 620

nm (*Eq. 4.8*) [221]. Presented mechanism of ECL generation by formation of oxidised and reduced species in the pre-electrode area is called annihilation (*Eq. 4.5 – 4.8*).

$$Ru(bpy)_3^{2+} \rightarrow Ru(bpy)_3^{3+} + e^- \qquad E^o_{Ru}{}^{2+/3+} = +\ 1.2\ V\ vs.\ SCE \qquad (Eq.\ 4.5)$$

$$Ru(bpy)_3^{2+} + e^- \rightarrow Ru(bpy)_3^{+} \qquad E^o_{Ru}{}^{2+/1+} = -\ 1.4\ V\ vs.\ SCE \qquad (Eq.\ 4.6)$$

$$Ru(bpy)_3^{3+} + Ru(bpy)_3^{+} \rightarrow Ru(bpy)_3^{2+*} + Ru(bpy)_3^{2+} \qquad (Eq.\ 4.7)$$

$$Ru(bpy)_3^{2+*} \rightarrow Ru(bpy)_3^{2+} + h\nu \qquad (Eq.\ 4.8)$$

This organometallic family of complexes is easily soluble in aqueous solution, depicts a high emission efficiency and possesses a stable intensity and an electrochemical regeneration during ECL generation.

The other way to generate ECL in a single-potential step is in presence of co-reactant. This pathway was observed by Tokel and Bard [220]. Upon oxidation or reduction, the produced intermediate from the co-reactant can react with the luminophore (ruthenium complex), what leads to its excited state. Oxalate anions were the first species showing this behaviour [222]. Two pathways of radical generation were suggested to explain the ECL mechanism. The first involves the direct reduction of oxalate at the working electrode (*Eq. 4.9*) with parallel oxidation of $Ru(bpy)_3^{2+}$ (*Eq. 4.12*), whereas the second is triggered by $C_2O_4^{2-}$ interaction with $Ru(bpy)_3^{3+}$ (*Eq. 4.10*) [223]. Both cases result in a highly reactive $C_2O_4^{\bullet-}$ radicals (*Eq. 4.11*), that excite $Ru(bpy)_3^{3+}$ to $Ru(bpy)_3^{2+*}$ (*Eq. 4.13*):

$$C_2O_4^{2-} \rightarrow C_2O_4^{\bullet-} + e^- \qquad (Eq.\ 4.9)$$

$$Ru(bpy)_3^{3+} + C_2O_4^{2-} \rightarrow Ru(bpy)_3^{2+} + C_2O_4^{\bullet-} \qquad (Eq.\ 4.10)$$

$$C_2O_4^{\bullet-} \rightarrow CO_2^{\bullet-} + CO_2 \qquad (Eq.\ 4.11)$$

$$Ru(bpy)_3^{2+} \rightarrow Ru(bpy)_3^{3+} + e^- \qquad (Eq.\ 4.12)$$

$$Ru(bpy)_3^{3+} + CO_2^{\bullet-} \rightarrow Ru(bpy)_3^{2+*} + CO_2^- \qquad (Eq.\ 4.13)$$

Among all co-reactants, amines are one of the most interesting compounds to be used. They are widely represented in environment, especially in biological systems and in pharmaceuticals. This is why, a number of bioassays were designed and commercialised in order to detect various pathologies and drugs by amine functional group [224,225].

The mechanism of co-reactant ECL reaction of $Ru(bpy)_3^{2+}$ with amine was extensively studied on the example of tripropylamine (TPrA) and represented on *Figure 56* [226]. Scheme 1 implies that oxidation of $Ru(bpy)_3^{2+}$ and TPA occurs at the electrode surface in parallel. As a consequence, amine radicals (marked as $TPrA^{\bullet}$ on *Figure 56*), created independently from complex, excite $Ru(bpy)_3^{3+}$ with emission of light according to *Eq. 4.8*. Scheme 2 supposes the same pathway as Scheme 1, with the only difference that complex can undergo more than one cycle of light emission, meaning it can be regenerated. Basically, Scheme 1 and Scheme 2 from *Figure 56* are corresponding to mechanism presented for oxalate by *Eq. 4.9* and *Eq. 4.12*. Scheme 3 on *Figure 56* illustrates the catalytic route, where TPrA is oxidised by $Ru(bpy)_3^{3+}$, leading to $TPrA^{\bullet+}$ generation. It is equal to the second mechanism proposed for oxalate co-reactant system (*Eq. 4.10*). Scheme 4 proposes another view on the ECL mechanism [226]. It refers to the case, when ECL is detected further from the electrode because of the diffusion of electrochemically generated $TPrA^{\bullet+}$ to bulk solution. This maximum distance (of 6 μm) is defined by diffusion coefficient and a half-life time of cation radical species. According to the Scheme 4, $TPrA^{\bullet}$ reduces $Ru(bpy)_3^{2+}$ to $Ru(bpy)_3^{+}$, which then is oxidised by $TPrA^{\bullet+}$ cation radicals to produce excited $Ru(bpy)_3^{2+*}$ species.

Direct oxidation of the co-reactant (Scheme 1 and 2, *Figure 56*) is observed for TPrA on glassy-carbon electrode [227]. Nevertheless, this step was not successful for Au and Pt electrodes because of the surface oxides, which inhibited the ECL signal, pointing on the importance of the electrode material. In this case, the reaction mechanism is more likely to follow Scheme 3. It was also shown that this pathway is preferable for higher concentrations of $Ru(bpy)_3^{2+}$ in solution [227].

Scheme 1:

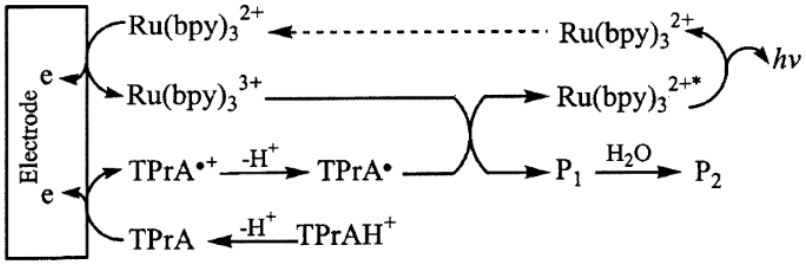

Scheme 2:

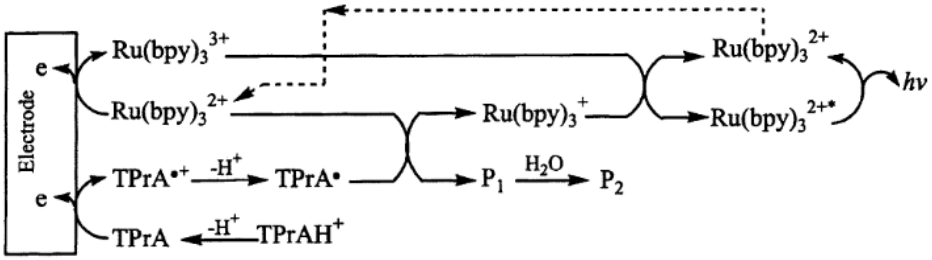

Scheme 3:

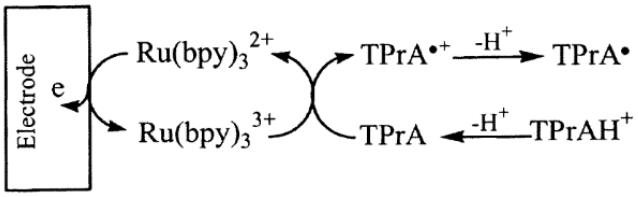

Scheme 4:

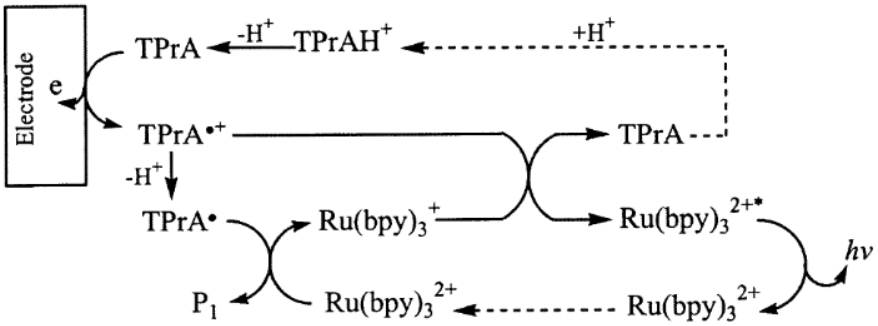

Figure 56 – Proposed mechanisms of ECL reaction of $Ru(bpy)_3^{2+}$ with tripropylamine (TPrA) as co-reactant [226]

Noteworthy, the structure of amine plays an important role in the ECL effectiveness. In order to obtain the best response, secondary and tertiary amines should be the choice because of their structure stabilisation after the deprotonation in the α-position, what is demonstrated on *Figure 57* [224,228]. Primary amines also give the ECL response, yet because of the worse radical stabilisation ECL intensity is suppressed. According to Noffsinger and Danielson [229], the signal response for methyl- and ethylamine is 60 times less than that for TPrA analogues. Nevertheless,

the quantitate transformation of primary amine to secondary or tertiary leads to increase of sensitivity of amine detection (so-called derivatisation step). This approach was used for aliphatic amines derivatisation with divinylsulfone to transform analytes to tertiary amines [230].

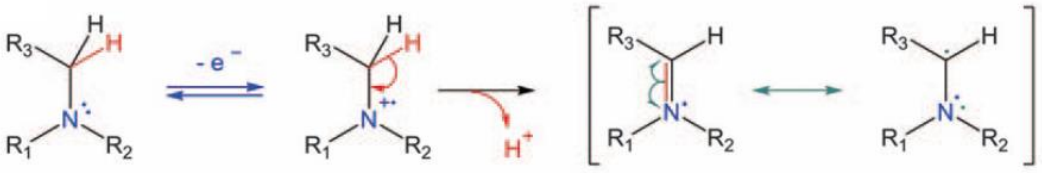

Figure 57 – Sequence of chemical reorganisation following the initial electron-transfer reactions for TPrA [224]

Another study included analysis of 21 amino acids by ECL. Depending on the structure of amine, minimum limit of detection varied from 1 µM for proline to 2.5 mM for asparagine, glycine and serine [231].

In addition to nature of amine, it was also shown that resonance stabilisation of radical intermediate in aromatic amines as well as presence of electron withdrawing substituents located close to amine functional group (carbonyl, halogen or hydroxyl) are causing the reduction of ECL intensity because of the reduction of intermediate reactivity and destabilisation of radical respectively. Conversely, electron-donating functionalities (like alkyl chain) are assisting in higher ECL signal [228].

The effect of pH on ECL reaction with amine co-reactants was studied as well. According to proposed mechanisms (*Figure 56*), one of the necessary steps is cation radical deprotonation. To facilitate this process, alkaline media (pH > 9) must be used [232].

4.1.2 Immobilisation of $Ru(bpy)_3^{2+}$ onto solid matrix

Immobilisation of the luminophore on the electrode surface is giving a number of advantages [233,234]. Admittedly, the experimental design becomes much simpler since it is not necessary to deliver the chemiluminescent reagent continuously (therefore pumps are of no need). Another positive side is the reduced consumption of $Ru(bpy)_3^{2+}$ due to its immobilisation and regeneration after being excited without a significant loss of luminescence activity. As for the ECL reaction, the control over it is performed by changing the potential, but the light emission is localised near

the surface of the electrode (prohibiting pathway presented on Scheme 4 on *Figure 56*). Immobilisation of $Ru(bpy)_3^{2+}$ was already performed by various approaches:

1) **Immobilisation of layers of $Ru(bpy)_3^{2+}$ onto the electrode surface, among which are**:

Self-assembled monolayers (SAM) and multilayers. The most evident route is attachment of complex through thiol bonds to gold electrode (thiol group was introduced to one of the bipyridine ligands), what was demonstrated by group of Bard [235]. Nevertheless, it was not clearly confirmed by authors that monolayer was formed through covalent bonds. Moreover, it was discussed that the bilayer could also be assembled under operated conditions. Later, the similar approach was conducted to immobilise luminophore onto surface of gold and ITO electrodes through covalent bond [236]. It this study, modification of one of the bipyridine ligands of ruthenium complex by thiol-terminated functional groups in two positions (4, 4'), what allowed to recover stable electrochemical signal from ITO-modified electrode, but not from the golden one. It was suggested that monolayer was detached due to Au-S bond break. Another way to immobilise $Ru(bpy)_3^{2+}$ was demonstrated for glassy carbon electrode modified with $-SO_3H$ groups (by benzenesulfonic acid) [237]. In this case, complex was electrostatically absorbed. The ECL signal was stable after storing it dried for a week. Direct absorption of $Ru(bpy)_3^{2+}$ on oxide-covered glassy carbon electrode resulted in much lower signal which was decreasing under consecutive scanning [238]. Contrary to this, the electrode with electrochemically deposited ruthenium complex, which was encapsulated within pores, is preferential to physical adsorption in terms of electrode stability.

Langmuir-Blodgett films. Langmuir-Blodgett films were deposited on In-doped tin oxide, Pt and Au [239] and on Ti-sputtered ITO [240] electrodes using surfactant-modified (tris)bipyridine ruthenium (II). These films were not compatible with organic solvents. There was also no mentions about the stability of formed layers and the CV curves were recorded right after film.

Apart from the monolayer obtained on Au electrode which was suffering from instability [236], all materials were demonstrating the electroactivity of attached (tris)bipyridine ruthenium (II) complex or its derivatives. Nevertheless, this approach did not continue developing further likely due to stability issues and too small signal (since the flat electrodes were used, limited amount of electroactive ruthenium complex could be immobilised).

2) **Modification by absorption of $Ru(bpy)_3^{2+}$ complex on Nafion and other cation-exchange matrixes**

Modification of the electrodes coated with the Nafion polymer coating became a popular direction due to the ion-exchange nature of matrix. Compared to previously discussed layers, it allows to absorb $Ru(bpy)_3^{2+}$ complex physically on its surface in larger quantity because of higher surface area provided by pores. Consequently, it resulted in an impressive increase of peak current switching from mono- or bilayer of ruthenium complex on the flat electrodes to its incorporation in porous Nafion film (the range from µA [239] to ~10^2 µA [241]). Pyrolytic graphite [241] Pt [242] or glassy carbon [242,243] were used as substrates. Using these systems, the ECL was generated in presence of oxalate, TPrA and proline [243] by co-reactant mechanism as well as following the annihilation by changing the electrode potential [241]. Despite the listed advantages, the limitations caused by mass and charge transport were observed within the film [241]. Also, the decrease of electrochemical signal was observed with time supposedly because of the migration of $Ru(bpy)_3^{2+}$ into inactive hydrophobic regions. The attempts to improve the electrode coating stability were done by addition of polymers (4-vinylpyridine [244] or Eastman-AQ cation exchange polymer with sol-gel silica [245]) and titania [246,247]. Zirconia-Nafion composite films for capillary electrophoresis were also studied [248]. Presence of Zr increased electrocatalytic current in comparison to pure Nafion. Lidocaine, TPrA and proline were detected. Nevertheless, leaching of ruthenium complex was still observed because of no covalent bonding.

Addition of sol-gel silica to Nafion matrix resulted in signal which is stable for 6 days before showing a decrease of peak current [249]. Incorporation of $Ru(bpy)_3^{2+}$ by electrostatic absorption onto the solid matrix was extensively studied by group of Wang [245,250,251]. By the addition of Triton X-100 the drying of the film was prevented [250]. The ECL signal from films containing poly(p-sterensulfonate) was higher than that of $Ru(bpy)_3^{2+}$ - Nafion films [250]. Strong electrostatic absorption provided up to 6 month stability of composite [251]. Yet, the preparation of such electrode coatings was not reproducible [251].

Similarly to Nafion, Eastman-AQ polymers, which have cation exchange sites, were used in combination with TEOS-based silica sol to immobilise $Ru(bpy)_3^{2+}$ by ion-exchanging mechanism [245]. Resulted matrix provided stronger adhering properties towards complex comparing to Nafion because of the more hydrophilic environment, what prevented the unwanted partition of

Ru complex. In aqueous solution, better accessibility was also reached. A higher stability of ECL signal while dry storage (up to 2 month) was reached, which could be used to detect TPA, oxalate and chlorpromazine. Mesoporous molecular sieves were modified from solution by $Ru(bpy)_3^{2+}$ exhibited the bright luminescence in aqueous media [252] and electrochemical response in supporting electrolyte [253], but no ECL experiments were conducted that time on these materials. Finally, $Ru(bpy)_3^{2+}$ was incorporated in mesoporous silica films with vertically aligned pores [120]. It allowed to use this material for ECL detection of TPrA, nicotine and atropine. The rise of ECL signal comparing to ITO electrode was promoted by silica layer which possesses a high surface area and assists in incorporation of more reagent. Observed CV signal in presence of co-reactant was better defined and had smaller capacitive current contribution comparing to performance of composite films with silica, more likely due to better electron transfer within vertical pores. Unfortunately, no stability tests were performed for this material.

Another direction is the immobilisation of $Ru(bpy)_3^{2+}$ in silica nanoparticles [254–256]. In one case, ruthenium-doped silica nanoparticles were obtained by TEOS polymerisation in presence of $Ru(bpy)_3^{2+}$ and were then combined with chitosan biopolymer on glassy carbon electrode [256]. Similar approach based on chitosan and Ru-doped silica nanoparticles was applied to deposit film on Au and Pt electrodes [254]. More complicated system was obtained from Au nanoparticles modified by ruthenium-silica nanocomposites and bonded to thiol-functionalised ITO surface [255]. It was reported that the use of $Ru(bpy)_3^{2+}$-modified silica nanoparticles leads to lower detection limits for TPA [256] and to better stability of ECL signal in time along with longer fluorescence response due to silica-$Ru(bpy)_3^{2+}$ interaction [255,256] in comparison Nafion-based composites.

3) Covalent attachment of $Ru(bpy)_3^{2+}$ and its derivatives

A valid solution to overcome the problem of reactant leaching is covalent bonding of redox complex to matrix. Polystyrene polymer chain was derivatised by $Ru(bpy)_3^{2+}$ through one bipyridine ligand and these units were introduced to silica gel films in presence of Triton X-100 [257] (surfactant was used to prevent material from drying as shown in [250]). No leaching after drying was exhibited and the range of current was comparable to Nafion-modified coating [241]. Triethoxysilane modified ruthenium complex was attached to polysiloxanes with co-condensation reagents, but no electrochemical behaviour of this coating was discussed [258].

Instead of modification of matrix by $Ru(bpy)_3^{2+}$, complex can be functionalised itself to provide functional groups capable to bond covalently. In this light, it was modified to become a Ru-containing organosilane precursor [259, 260]. An interesting approach was demonstrated by Lee and colleagues, which was based on modification of bipyridine ligands with trimethoxysilyl groups. As a result, an organosilicate coating was deposited on ITO electrode with covalently incorporated $Ru(bpy)_3^{2+}$ moieties in its matrix [259]. According to authors, this electrode exhibited a decrease of ECL intensity after 6 months storage of 10%, the same as in case of continuous operation in solution for 8 hours. In both examples ruthenium complex was entrapped inside silica matrix resulting in no leaching of reactant. In the second case [260], despite a dense matrix and entrapped redox complex, a distinguishable electrochemical signal was obtained comparable to that in solution with free probe.

4.1.3 Glyphosate and its detection

Glyphosate (GLYP, N-(phosphonomethyl)glycine) is a derivative of a natural amino acid glycine substituted by phosphorous functional group (*Figure 58*). In 1971, its herbicidal properties, which later provided an effective control over the world's worst weeds, were reported by Baird in 1971 [261]. The way of its action is unique [262]. It targets and binds a specific enzyme produced by plants, which is necessary for their growth. As a result, the development of the organism stops because of the lack of aromatic amino acids (tyrosine, phenylaniline, triptophan). In the late 1990s and 2000s the use of glyphosate increased significantly [263] (15-fold increase of its use was observed from 1996 to 2016 [264]), what made it one of the most frequently detected residue in soils along with a product of its decomposition aminomethylphosphonic acid (AMPA) [265].

In the study of Franz et al. from 1997 it was demonstrated, that 79-86% of glyphosate can be biodegraded in soil, what is comparable to results obtained by Giesly et al., that confirms the decomposition of herbicide in less than a year [266]. Its wide application in agriculture impacted the burst of publications about the cancer incidence cases [267]. However some controversies exist because herbicide is claimed to be harmless in the used concentrations [268,269].

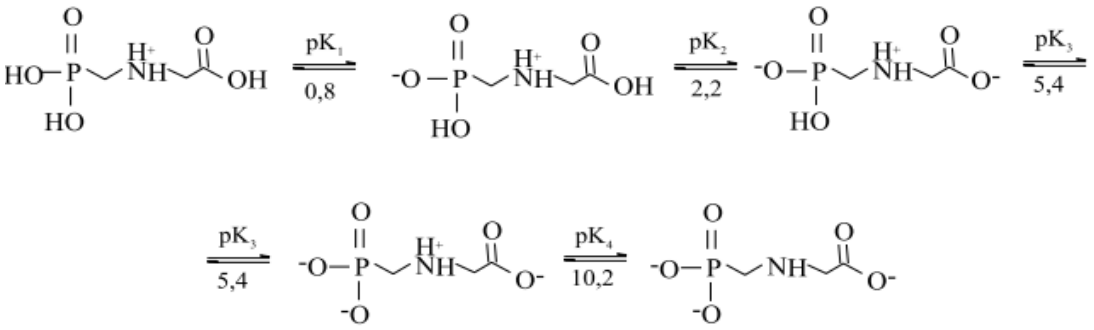

Figure 58 – Ionic states of glyphosate and constants of deprotonation [270]

Nevertheless, the need to detect herbicide and products of its decomposition is of the big necessity, as it tends to adsorb and accumulate in soil, clay and humic substances due to its low mobility. Despite the fact it is the most used herbicide compound, it is still not easy to analyse. The biggest challenge of its detection is a sample preparation step. The common preparation methods are not applicable for glyphosate as the compound has ionic nature, low volatility and, consequently, difficult evaporation, high polarity and solubility in water and therefore, poor solubility in organic solvents, what makes the use of classical organic solvent extraction complicated [271]. In addition, the other features as the absence of chromophore and fluorophore groups in its structure do not allow photometric and fluorometric detection [272], and favoured complexing behaviour with soil, minerals and metal cations demands a specific preparation of samples in order to separate analyte from the matrix [273,274]. Normally, the analysis of glyphosate and AMPA by chromatographic methods requires the derivatisation step [275,276], what is basically a modification of the analyte's structure to make it suitable for the chosen method of detection (for instance, introduction of luminophore or chromophore groups allows detection by spectroscopic methods) [277]. Chromatographic, spectroscopic and electrochemical methods, along with capillary electrophoresis and enzyme-linked immunosorbent assays were described in details in the recent review [275]. Among them, chromatography coupled with mass spectrometry (LC/MS or HPLC/MS) is the best choice to detect this herbicide and its metabolite without derivatisation. Even a higher sensitivity can be reached by using tandem mass spectrometry analysers MS/MS because of the noise reduction.

Having a secondary amine in its structure makes glyphosate a good candidate for ECL detection with $Ru(bpy)_3^{2+}$ [278]. In the literature, no mentioning of herbicide detection using $Ru(bpy)_3^{2+}$-

modified electrodes was found. However, some studies were referring to planar electrodes with luminophore in solution. The evolution of main parameters of $Ru(bpy)_3^{2+}$-based systems for glyphosate detection are presented in *Table 5*.

Table 5 – Conditions for glyphosate detection by the ECL and related limits of detection (LOD)

Working electrode	Operated pH	$[Ru(bpy)_3^{2+}]$, mM	LOD_{GLYP}, µM	Reference
Glassy Carbon	9	0.5	0.1	[278]
ITO	8	3.5	0.4	[279]
Glassy Carbon	8	0.5	-	[280]
Carbon fibre paste-ionic liquid electrode (CFILE)	9	0.05	20	[281]
ITO	9	4.0	0.2	[282]
Au / Au-SAM-CH_3 / Au-SAM-COOH	8	0.1	46.5 20.6 2.8	[283]
Multi-walled carbon nanotube screen-printed electrode with nano-ZnO	7	0.1	0.3	[284]

SAM - self-assembled monolayers

In all cases, phosphate buffer solution (PBS) with concentration from 20 [282] to 300 mM [279] and either pH 8 or 9 were the most commonly used to ensure the maximum ECL response as required by co-reactant mechanism with amines (*Figure 56*). Electrochemical and luminescent responses from $Ru(bpy)_3^{2+}$ exhibited a typical increase in presence of glyphosate. Interesting results were obtained by Fungo and colleagues regarding the use of bare and modified Au electrodes [283]. The highest limit of detection of glyphosate was observed for bare electrode. It could be an outcome of the reduction of active surface area due to oxide formation, what was reported before [227]. Electrode modification by self-assembled monolayers improved the sensitivity of herbicide detection. Authors suggested that organic deposit acts as a protective coating for the electrode against the surface oxide formation and against the products of decomposition of glyphosate, which can potentially block the electrode surface. Carboxylic functional groups were favouring the $Ru(bpy)_3^{2+}$ pre-concentration near the working electrode, therefore the limit of detection was lower comparing to methyl-modified Au (2.8 and 20.6 µM respectively).

By using $Ru(bpy)_3^{2+}$ in solution, the methods for the glyphosate detection in natural samples (soybeans) were investigated. Limit of detection in soybean samples was 8.5 µg of herbicide per 1 g of beans [281]. With more suitable sample preparation procedure, which included capillary electrophoresis separation, the LOD was lowered to 0.6 µg/g [279]. Screen-printed electrodes modified with carbon nanotubes and ZnO nanoparticles were tested in miniaturised ECL system, increasing the ECL signal intensity by 3-4 times (reduction of LOD is from 1 to 0.3 µM) [284].

As it was presented above, silica matrix is one of the most common materials, which is used for the immobilisation of various species. Therefore, the following chapter is dedicated to (1) preparation of modified silica films with Ru complex by click approach and to (2) evaluation of the possibility to apply this electrode for ECL detection of glyphosate. In **Chapter IV** only the preliminary results for covalently-modified films are shown. This study is not completed because of the problems which were faced in the course of research. They are discussed in details in **Section 4.5.**

4.2 Glyphosate detection by ECL – $Ru(bpy)_3^{2+}$ complex system: solution approach

4.2.1 ITO working electrode

$Ru(bpy)_3^{2+}$ - glyphosate system was studied first on ITO electrode on *Figure 59*. Electrochemical response from 0.1 mM $Ru(bpy)_3^{2+}$ was recorded without and in presence of 0.5 mM glyphosate in phosphate buffer solution (PBS) at pH 7. Ruthenium complex gives a CV signal at the electrode surface, that corresponds to one electron transfer [212], with oxidation and reduction peaks at 0.93 and 0.85 V respectively. The process is close to electrochemically reversible with $\Delta Ep = 0.075$ V and $Ip_a/Ip_c = 1.1$. After the addition of glyphosate, the recorded CV (*Figure 59A*, red curve) shows the disappearance of the reduction peak (reverse peak). Following one of the proposed co-reactant mechanisms for ECL reaction for $Ru(bpy)_3^{2+}$ – glyphosate system [280] it can be seen that reduction occurs through complex – co-reactant interaction (*Eq. 4.14 – 4.18*) known for amines [229,285] and, hence, explains the change in the shape of the cyclic voltammogram. At the same time, the presence of 0.5 mM herbicide in 0.1 mM $Ru(bpy)_3^{2+}$ leads to an anodic CV peak intensity ten times higher comparing to solution without co-reactant. The current increase is also well known and is also due to the electrocatalytic effect of the amine compound.

$$Ru(bpy)_3^{2+} \rightarrow Ru(bpy)_3^{3+} + e^- \quad (Eq.\ 4.14)$$

$$Ru(bpy)_3^{3+} + HOOC\text{-}H_2C\text{-}HN\text{-}CH_2\text{-}PO_3H_2 \rightarrow HOOC\text{-}H_2C\text{-}HN^{\bullet+}\text{-}CH_2\text{-}PO_3H_2 + Ru(bpy)_3^{2+} \quad (Eq.\ 4.15)$$

$$HOOC\text{-}H_2C\text{-}HN^{\bullet+}\text{-}CH_2\text{-}PO_3H_2 \rightarrow HOOC\text{-}HC^{\bullet}\text{-}HN\text{-}CH_2\text{-}PO_3H_2 + H^+ \quad (Eq.\ 4.16)$$

$$Ru(bpy)_3^{3+} + HOOC\text{-}HC^{\bullet}\text{-}HN\text{-}CH_2\text{-}PO_3H_2 \rightarrow Ru(bpy)_3^{2+*} + products \quad (Eq.\ 4.17)$$

$$Ru(bpy)_3^{2+*} \rightarrow Ru(bpy)_3^{2+} + h\nu \quad (Eq.\ 4.18)$$

(A)

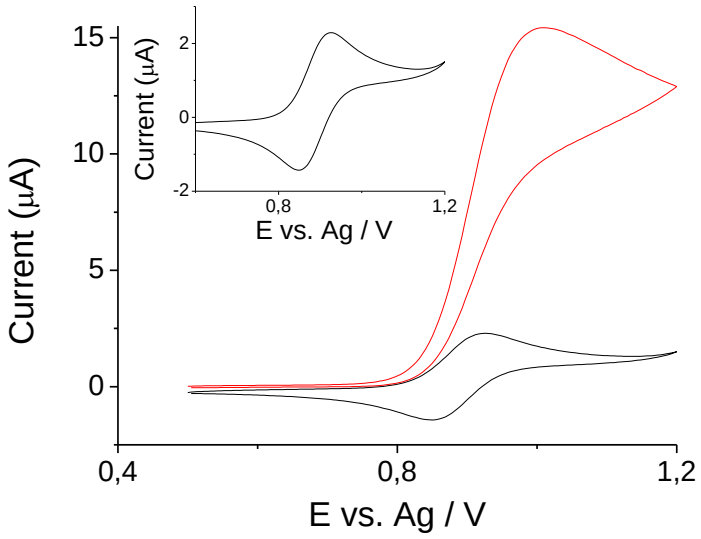

(B)

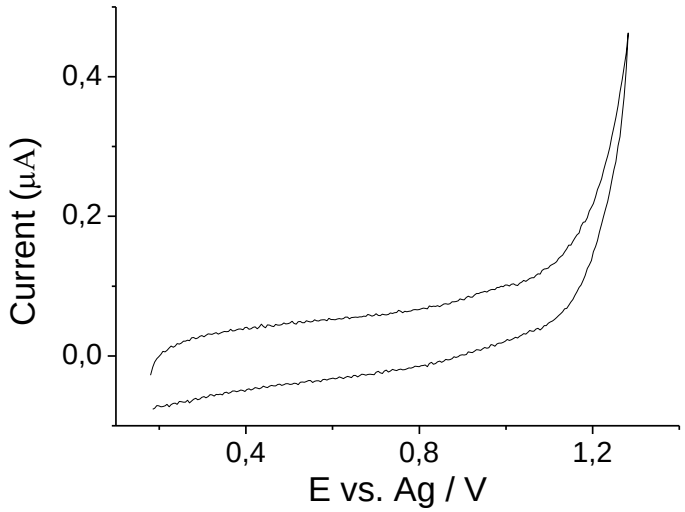

Figure 59 – (A) Effect of the 0.5 mM glyphosate addition (red line) on electrochemical signal of 0.1 mM $Ru(bpy)_3^{2+}$ (black line) using ITO electrode; Inset –CV of 0.1 mM $Ru(bpy)_3^{2+}$
(B) CV of 1 mM GLYP (scan 1, 50 mV/s; 50mM PBS, pH 7)

During reaction, $Ru(bpy)_3^{2+}$ is regenerated after the interaction of $Ru(bpy)_3^{3+}$ with glyphosate (*Eq. 4.15*). It leads to higher concentration of Ru(II) complex near the electrode which in turn enhances anodic peak current as it can be re-oxidised. On the other hand, it was verified that glyphosate does

not give any redox signal onto ITO (*Figure 59B*) meaning that herbicide cannot be detected directly on ITO electrode. But, in presence of $Ru(bpy)_3^{3+}$ its indirect detection becomes possible.

The effect of increasing concentration of glyphosate in presence of 0.1 mM $Ru(bpy)_3^{2+}$ in solution was investigated in the range of 0.01 to 1 mM of herbicide. Results are presented on *Figure 60*. As expected, higher content of glyphosate leads to a gradual increase of the anodic peak current. A 10-fold excess of $Ru(bpy)_3^{2+}$ over herbicide (*Figure 60*, curve *b*) is enough to report the catalytic mechanism. At the ratio 1:5 between ruthenium complex to amine, the reversed peak decreases sufficiently.

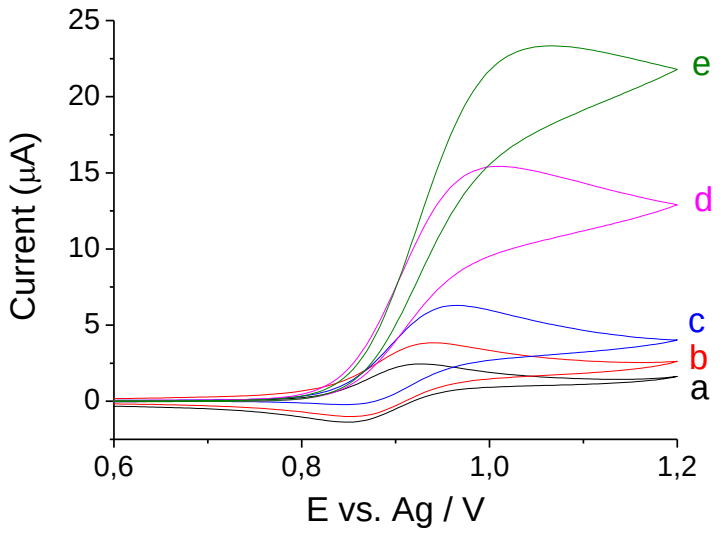

Figure 60 – CV curves recorded on ITO electrode with 0.1 mM $Ru(bpy)_3^{2+}$ a) without and with addition of b) 0.01 mM, c) 0.1 mM, d) 0.5 mM and e) 1 mM, glyphosate (scan 1, 50 mV/s; 50 mM PBS, pH 7)

The influence of the pH was studied in 0.1 mM $Ru(bpy)_3^{2+}$ solution containing 0.5 mM of glyphosate. In case of $Ru(bpy)_3^{2+}$ solution (*Figure 61A*), no sufficient dependence is observed in tested pH range, apart from slightly higher resistance for condition with pH 4.

Addition of glyphosate causes a gradual increase of anodic peak current (*Figure 61B*). These results are in accordance with co-reactant mechanism [280], which leads to higher detected response in more basic pH. More detailed information about influence of pH on CV peak of glyphosate is given in **Appendix 4**.

(A) (B)

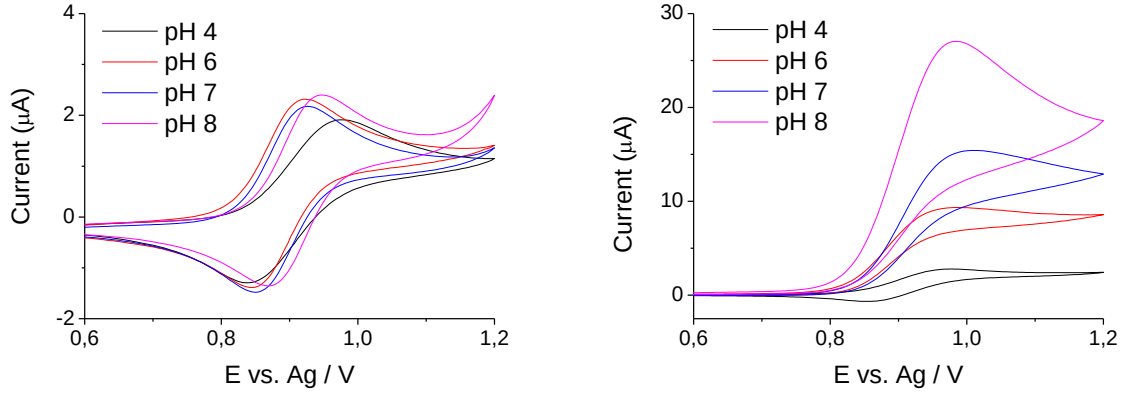

Figure 61 –CV response recorded in function of pH on bare ITO with solution of 0.1 mM $Ru(bpy)_3^{2+}$ (A) without and (B) in presence of 0.5 mM glyphosate (scan 1, 50 mV/s)

4.2.2 ITO working electrode modified by mesoporous silica film

Presence of mesoporous silica films with vertically aligned pores are known to increase the electrochemical signal of positively charged species due to negative channels in which a pre-concentration of analytes is possible. Following this, ITO electrode modified by unmodified MSF (~~conditions of synthesis of unmodified MSFs with~~ thickness of 80 ± 9 nm ~~are presented in **Section 3.4**~~) was tested in $Ru(bpy)_3^{2+}$ solution with and without glyphosate to study the effect of deposit.

CV curves were recorded from 0.1 mM $Ru(bpy)_3^{2+}$ solution at pH 7 on ITO electrode covered with unmodified MSF. Well-defined redox peaks of ruthenium complex are observed (*Figure 62*, black solid line). Silica film does not block the transport of $Ru(bpy)_3^{2+}$ complex to electrode where electrochemical reaction takes place [102]. Location of anodic and cathodic peaks is comparable to that obtained in the same solution on bare ITO electrode. They appeared at 0.93 (Ip_a = 11.5 µA) and 0.84 V (Ip_c = 8.4 µA). Consequently, peak-to-peak separation is ΔEp = 0.081 V and Ip_a/Ip_c ratio is equal to 1.4 are showing that in presence of mesoporous silica film ruthenium complex exhibits less reversibility comparing to its electrochemical response on bare ITO electrode.

An increase of current intensity in presence of mesoporous film is supposedly caused by the pre-concentration effect well-known for positively charged species on negative silica matrix, what was described for methylene blue [286] and paraquat [181].

The addition of glyphosate in concentration of 0.5 mM causes a sharp increase of peak current to $Ip_a = 22.5$ μA (*Figure 62*, red solid line). A signal typical for the electrocatalytic effect is recovered. In presence of mesoporous silica coating, the peak current is around 1.5 times larger comparing to that obtained on bare ITO electrode (red solid and red dashed lines on *Figure 62* respectively). It shows that the sensitivity of amine detection can be potentially improved by electrode modification by silica film.

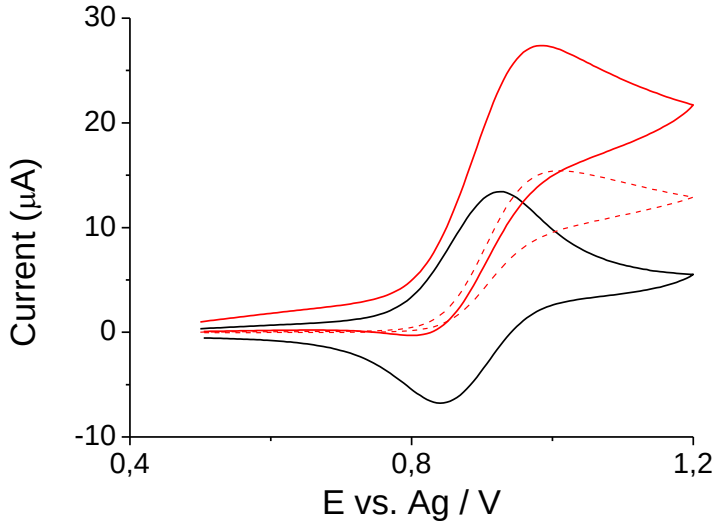

Figure 62 – Effect of 0.5 mM glyphosate addition (red solid line) on electrochemical signal of 0.1 mM $Ru(bpy)_3^{2+}$ (black solid line) using MSF-modified ITO electrode comparing to bare ITO (red dashed line) (scan 1, 50 mV/s; 50 mM PBS, pH 7)

In order to provide a good ECL performance, a control over pH must be held. As it is shown in *Table 5*, the majority of presented publications show that the optimum pH for the GLYP detection is 8 or 9. In the alkaline media silica undergoes dissolution and these conditions are likely to ruin the mesoporous structure of silica film. Therefore, it is necessary to find the optimum pH which can provide the maximum ECL efficiency and at the same time keep the silica coating undamaged.

The effect of pH on CV anodic peak current was checked on bare ITO electrode and on ITO with deposited MSF (*Figure 63*). While using ITO (blank squares on *Figure 63*), the peak current increases with changing pH from 4 to 8. Growth of Ip_a continues steadily up to pH 7 and then more sufficient current rise is seen at pH 8 In total, the signal observed at pH 8 is 11 times higher than the one obtained at pH 4. In contrast, the anodic current, which was recorded with modified ITO

electrode (black squares on *Figure 63*), was growing up to pH 7 with following drop of Ip_a at pH 8.

Normally, the required media for system with amine co-reactant must be alkaline [278]. A closer look on *Eq. 4.16* implies that one of the necessary steps is deprotonation of amine. High pH facilitates this process and favours the formation of amine radicals, which are driving excitation of ruthenium complex, hence the luminescence. It is also consistent with the increase of CV peak current on *Figure 63.* A favourable pH for each amine can vary depending on its structure [278]. The same study showed that the ECL signal was enhanced at pH values near the pK_a. For glyphosate, it refers to the pK_{a4} = 10.2 [270]. However, a number of studies [278–280,283] are claiming that the most suitable pH for ECL detection of chosen herbicide is 8.

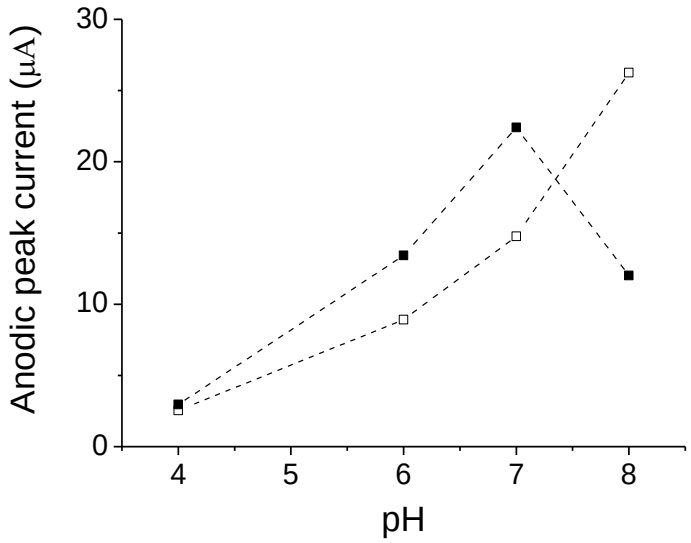

Figure 63 – The effect of pH on CV anodic peak current of 0.1 mM $Ru(bpy)_3^{2+}$ solution with 0.5 mM glyphosate on ITO (blank squares) and MSF-covered ITO electrode (black squares) (scan 1, 50 mV/s)

Different reasons can explain the decrease of the anodic peak intensity at pH 8 (*Figure 63*, black squares) observed on ITO covered with a mesoporous silica film. In alkaline medium, silica does not last long and starts dissolving [88]. It can be accompanied by collapsing of mesostructure known for mesoporous silica material which underwent damaging under aggressive exposure of alkaline [192]. Lower ECL signal was also noticed for the electrodes modified by silica-containing composite at pH 8 with TPrA as co-reactant, whereas till pH 7 it was increasing [249,251].

Finally, a compromise was found at pH 7, where the maximum preservation of silica surface is ensured and the largest electrochemical signal is detected.

While recording multiple scans of $Ru(bpy)_3^{2+}$ – glyphosate solution on bare ITO electrode (*Figure 64*, red line) and ITO modified with MSF (*Figure 64*, blue line), a decrease of the peak current intensity was noticed as scan progressed. As discussed above, higher peak current recorded with modified electrode is caused by interaction between positive analyte and negative silica surface. After 25 consecutive CV scans in solution containing amine, the same decay was observed whatever the electrode was used. It resulted in 50-60% loss of the current comparing to the first scan. For comparison, on bare ITO electrode anodic peak of $Ru(bpy)_3^{2+}$ stays stable. It shows that presence of glyphosate affects the stability of electrochemical signal.

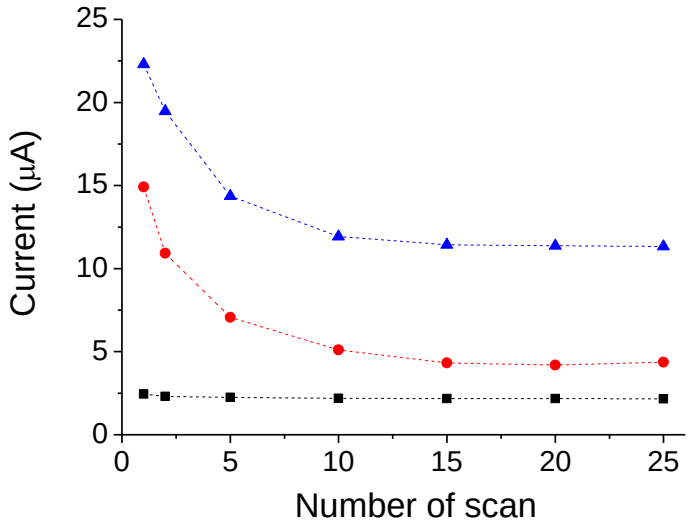

Figure 64 – Evolution of anodic peak current while multiple scanning of 0.1 mM $Ru(bpy)_3^{2+}$ on bare ITO in absence of glyphosate (black squares) and with 0.5 mM glyphosate on ITO (red circles) and ITO modified by MSF (blue triangles) (50 mV/s, 50 mM PBS, pH 7)

Two possible reasons of current reduction based on the ECL co-reactant mechanism and electrode fouling are proposed below.

The first hypothesis is a partial blocking of the electrode surface by products of glyphosate decomposition, namely electrode fouling. Step represented in *Eq. 4.17* implies the creation of products of decomposition of glyphosate. These compounds can lead to the electrode fouling

because of their possible physical adsorption on the electrode surface [283]. Consequent reduction of the active surface area and current decrease are expected if the fouling occurs.

The evolution of anodic current after normalisation by maximum Ip_a is depicted on *Figure 65*. The first two scans have the same current decrease in presence of co-reactant and without it using ITO electrode modified with film. However, after the second scan the decay of Ip_a is larger for a system with herbicide. Fouling may be taking place. To check this, electrodes after their rinsing were placed in new solution containing $Ru(NH_3)_6^{3+}$ and $Ru(bpy)_3^{2+}$ species. Recorded CV signals are depicted on *Figure 66*. No decrease of peak current was observed for reduction peak of $Ru(NH_3)_6^{3+}$, whereas the intensity of oxidation peak related to $Ru(bpy)_3^{2+}$ was reduced by 10%. No electrode fouling seems to take place in the case of bare ITO.

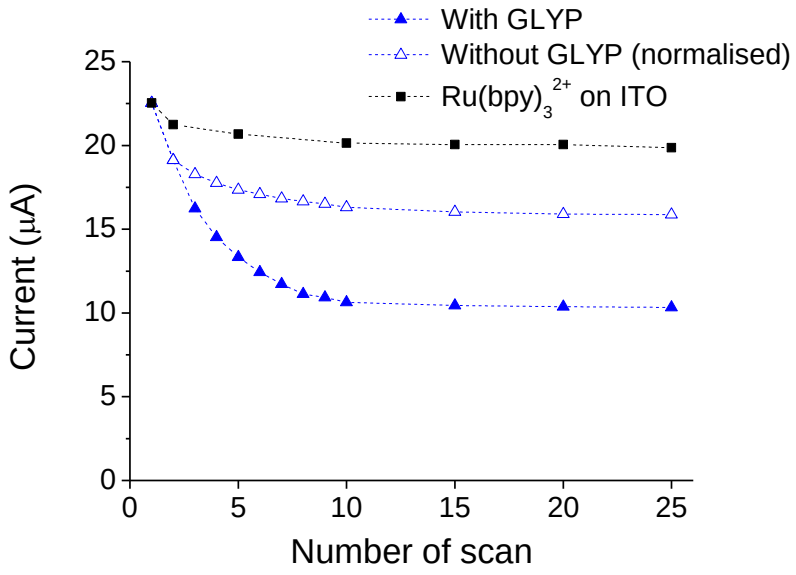

Figure 65 – Evolution of anodic peak current after normalisation while multiple scanning of 0.1 mM $Ru(bpy)_3^{2+}$ on bare ITO (black squares) and MSF-modified ITO in absence (unfilled blue triangles) and with 0.5 mM glyphosate on ITO (blue triangles) (50 mV/s, 50 mM PBS, pH 7)

The second possible explanation of Ip_a decrease is glyphosate consumption in the pre-electrode area. Additional observation of the CV curves shows that along with the reduction of the peak intensity of forward scan, the cathodic peak starts appearing as well (*Figure 67*). It can mean that a transition from co-reactant mechanism occurs in favour of reduction from $Ru(bpy)_3^{3+}$ to $Ru(bpy)_3^{2+}$ at the electrode. The current intensity for scan 25 in presence of glyphosate on modified

and bare ITO is larger comparing to $Ru(bpy)_3^{2+}$ signal on bare ITO. It proves that the active surface area of electrode was not decreased, hence, it serves as another evidence of no fouling.

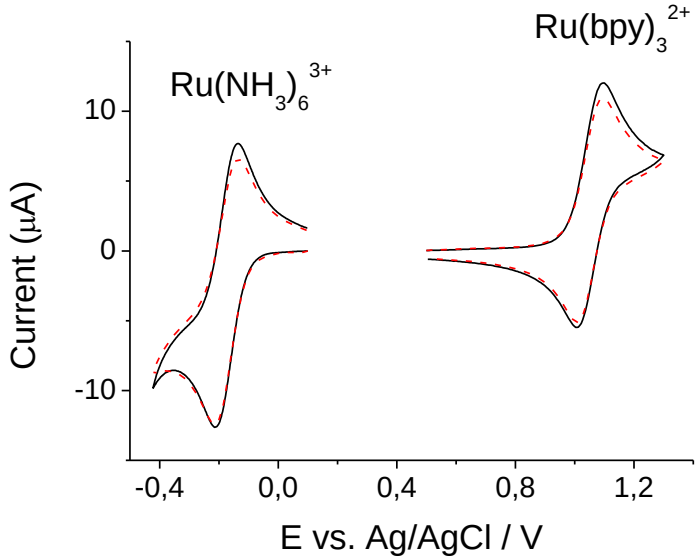

Figure 66 – CV curves of 0.5 mM $Ru(NH_3)_6^{3+}$ and 0.5 mM $Ru(bpy)_3^{2+}$ solution in 0.1 M $NaNO_3$ before (black solid line) and after (red dashed line) 5 consecutive scans of 0.5 mM $Ru(bpy)_3^{2+}$ - 0.5 mM glyphosate solution on bare ITO electrode (1st scans, 50 mV/s)

Even though the consumption of glyphosate seems to take place, a catalytic pathway still prevails while using ITO electrode for 25 scans (*Figure 67A*). The products of herbicide decomposition, which include aminomethylphosphonic acid (AMPA, primary amine) [287,288] and sarcosine (secondary amine) [288], can be the cause of it. These amines can cause electrocatalytic ECL mechanism as well as glyphosate, although the increase of the response is less sufficient. In particular, Ridlen [278], Chiu [279], and Haberkost [284] confirmed the feasibility to detect AMPA by ECL co-reactant mechanism, but the sensitivity of this analysis is normally much worse (10 [284] to 1000 [278] times) than in case of glyphosate detection.

Interestingly, there was a mentioning of signal instability in publication of Zhou and co-authors [120] with no arguments. As for results presented on *Figure 64*, peak currents of bare and modified ITO electrode were stabilised after scan 15, what is comparable to conditions used in paper [120].

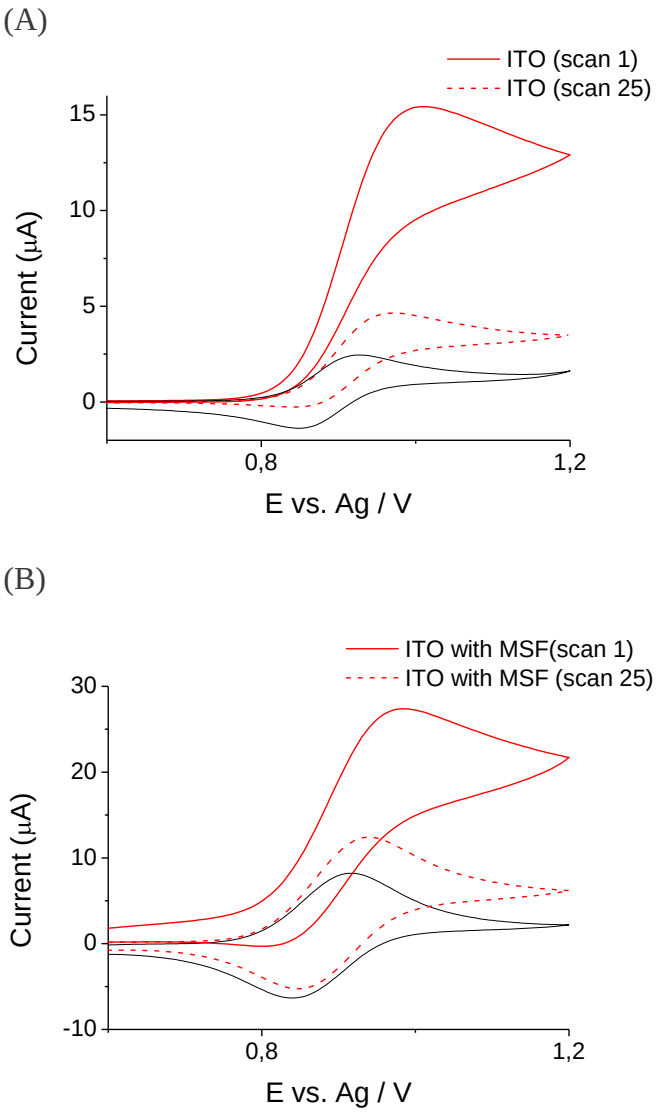

Figure 67 – Comparison of scan 1 (red line) and scan 25 (red dashed line) of CV curves recorded with 0.1 mM $Ru(bpy)_3^{2+}$ solution with 0.5 mM glyphosate on (A) ITO electrode and (B) MSF-modified ITO CV of 0.1 mM $Ru(bpy)_3^{2+}$ on bare ITO (black line) presented as a reference (50 mV/s, 50 mM PBS, pH 7)

4.3 Impregnation of $Ru(bpy)_3^{2+}$ complex onto silica film surface

4.3.1 Electrode preparation

The physical immobilisation of ruthenium complex onto the surface of silica film after template extraction (in acidic EtOH solution) was performed by the immersion of a unmodified MSF (thickness 80 ± 9 nm) -covered ITO electrode in solutions of $Ru(bpy)_3^{2+}$ of different concentrations (from 0.1 µM to 1 mM) for 2 hours. Afterwards, films were rinsed with water and dried on air before the use.

4.3.2 Characterisation of mesoporous silica films with physically adsorbed $Ru(bpy)_3^{2+}$ complex

On *Figure 68* presents the first scan out of 15 recorded from impregnated MSF-covered ITO electrode in PBS solution with pH 7. The presence of electrochemical response in PBS solution from the film, which was placed in 1 mM $Ru(bpy)_3^{2+}$ solution for 2 hours, proves the physical adsorption of complex onto the silica film surface. Favourable interaction between soluble positively charged species and the negatively charged silica explains the accumulation of the complex into silica films. Well-defined anodic and cathodic peaks are located at 1.07 and 1.03 V, respectively. Note, that the peak positions are shifted in the higher potentials (+0.1 V) comparing to plots presented in **Section 4.2** due to the use of Ag/AgCl reference electrode. The parameter ΔE_p strongly depends on the state of the complex. The increase of the peak-to-peak separation for curves is observed in the row impregnated $Ru(bpy)_3^{2+}$ – free $Ru(bpy)_3^{2+}$ on bare electrode – free $Ru(bpy)_3^{2+}$ on MSF-covered ITO and has the values 0.04, 0.075 and 0.081 V respectively.

Electrostatically modified mesoporous silica particles were also successively obtained in the same way by keeping them in $Ru(bpy)_3^{2+}$ solutions in DMF [252], and in aqueous media for molecular sieve silica [253] and vertically aligned MSF [120].

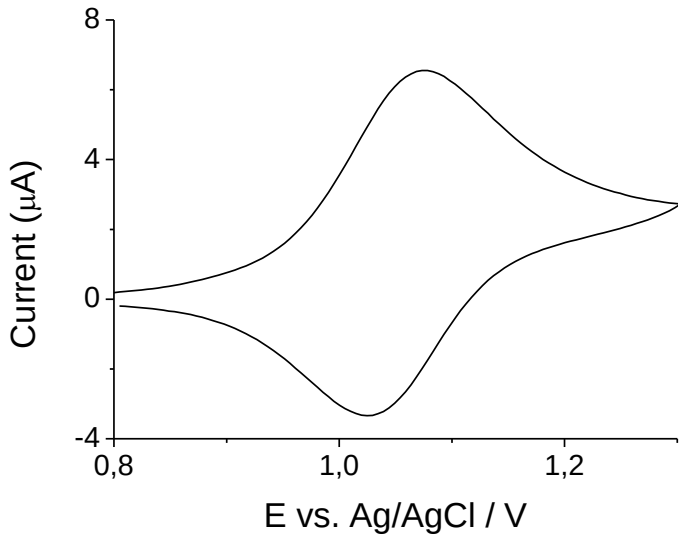

Figure 68–The CV response of $Ru(bpy)_3^{2+}$ impregnated onto MSF-covered ITO from 0.1 mM $Ru(bpy)_3^{2+}$ (scan 1, scan rate 50 mV/s, 50 mM PBS, pH 7)

The presence of impregnated $Ru(bpy)_3^{2+}$ near the electrode surface facilitates the charge transfer and does not require diffusion of redox probe through mesochannels, leading to low value of ΔE_p. On contrary, for bare ITO and electrode covered with silica film the peak separation ΔE_p is almost two times larger. More sufficient capacitive current in case of film presence is detected because of the necessity to diffuse to the electrode surface through porous coating. The value of ΔE_p smaller than the one for reversible process was also registered for poly(sodium 4-styrene- sulfonate)-silica composite and for ruthenium-doped Au nanoparticles ($\Delta E_p \approx 0.05$ V) with impregnated ruthenium complex. It is typical for redox-active surface-bound $Ru(bpy)_3^{2+}$.

In order to study the stability of the impregnated electrode, 15 consecutive scans were recorded (*Figure 69*). Anodic peak current intensity decreases from 5.6 to 2.9 μA after 15 consecutive scans were performed. The decrease of the peak current (about 54% after 15 scans) can signify about the release of the complex with time because of relatively weak electrostatic forces between silica and $Ru(bpy)_3^{2+}$. It was also noticed for impregnated $Ru(bpy)_3^{2+}$ aluminium-rich mesoporous alumosilicate deposited on ITO. The peak decrease in case of this material reached 75% after the first 90 minutes of analysis [253]. From the decreasing Ip_a/Ip_c ratio from 1.5 for the 1st scan and to 0.9 for the 15th scan it can be concluded, that in the beginning, the system is not chemically

reversible. Reduction of this ratio is more likely caused by processes of sorption-desorption of ruthenium complex occur at the silica surface.

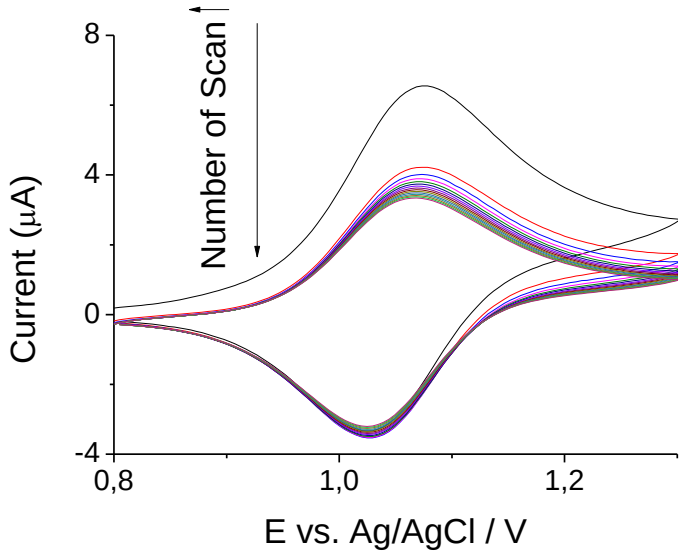

Figure 69– CV signal while multiple scanning of ITO electrode covered by MSF with impregnated $Ru(bpy)_3^{2+}$ (adsorbed from 1 mM $Ru(bpy)_3^{2+}$ solution; 2 hours time contact) (15 scans recorded at 50 mV/s scan rate in 50 mM PBS, pH 7)

The study for determination of maximum quantity that can be introduced inside porous films was performed by varying the concentration of $Ru(bpy)_3^{2+}$ solution, from which adsorption was conducted. The range of tested concentrations for impregnation of Ru (II) complex onto MSF-modified ITO electrodes was from 0.1 μM to 1 mM. After films immersion in solution for 2 hours, their rinsing and drying, they were tested in PBS solution (pH 7). Obtained results are presented on *Figure 70.*

As expected, the greater concentration of $Ru(bpy)_3^{2+}$ is, the higher anodic peak current appears as a result of more species adsorbed onto silica film. The increase of the anodic peak current is becoming less important (*Figure 70*), seeming to reach a stationary state probably related to saturation of the silica pores with the complex or a limitation of its diffusion. For further experiments, films modified from 1 mM $Ru(bpy)_3^{2+}$ solution are used because of the highest recorded current response.

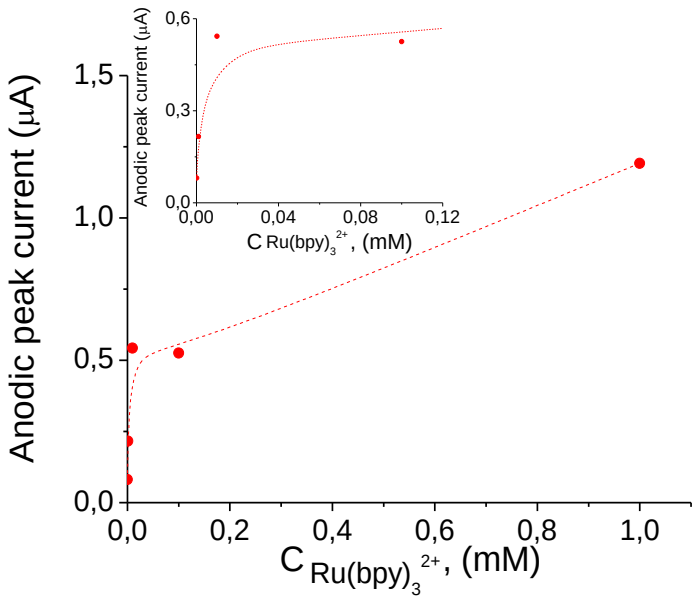

Figure 70 – The evolution of anodic peak current of $Ru(bpy)_3^{2+}$ impregnated MSF in function of $Ru(bpy)_3^{2+}$ concentration in solution for film modification presented (scan 2, 20 mV/s, 50 mM PBS pH 7)

4.3.3 Electrochemical response in presence of glyphosate

The effect of glyphosate addition (in the range of 0.05 – 1 mM) on the CV signal of impregnated $Ru(bpy)_3^{2+}$ recorded at 50 mV/s scan rate is shown on *Figure 71*. The shape of CV curves was changed to the one typical for co-reactant mechanism when more than 0.5 mM of herbicide was present in solution at tested scan rate.

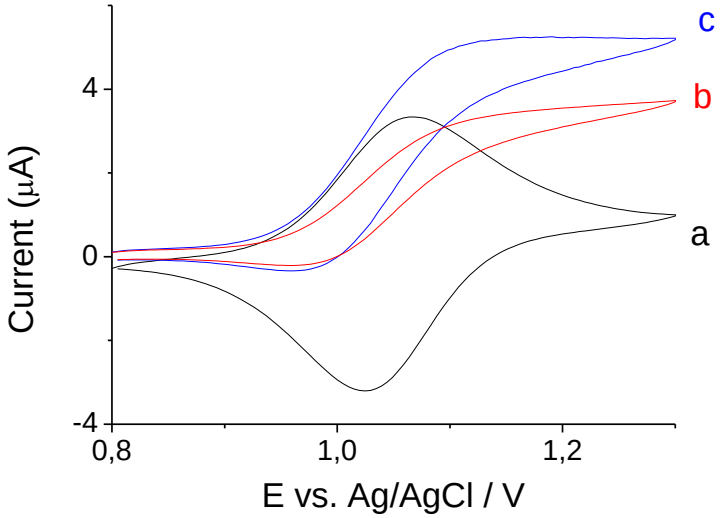

Figure 71 – The CVs recorded on impregnated MSF-modified ITO electrode in function of glyphosate addition: a) 0 mM, b) 0.5 mM, and c) 1.0 mM (Scan 1, 50 mV/s, 50 mM PBS, pH 7)

The investigation of anodic peak current stability for impregnated films while multiple scanning (5 scans, *Figure 72*) with glyphosate in solution shows the same declining evolution as for systems presented with free $Ru(bpy)_3^{2+}$ and co-reactant. This comparable behaviour confirms the same nature of electrochemical signal reduction, which is glyphosate decomposition in the pre-electrode area.

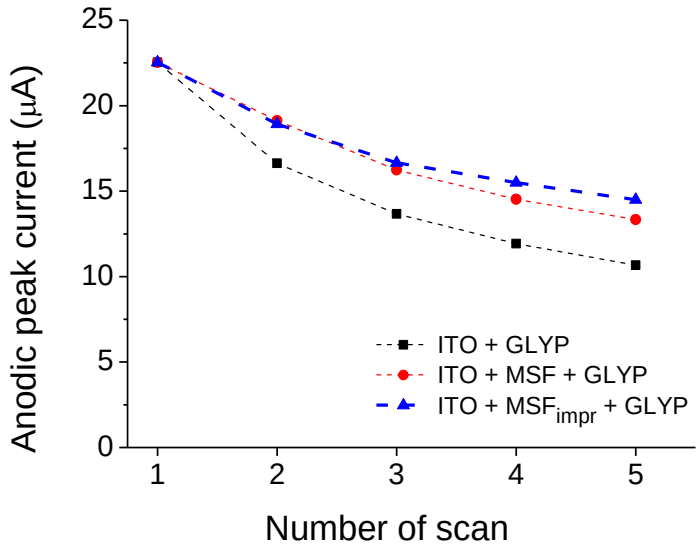

Figure 72 – Evolution of anodic peak current while multiple scanning of impregnated ITO MSF electrode in presence of 0.5 mM glyphosate (bold blue line, triangles) comparing to signal of 0.1 mM $Ru(bpy)_3^{2+}$ - 0.5 mM glyphosate on bare ITO (black squares) and on ITO modified by MSF (red circles) (50 mV/s, 50 mM PBS, pH 7)

4.4 Covalent immobilisation of $Ru(bpy)_2(bpy')^{2+}$ onto mesoporous silica film surface

Similarly to the films with impregnated ruthenium complex, covalent entrapment of reactant onto solid matrix helps to avoid the use of its solution, what simplifies the design of sensor. One of the advantages of covalent grafting is a possibility to reduce the leaching of the modifier. Mesoporous silica films with covalently bonded (tris)bipyridine ruthenium (II) complex were synthesised from azide-terminated MSFs, which were post-grafted following Huisgen 1,3-cycloaddition with propargyl derivative of $Ru(bpy)_3^{2+}$. Since there is no commercially available (tris)bipyridine ruthenium (II) complex with required alkyl-containing functional group, this complex was synthesised in the laboratory.

4.4.1 $Ru(bpy)_2(bpy')^{2+}$ complex preparation

Synthesis of 4-[2-propyn-1-yloxymethyl]-4'-methyl-2,2'-bipyridine ligand (bpy') was carried out from 4,4'-dimethyl-2,2'-bipyridyl starting compound according to the literature [289]. It consists of the prior three-step preparation of bpy' ligand. The final fourth step includes the coordination of synthesised ligand to commercially available $Ru(bpy)_2Cl_2$. The sequence of synthesis is depicted on *Figure 73.*

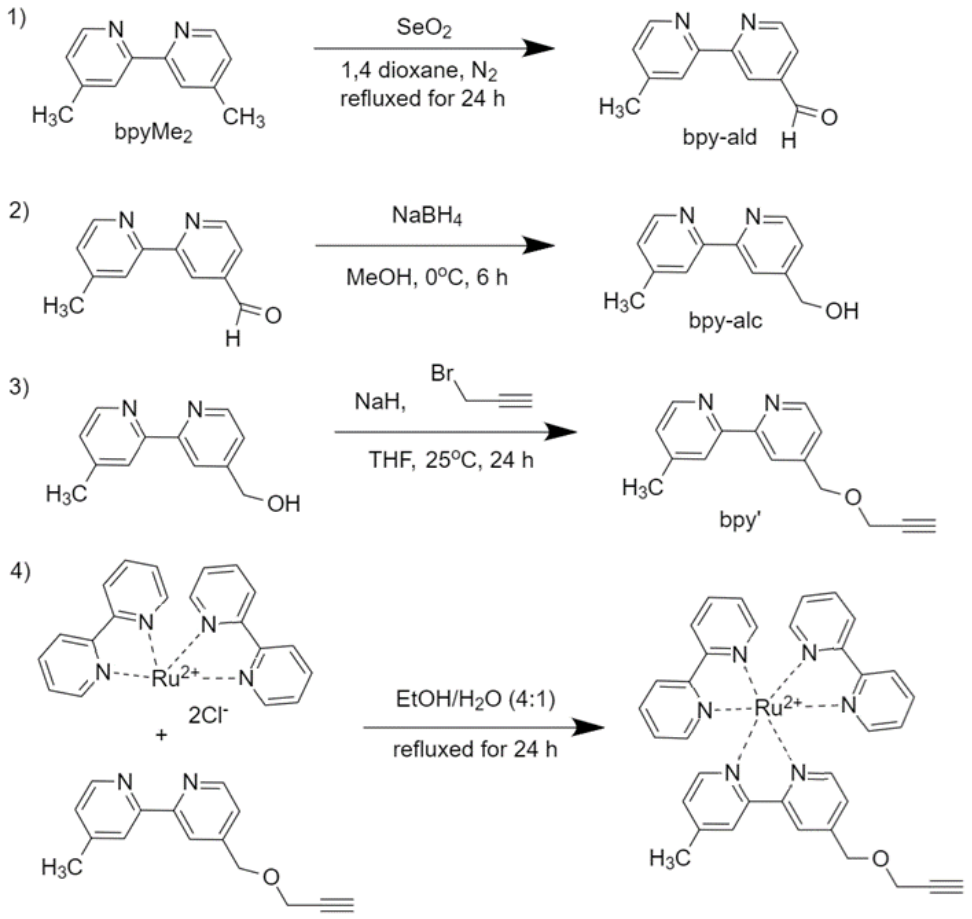

Figure 73 – Scheme of $Ru(bpy)_2(bpy)'$ synthesis

Step 1. Synthesis of 4-(carboxyaldehyde)-4'-methyl-2,2'-bipyridine (bpy-ald, *Figure 73*)

The first step of the ligand preparation was carried out following procedure [290]**.** 4,4'-dimethyl-2,2'-bipyridyl (1,8 g, 9.7 mmol) was dissolved in 1,4-dioxane (50 ml). Solution was purged with N_2 for 20 minutes while stirring to remove oxygen. Then, in order to oxidise aromatic methyl

group to aldehyde SeO_2 (1.1 g, 9.8 mmol) was added to the flask and system was purged with N_2 for another 20 minutes. Afterwards, the mixture was refluxed under N_2 with continuous stirring for 24 hours. The hot solution was filtered and left for 1 hour to cool down to the room temperature and then it was filtered once again. The 1,4-dioxane was evaporated under the vacuum pressure. The solid residue was dissolved in 500 ml of ethyl acetate (EtOAc). Subsequent liquid-liquid extractions by 20 ml of 0.2 M aqueous solution of $NaHCO_3$ (organic phase was kept) following by 5×20 ml of 0.2 M $Na_2S_2O_5$ (aqueous phase was collected) were performed. The pH of obtained pink solution was set to 9 by adding 1 M Na_2CO_3 solution. The final extraction was done with dichloromethane (DCM) (5×20 ml), organic phase was collected, then it was dried with $MgSO_4$, filtered and solvent was evaporated under vacuum. Obtained light pink powder was a compound of interest.
Yield: 17 – 20 %.

1H NMR (400 MHz, CDCl3) δ : 2.48 (s, 3H), 7.23 (d, J=5.0 Hz, 1H), 7.74-7.78 (m, 1H), 8.32 (s, 1H), 8.62 (d, J=4.9 Hz, 1H), 8.95 (d, J=4.9 Hz, 1H), 10.23 (s, 1H) (**Appendix 5**).

Step 2. Synthesis of 4-(hydroxymethyl)-4'-methyl-2,2'-bipyridine (bpy-alc, *Figure 73*)

4-(hydroxymethyl)-4'-methyl-2,2'-bipyridine was synthesised according to procedure showed in literature [291]**.** Before setting the reaction, 10 ml of methanol (MeOH) was cooled down to 0°C. In the flask with pre-prepared solvent, 4-(carboxyaldehyde)-4'-methyl-2,2'-bipyridine (500 mg, 2.53 mmol) was added to solvate. Further, $NaBH_4$ (96 mg, 2.53 mmol) was introduced and the mixture was left for 6 hours at 0°C under stirring. Then, MeOH was evaporated and the dry residue was dissolved in 10 ml of H_2O. The product from solution was extracted with 5×20 ml of DCM. Collected organic phase was extracted afterwards with 0.5 M $NaHCO_3$ (5 ml) and with 0.2 M NaCl (5 ml) respectively, which were not used further. Organic part was dried with $MgSO_4$ and then DCM was removed under reduced pressure to result in the pinkish product of interest. Yield: 81 – 94 %.

1H NMR (400 MHz, CDCl3) δ : 2.49 (s, 3H), 5.03 (s, 2H), 7.18-7.25 (m, 1H), 7.41-7.48 (m, 1H), 8.30-8.35 (m, 1H), 8.40-8.42 (m, 1H), 8.59 (d, J=4.9 Hz, 1H), 8.72 (d, J=5.0 Hz, 1H) (**Appendix 5**).

Step 3. Synthesis of 4-(2-propyn-1-yloxymethyl)-4'-methyl-2,2'-bipyridine (bpy', *Figure 73*)

Sodium hydride (114 mg, 6 mmol) was suspended in 10 ml of THF and 4-(hydroxymethyl)-4'-methyl-2,2'-bipyridine (600 mg, 3 mmol) was added in the flask while stirring to deprotonate the alcohol and form alkoxide $R\text{-}O^-$. Conjugate nucleophile $R\text{-}O^-$ is more preferable as it reacts faster than R-OH due to higher electron density on Oxygen. After 15 minutes, propargyl bromide (535 mg, 4.5 mmol) was slowly introduced. The solution with all components was left stirring for 24 hours at the room temperature to complete reaction. After the passed time, reactant mixture becomes orange. For cleaning, 0.5 M solution of $NaHCO_3$ (10 ml) was introduced to the products of the reaction and following extraction was performed with 5×20 ml of DCM. Polar orange compounds (tertiary ammonium salts of bipyridine derivatives) stayed in the aqueous phase, when less polar products (with ethoxylated compound of interest among them) were transferred to DCM. Organic parts were combined and dried over $MgSO_4$, filtrated through paper filter and solvent was evaporated under reduced pressure. The solid residue was dissolved in a small volume of EtOAc : Hexane : Et_3N (100:100:10) eluent and cleaned by the column chromatography on SiO_2. The least polar bpy' product was obtained from the first fractions, while more polar impurities were retained stronger by silica gel surface. After the final evaporation of organic solvent, a powder with slightly pink colour was obtained.
Yield: 10 – 13 %.

1H NMR (400 MHz, CDCl3) δ : 2.36 (s, 3H), 2.40 (t, J=2.40 Hz, 2H), 4.23 (d, J=2.40 Hz, 2H), 4.67 (s, 2H), 7.15-7.18 (m, 1H), 7.19-7.20 (m, 1H), 8.24-8.28 (m, 1H), 8.30-8.33 (m, 1H), 8.49 (d, J=5.0 Hz, 1H), 8.68 (d, J=5.0 Hz, 1H).

Comments on Step 3

The large loss of product is considered to be due to the low selectivity of ethoxylation reaction performed in described conditions. The nucleophilic attack can occur at two positions: alkoxide group (targeted process) and amine group of bipyridine (side process). The second path leads to formation of tertiary salts, which are charged. N-alkylation of pyridine in DMF at the room temperature overnight resulted in 75% yield [292]. In case of 4-hydroxymethylpyridinium alkylation, the yield of quaternary salt was 48% after performing reaction in DMF at 70°C (time of reaction varied from 2 to 48 hours) [293]. Even though, in these two proposed examples no

strong base (i.e. NaH) was used to deprotonate hydroxy group, they show that the attack of alkyl halide can be performed by amine of pyridine. Considering this, formed quaternary salt can transfer to aqueous phase causing its coloration in orange colour while extraction with DCM (was observed at the first extraction step during cleaning). In order to improve the yields of this reaction, synthesis at lower temperatures can be proposed. This approach was used to obtain bipyridine-derived ligand for iridium complex in THF at 0^oC under the nitrogen flow [291]. The yield for this step was not reported by authors.

Step 4. Synthesis of $Ru(bpy)_2(bpy)'(PF_6)_2$ ($Ru(bpy)_2(bpy')(PF_6)_2$, *Figure 73*)

The final step was carried out following the modified procedure described in [294]. To 15 ml of H_2O:EtOH solution (1:4), 4-[2-propyn-1-yloxy)methyl]-4'-methyl-2,2'-bipyridine (30 mg, 0.13 mmol) was added along with $Ru(bpy)_2Cl_2$ (67 mg, 0.1 mmol). The solution was refluxed while stirring for 24 hours. After content of the flask was cooled down, ethanol was evaporated under the vacuum pressure (traces of water left were acceptable) and 7 ml of 0.1 M NH_4PF_6 were added in flask to form required hexafluorophosphate salt of ruthenium complex at 0°C. To ensure the reaction was completed, it was kept at these conditions for 48 hours. Following step included filtration of orange crystals and their drying using diethyl ether during 1-2 days.
Yield: 100%

1H NMR (400 MHz, CDCl3) δ : 2.45 (s, 3H), 2.72 (s, J=2.60 Hz, 1H), 4.23 (d, J=2.40 Hz, 2H), 4.67 (s, 2H), 7.65-7.68 (m, 1H), 7.83-7.96 (m, 4H), 8.14-8.21 (m, 4H), 8.30-8.33 (m, 4H), 8.41 (d, J=5.0 Hz, 1H), 8.49 (d, J=5.0 Hz, 2H), 8.53 (m, J=5.0 Hz, 2H).8.72 (m, J=5.0 Hz, 4H).

4.4.2 Huisgen "click" reaction

Incorporation of $Ru(bpy)_2(bpy')^{2+}$ in MSFs through covalent bonding was performed using azide-modified films and 1,3-cycloaddition pathway (Huisgen click reaction, see more in **Section 2.3.3**). Prior to click reaction itself, in order to empty pores extraction of soft template was performed by placing MSFs in 0.1 M HCl ethanol solution for 15 minutes.

The presence of azide functional groups was confirmed by IR spectroscopy (*Figure 74A*). The characteristic peak around 2095 cm^{-1} is related to N=N=N stretching. With the increase of AzPTES

content in starting sol peak of azide grows linearly so as the content of azide groups (*Figure 74B*), as it was shown previously by Vilà et al. [107].

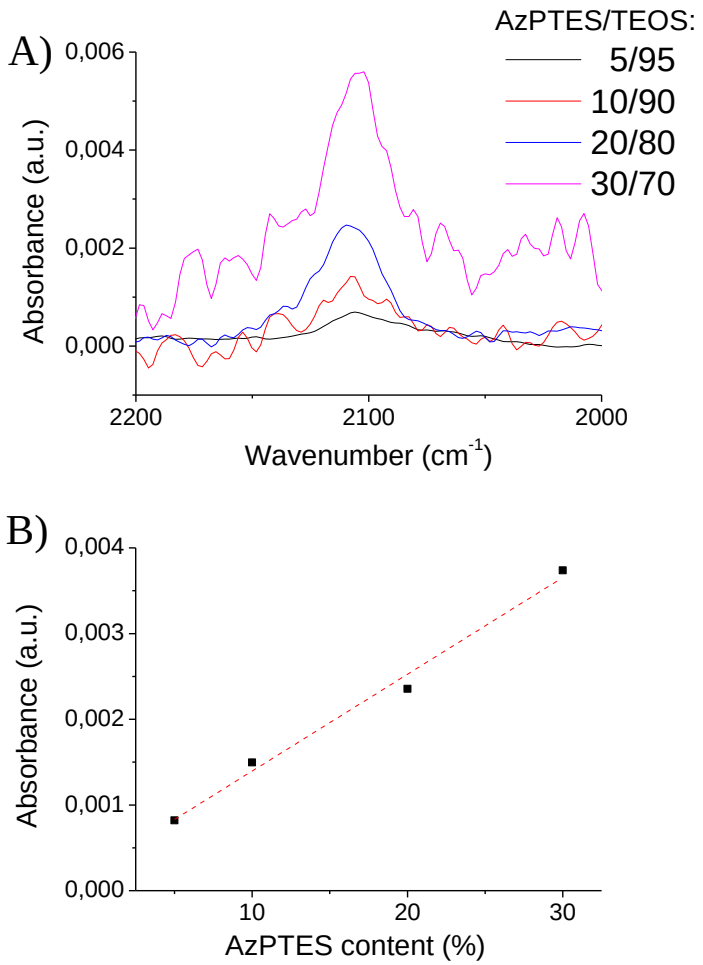

Figure 74 –(A) IR peak of azide and (B) its evolution with respect to AzPTES content in starting sol

Solution for click reaction was prepared in two steps. Firstly, in the aqueous part (10 ml H_2O), Cu (II) nitrate (4.8 mg, 1.0 mmol) and ascorbic acid (8.8 mg, 2.5 mmol) were dissolved to form Cu(I), which acts as a regioselective catalyst for 1,3-cycloaddition. In parallel, $Ru(bpy)_2(bpy)'(PF_6)_2$ (1.0 mmol, 20.0 mg) was added to DMF (10 ml) to result in orange transparent solution. Aqueous and organic fractions were then mixed together and azide-functionalised MSFs were placed in this solution in the absence of light at room temperature. After 48 hours, the excess of copper catalyst on films was removed by its complexation with NaDDTC. MSFs were put in 0.05 M ethanol solution for 30 minutes with following rinsing with ethanol and drying on air before use.

4.4.3 Characterisation of $Ru(bpy)_2(bpy)$'-modified mesoporous silica films

In this subchapter, the preliminary results of the covalent bonding of $Ru(bpy)_2(bpy)$'- species onto mesoporous silica film are presented.

After click reaction, in the region of azide stretching (2095 cm^{-1}, *Figure 75*) for all tested samples maximum from N_3 functional group is seen. Intense peak at 1595 cm^{-1} appears after the click with ruthenium complex, corresponding to C=C stretches of bipyridine ligand [295].

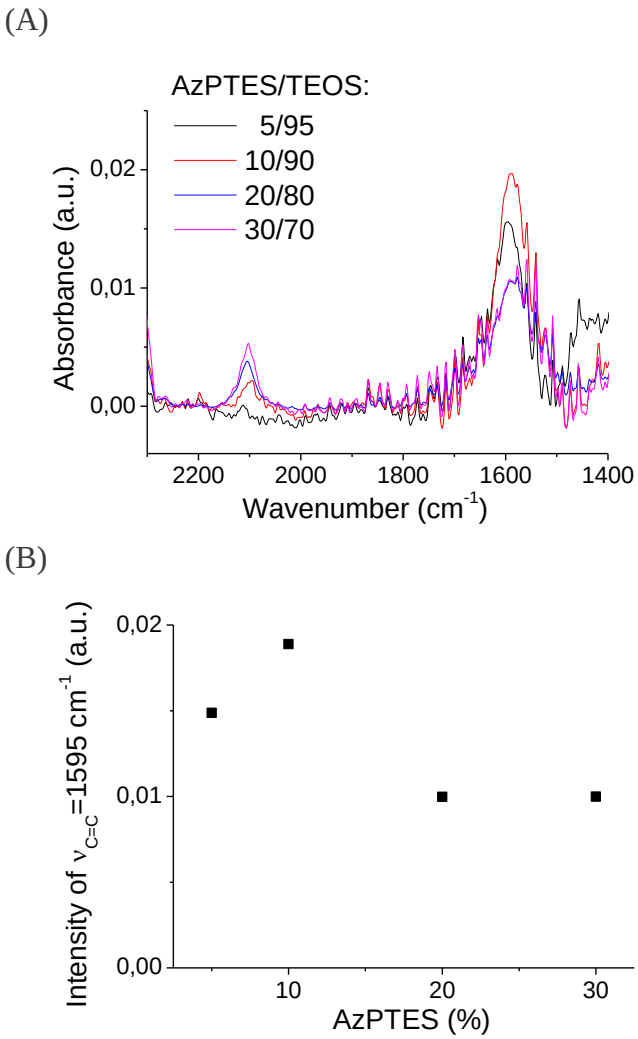

Figure 75 – (A) Selected region of IR spectra collected after click reaction and (B) evolution of $\nu_{C=C}$ peak intensity for post-grafted MSFs in function of different AzPTES content in starting sol (5, 10, 20 and 30 %)

For films synthesised with 5 to 10% of AzPTES the peak related to bipyridine ligand increases, while for 20 and 30% it reduces to the equal value (*Figure 75B*). This variation gives the

information about the quantity of complex grafted onto silica film, which follows the same evolution. The rise of $Ru(bpy)_2(bpy)$'-bonded species for films with 5 and 10% of AzPTES is observed due to more azide sites to which more complex can be attached. Lower signals recorded for films with higher content of azide modifier (20/80 and 30/70 AzPTES/TEOS) can be explained by thinner deposits obtained while addition of more co-precursor [107]. Denser location of N_3-functional groups results in unfavourable steric effects during click reaction, making it impossible to incorporate more redox species for films with high AzPTES/TEOS ratio, as it was also discussed for Fc-modified films [108]. According to IR results, maximum amount of $Ru(bpy)_2(bpy)$' attached is reached for samples deposited from 10/90 AzPTES/TEOS sol.

The electrochemical response from films after Huisgen click reaction with $Ru(bpy)_2(bpy')^{2+}$ is shown on *Figure 76A*. Electrochemical characterisation of (tris)bipyridine ruthenium functionalised films carried out in 0.1 M $NaNO_3$ solution shows a well-defined redox peak, which confirms the presence of $Ru(bpy)_2(bpy)$'-species.

Evolution of CV peak intensity from grafted to silica film complex in function of AzPTES loading was also studied. Whatever the addition of AzPTES was, electrochemical signal from grafted $Ru(bpy)_3^{2+}$ derivative was recovered. Recorded anodic current slightly increases for films obtained by addition of 5-10% of N_3-containing co-precursor. Samples which contained 20 and especially 30% of AzPTES exhibited a decrease of anodic peak current (*Figure 76B*). Sufficiently decreased electrochemical signal from films obtained from 30/70 AzPTES/TEOS sol is attributed to lower amount of ruthenium complex for these samples.

Electrochemical signal, which was recorded, appears due to the electron hopping between neighbouring ruthenium centres as it was shown for Fc-modified films after click reaction [107] (*Eq. 4.19*) [108].

$$Ru(bpy)_2(bpy')^{2+} - 1\ e^- + NO_3^-(solution) \Leftrightarrow Ru(bpy)_2(bpy')^{3+}, NO_3^-(film) \quad (Eq.\ 4.19)$$

(A)

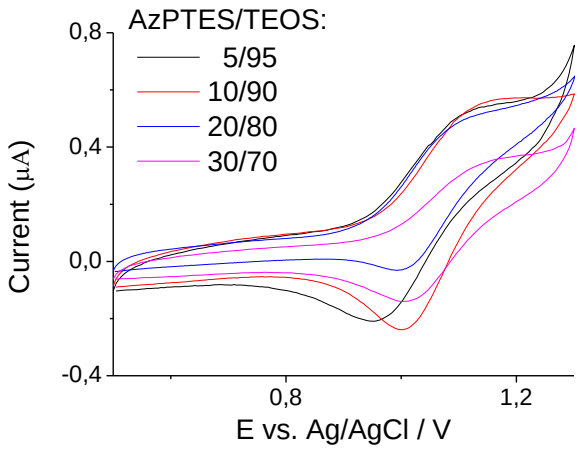

(B)

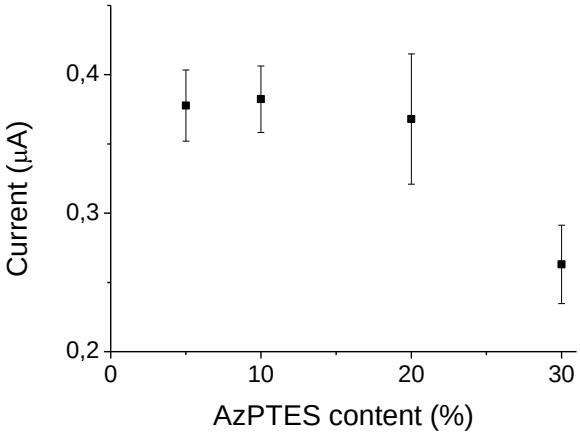

Figure 76 – (A) CV activity of covalently bonded $Ru(bpy)_2(bpy)'^{2+}$ complex to MSFs modified with different content of azide and
(B) anodic peak current values (5, 10, 20 and 30 % recorded in 0.1 M $NaNO_3$ at 50 mV/s)

Comparison of electrochemical signal of grafted complex and impregnated system is illustrated on *Figure 77*. As-prepared covalently modified electrode exhibits much lower current intensity comparing to the response on the other types of electrodes. Therefore, on *Figure 77* the original CV curve recorded using covalently modified film was amplified 10 times. The position of anodic peak around 1.1 V is in good agreement with $Ru(bpy)_3$-modified silica [255, 296]. Increase of peak-to-peak separation from 0.04 to 0.12 V respectively for impregnated and grafted ruthenium complex was noticed. It can be explained by fewer amount of incorporated redox species (lower

I_p) and hence, slower electron transfer kinetics between their centres in case for covalent bonding of $Ru(bpy)_2(bpy')^{2+}$.

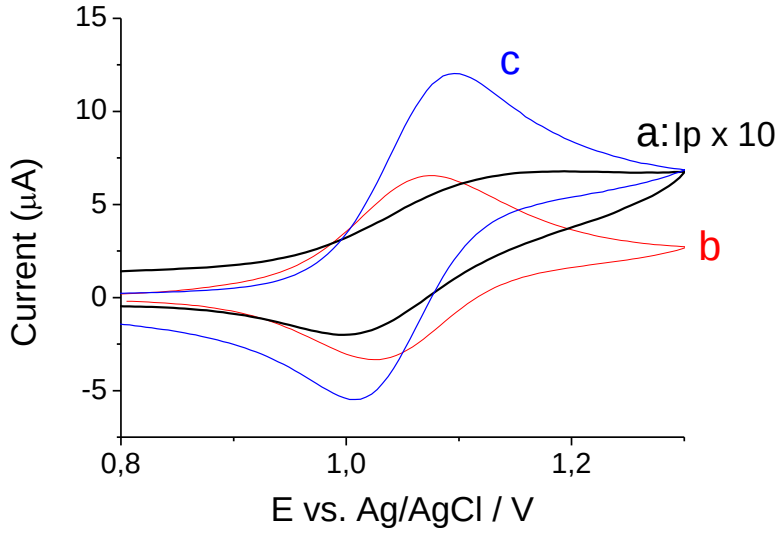

Figure 77 – The comparison of CV responses of immobilised $Ru(bpy)_3^{2+}$ by a) grafting (0.1 M $NaNO_3$, I_p amplified 10 times) and b) impregnation onto MSF (50 mM PBS, pH 7) with free system of c) 0.5 mM $Ru(bpy)_3^{2+}$ on bare ITO (scan 1, scan rate 50 mV/s)

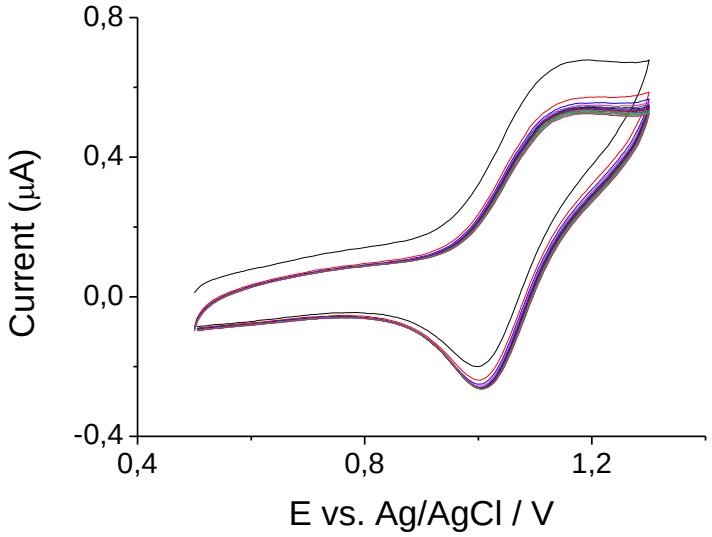

Figure 78 – CV signal recorded in 0.1 M $NaNO_3$ solution using azide-modified MSF (AzPTES/TEOS ratio: 10/90) after click reaction with $Ru(bpy)_2(bpy')$ (15 consecutive scans, 50 mV/s scan rate)

The stability of CV signal under multiple scanning is shown on *Figure 78*. After 15 consecutive scans performed in 0.1 M $NaNO_3$ with MSF-modified ITO after click reaction with

$Ru(bpy)_2(bpy)'^{2+}$ the peak current decreased only by 18%, when for electrostatically adsorbed $Ru(bpy)_3^{2+}$ peak current reduced by 50%. It confirms that covalent immobilisation leads to stronger binding of ruthenium complex with silica matrix, resulting in less leaching of reactant.

Figure 79A depicts the UV/vis spectra collected from MSF which underwent click reaction with ruthenium complex. A peak of interest is located at 445 nm and is related to incorporated (tris)bipyridine ruthenium (II) complex [214], confirming its presence inside the film in addition to IR and CV characterisation.

(A)

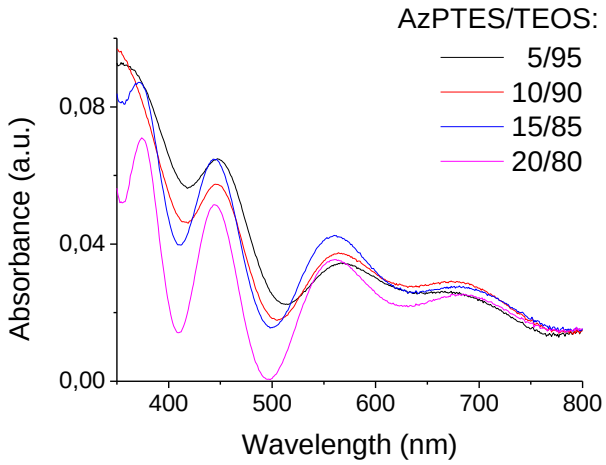

(B)

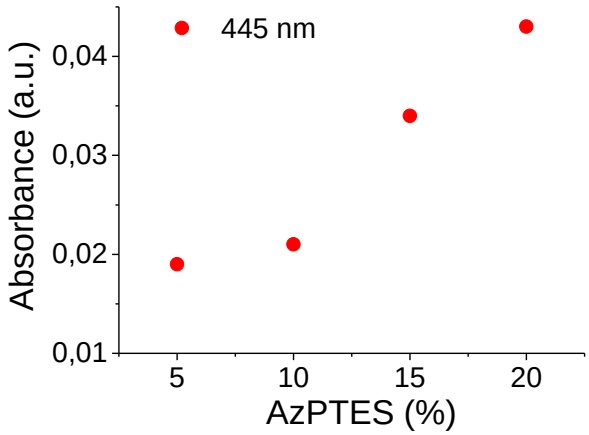

Figure 79 – (A) UV/vis spectra of azide-modified MSF after click reaction with $Ru(bpy)_2(bpy')^{2+}$ and (B) the intensity of peak at 445 nm related to MLCT in complex in function of AzPTES content in sol

Similar absorbance maximum of metal-ligand charge transfer, MLCT, about 450 nm was observed for incorporated in porous solid silica matrix ruthenium complexes with various substitutes [260]

as well as for covalently bonded to mesoporous silica species [297] (in aqueous solution the adsorption peak is located at 452 nm [209]). With an increase of AzPTES/TEOS ratio in azide-modified films to 10% (*Figure 79B*), a slight rise of intensity at 445 nm is observed. Further evolution of peaks has the increasing character till 20% of AzPTES in films. According to UV/vis spectra, maximum content of ruthenium complex is reached for films prepared at 20/80 AzPTES/TEOS ratio. This value is different from FTIR and electrochemical characterisation, where the maximum of incorporated complex was reached for samples with 10% of azide co-precursor. Smaller current response for films with 20/80 AzPTES/TEOS composition can be due to the fact, that some of the attached redox groups can be not electroactive.

4.4.4 Electrochemical response in presence of glyphosate

The effect of herbicide addition on CV response from incorporated $Ru(bpy)_2(bpy')^{2+}$ is shown on *Figure 80*. Tested mesoporous silica film was deposited from sol containing 10% of AzPTES. Introduction of concentrated glyphosate aliquot to tested media resulted in final herbicide concentration in solution equal to C_{GLYP} = 4 µM. After addition of this co-reactant, anodic peak current increased sufficiently, while the reversed signal was less distinguishable than that without amine.

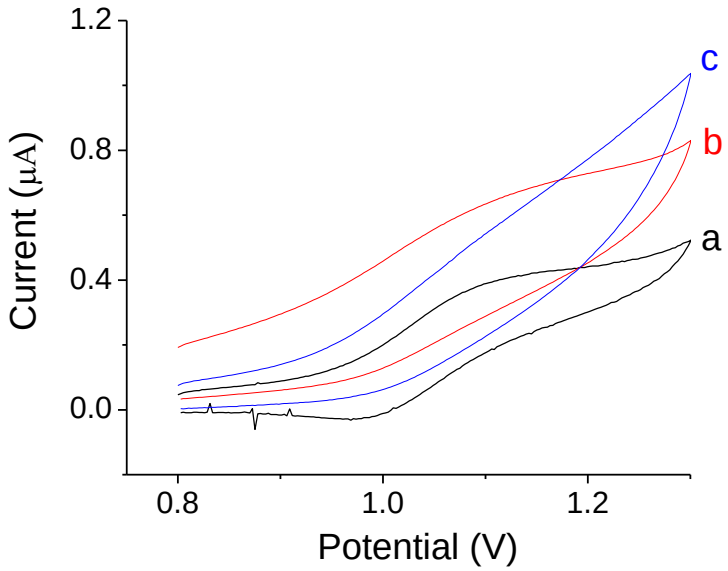

Figure 80 – CV response from $Ru(bpy)_2(bpy')$ covalently bonded to MSF (AzPTES/TEOS 10/90) recorded in a) 0.1 M $NaNO_3$, b) 4 µM and c) 40 µM glyphosate solution (scan 1, 20 mV/s, 0.1 M $NaNO_3$)

Analysis of solution, which contained higher final glyphosate concentration (40 µM), resulted in high capacitive current with no visible redox peaks. Addition of co-reactant to solution of supporting electrolyte causes the rise of anodic peak current. It means that co-reactant ECL mechanism occurs in presence of bonded to silica surface $Ru(bpy)_2(bpy')$- species and amine, as it was also observed for $Ru(bpy)_3^{2+}$-doped silica nanoparticles in presence of TPA [256]. The observed increase for MSF grafted with $Ru(bpy)_2(bpy')$ species was not as sufficient, as for other materials, which were investigated for this purpose.

Further addition of glyphosate deforms the shape of the CV curve and makes it difficult to distinguish any electrochemical signal apart of capacitive current. After a test in presence of higher concentration of co-reactant, the electroactivity of $Ru(bpy)_2(bpy')$-modified film reduced dramatically and no evidence of electroactive ruthenium species was noticed.

Stability of the electrode during storing is also important parameter, which was checked. MSFs with grafted ruthenium complex were exhibiting the loss of their electrochemical activity while storing them on air. As presented on *Figure 81*, in four days a decrease of anodic peak current was noted to be 2 times.

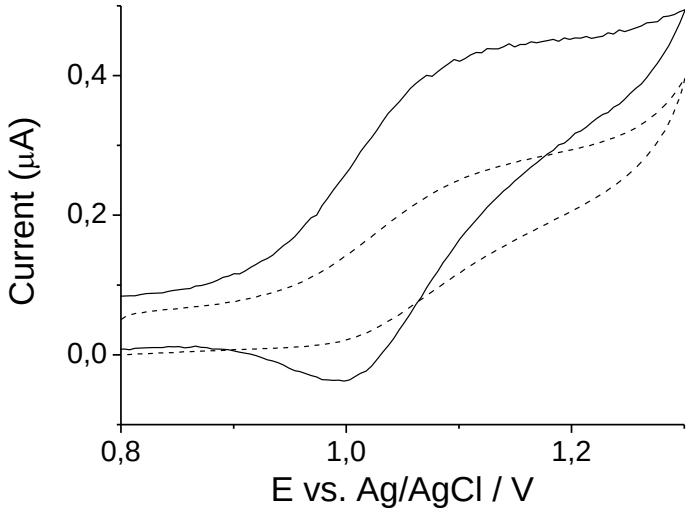

Figure 81 – CV signal recorded on grafted film(10/90 AzPTES/TEOS) right after click reaction with $Ru(bpy)_2(bpy')^{2+}$ (solid line) and after storing a film for 4 days (dashed line) (scan 1, 20 mV/s, 0.1 M $NaNO_3$)

4.5 Analytical aspect of electrochemical detection of glyphosate

The growth of the anodic peak current from either free $Ru(bpy)_3^{2+}$ in solution or immobilised onto mesoporous silica film with the addition of glyphosate can be used for its quantitative detection. In order to estimate the possibility to use electrode for amine detection, calibration curves were plotted for each tested system. The effect of glyphosate addition on CV peak of $Ru(bpy)_3^{2+}$ in solution was checked in the range from 0 to 1 mM. Since it was demonstrated that pH variation leads to sufficient changes in anodic peak current (*Figure 61*), comparison between bare ITO electrode, ITO covered with mesoporous silica film and impregnated electrode were done at pH 7.

Recorded cyclic voltammograms and corresponding calibration curves built in function of herbicide concentration are presented on *Figure 82 – Figure 84*. As it was expected, the increase of co-reactant concentration in solution leads to higher current intensity whatever the electrode was used. Reducing the scan rate to 20 mV/s the steady increase of Ip was obtained for impregnated electrode (*Figure 84*) comparing to 50 mV/s shown on *Figure 71*. In these conditions, more $Ru(bpy)_3^{2+}$ can be oxidised, hence more $Ru(bpy)_3^{3+}$ species will react with co-reactant giving more enhanced CV response.

Calibration plots exhibit a linear relation between herbicide concentration and peak current. The higher slopes for bare ITO and MSF-covered ITO electrodes (19.81 on *Figure 82* and 19.69 on *Figure 83* respectively) show higher sensitivity of glyphosate detection comparing to impregnated system. Calculated values of limit of detection for herbicide ($LOD=3\sigma/b$) are respectively 0.09, 0.12 and 0.27 mM for bare ITO, ITO with deposited mesoporous silica film and impregnated electrode. Low number of points used to calculate LOD value can be a reason of its increase in presence of silica coating. Nevertheless, film presence can be used as a barrier against larger molecules that can potentially affect glyphosate detection [195].

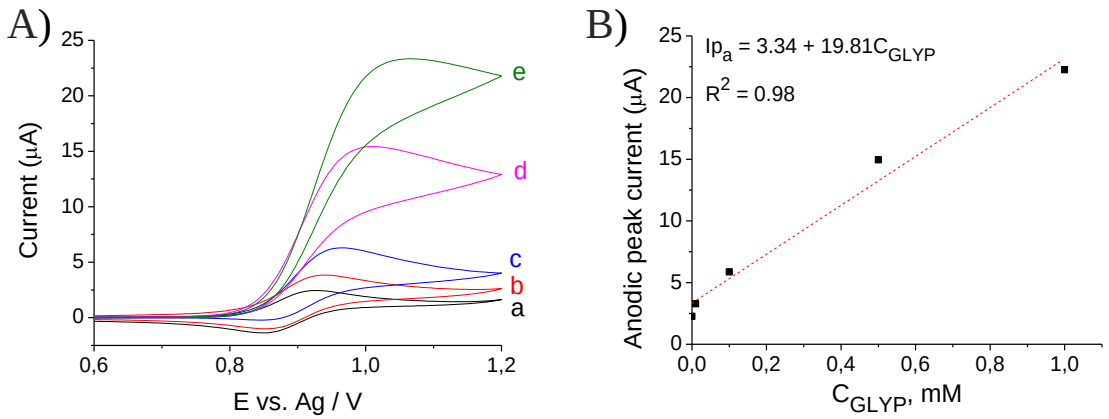

Figure 82 – (A) CV curves recorded on ITO electrode with 0.1 mM $Ru(bpy)_3^{2+}$ a) without and with addition of b) 0.01 mM, c) 0.1 mM, d) 0.5 mM and e) 1 mM, glyphosate and (B) corresponding calibration curve (scan 1, 50 mV/s, 50 mM PBS, pH 7)

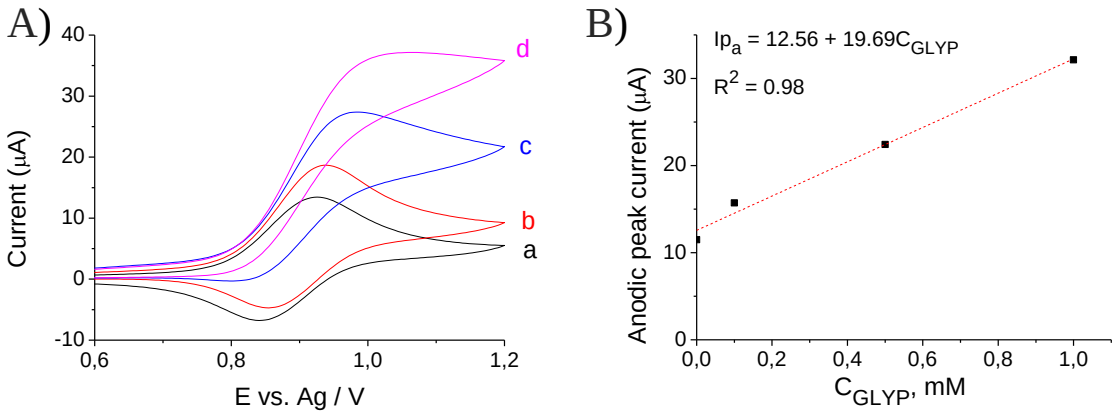

Figure 83 – (A) CV curves recorded on MSF-covered ITO electrode with 0.1 mM $Ru(bpy)_3^{2+}$ a) without and with addition of b) 0.1 mM, c) 0.5 mM and d) 1 mM glyphosate and (B) corresponding calibration curve (scan 1, 50 mV/s, 50 mM PBS, pH 7)

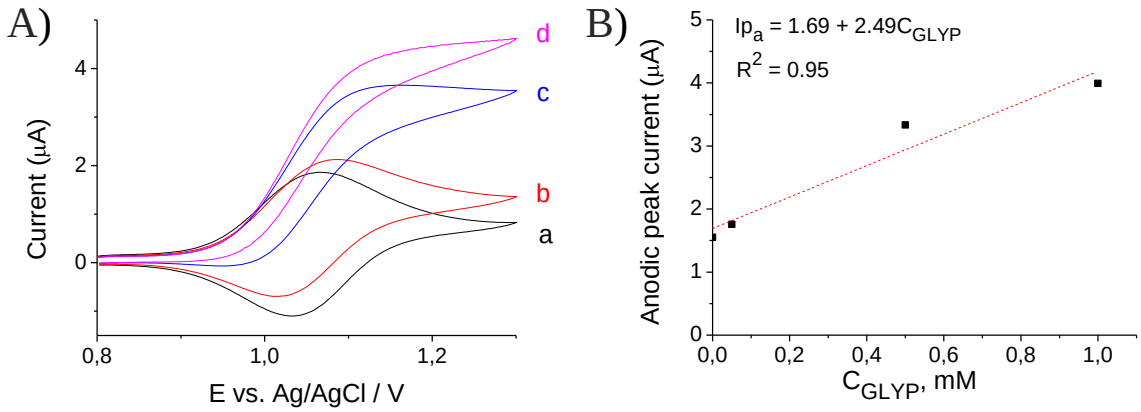

Figure 84 – (A) CV curves recorded on MSF-covered ITO electrode impregnated with $Ru(bpy)_3^{2+}$ a) without and with addition of b) 0.01 mM, c) 0.5 mM and d) 1 mM glyphosate and (B) corresponding calibration curve (scan 1, 50 mV/s, 50 mM PBS, pH 7)

4.6 ECL measurements: challenges and complications in course of the project

Initially, the ECL detection of glyphosate was planned to be used due to higher sensitivity of this technique comparing to simple electrochemical analysis. Miniaturisation of the ECL setup is of big interest as it can be used further in the sensitive in-field analysis.

In this project, the first ECL experiments were performed on portable µStat ECL from DropSens with commercial screen-printed electrodes. The used ECL cell is equipped in the way that electrochemical signal can be recorded with further luminescence detection. To obtain the ECL signal, screen-printed electrode (SPE) was placed in the bottom of the chamber that can be filled with working solution. Three-electrode configuration is implemented by introduction of miniaturised planar working electrode (carbon or ITO), silver reference and carbon counter electrodes. In order to detect light emission, chamber must be closed. No external light is accepted as it can interfere the final ECL spectrum. Application of suitable for a chosen system potential initiates the light emission, which is then detected using luminescence detector. In case of collecting a spectrum, resultant ECL emission is registered in function of applied potential.

The first attempts to detect glyphosate in co-reactant system with $Ru(bpy)_3^{2+}$ in solution were carried out on carbon screen-printed electrode. The electrochemical performance of this system was not reproducible and obtained results could not have been added in this manuscript. ITO screen-printed electrodes were also tested, but the experiments were not proceeded with this system because it was not possible to maintain generated mesoporous silica film on their surface during all required electrode preparation steps.

Glass plates covered with a layer of ITO were more suitable and reliable, therefore they were chosen for this study. They fulfil such requirements as a stable and reproducible electrochemical signal, possibility to be modified and transparency which made UV/vis analysis possible. In order to continue research using this type of electrodes, modification of the ECL cell was necessary because the plate could not be placed inside the commercial ECL. The ways to introduce reference and counter electrodes also had to be found for this new cell configuration. Silver wire and platinum grid were supposed to be used as pseudo-reference and counter electrodes respectively. Ag wire was chosen due to its smaller size comparing to classical Ag/AgCl reference. Apart from the shift of peak positions (- 0.1 V), the electrochemical signal obtained using pseudo-reference

electrode was the same as with Ag/AgCl. In the allocated time given for this project, it was not possible to perform the changes of the ECL cell and only electrochemical tests were performed.

One more complication for the project arose at the point of $Ru(bpy)_2(bpy')(PF_6)_2$ preparation for its grafting onto silica matrix. As described in **Section 4.4.1**, the **Step 3** of (bpy') synthesis (reaction of ether synthesis) resulted in low yields of 10-13%. The attempts to improve the procedure given in literature were performed by changing of conditions of ligand preparation (such as the speed of reactant addition, filtration of unreacted NaH after alkoxide formation, drying of solvent before the synthesis, variation of parameters for column chromatography on the step of cleaning of product), but none of them increased the yields. Because of the lack of $Ru(bpy)_2(bpy')(PF_6)_2$ modifier, only the preliminary experiments were conducted on electrodes covered with grafted mesoporous silica film in **Section 4.4**.

Herbicide detection on the ITO electrodes with $Ru(bpy)_2(bpy')$-grafted mesoporous silica films was supposed to be studied for films with their regular (≈80 nm thick) and reduced thicknesses. In this way, wet etching procedure presented in **Chapter III** could be applied for thickness decrease of samples containing covalently bonded ruthenium complex discussed in **Chapter IV**. It was suggested that thickness reduction could improve the glyphosate diffusion through channels modified with bulky redox species and at some particular film thickness the maximum ECL signal could be detected. Because of the described complications faced in the course of this work, the link between two studies was not made.

4.7 Conclusions

The electrochemical behaviour of (tris)bipyridine ruthenium (II) complex is different in terms of its state. In solution, the system is close to electrochemically reversible for bare electrode (Ip_a/Ip_c = 1.1, ΔE = 0.075 V). Presence of mesoporous silica film does not impact the mass transport sufficiently, but leads to an increase of peak current as a result of pre-concentration of ruthenium complex on silica matrix, causing increased Ip_a/Ip_c (Ip_a/Ip_c = 1.4, ΔE = 0.081 V). For films with impregnated $Ru(bpy)_3^{2+}$ the peak-to-peak separation is the smallest (0.04 V) because of the easier charge transfer of immobilised complex close to the electrode surface. The current ratio decreases as a result of desorption processes (from 1.5 for the first scan to 0.9 for the fifteenth). The electrochemical signal of $Ru(bpy)_3^{2+}$ is stable on bare electrodes, although impregnated ones exhibited the current decrease (up to 50% of signal loss after 15 scans performed) because of the weak electrostatic forces between silica and ruthenium complex.

Covalent immobilisation was implemented for N_3-modified MSF by Huisgen 1,3-cycloaddition with propargyl derivative of $Ru(bpy)_3^{2+}$. The level of functionalisation with azide affects the final quantity of $Ru(bpy)_2(bpy')$-species in film. According to obtained results, the maximum content of complex was reached for films with AzPTES/TEOS ratio equal to 10/90. The first tests confirmed that incorporated species are electrochemically active due to the electron hopping between neighbouring ruthenium centres. Films possess a stable signal while multiple scanning with minimum loss of grafted reagent (decrease of current intensity after 15 consecutive scans is only 20%), but the electrochemical stability in time was rather low and in 4 days 50% of CV signal intensity was lost.

Co-reactant mechanism of ECL reaction between $Ru(bpy)_3^{2+}$ complex and glyphosate in solution is observed for bare ITO electrode and ITO electrode covered by MSF, as well as for incorporated complex inside MSF by electrostatic and covalent bonding. It shows that these systems have a potential to be used with free ECL reactant in solution and with incorporated inside solid silica matrix reactant. Presence of MSF on ITO electrode does not interfere the herbicide detection by ECL co-reactant mechanism in presence of $Ru(bpy)_3^{2+}$ in solution. Conditions for the ECL reaction with glyphosate require a pH of solution to be set to 7 in order to obtain maximum electrochemical response and to slow down the damage of silica by alkaline media. However, on bare ITO electrode

co-reactant system can be operated at pH 8 with higher anodic peak current to that at pH 7. Subsequent decrease of peak current while operating $Ru(bpy)_3^{2+}$ - glyphosate system was observed for all types of electrode and is believed to be due to consumption of co-reactant in the pre-electrode area.

Based on the first experiments, calibration curves for glyphosate detection were plotted. Calculated limits of glyphosate detection for systems operated at pH 7 on bare, modified by mesoporous silica film ITO and impregnated electrode are 0.09, 0.12 and 0.27 mM respectively.

The study on films with grafted $Ru(bpy)_2(bpy')$ species showed that with their use the glyphosate detection is also possible. The presence of herbicide causes change in the electrochemical signal from bonded ruthenium complex, that can be attributed to co-reactant mechanism. However, this change is less distinguishable than that presented for free $Ru(bpy)_3^{2+}$ complex in solution and electrostatically bonded to the silica matrix, and requires further study.

General conclusion and perspectives

Mesoporous silica films synthesised by combination of sol-gel process and electrodeposition named EASA method (Electro-Assisted Self-Assembly) is an easy and highly effective way to modify electrode and develop new sensors. The films with vertically oriented cylindrical mesochannels on the electrode surface present some main advantages as a high specific surface area, easily accessible mesochannels and a narrow pore size distribution with beneficial for mass transport orientation and a feasibility to modify silica surface by co-condensation and post-grafting. However, non-inert silanol groups, which are present on the surface of silica, can be an advantage or disadvantage depending on film application. On the one hand, negatively charged surface can be used for pre-concentration organic and inorganic species, while the reactivity of silanol groups allows functionalisation of surface improving the selectivity of analyte detection. On the other hand, the excess of negative charge can hinder mass transport through mesopores to the electrode surface, suppressing electrochemical response. Therefore, a control over the film thickness, particularly its reduction, is needed.

The first part of the study was devoted to the control of the thickness of mesoporous silica films obtained by EASA method. The composition of the sol to prepare all films was fixed to 100 mM silica precursor (TEOS or AzPTES/TEOS mixture) and 32 mM CTAB as the template. We determined that the minimum deposition time to obtain full covering of the electrode is 10 seconds at -1.3V onto ITO electrode. The thickness of such defectless deposits is 80 ± 9 nm. Since it was not possible to prepare thinner perfect films by this approach, a post synthesis treatment was essential. After it, the final deposit on the electrode must keep its good structuration with opened and vertically oriented pores. For this reason, the approach with the wet etching technique using ammonium fluoride (NH_4F) soft etching agent was chosen. The adopted method is drop casting method for wet-etching. With the idea to know the best way to control the mesoporous silica film dissolution, different experiments were conducted with the template kept inside the silica pores and after its extraction by calcination or with acidic ethanol solution. The etching reaction was followed with stylus profilometry measurements of thickness, electrochemistry with electroactive probes ($Ru(NH_3)_6^{3+}$ and haemoglobin) or on films modified with ferrocene entities. The evolution of the structure was followed with TEM images and GISAXS diffractograms. In presence of surfactant inside the film, the dissolution rate is faster, but better controlled. The minimum

thickness, which was reached for MSF with keeping hexagonal mesostructure, was 28 ± 9 nm after 1 hour of 0.05M NH_4F treatment. In the case of sample with free pores, the silica film that kept its perfect structure is only 57 ± 11 nm after 1 hour of the same treatment. The extraction mode of the surfactant does not have any effect on the etching process. Longer times led to more flaws of silica film and, finally, to its dissolution.

In the second part of this study, ITO electrode modified with mesoporous material was tested for glyphosate detection. Because of its non-electroactive property on ITO and its belonging to the amine family, the analysis of this herbicide was considered by electrochemiluminescence (ECL) approach. The aim was to see if a sensor with the covalently immobilised (tris)bipyridine ruthenium (II) onto mesoporous silica film can be proposed. Firstly, the alkyne derivates of the ruthenium bipyridine complex were prepared because of their commercial unavailability. The Huisgen 1,3-cycloaddition was then conducted on azide-modified mesoporous silica films. Spectroscopic and electrochemical techniques gave the evidences of the immobilised ruthenium complex in the film and the interesting result that its redox activity in the confined media is maintained even if a shift in potential range of the complex response was observed. The response of this kind of modified electrode was compared with those where silica deposit was previously impregnated with $Ru(bpy)_3^{2+}$ or put in contact with a solution of ruthenium. The stability of the response was also investigated and, as expected, covalently modified films exhibit better stability due to a chemical nature of bonding between film and reagent. From the first preparations, the maximum amount of covalently bonded ruthenium complex was reached for films prepared with 10% of azidosilane in the sol and could be explained by a steric effect due to the size of the complex molecule and the limitation of the access to the azide functions. Electrodes modified following these two approaches were investigated for the feasibility to be used for detection of amine-containing herbicide glyphosate by ECL. Due to the sanitary situation and some technical problems with the conception of an ECL cell adaptation for commercial apparatus, only electrochemical characterisation was done. From these first analysis, it appears that whatever the electrode is, the presence of the herbicide leads to a modification of the electrochemical signal. If for system with free $Ru(bpy)_3^{2+}$ or the impregnated complex electrocatalytic effect is well observed and is in good consistence with the theoretical detection mechanism, the change on the electrochemical signal for the covalently bonded ruthenium complex is different and not totally explained at this time.

Based on conducted study, future perspectives can be proposed:

A study for optimum conditions for synthesis of mesoporous silica films with covalently bonded $Ru(bpy)_2(bpy')$ species. The preliminary results showed that introduction of 10% of AzPTES leads to the highest concentration of complex with respect to FTIR and CV characterisation. However, the maximum capacitance of films with respect to ruthenium complex in an interesting parameter to verify. The quantity of grafted species can be controlled by the AzPTES/TEOS ratio. Estimation of quantity of attached complex can be performed by electrochemistry of bonded redox moieties or by UV-vis spectroscopy.

A study of the ECL response in function of $Ru(bpy)_2(bpy')^{2+}$ quantity incorporated in mesoporous silica film. It is known that the family of (tris)bipyridine ruthenium (II) complexes emit the light. Recorded ECL signal in the absence of co-reactant can be also used to determine the amount of grafted species. Logically, generation of the highest ECL response should be related to maximum loading with ruthenium complex, but this hypothesis requires checking. Films with the most intense emission can be selected for sensing purposes in ECL co-reactant systems.

A study for glyphosate detection by co-reactant mechanism using covalently modified mesoporous silica films with $Ru(bpy)_2(bpy')^{2+}$ species. No information about using similar systems was found in the literature. For the films obtained in conditions that result in the highest luminescence response, the electrocatalytic behaviour with herbicide can be checked using ECL co-reactant system. In case if a gradual increase of emission is detected, calibration curve could be plotted and the electrode could be tested as a sensor for glyphosate detection.

A study on the effect of film thickness for the ECL detection of glyphosate. Verification of the effect of the film thickness on resultant ECL response of grafted film in presence of co-reactant is also interesting to be carried out. With the thinner films easier diffusion of glyphosate is expected. But at the same time, thickness decrease reduces the amount of grafted ruthenium complex in silica film, what can potentially lower the ECL response from luminophore groups. In this way, an optimum thickness can be determined in order to achieve the highest ECL signal.

A study of ITO electrodes modified with electrografted layer. Immobilisation of ruthenium complex can be also performed directly on the electrode surface. For this approach, diazonium salts with azide functions (such as 4-azidoaniline) can be used for their grafting onto ITO surface.

Terminated N_3- functions can be used for Huisgen coupling. Hence, (tris)bipyridine ruthenium (II) complex (such as $Ru(bpy)_2(bpy')^{2+}$) can be covalently attached to the electrode surface. The ECL response of these type of electrodes could be also studied because in this system no diffusion issues are expected as in case of electrodes covered with mesoporous silica films.

Appendix 1: Chemicals

Table I – List of chemicals

Name	Abbreviation	Source	Molecular weight, g/mol	Purity, %
Silica precursors and ITO substrates				
Tetraethyl orthosilicate	TEOS	Alfa Aesar	208.33	98
(3-Chloropropyl)triethoxysilane	ClPTES	Sigma-Aldrich	240.80	95
(3-Azidopropyl)-triethoxysilane	AzPTES	Synthesised in laboratory	247.37	N/A
Indium-tin oxide plates (8-12 Ω)	ITO	Delta Technologies	-	N/A
Indium-tin oxide plates (8-12 Ω)	ITO	Solems	-	N/A
Inorganic salts used for electrolyte and organic synthesis				
Sodium nitrate	$NaNO_3$	Prolabo	84.99	99.5
Ammonium fluoride	NH_4F	Prolabo	37.04	98
Ammonium chloride	NH_4Cl	Sigma	53.49	99.5
Potassium fluoride	KF	Fluka	58.10	99.5
Copper (II) acetate monohydrate	$Cu(Ac)_2$	UCB	199.65	100
Copper (II) nitrate trihydrate	$Cu(NO_3)_2$	Sigma-Aldrich	241.60	99
Sodium acetate trihydrate	CH_3COONa	Sigma-Aldrich	136.08	99
Sodiumium phosphate dibasic dihydrate	Na_2HPO_4	Fluka	177.99	99
Sodium phosphate monobasic	NaH_2PO_4	Sigma	119.98	99
Sodium azide	NaN_3	Sagma-Aldrich	65.01	99.5
Sodium carbonate	Na_2CO_3	Sigma-Aldrich	105.99	99.95
Sodium bicarbonate	$NaHCO_3$	Sigma	84.01	99.5
Sodium metabisulfite	$Na_2S_2O_5$	Merck	190.10	96
Sodium borohydride	$NaBH_4$	Aldrich	37.83	98.0
Sodium chloride	NaCl	Prolabo	58.44	N/A
Magnesium sulfate	$MgSO_4$	Prolabo	120.37	N/A
Tetrabutyl-ammonium bromide	NBu_4Br	Fluka	322.37	99
Cis-bis(2,2'-bipyridine) dichlororuthenium(II)	$Ru(bpy)_2Cl_2$	Sigma-Aldrich	484.35	97
Ammonium hexafluorophosphate	NH_4PF_6	Sigma-Aldrich	163.00	98
Sodium diethyldithiocarbamate trihydrate	NaDDTC	Sigma-Aldrich	225.31	N/A
Redox probes				
Hexaammineruthenium (III) chloride	$Ru(NH_3)_6Cl_3$	Alfa-Aesar	309.61	99.9
Ferrocenedimethanol	$Fc(MeOH)_2$	Sigma-Aldrich	246.08	98
Tris(bipyridyl)ruthenium(II) chloride hexahydrate	$Ru(bpy)_3Cl_2$	Acros Organics	748.63	98
Haemoglobin	Hb	Sigma-Aldrich	64500	N/A

Solvents				
Water	H_2O	Millipore Milli-Q system	18.02	N/A
Ethanol	EtOH	Merk	46.07	95-96
Acetone	-	Carlo Erba	58.08	99.8
N,N-dimethylformamide	DMF	Fisher Chemical	73.09	99.94
Acetonitrile	ACN	Biosolve	41.04	99.95
Cyclohexane	-	Merk	84.16	99.0
Hexane	-	Carlo Erba	86.18	95
1,4-dioxane	-	Acros Organics	88.11	99
Ethyl acetate	EtOAc	Merk	88.11	N/A
Dichloromethane	DCM	Biosolve	84.93	99.9
Methanol	MeOH	Carlo Erba	32.04	99.9
Tetrahydrofuran	THF	Prolabo	72.11	99.7
Diethyl ether	-	Sigma Aldrich	74.12	99
Other chemicals				
Hexadecyltrimethylammonium bromide	CTAB	Sigma	364.45	99
Ascorbic acid	AscAc	Merck	176.13	99.7
Hydrochloric acid (1 M)	HCl	BDH Chemicals	36.46	N/A
Sodium hydroxide (1 M)	NaOH	BDH Chemicals	40.00	N/A
Hydrofluoric acid	HF	Sigma-Aldrich	20.01	40%
Ethynyl ferrocene	EtFc	Aldrich	210.05	97
4,4′-Dimethyl-2,2′-dipyridyl	$bpyMe_2$	Sigma-Aldrich	184.24	99.5
Selenium dioxide	SeO_2	Alfa Aesar	110.96	99.4
Sodium hydride	NaH	Sigma-Aldrich	24.00	60
Propargyl bromide	PrBr	Sigma-Aldrich	118.96	80
Triethylamine	Et_3N	Sigma-Aldrich	101.19	99
Silica gel	SiO_2	Merk	60.09	N/A
Acetic acid	AcAc	Sigma-Aldrich	60.05	99.8
4-(carboxyaldehyde)-4’-methyl-2,2’-bipyridine	bpy-ald	Synthesised in laboratory	198	N/A
4-(hydroxymethyl)-4’-methyl-2,2’-bipyridine	bpy-alc	Synthesised in laboratory	200	N/A
4-[2-propyn-1-yloxymethyl]-4’-methyl-2,2’-bipyridine	bpy’	Synthesised in laboratory	238	N/A
Ruthenium(2,2’-bipyridine)2-(4-[2-propyn-1-yloxymethyl]-4’-methyl-2,2’-bipyridine)	$Ru(bpy)_2(bpy')(PF_6)_2$	Synthesised in laboratory	997	N/A
Glyphosate	GLYP	Sigma-Aldrich	169.07	N/A

Appendix 2: Determination of ammonium fluoride concentration

Ammonium fluoride is known to be hydroscopic, what means that it can adsorb water from the environment. Based on this, the weighted amount of NH_4F may have water, which will decrease the part of salt in the weighted sample. In order to be sure that the calculated concentration of NH_4F is the exact concentration of the volumetric solution, titration and ion chromatography were used on solutions with 0.05 M NH_4F.

The back titration of ammonium [298] was the basis to determine the concentration of fluoride, because after the salt dissociation the concentration of NH_4^+ is equal to F^-:

$$NH_4F \rightleftharpoons NH_4^+ + F^-, \text{ where } [NH_4^+] = [F^-]$$

Ammonium fluoride solutions (0.05 M) were prepared by dissolution of 0.0185 g of salt in 10 ml of deionised water in the plastic tube. By adding the access of NaOH (10 ml 0.10 M) to NH_4F solution (10 ml, 0.05 M), NH_4OH was formed. Following heating of solution led to a decomposition of a weak base:

$$NH_4F + NaOH \rightarrow NH_4OH + NaF$$

$$NH_4OH + NaF \xrightarrow{T=100^oC} NaF + H_2O + NH_3\uparrow$$

The vapour from boiling solution was regularly checked by the litmus paper till the point when it was not turning blue, signifying the end of the reaction of decomposition of NH_4OH. After cooling down, two drops of phenol phthalein indicator were added and the unreacted NaOH was titrated by solution of HCl (0.1 M) till the pink colour appears. The procedure was repeated six times. Results and calculations are shown in the *Table II*.

Determined ammonium fluoride concentration in etching solution was equal to 0.054 ± 0.002 M (based on six titrations). In parallel, the ion chromatography confirmed the presence of 0.049 M of F^- (one measurement).

Table II – Results and calculations of back titration of NH_4F

	V_{HCl}, ml	n_{HCl}, moles	n_{NaOH}, moles	n_{NH4F}, moles	C_{NH4F}, M	$\bar{C}_{NH4F}$, M
1	3.9	$3.9 \cdot 10^{-4}$	$3.9 \cdot 10^{-4}$	$5.8 \cdot 10^{-4}$	0.058	0.054
2	4.3	$4.3 \cdot 10^{-4}$	$4.3 \cdot 10^{-4}$	$5.4 \cdot 10^{-4}$	0.054	
3	4.4	$4.4 \cdot 10^{-4}$	$4.4 \cdot 10^{-4}$	$5.3 \cdot 10^{-4}$	0.053	
4	4.1	$4.1 \cdot 10^{-4}$	$4.1 \cdot 10^{-4}$	$5.6 \cdot 10^{-4}$	0.056	
5	4.5	$4.5 \cdot 10^{-4}$	$4.5 \cdot 10^{-4}$	$5.2 \cdot 10^{-4}$	0.052	
6	4.4	$4.4 \cdot 10^{-4}$	$4.4 \cdot 10^{-4}$	$5.3 \cdot 10^{-4}$	0.053	

Based on this experimental data it was considered that the water content in the commercially available NH_4F was negligible. Solutions, prepared by weighting the exact amount of salt had the concentration equal to the calculated 0.05 M.

Appendix 3: Surfactant extraction from mesopores during etching

The shortest checked time of etching (10 minutes) caused the appearance of In signal on XPS spectrum. Electrochemical characterisation also showed the peaks related to reduction of $Ru(NH_3)_6^{3+}$ probe. The main hypothesis why it was observed is silica film damage while etching. However, there might be another explanation. Dealing with NH_4F solution it is fair to assume, that CTA^+ extraction may take place under the influence of F^- anions.

It was assumed that if the MSF is etched with the soft template in the course of all process, its content should always stay proportional to the content of silica matrix, as the film dissolution is followed by gradual decrease of both components: silica and surfactant. In order to detect the template extraction, the Fourier-transform Infrared Spectroscopy (FTIR) was used to follow the changes of silica/surfactant ratio by their characteristic bonds, which are [299, 300]:

1) Si-O-Si bond from silica network at 1100-1000 cm^{-1};

2) C-H bond of $-CH_3$ and $-CH_2-$ domains from CTA^+ ($C-H_{CTAB}$) in the region of 2960-2850 cm^{-1}. For this bond, incompletely hydrolysed during sol preparation TEOS moieties ($C-H_{TEOS}$) can have minor contribution.;

3) C-N bond of hydrophilic H_3C-N^+ part of cationic surfactant located at 1489 and 1478 cm^{-1}.

Consequently, after etching the ratio between Si-O and $C-H_{CTAB}$ / C-N peaks should stay the same in case if the CTA^+ extraction does not occur. Moreover, the intensities of normalised peaks should be equal before and after chemical treatment.

For this experiment, samples of gCTAB group with surfactant in pores were etched for 30 minutes with 0.05 M NH_4F solution. *Figure I* presents normalised spectra before etching (solid line) and after etching (dashed line). The control sample without surfactant in pores after acidic extraction is also presented (gEXTR batch, dotted line). Normalisation of all spectra was performed by Si-O-Si peak to equalise the film thickness for samples.

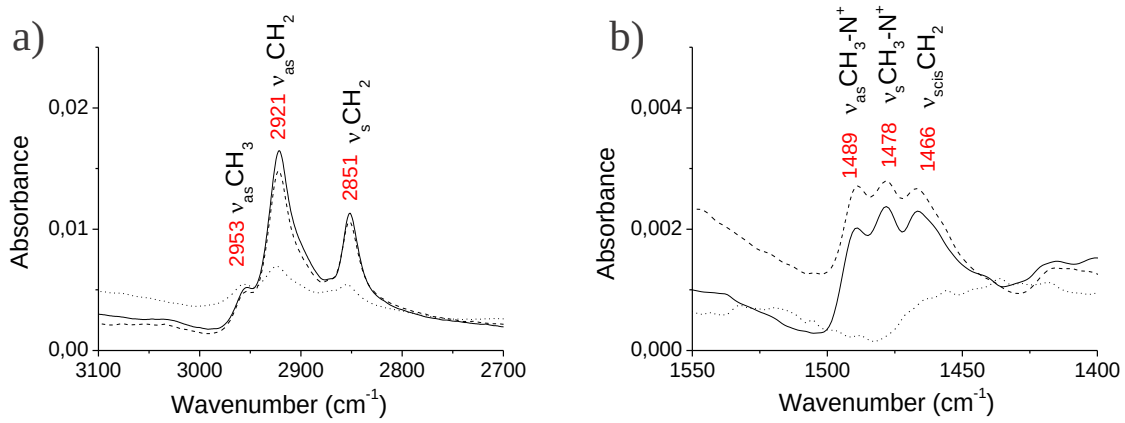

Figure I – IR spectra of (a) C-H stretching region and (b) C-N and C-H scissoring stretching region of film before (solid line) and after (dashed line) etching in 0.05 M NH_4F for 30 minutes and film after CTA^+ extraction of in 0.1 M HCl EtOH solution (dotted line)

The presence of peaks referred to C-H bonds before and after treatment with ammonium fluoride solution confirms the presence of CTA^+. For the film after solvent extraction of template this bond is less intense and is believed to be related to unhydrolysed TEOS ($C\text{-}H_{TEOS}$), what is typical for the sol-gel prepared silica [301]. Similar peak intensities of C-H and C-N stretching on *Figure I* indicate that the surfactant stays in pores of MSF while etching and no sufficient CTA^+ extraction occurs under the fluoride anion exposure. The same conclusion was made for a number of other gCTAB samples etched with NH_4F.

Appendix 4: Effect of pH on glyphosate detection using $Ru(bpy)_3^{2+}$ glyphosate co-reactant system on ITO electrode

Quantitative detection of glyphosate using co-reactant mechanism in present of $Ru(bpy)_3^{2+}$ is known to be affected by pH. This effect was studied 0.1 mM $Ru(bpy)_3^{2+}$ solution in the range of pH from 4 to 8 as presented. In function of herbicide concentration (from 0 to 1 mM), the calibration curves were plotted (*Figure II*) and their parameters were determined to calculate the $LOD_{GLYP,}$ presented in *Table III*.

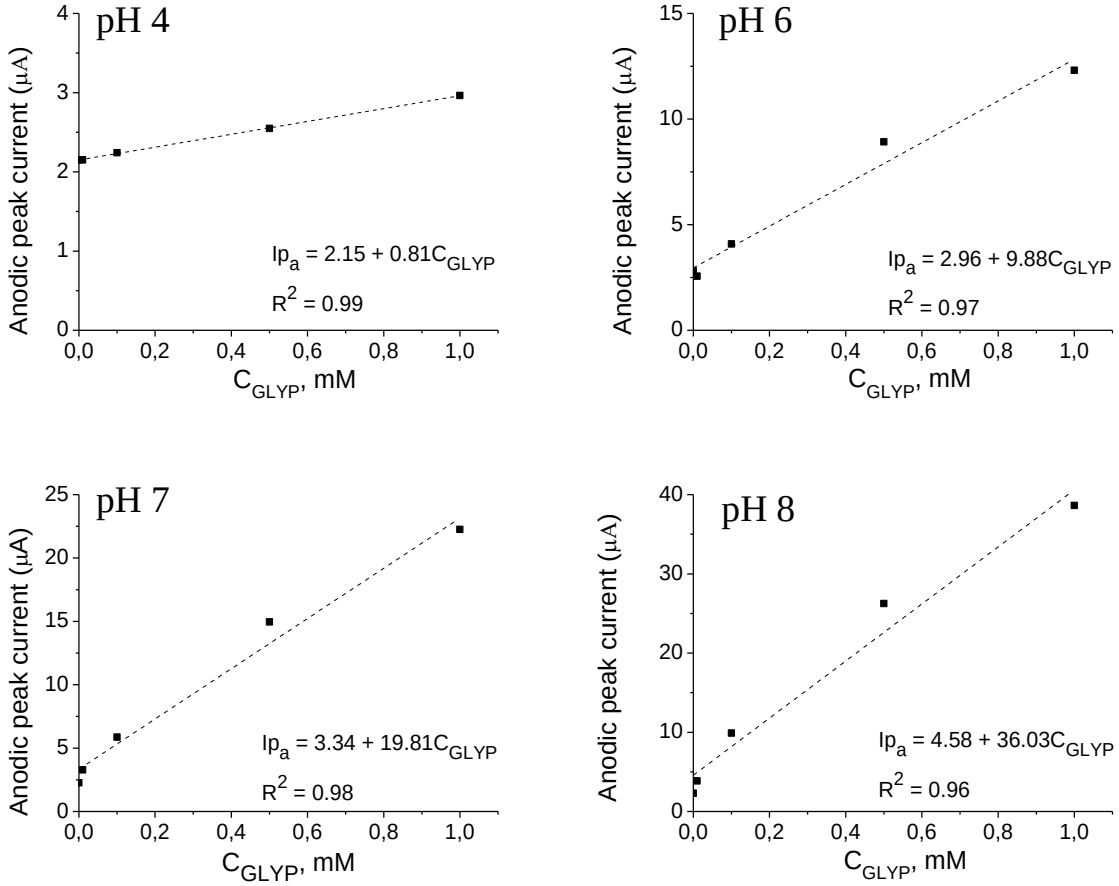

Figure II – The calibration curves for glyphosate detection by co-reactant system with 0.1 mM $Ru(bpy)_3^{2+}$ on ITO electrode at different pH
(scan 1, CVs recorded at 50 mV/s in 50 mM buffer solutions)

For all presented pH, the increase of the CV anodic signal was observed. The lower pH, the less intense electrochemical response is recorded. The value of the slope for pH 4 is the smallest (b = 0.81), whereas with increase of pH it increases sharply (to b = 36 for pH 8), what indicates that the sensitivity of glyphosate detection according to this parameter of calibration curve is the highest

LOD_{GLYP} varies from 0.02 to 0.14 in the range of pH 4 to 8. At pH 4 the value of LOD_{GLYP} is much smaller and is equal to 0.02 mM. It is caused by a smaller standard deviation of the intercept σ, provided by more linear current-concentration dependence.

Table IIIVI – Calculations for the limit of detection of GLYP (LOD_{GLYP}) from calibration curves at different pH

	pH 4	**pH 6**	**pH 7**	**pH 8**
σ, mM	0.005	0.428	0.613	1.737
b (slope)	0.811	9.876	20.526	36.026
R^2	0.99	0.98	0.99	0.97
$LOD_{GLYP,}$ mM	**0.02**	**0.13**	**0.09**	**0.14**

Note, that presented values of LOD_{GLYP} give only an idea about the sensitivity of the electrochemical detection of herbicide on ITO. Plotting the proper calibration curves require more precision.

Appendix 5: NMR characterisation

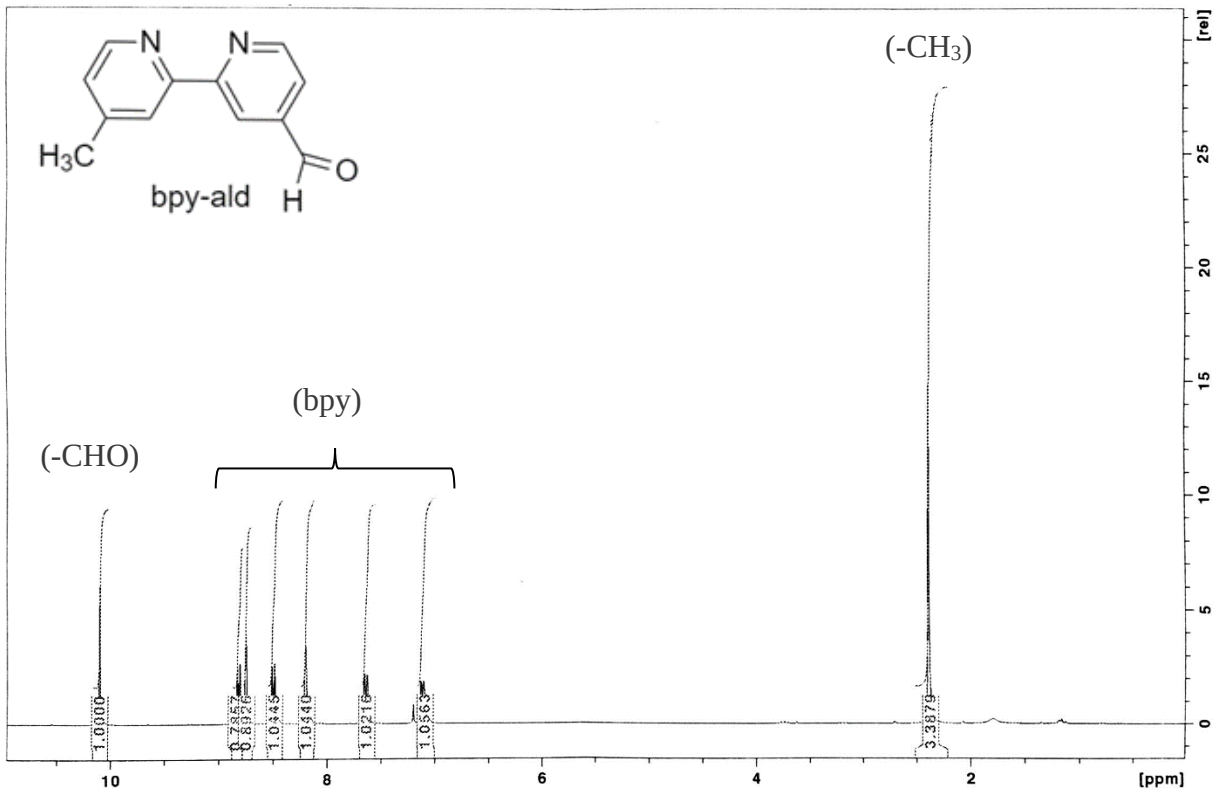

Figure III – 1H NMR spectrum of 4-(carboxyaldehyde)-4'-methyl-2,2'-bipyridine (bpy-ald) recorded in $CDCl_3$; Inset – bpy-ald structural formula

1H NMR (400 MHz, $CDCl_3$) δ : 10.23 (s, 1H), 8.95 (d, J=4.9 Hz, 1H), 8.62 (d, J=4.9 Hz, 1H), 8.32 (s, 1H), 7.74-7.78 (m, 1H), 7.23 (d, J=5.0 Hz, 1H), 2.48 (s, 3H).

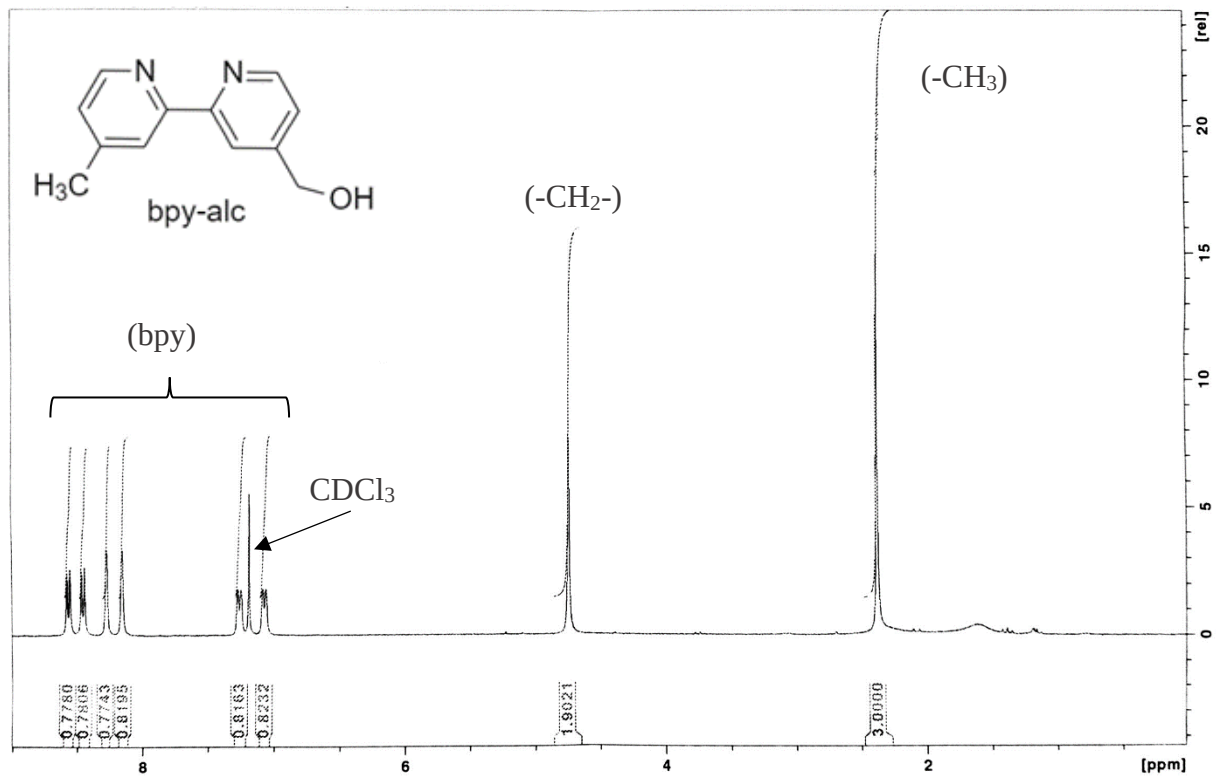

Figure IV– 1H NMR spectrum of 4-(hydroxymethyl)-4’-methyl-2,2’-bipyridine (bpy-alc) recorded in $CDCl_3$; Inset – bpy-alc structural formula

1H NMR (400 MHz, $CDCl_3$) δ : 8.72 (d, J=5.0 Hz, 1H), 8.59 (d, J=4.9 Hz, 1H), 8.40-8.42 (m, 1H), 8.30-8.35 (m, 1H), 7.41-7.48 (m, 1H), 7.18-7.25 (m, 1H), 5.03 (s, 2H), 2.49 (s, 3H).

Bibliography

[1] A. Walcarius, E. Sibottier, M. Etienne, J. Ghanbaja, Electrochemically assisted self-assembly of mesoporous silica thin films, Nat. Mater. 6 (2007) 602–608. https://doi.org/10.1038/nmat1951.

[2] A. Goux, M. Etienne, E. Aubert, C. Lecomte, J. Ghanbaja, A. Walcarius, Oriented mesoporous silica films obtained by Electro-Assisted Self-Assembly (EASA), Chem. Mater. 21 (2009) 731–741. https://doi.org/10.1021/cm8029664.

[3] M. Kobayashi, K. Susuki, T. Otani, S. Enomoto, H. Otsuji, Y. Kuroda, H. Wada, A. Shimojima, T. Homma, K. Kuroda, Thickness control of 3-dimensional mesoporous silica ultrathin films by wet-etching, Nanoscale. 9 (2017) 8321–8329. https://doi.org/10.1039/c7nr01560g.

[4] C.T. Kresge, M.E. Leoniwicz, W.J. Roth, J.C. Vartuli, J.S. Beck, Ordered mesoporous molecular sieves synthesized by a liquid-crystall template mechanism, Lett. To Nat. 359 (1992) 710–712.

[5] J.A.S. Costa, R.A. de Jesus, D.O. Santos, J.F. Mano, L.P.C. Romão, C.M. Paranhos, Recent progresses in the adsorption of organic, inorganic, and gas compounds by MCM-41-based mesoporous materials, Microporous Mesoporous Mater. 291 (2020) 109698. https://doi.org/10.1016/j.micromeso.2019.109698.

[6] A. Walcarius, Electrochemical applications of silica-based organic-inorganic hybrid materials, Chem. Mater. 13 (2001) 3351–3372. https://doi.org/10.1021/cm0110167.

[7] A. Walcarius, C. Despas, P. Trens, M.J. Hudson, J. Bessière, Voltammetric in situ investigation of an MCM-41-modified carbon paste electrode - a new sensor, J. Electroanal. Chem. 453 (1998) 249–252. https://doi.org/10.1016/S0022-0728(98)00203-4.

[8] A. Walcarius, Silica-based electrochemical sensors and biosensors: Recent trends, Curr. Opin. Electrochem. 10 (2018) 88–97. https://doi.org/10.1016/j.coelec.2018.03.017.

[9] O.W. Fl, F. Brunk, C.O.F. Gmbh, F. Republic, D.M. Chapman, G. Davison, W.R. Grace, U.S. Chap, S. Wolfgang, F. Republic, S. Wolfgang, F. Republic, S. Wolfgang, F. Republic, S.O. Bond, C. Structures, Ullmann's Encyclopedia of Industrial Chemistry, Wiley, 2000. https://doi.org/10.1002/14356007.

[10] M. Vallet-Regí, F. Balas, Silica Materials for Medical Applications, Open Biomed. Eng. J. 2 (2008) 1–9. https://doi.org/10.2174/1874120700802010001.

[11] R. Brady, B. Woonton, M.L. Gee, A.J. O'Connor, Hierarchical mesoporous silica materials for separation of functional food ingredients - A review, Innov. Food Sci. Emerg. Technol. 9 (2008) 243–248. https://doi.org/10.1016/j.ifset.2007.10.002.

[12] E.F. Vansant, P. Van Der Voort, K.C. Vrancken, eds., Modification with silicon compounds: Mechanistic studies, in: Charact. Chem. Modif. Silica Surf., 1995: pp. 193–297. https://doi.org/10.1016/S0167-2991(06)81517-X.

[13] K.K. Unger, Surface chemistry of porous silica, in: Porous Silica, 1st ed., 1979: pp. 57–146.

https://doi.org/10.1016/S0301-4770(08)60807-6.

[14] E.F. Vansant, P. Van Der Voort, K.C. Vrancken, eds., Chemical modification of silica: applications and procedures, in: Charact. Chem. Modif. Silica Surf., 1995: pp. 149–192. https://doi.org/10.1016/S0167-2991(06)81516-8.

[15] Y. Goto, N. Mizoshita, M. Waki, M. Ikai, Y. Maegawa, S. Inagaki, Synthesis and Applications of Periodic Mesoporous Organosilicas, in: Chem. Silica Zeolite-Based Mater., Elsevier Inc., 2019: pp. 1–25. https://doi.org/10.1016/b978-0-12-817813-3.00001-8.

[16] S.A. Greenberg, THE CHEMISORPTION OF CALCIUM HYDROXIDE BY SILICA, J. Phys. Chem. 60 (1956) 325–330. https://doi.org/10.1021/j150537a019.

[17] M. Allingham, J.M. Cullen, C.H. Giles, S.K. Jain, J.S. Woods, Adsorption at Inorganic Surfaces. II.* Adsorption of Dyes and Related Compounds By Silica, J. Appl. Chem. 8 (1958) 108–116.

[18] Z.A. Alothman, A review: Fundamental aspects of silicate mesoporous materials, Materials (Basel). 5 (2012) 2874–2902. https://doi.org/10.3390/ma5122874.

[19] B.D. Zdravkov, J.J. Čermák, M. Šefara, J. Janků, Pore classification in the characterization of porous materials: A perspective, Cent. Eur. J. Chem. 5 (2007) 385–395. https://doi.org/10.2478/s11532-007-0017-9.

[20] L.L. Hench, J.K. West, The Sol-Gel Process, Chem. Rev. 90 (1990) 33–72. https://doi.org/10.1021/cr00099a003.

[21] A.M. Buckley, M. Greenblatt, The sol-gel preparation of silica gels, J. Chem. Educ. 71 (1994) 599–602. https://doi.org/10.1021/ed071p599.

[22] E.J.A. Pope, J.D. Mackenzie, SOL-GEL PROCESSING OF SILICA. II. The role of the catalyst, J. Non. Cryst. Solids. 87 (1986) 185–198. https://doi.org/10.1016/S0022-3093(86)80078-3.

[23] C.J. Brinker, HYDROLYSIS AND CONDENSATION OF SILICATES: EFFECTS ON STRUCTURE, J. Non. Cryst. Solids. 100 (1988) 31–50. https://doi.org/10.1016/0022-3093(88)90005-1.

[24] Y. Xi, Z. Liangying, W. Sasa, Pore size and pore-size distribution control of porous silica, Sensors Actuators B. 24–25 (1995) 347–352. https://doi.org/10.1016/0925-4005(95)85078-3.

[25] K. Egeblad, C.H. Christensen, M. Kustova, C.H. Christensen, Templating Mesoporous Zeolites, Chem. Mater. 20 (2008) 946–960. https://doi.org/10.1021/cm702224p.

[26] J.S. Beck, J.C. Vartuli, W.J. Roth, M.E. Leonowicz, C.T. Kresge, K.D. Schmitt, C.T.W. Chu, D.H. Olson, E.W. Sheppard, S.B. McCullen, J.B. Higgins, J.L. Schlenker, A New Family of Mesoporous Molecular Sieves Prepared with Liquid Crystal Templates, J. Am. Chem. Soc. 114 (1992) 10834–10843. https://doi.org/10.1021/ja00053a020.

[27] B.M. Lok, T.R. Cannan, C.A. Messina, The role of organic molecules in molecular sieve synthesis, Zeolites. 3 (1983) 282–291. https://doi.org/10.1016/0144-2449(83)90169-0.

[28] D. Zhao, J. Feng, Q. Huo, N. Melosh, G.H. Fredrickson, B.F. Chmelka, G.D. Stucky, Triblock Copolymer Syntheses of Mesoporous Silica with Periodic 50 to 300 Angstrom Pores, Science (80-.). 279 (1998) 548–552. https://doi.org/10.1126/science.279.5350.548.

[29] L.A. Murray, N. Goldsmith, Nondestructive Determination of Thickness and Perfection of Silica Films, J. Electrochem. Soc. 113 (1966) 1297–1300. https://doi.org/10.1149/1.2423809.

[30] C.J. Brinker, Y. Lu, A. Sellinger, H. Fan, Evaporation-Induced Self-Assembly: Nanostructures Made Easy, Adv. Mater. 11 (1999) 579–585. https://doi.org/10.1002/(SICI)1521-4095(199905)11:7<579::AID-ADMA579>3.0.CO;2-R.

[31] F. Hoffmann, M. Cornelius, J. Morell, M. Fröba, Silica-Based Mesoporous Organic-Inorganic Hybrid Materials, Angew. Chemie - Int. Ed. 45 (2006) 3216–3251. https://doi.org/10.1002/anie.200503075.

[32] G.S. Attard, J.C. Glyde, C.G. Göltner, Liquid-crystalline phases as templates for the synthesis of mesoporous silica, Nature. 378 (1995) 366–368. https://doi.org/10.1038/378366a0.

[33] A. Monnier, F. Schüth, Q. Huo, D. Kumar, D. Margolese, R.S. Maxwell, G.D. Stucky, M. Krishnamurty, P. Petroff, A. Firouzi, M. Janicke, B.F. Chmelka, Cooperative Formation of Inorganic-Organic Interfaces in the Synthesis of Silicate Mesostructures, Science (80-.). 261 (1993) 1299–1303. https://doi.org/10.1126/science.261.5126.1299.

[34] S.S. Park, C.H. Lee, J.H. Cheon, S.J. Choe, D.H. Park, Morphological Control of Periodic Mesoporous Organosilica with Agitation, Bull. Korean Chem. Soc. 22 (2001) 948–952.

[35] C.H. Lee, S. Soo Park, S. Joon Choe, D.H. Park, Synthesis of periodic mesoporous organosilica with remarkable morphologies, Microporous Mesoporous Mater. 46 (2001) 257–264. https://doi.org/10.1016/S1387-1811(01)00305-5.

[36] S.S. Park, C.H. Lee, J.H. Cheon, D.H. Park, Formation mechanism of PMO with rope- and gyroid-based morphologies via close packing of secondary building units, J. Mater. Chem. 11 (2001) 3397–3403. https://doi.org/10.1039/b105062c.

[37] S. Sohrabnezhad, A. Jafarzadeh, A. Pourahmad, Synthesis and characterization of MCM-41 ropes, Mater. Lett. 212 (2018) 16–19. https://doi.org/10.1016/j.matlet.2017.10.059.

[38] M. Grün, I. Lauer, K.K. Unger, The Synthesis of Micrometer- and Submicrometer-Size Spheres of Ordered Mesoporous Oxide MCM-41, Adv. Mater. 9 (1997) 254–257. https://doi.org/10.1002/adma.19970090317.

[39] M. Grün, K.K. Unger, A. Matsumoto, K. Tsutsumi, Novel pathways for the preparation of mesoporous MCM-41 materials: control of porosity and morphology, Microporous Mesoporous Mater. 27 (1999) 207–216. https://doi.org/10.1016/S1387-1811(98)00255-8.

[40] Á. Szegedi, Z. Kónya, D. Méhn, E. Solymár, G. Pál-Borbély, Z.E. Horváth, L.P. Biró, I. Kiricsi, Spherical mesoporous MCM-41 materials containing transition metals: Synthesis and characterization, Appl. Catal. A Gen. 272 (2004) 257–266. https://doi.org/10.1016/j.apcata.2004.05.057.

[41] L. Nicole, C. Boissière, D. Grosso, A. Quach, C. Sanchez, Mesostructured hybrid organic-inorganic thin films, J. Mater. Chem. 15 (2005) 3598–3627. https://doi.org/10.1039/b506072a.

[42] P. Innocenzi, L. Malfatti, Mesoporous thin films: Properties and applications, Chem. Soc. Rev. 42 (2013) 4198–4216. https://doi.org/10.1039/c3cs35377j.

[43] M. Ogawa, Formation of Novel Oriented Transparent Films of Layered Silica-Surfactant Nanocomposites, J. Am. Chem. Soc. 116 (1994) 7941–7942. https://doi.org/10.1021/ja00096a079.

[44] I.A. Aksay, M. Trau, S. Manne, I. Honma, N. Yao, L. Zhou, P. Fenter, P.M. Eisenberger, S.M. Gruner, Biomimetic Pathways for Assembling Inorganic Thin Films, Science (80-.). 273 (1996) 892–898. https://doi.org/10.1126/science.273.5277.892.

[45] M. Ogawa, A simple sol-gel route for the preparation of silica-surfactant mesostructured materials, Chem. Commun. (1996) 1149–1150. https://doi.org/10.1039/CC9960001149.

[46] H. Yang, A. Kuperman, N. Coombs, S. Mamiche-Afara, G.A. Ozin, Synthesis of oriented films of mesoporous silica on mica, Nature. 379 (1996) 703–705. https://doi.org/10.1038/379703a0.

[47] C.J. Brinker, G.C. Frye, A.J. Hurd, C.S. Ashley, Fundamentals of sol-gel dip coating, Thin Solid Films. 201 (1991) 97–108. https://doi.org/10.1016/0040-6090(91)90158-T.

[48] D. Grosso, F. Cagnol, G.J.D.A.A. Soler-Illia, E.L. Crepaldi, H. Amenitsch, A. Brunet-Bruneau, A. Bourgeois, C. Sanchez, Fundamentals of Mesostructuring Through Evaporation-Induced Self-Assembly, Adv. Funct. Mater. 14 (2004) 309–322. https://doi.org/10.1002/adfm.200305036.

[49] F. Cagnol, D. Grosso, G.J.D.A.A. Soler-Illia, E.L. Crepaldi, F. Babonneau, H. Amenitsch, C. Sanchez, Humidity-controlled mesostructuration in CTAB-templated silica thin film processing. The existence of a modulable steady state, J. Mater. Chem. 13 (2003) 61–66. https://doi.org/10.1039/b209640b.

[50] F. Cagnol, D. Grosso, C. Sanchez, A general one-pot process leading to highly functionalised ordered mesoporous silica films, Chem. Commun. 4 (2004) 1742–1743. https://doi.org/10.1039/b403753g.

[51] P. Innocenzi, P. Falcaro, D. Grosso, F. Babonneau, Order-Disorder Transitions and Evolution of Silica Structure in Self-Assembled Mesostructured Silica Films Studied Through FTIR Spectroscopy, J. Phys. Chem. B. 107 (2003) 4711–4717. https://doi.org/10.1021/jp026609z.

[52] D. Zhao, P. Yang, N. Melosh, J. Feng, B.F. Chmelka, G.D. Stucky, Continuous Mesoporous Silica Films with Highly Ordered Large Pore Structures, Adv. Mater. 10 (1998) 1380–1385. https://doi.org/10.1002/(SICI)1521-4095(199811)10:16<1380::AID-ADMA1380>3.0.CO;2-8.

[53] Y. Lu, R. Ganguli, C.A. Drewien, M.T. Anderson, C. Jeffrey Brinker, W. Gong, Y. Guo, H. Soyez, B. Dunn, M.H. Huang, J.I. Zink, Continuous formation of supported cubic and hexagonal mesoporous films by sol-gel dip-coating, Nature. 389 (1997) 364–368.

https://doi.org/10.1038/38699.

[54] D. Grosso, A.R. Balkenende, P.A. Albouy, M. Lavergne, L. Mazerolles, F. Babonneau, Highly oriented 3D-hexagonal silica thin films produced with cetyltrimethylammonium bromide, J. Mater. Chem. 10 (2000) 2085–2089. https://doi.org/10.1039/b003178j.

[55] S. Besson, T. Gacoin, C. Jacquiod, C. Ricolleau, D. Babonneau, J.P. Boilot, Structural study of 3D-hexagonal mesoporous spin-coated sol-gel films, J. Mater. Chem. 10 (2000) 1331–1336. https://doi.org/10.1039/a908845h.

[56] S. Besson, C. Ricolleau, T. Gacoin, C. Jacquiod, J.P. Boilot, A New 3D Organization of Mesopores in Oriented CTAB Silica Films, J. Phys. Chem. B. 104 (2000) 12095–12097. https://doi.org/10.1021/jp0026538.

[57] Y. Lu, H. Fan, A. Stump, T.L. Ward, T. Rieker, C.J. Brinker, Aerosol-assisted self-assembly of mesostructured spherical nanoparticles, Nature. 398 (1999) 223–226. https://doi.org/10.1038/18410.

[58] H. Fan, Y. Lu, A. Stump, S.T. Reed, T. Baer, R. Schunk, V. Perez-Luna, G.P. López, C.J. Brinker, Rapid prototyping of patterned functional nanostructures, Lett. To Nat. 405 (2000) 56–60. https://doi.org/10.1038/35011026.

[59] A. Walcarius, A. Kuhn, Ordered porous thin films in electrochemical analysis, Trends Anal. Chem. 27 (2008) 593–603. https://doi.org/10.1016/j.trac.2008.03.011.

[60] C. Song, G. Villemure, Electrode modification with spin-coated films of mesoporous molecular sieve silicas, Microporous Mesoporous Mater. 44–45 (2001) 679–689. https://doi.org/10.1016/S1387-1811(01)00249-9.

[61] J. Janata, PRINCIPLES OF CHEMICAL SENSORS, 2nd ed., Springer, 2009. https://doi.org/10.1007/978-0-387-69931-8.

[62] A.J. Bard, L.R. Faulkner, ELECTROCHEMICAL METHODS. Fundamentals and Applications, 2nd ed., 2000.

[63] E. Herrero, A. Fernández-Vega, J.M. Feliu, A. Aldaz, Poison formation reaction from formic acid and methanol on Pt(111) electrodes modified by irreversibly adsorbed Bi and As, J. Electroanal. Chem. 350 (1993) 73–88. https://doi.org/10.1016/0022-0728(93)80197-P.

[64] M.J. Llorca, E. Herrero, J.M. Feliu, A. Aldaz, Formic acid oxidation on Pt(111) electrodes modified by irreversibly adsorbed selenium, J. Electroanal. Chem. 373 (1994) 217–225. https://doi.org/10.1016/0022-0728(94)03326-9.

[65] G. Liu, T. Böcking, J.J. Gooding, Diazonium salts: Stable monolayers on gold electrodes for sensing applications, J. Electroanal. Chem. 600 (2007) 335–344. https://doi.org/10.1016/j.jelechem.2006.09.012.

[66] E. Katz, D.D. Schlereth, H.L. Schmidt, Electrochemical study of pyrroloquinoline quinone covalently immobilized as a monolayer onto a cystamine-modified gold electrode, J. Electroanal. Chem. 367 (1994) 59–70. https://doi.org/10.1016/0022-0728(93)03010-M.

[67] A.J. Downard, Electrochemically assisted covalent modification of carbon electrodes, Electroanalysis. 12 (2000) 1085–1096. https://doi.org/10.1002/1521-4109(200010)12:14<1085::AID-ELAN1085>3.0.CO;2-A.

[68] J. Liu, L. Cheng, B. Liu, S. Dong, Covalent modification of a glassy carbon surface by 4-aminobenzoic acid and its application in fabrication of a polyoxometalates-consisting monolayer and multilayer films, Langmuir. 16 (2000) 7471–7476. https://doi.org/10.1021/la9913506.

[69] T. Moriizumi, Langmuir-Blodgett films as chemical sensors, Thin Solid Films. 160 (1988) 413–429. https://doi.org/10.1016/0040-6090(88)90088-0.

[70] M. Majda, R. Bilewicz, Monomolecular Langmuir-Blodgett Films at Electrodes. Formation of Passivating Monolayers and Incorporation of Electroactive Reagents, Langmuir. 7 (1991) 2794–2802. https://doi.org/10.1021/la00059a063.

[71] M. Fujihira, K. Nishiyama, H. Yamada, Photoelectrochemical responses of optically transparent electrodes modified with Langmuir-Blodgett films consisting of surfactant derivatives of electron donor, acceptor and sensitizer molecules, Thin Solid Films. 132 (1985) 77–82. https://doi.org/10.1016/0040-6090(85)90459-6.

[72] A. Merz, A.J. Bard, A stable surface modified platinum electrode prepared by coating with electroactive polymer, J. Am. Chem. Soc. 100 (1978) 3222–3223. https://doi.org/10.1021/ja00478a049.

[73] H.S. White, J. Leddy, A.J. Bard, Polymer films on electrodes. 8. Investigation of charge-transport mechanisms in Nafion polymer modified electrodes, J. Am. Chem. Soc. 104 (1982) 4811–4817. https://doi.org/10.1021/ja00382a013.

[74] X. Cui, V.A. Lee, Y. Raphael, J.A. Wiler, J.F. Hetke, D.J. Anderson, D.C. Martin, Surface modification of neural recording electrodes with conducting polymer/biomolecule blends, J. Biomed. Mater. Res. 56 (2001) 261–272. https://doi.org/10.1002/1097-4636(200108)56:2<261::AID-JBM1094>3.0.CO;2-I.

[75] R.M. Iannlello, A.M. Yacynych, Immobilized Enzyme Chemically Modified Electrode as an Amperometric Sensor, Anal. Chem. 53 (1981) 2090–2095. https://doi.org/10.1021/ac00236a033.

[76] E. Albert, N. Cotolan, N. Nagy, G. Sáfrán, G. Szabó, L.M. Mureşan, Z. Hórvölgyi, Mesoporous silica coatings with improved corrosion protection properties, Microporous Mesoporous Mater. 206 (2015) 102–113. https://doi.org/10.1016/j.micromeso.2014.12.021.

[77] A. Walcarius, M. Etienne, B. Lebeau, Rate of access to the binding sites in organically modified silicates. 2. Ordered mesoporous silicas grafted with amine or thiol groups, Chem. Mater. 15 (2003) 2161–2173. https://doi.org/10.1021/cm021310e.

[78] A. Palaniappan, X. Su, F.E.H. Tay, Functionalized mesoporous silica films for gas sensing applications, J. Electroceramics. 16 (2006) 503–505. https://doi.org/10.1007/s10832-006-9906-0.

[79] J.M. Bertolo, A. Bearzotti, A. Generosi, L. Palummo, V.R. Albertini, X-rays and electrical

characterizations of ordered mesostructurated silica thin films used as sensing membranes, Sensors Actuators, B. 111–112 (2005) 145–149. https://doi.org/10.1016/j.snb.2005.07.001.

[80] P. Innocenzi, A. Martucci, M. Guglielmi, A. Bearzotti, E. Traversa, J.C. Pivin, Mesoporous silica thin films for alcohol sensors, J. Eur. Ceram. Soc. 21 (2001) 1985–1988. https://doi.org/10.1016/S0955-2219(01)00156-X.

[81] A. Sanchez, A. Walcarius, Surfactant-templated sol-gel silica thin films bearing 5-mercapto-1-methyl-tetrazole on carbon electrode for Hg(II) detection, Electrochim. Acta. 55 (2010) 4201–4207. https://doi.org/10.1016/j.electacta.2010.02.016.

[82] I. Cesarino, É.T.G. Cavalheiro, Thiol-functionalized silica thin film modified electrode in determination of mercury ions in natural water, Electroanalysis. 20 (2008) 2301–2309. https://doi.org/10.1002/elan.200804325.

[83] R. Makote, M.M. Collinson, Template Recognition in Inorganic-Organic Hybrid Films Prepared by the Sol-Gel Process, Chem. Mater. 10 (1998) 2440–2445. https://doi.org/10.1021/cm9801136.

[84] X. Zhang, J. Wang, W. Wu, S. Qian, Y. Man, Immobilization and electrochemistry of cytochrome c on amino-functionalized mesoporous silica thin films, Electrochem. Commun. 9 (2007) 2098–2104. https://doi.org/10.1016/j.elecom.2007.05.025.

[85] L. Zhang, Q. Zhang, J. Li, Direct electrochemistry and electrocatalysis of hemoglobin immobilized in bimodal mesoporous silica and chitosan inorganic-organic hybrid film, Electrochem. Commun. 9 (2007) 1530–1535. https://doi.org/10.1016/j.elecom.2007.02.015.

[86] O.Y. Nadzhafova, V.N. Zaitsev, M. V. Drozdova, A. Vaze, J.F. Rusling, Heme proteins sequestered in silica sol-gels using surfactants feature direct electron transfer and peroxidase activity, Electrochem. Commun. 6 (2004) 205–209. https://doi.org/10.1016/j.elecom.2003.11.013.

[87] J.J. Yu, S. Lu, J.W. Li, F.Q. Zhao, B.Z. Zeng, Characterization of gold nanoparticles electrochemically deposited on amine-functioned mesoporous silica films and electrocatalytic oxidation of glucose, J. Solid State Electrochem. 11 (2007) 1211–1219. https://doi.org/10.1007/s10008-007-0272-x.

[88] G.B. Alexander, W.M. Heston, R.K. Iler, The solubility of amorphous silica in water, J. Phys. Chem. 58 (1954) 453–455. https://doi.org/10.1021/j150516a002.

[89] M. Etienne, A. Quach, D. Grosso, L. Nicole, C. Sanchez, A. Walcarius, Molecular transport into mesostructured silica thin films: Electrochemical monitoring and comparison between p6m, P63/mmc, and Pm3n structures, Chem. Mater. 19 (2007) 844–856. https://doi.org/10.1021/cm0625068.

[90] A. Wang, T. Kabe, Fine-tuning of pore size of MCM-41 by adjusting the initial pH of the synthesis mixture, Chem. Commun. (1999) 2067–2068. https://doi.org/10.1039/a906275k.

[91] S.K. Jana, A. Mochizuki, S. Namba, Progress in pore-size control of mesoporous MCM-41 molecular sieve using surfactant having different alkyl chain lengths and various organic auxiliary chemicals, Catal. Surv. from Asia. 8 (2004) 1–13.

https://doi.org/10.1023/B:CATS.0000015110.85694.d9.

[92] T.C. Wei, H.W. Hillhouse, Mass transport and electrode accessibility through periodic self-assembled nanoporous silica thin films, Langmuir. 23 (2007) 5689–5699. https://doi.org/10.1021/la062699d.

[93] Y. Yamauchi, M. Sawada, T. Noma, H. Ito, S. Furumi, Y. Sakka, K. Kuroda, Orientation of mesochannels in continuous mesoporous silica films by a high magnetic field, J. Mater. Chem. 15 (2005) 1137–1140. https://doi.org/10.1039/b418478e.

[94] Y. Yamauchi, M. Sawada, M. Komatsu, A. Sugiyama, T. Osaka, N. Hirota, Y. Sakka, K. Kuroda, Magnetically induced orientation of mesochannels in mesoporous silica films at 30 Tesla, Chem. - An Asian J. 2 (2007) 1505–1512. https://doi.org/10.1002/asia.200700244.

[95] S. Nagarajan, M. Li, R.A. Pai, J.K. Bosworth, P. Busch, D.M. Smilgies, C.K. Ober, T.P. Russell, J.J. Watkins, An efficient route to mesoporous silica films with perpendicular nanochannels, Adv. Mater. 20 (2008) 246–251. https://doi.org/10.1002/adma.200701766.

[96] K.S. Choi, E.W. McFarland, G.D. Stucky, Electrocatalytic properties of thin mesoporous platinum films synthesized utilizing potential-controlled surfactant assembly, Adv. Mater. 15 (2003) 2018–2021. https://doi.org/10.1002/adma.200304557.

[97] Z. Teng, G. Zheng, Y. Dou, W. Li, C.Y. Mou, X. Zhang, A.M. Asiri, D. Zhao, Highly ordered mesoporous silica films with perpendicular mesochannels by a simple Stöber-solution growth approach, Angew. Chemie - Int. Ed. 51 (2012) 2173–2177. https://doi.org/10.1002/anie.201108748.

[98] K.C. Kao, C.H. Lin, T.Y. Chen, Y.H. Liu, C.Y. Mou, A General Method for Growing Large Area Mesoporous Silica Thin Films on Flat Substrates with Perpendicular Nanochannels, J. Am. Chem. Soc. 137 (2015) 3779–3782. https://doi.org/10.1021/jacs.5b01180.

[99] Y. Liu, D. Shen, G. Chen, A.A. Elzatahry, M. Pal, H. Zhu, L. Wu, J. Lin, D. Al-Dahyan, W. Li, D. Zhao, Mesoporous Silica Thin Membranes with Large Vertical Mesochannels for Nanosize-Based Separation, Adv. Mater. 29 (2017) 1–8. https://doi.org/10.1002/adma.201702274.

[100] A. Walcarius, Mesoporous Materials-Based Electrochemical Sensors, Electroanalysis. 27 (2015) 1303–1340. https://doi.org/10.1002/elan.201400628.

[101] F. Yan, X. Lin, B. Su, Vertically ordered silica mesochannel films: Electrochemistry and analytical applications, Analyst. 141 (2016) 3482–3495. https://doi.org/10.1039/c6an00146g.

[102] M. Etienne, A. Goux, E. Sibottier, A. Walcarius, Oriented Mesoporous Organosilica Films on Electrode: A New Class of Nanomaterials for Sensing, J. Nanosci. Nanotechnol. 9 (2009) 2398–2406. https://doi.org/10.1166/jnn.2009.SE39.

[103] M. Rafiee, B. Karimi, S. Arshi, H. Vali, Ethylenediamine-modified oriented MCM-41 at the electrode surface, cobalt adsorption ability and electrochemical performance, Dalt. Trans. 43 (2014) 4901–4908. https://doi.org/10.1039/c3dt52343h.

[104] Y. Guillemin, M. Etienne, E. Aubert, A. Walcarius, Electrogeneration of highly methylated

mesoporous silica thin films with vertically-aligned mesochannels and electrochemical monitoring of mass transport issues, J. Mater. Chem. 20 (2010) 6799–6807. https://doi.org/10.1039/c0jm00305k.

[105] C. Despas, N.A. Vodolazkaya, J. Ghanbaja, A. Walcarius, Preparation of ordered and oriented mesoporous silica thin films bearing octyl or hexadecyl groups by electrochemically assisted self-assembly and evaluation of their transport properties, J. Solid State Electrochem. 19 (2015) 2075–2085. https://doi.org/10.1007/s10008-014-2726-2.

[106] G. Herzog, N.A. Vodolazkaya, A. Walcarius, Platinum ultramicroelectrodes modified with electrogenerated surfactant-templated mesoporous organosilica films: Effect of film formation conditions on its performance in preconcentration electroanalysis, Electroanalysis. 25 (2013) 2595–2603. https://doi.org/10.1002/elan.201300415.

[107] N. Vilà, J. Ghanbaja, E. Aubert, A. Walcarius, Electrochemically assisted generation of highly ordered azide-functionalized mesoporous silica for oriented hybrid films, Angew. Chemie - Int. Ed. 53 (2014) 2945–2950. https://doi.org/10.1002/anie.201309447.

[108] N. Vilà, A. Walcarius, Electrochemical response of vertically-aligned, ferrocene-functionalized mesoporous silica films: Effect of the supporting electrolyte, Electrochim. Acta. 179 (2015) 304–314. https://doi.org/10.1016/j.electacta.2015.02.169.

[109] C. Karman, N. Vilà, C. Despas, A. Walcarius, Indirect amperometric detection of non-redox ions using a ferrocene-functionalized and oriented mesoporous silica thin film electrode, Electrochim. Acta. 228 (2017) 659–666. https://doi.org/10.1016/j.electacta.2017.01.126.

[110] N. Vilà, C. Allain, P. Audebert, A. Walcarius, Tetrazine-functionalized and vertically-aligned mesoporous silica films with electrochemical activity and fluorescence properties, Electrochem. Commun. 59 (2015) 9–12. https://doi.org/10.1016/j.elecom.2015.06.012.

[111] N. Vilà, J. Ghanbaja, A. Walcarius, Clickable Bifunctional and Vertically Aligned Mesoporous Silica Films, Adv. Mater. Interfaces. 3 (2016) 1500440. https://doi.org/10.1002/admi.201500440.

[112] W. Li, L. Ding, Q. Wang, B. Su, Differential pulse voltammetry detection of dopamine and ascorbic acid by permselective silica mesochannels vertically attached to the electrode surface, Analyst. 139 (2014) 3926–3931. https://doi.org/10.1039/c4an00605d.

[113] M. Rafiee, B. Karimi, S. Farrokhzadeh, H. Vali, Hydroquinone functionalized oriented MCM-41 mesochannels at the electrode surface, Electrochim. Acta. 94 (2013) 198–205. https://doi.org/10.1016/j.electacta.2013.01.147.

[114] P. Audebert, N. Vilà, C. Allain, F. Maisonneuve, A. Walcarius, P. Hapiot, Highly Organized Ferrocene-Functionalized Nanoporous Silica Films with an Extremely Fast Electron-Transfer Rate for an Intrinsically Nonconducting Oxide-Modified Electrode, ChemElectroChem. 2 (2015) 1695–1698. https://doi.org/10.1002/celc.201500227.

[115] Q. Sun, F. Yan, L. Yao, B. Su, Anti-Biofouling Isoporous Silica-Micelle Membrane Enabling Drug Detection in Human Whole Blood, Anal. Chem. 88 (2016) 8364–8368. https://doi.org/10.1021/acs.analchem.6b02091.

[116] F. Yan, Y. He, L. Ding, B. Su, Highly ordered binary assembly of silica mesochannels and surfactant micelles for extraction and electrochemical analysis of trace nitroaromatic explosives and pesticides, Anal. Chem. 87 (2015) 4436–4441. https://doi.org/10.1021/acs.analchem.5b00433.

[117] X. Huang, L. Xie, X. Lin, B. Su, Detection of Metoprolol in Human Biofluids and Pharmaceuticals via Ion-Transfer Voltammetry at the Nanoscopic Liquid/Liquid Interface Array, Anal. Chem. 89 (2017) 945–951. https://doi.org/10.1021/acs.analchem.6b04099.

[118] N. Vilà, E. André, R. Ciganda, J. Ruiz, D. Astruc, A. Walcarius, Molecular Sieving with Vertically Aligned Mesoporous Silica Films and Electronic Wiring through Isolating Nanochannels, Chem. Mater. 28 (2016) 2511–2514. https://doi.org/10.1021/acs.chemmater.6b00716.

[119] T. Nasir, G. Herzog, M. Hébrant, C. Despas, L. Liu, A. Walcarius, Mesoporous Silica Thin Films for Improved Electrochemical Detection of Paraquat, ACS Sensors. 3 (2018) 484–493. https://doi.org/10.1021/acssensors.7b00920.

[120] Z. Zhou, W. Guo, L. Xu, Q. Yang, B. Su, Two orders-of-magnitude enhancement in the electrochemiluminescence of Ru(bpy)32+ by vertically ordered silica mesochannels, Anal. Chim. Acta. 886 (2015) 48–55. https://doi.org/10.1016/j.aca.2015.06.005.

[121] L. Ding, W. Li, Q. Wang, Q. Sun, Y. He, B. Su, Vertically oriented silica mesochannels as the template for electrodeposition of polyaniline nanostructures and their electrocatalytic and electroanalytical applications, Chem. - A Eur. J. 20 (2014) 1829–1833. https://doi.org/10.1002/chem.201303807.

[122] M. Saadaoui, I. Fernández, G. Luna, P. Díez, S. Campuzano, N. Raouafi, A. Sánchez, J.M. Pingarrón, R. Villalonga, Label-free electrochemical genosensor based on mesoporous silica thin film, Anal. Bioanal. Chem. 408 (2016) 7321–7327. https://doi.org/10.1007/s00216-016-9608-7.

[123] S. Ahoulou, N. Vilà, S. Pillet, D. Schaniel, A. Walcarius, Non-covalent Immobilization of Iron-triazole (Fe(Htrz)3) Molecular Mediator in Mesoporous Silica Films for the Electrochemical Detection of Hydrogen Peroxide, Electroanalysis. 32 (2020) 690–697. https://doi.org/10.1002/elan.201900444.

[124] H. Maheshwari, N. Vilà, G. Herzog, A. Walcarius, Selective Detection of Cysteine at a Mesoporous Silica Film Electrode Functionalized with Ferrocene in the Presence of Glutathione, ChemElectroChem. 7 (2020) 2095–2101. https://doi.org/10.1002/celc.202000396.

[125] P. Zanello, Voltammetric Techniques, in: Inorg. Electrochem. Theory, Pract. Appl., 2003: pp. 49–136. https://doi.org/10.1039/9781847551146-00049.

[126] M. Baia, S. Astilean, T. Iliescu, Raman and SERS Investigations of Pharmaceuticals, Springer Berlin Heidelberg, Berlin, Heidelberg, 2008. https://doi.org/10.1007/978-3-540-78283-4.

[127] M.A. Mohamed, J. Jaafar, A.F. Ismail, M.H.D. Othman, M.A. Rahman, Fourier Transform Infrared (FTIR) Spectroscopy, in: Membr. Charact., Elsevier B.V., 2017: pp. 3–29.

https://doi.org/10.1016/B978-0-444-63776-5.00001-2.

[128] R. Kötz, Spectroscopic and Diffraction Techniques in Interfacial Electrochemistry, Springer Netherlands, Dordrecht, 1990. https://doi.org/10.1007/978-94-011-3782-9.

[129] D. Harvey, Modern Analytical Chemistry, 1st ed., McGraw-Hill, 2000.

[130] G. Renaud, R. Lazzari, F. Leroy, Probing surface and interface morphology with Grazing Incidence Small Angle X-Ray Scattering, Surf. Sci. Rep. 64 (2009) 255–380. https://doi.org/10.1016/j.surfrep.2009.07.002.

[131] I.M. Watt, The Principles and Practice of Electron Microscopy, 1997. https://doi.org/10.1017/cbo9781139170529.

[132] G.H. Michler, Electron Microscopy of Polymers, Springer Berlin Heidelberg, Berlin, Heidelberg, 2008. https://doi.org/10.1007/978-3-540-36352-1.

[133] J.M. Zuo, J.C.H. Spence, Advanced Transmission Electron Microscopy, Springer New York, New York, NY, 2017. https://doi.org/10.1007/978-1-4939-6607-3.

[134] Z.-L. Hua, J.-L. Shi, L. Wang, W.-H. Zhang, Preparation of mesoporous silica films on a glass slide: surfactant template removal by solvent extraction, J. Non. Cryst. Solids. 292 (2001) 177–183. https://doi.org/10.1016/S0022-3093(01)00806-7.

[135] V. V. Rostovtsev, L.G. Green, V. V. Fokin, K.B. Sharpless, A Stepwise Huisgen Cycloaddition Process: Copper(I)-Catalyzed Regioselective "Ligation" of Azides and Terminal Alkynes, Angew. Chemie - Int. Ed. 41 (2002) 2596–2599. https://doi.org/10.1002/1521-3773(20020715)41:14<2596::AID-ANIE2596>3.0.CO;2-4.

[136] C.W. Tornøe, C. Christensen, M. Meldal, Peptidotriazoles on solid phase: [1,2,3]-Triazoles by regiospecific copper(I)-catalyzed 1,3-dipolar cycloadditions of terminal alkynes to azides, J. Org. Chem. 67 (2002) 3057–3064. https://doi.org/10.1021/jo011148j.

[137] L. Liang, D. Astruc, The copper(I)-catalyzed alkyne-azide cycloaddition (CuAAC) "click" reaction and its applications. An overview, Coord. Chem. Rev. 255 (2011) 2933–2945. https://doi.org/10.1016/j.ccr.2011.06.028.

[138] F.A. Cotton, G. Wilkinson, ADVANCED INORGANIC CHEMISTRY. A Comprehensive Text, 4th ed., 1980.

[139] Y. Ayato, K. Yamagiwa, H. Shiroishi, J. Kuwano, Direct Electron Transfer and Electrocatalysis of Hemoglobin on ITO Nanoparticle Electrodes, ECS Trans. 50 (2013) 1–10. https://doi.org/10.1149/05017.0001ecst.

[140] F.W. Scheller, N. Bistolas, S. Liu, M. Jänchen, M. Katterle, U. Wollenberger, Thirty years of haemoglobin electrochemistry, Adv. Colloid Interface Sci. (2005). https://doi.org/10.1016/j.cis.2005.05.006.

[141] X. Han, W. Huang, J. Jia, S. Dong, E. Wang, Direct electrochemistry of hemoglobin in egg-phosphatidylcholine films and its catalysis to H2O2, Biosens. Bioelectron. 17 (2002) 741–746. https://doi.org/10.1016/S0956-5663(02)00052-0.

[142] Q. Wang, G. Lu, B. Yang, Hydrogen peroxide biosensor based on direct electrochemistry

of hemoglobin immobilized on carbon paste electrode by a silica sol–gel film, Sensors Actuators B. 99 (2004) 50–57. https://doi.org/10.1016/J.SNB.2003.10.008.

[143] A. Rimola, D. Costa, M. Sodupe, J.F. Lambert, P. Ugliengo, Silica surface features and their role in the adsorption of biomolecules: Computational modeling and experiments, Chem. Rev. 113 (2013) 4216–4313. https://doi.org/10.1021/cr3003054.

[144] O.O. Abegunde, E.T. Akinlabi, O.P. Oladijo, S. Akinlabi, A.U. Ude, Overview of thin film deposition techniques, AIMS Mater. Sci. 6 (2019) 174–199. https://doi.org/10.3934/MATERSCI.2019.2.174.

[145] W. KERN, V.S. BAN, Chemical Vapor Deposition of Inorganic Thin Films, in: Thin Film Process., ACADEMIC PRESS, INC., 1978: pp. 257–331. https://doi.org/10.1016/b978-0-12-728250-3.50012-x.

[146] C. Henrist, J. Dewalque, F. Mathis, R. Cloots, Control of the porosity of anatase thin films prepared by EISA: Influence of thickness and heat treatment, Microporous Mesoporous Mater. 117 (2009) 292–296. https://doi.org/10.1016/j.micromeso.2008.07.001.

[147] R. Dorey, Patterning: How to go from a coating to a shape, in: Ceram. Thick Film. MEMS Microdevices, 2012: pp. 113–143. https://doi.org/10.1016/b978-1-4377-7817-5.00005-5.

[148] P.A. Nayak, M. Saif Islam, V.J. Logeeswaran, Encyclopedia of Nanotechnology, in: Encycl. Nanotechnol., 2012: pp. 517–621. https://doi.org/10.1007/978-90-481-9751-4.

[149] N.-T. Nguyen, Fabrication technologies, in: Micromixers, 2012: pp. 113–161. https://doi.org/10.1016/b978-1-4377-3520-8.00004-8.

[150] J.X.J. Zhang, K. Hoshino, Fundamentals of nano/microfabrication and scale effect, in: Mol. Sensors Nanodevices, 2019: pp. 43–111. https://doi.org/10.1016/b978-0-12-814862-4.00002-8.

[151] T.L. Chu, Dielectric Materials in Semiconductor Devices, J. Vac. Sci. Technol. 6 (1969) 25–33. https://doi.org/10.1116/1.1492617.

[152] M. Miyamoto, N. Kita, S. Ishida, T. Tatsuno, Prevention of Microroughness Generation on the Silicon Wafer Surface in Buffered Hydrogen Fluoride by a Surfactant Addition, J. Electrochem. Soc. 141 (1994) 2899–2903. https://doi.org/10.1149/1.2059253.

[153] B. Garrido, J. Montserrat, J.R. Morante, The role of chemical species in the passivation of <100> silicon surfaces by HF in water-ethanol solutions, J. Electrochem. Soc. 143 (1996) 4059–4066. https://doi.org/10.1149/1.1837336.

[154] H. Kikuyama, N. Miki, K. Saka, J. Takano, I. Kawanabe, M. Miyashita, T. Ohmi, Surface Active Buffered Hydrogen Fluoride Having Excellent Wettability for ULSI Processing, IEEE Trans. Semicond. Manuf. 3 (1990) 99–108. https://doi.org/10.1109/66.56567.

[155] D.M. Knotter, The Chemistry of Wet Etching, in: Handb. Clean. Semicond. Manuf. Fundam. Appl., 2011: pp. 95–142. https://doi.org/10.1002/9781118071748.ch3.

[156] J. Bühler, F.P. Steiner, H. Baltes, Silicon dioxide sacrificial layer etching in surface micromachining, J. Micromechanics Microengineering. 7 (1997) R1–R13.

https://doi.org/10.1088/0960-1317/7/1/001.

[157] J. Loizillon, M. Putero, D. Grosso, Tuning Mesoporous Silica Film Accessibility through Controlled Dissolution in NH4F: Investigation of Structural Change by Ellipsometry Porosimetry and X-ray Reflectivity, J. Phys. Chem. C. (2019) 30398–30406. https://doi.org/10.1021/acs.jpcc.9b09109.

[158] K. Osseo-Asare, Etching Kinetics of Silicon Dioxide in Aqueous Fluoride Solutions: A Surface Complexation Model, J. Electrochem. Soc. 143 (1996) 1339–1347. https://doi.org/10.1149/1.1836640.

[159] D. Liang, D.W. Readey, Dissolution Kinetics of Crystalline and Amorphous Silica in Hydrofluoric-Hydrochloric Acid Mixtures, J. Am. Ceram. Soc. 70 (1987) 570–577. https://doi.org/10.1111/j.1151-2916.1987.tb05708.x.

[160] J.S. Judge, A Study of the Dissolution of SiO2 in Acidic Fluoride Solutions, J. Electrochem. Soc. 118 (1971) 1772–1775. https://doi.org/10.1149/1.2407835.

[161] G.A.C.M. Spierings, Wet chemical etching of silicate glasses in hydrofluoric acid based solutions, J. Mater. Sci. 28 (1993) 6261–6273. https://doi.org/10.1007/BF01352182.

[162] Y. Kunii, S. Nakayama, M. Maeda, Wet Etching of Doped and Nondoped Silicon Oxide Films Using Buffered Hydrogen Fluoride Solution, J. Electrochem. Soc. 142 (1995) 3510–3513. https://doi.org/10.1149/1.2050013.

[163] S. Verhaverbeke, I. Teerlinck, G. Stevens, R. Cartuyvels, M.M. Heyns, The Etching Mechanisms of SiO2 in Hydrofluoric Acid, J. Electrochem. Soc. 141 (1994) 2852. https://doi.org/10.1149/1.2059243.

[164] D.M. Knotter, Etching mechanism of vitreous silicon dioxide in HF-based solutions, J. Am. Chem. Soc. 122 (2000) 4345–4351. https://doi.org/10.1021/ja993803z.

[165] W.E. Kline, H.S. Fogler, Dissolution kinetics: Catalysis by strong acids, J. Colloid Interface Sci. 82 (1981) 93–102. https://doi.org/10.1016/0021-9797(81)90127-2.

[166] H. Proksche, G. Nagorsen, The Influence of NH4F on the Etch Rates of Undoped SiO2 in Buffered Oxide Etch, J. Electrochem. Soc. 139 (1992) 521–524. https://doi.org/10.1149/1.2069249.

[167] C. Orfescu, C. Pavelescu, M. Badila, An etch rate study on thermally annealed SiO2 films deposited in a TEOS-LPCVD system, J. Mater. Sci. 25 (1990) 1366–1368. https://doi.org/10.1007/BF00585451.

[168] W.L. Warren, P.M. Lenahan, C.J. Brinker, C.S. Ashley, S.T. Reed, G.R. Shaffer, Sol-gel silicate thin-film electronic properties, J. Appl. Phys. 69 (1991) 4404–4408. https://doi.org/10.1063/1.348366.

[169] S. Rojas, L. Zanotti, A. Borghesi, A. Sassella, G.U. Pignatel, Characterization of silicon dioxide and phosphosilicate glass deposited films, J. Vac. Sci. Technol. B Microelectron. Nanom. Struct. 11 (1993) 2081–2089. https://doi.org/10.1116/1.586546.

[170] D.J. Monk, D.S. Soane, R.T. Howe, A review of the chemical reaction mechanism and

kinetics for hydrofluoric acid etching of silicon dioxide for surface micromachining applications, Thin Solid Films. 232 (1993) 1–12. https://doi.org/10.1016/0040-6090(93)90752-B.

[171] W. KERN, C.A. DECKERT, Chemical Etching, in: Thin Film Process., ACADEMIC PRESS, INC., 1978: pp. 401–496. https://doi.org/10.1016/b978-0-12-728250-3.50015-5.

[172] T.W. O'Keeffe, R.M. Handy, Fabrication of planar silicon transistors without photoresist, Solid State Electron. 11 (1968) 261–266. https://doi.org/10.1016/0038-1101(68)90087-7.

[173] P. Allongue, V. Kieling, H. Gerischer, Etching mechanism and atomic structure of H-Si(111) surfaces prepared in NH4F, Electrochim. Acta. 40 (1995) 1353–1360. https://doi.org/10.1016/0013-4686(95)00071-L.

[174] P. Dumas, Y.J. Chabal, Electron-energy-loss characterization of the H-terminated Si(111) and Si(100) surfaces obtained by etching in NH4F, Chem. Phys. Lett. 181 (1991) 537–543. https://doi.org/10.1016/0009-2614(91)80309-L.

[175] H. Kikyuama, N. Miki, K. Saka, J. Takano, I. Kawanabe, M. Miyashita, T. Ohmi, Principles of Wet Chemical Processing in ULSI Microfabrication, IEEE Trans. Semicond. Manuf. 4 (1991) 26–35. https://doi.org/10.1109/66.75861.

[176] K.R. Williams, R.S. Muller, Etch rates for micromachining processing, J. Microelectromechanical Syst. 5 (1996) 256–269. https://doi.org/10.1109/84.546406.

[177] K. Ijichi, A. Fukuoka, A. Shimojima, M. Sugiyama, T. Okubo, A combined top-down and bottom-up approach to fabricate silica films with bimodal porosity, Mater. Lett. 65 (2011) 828–831. https://doi.org/10.1016/j.matlet.2010.11.064.

[178] M. Matheron, A. Bourgeois, A. Brunet-Bruneau, P.A. Albouy, J. Biteau, T. Gacoin, J.P. Boilot, Highly ordered CTAB-templated organosilicate films, J. Mater. Chem. 15 (2005) 4741–4745. https://doi.org/10.1039/b510554d.

[179] Y. Guillemin, M. Etienne, E. Sibottier, A. Walcarius, Microscale controlled electrogeneration of patterned mesoporous silica thin films, Chem. Mater. 23 (2011) 5313–5322. https://doi.org/10.1021/cm202668t.

[180] G. Giordano, N. Vilà, E. Aubert, J. Ghanbaja, A. Walcarius, Multi-layered, vertically-aligned and functionalized mesoporous silica films generated by sequential electrochemically assisted self-assembly, Electrochim. Acta. 237 (2017) 227–236. https://doi.org/10.1016/j.electacta.2017.03.220.

[181] T. Nasir, N.A. Vodolazkaya, G. Herzog, A. Walcarius, Critical Effect of Film Thickness on Preconcentration Electroanalysis with Oriented Mesoporous Silica Modified Electrodes, Electroanalysis. (2018) 202–207. https://doi.org/10.1002/elan.201800533.

[182] M.J. Owen, P.R. Dvornic, ADVANCES IN SILICON SCIENCE, Volume 4, 2012. https://doi.org/10.1007/978-94-007-3876-8.

[183] H. Schnablegger, Y. Singh, The SAXS Guide, 2013. https://doi.org/10.1006/aphy.1994.1055.

[184] J. Cheng, S.J. Rathi, P. Stradins, G.L. Frey, R.T. Collins, S.K.R. Williams, Free standing silica thin films with highly ordered perpendicular nanopores, RSC Adv. 4 (2014) 7627–7633. https://doi.org/10.1039/c3ra46666c.

[185] S. Besson, T. Gacoin, C. Ricolleau, C. Jacquiod, J.P. Boilot, Phase diagram for mesoporous CTAB-silica films prepared under dynamic conditions, J. Mater. Chem. 13 (2003) 404–409. https://doi.org/10.1039/b206698j.

[186] J.M. Kim, J.H. Kwak, S. Jun, R. Ryoo, Ion exchange and thermal stability of MCM-41, J. Phys. Chem. 99 (1995) 16742–16747. https://doi.org/10.1021/j100045a039.

[187] C.Y. Chen, H.X. Li, M.E. Davis, Studies on mesoporous materials. I. Synthesis and characterization of MCM-41, Microporous Mater. 2 (1993) 17–26. https://doi.org/10.1016/0927-6513(93)80058-3.

[188] E.I. Kamitsos, A.P. Patsis, G. Kordas, Infrared-reflectance spectra of heat-treated sol-gel-derived silica, Phys. Rev. B. 48 (1993) 12499–12505. https://doi.org/10.1103/PhysRevB.48.12499.

[189] T. Murakata (Aita), K. Takekoshi, S. Sato, Electrochemical Properties of TiO2 Coated ITO Electrodes Prepared by Sol-Gel Method., J. Chem. Eng. JAPAN. 32 (1999) 825–829. https://doi.org/10.1252/jcej.32.825.

[190] M. Etienne, S. Sallard, M. Schröder, Y. Guillemin, S. Mascotto, B.M. Smarsly, A. Walcarius, Electrochemical generation of thin silica films with hierarchical porosity, Chem. Mater. 22 (2010) 3426–3432. https://doi.org/10.1021/cm1004278.

[191] N.K. Raman, C.J. Brinker, Organic "template" approach to molecular sieving silica membranes, J. Memb. Sci. 105 (1995) 273–279. https://doi.org/10.1016/0376-7388(95)00067-M.

[192] Y. Minhao, M.J. Henderson, A. Gibaud, On the etching of silica and mesoporous silica films determined by X-ray reflectivity and atomic force microscopy, Thin Solid Films. 517 (2009) 3028–3035. https://doi.org/10.1016/j.tsf.2008.12.017.

[193] S. Inagaki, Y. Fukushima, Adsorption of water vapor and hydrophobicity of ordered mesoporous silica, FSM-16, Microporous Mesoporous Mater. 21 (1998) 667–672. https://doi.org/10.1016/S1387-1811(98)00075-4.

[194] E. Papirer, Adsorption on Silica Surfaces, 2000. https://doi.org/10.1201/9781482269703.

[195] M.B. Serrano, C. Despas, G. Herzog, A. Walcarius, Mesoporous silica thin films for molecular sieving and electrode surface protection against biofouling, Electrochem. Commun. 52 (2015) 34–36. https://doi.org/10.1016/j.elecom.2015.01.010.

[196] M. Zhang, J. Hu, Indium tin oxide electrode modified by a SH+ ion implantation technique for direct electrocatalytic sensing of hydrogen peroxide, Anal. Methods. 5 (2013) 1273–1278. https://doi.org/10.1039/c2ay26245b.

[197] C. Robertson, R. Beanland, S.A. Boden, A.L. Hector, R.J. Kashtiban, J. Sloan, D.C. Smith, A. Walcarius, Ordered mesoporous silica films with pores oriented perpendicular to a titanium nitride substrate, Phys. Chem. Chem. Phys. 17 (2015) 4763–4770.

https://doi.org/10.1039/c4cp05730a.

[198] F. Aydin, C. Zhan, C. Ritt, R. Epsztein, M. Elimelech, E. Schwegler, T.A. Pham, Similarities and differences between potassium and ammonium ions in liquid water: A first-principles study, Phys. Chem. Chem. Phys. 22 (2020) 2540–2548. https://doi.org/10.1039/c9cp06163k.

[199] Y. Marcus, Thermodynamics of solvation of ions. Part 5. - Gibbs free energy of hydration at 298.15 K, J. Chem. Soc. Faraday Trans. 87 (1991) 2995–2999. https://doi.org/10.1039/FT9918702995.

[200] H. Luo, C.E.D. Chidsey, D–Si(111)(1×1) surface for the study of silicon etching in aqueous solutions, Appl. Phys. Lett. 72 (1998) 477–479. https://doi.org/10.1063/1.120791.

[201] P. V. Brady, J. V. Walther, Controls on silicate dissolution rates in neutral and basic pH solutions at 25°C, Geochim. Cosmochim. Acta. 53 (1989) 2823–2830. https://doi.org/10.1016/0016-7037(89)90160-9.

[202] J.D. Rimstidt, Rate equations for sodium catalyzed quartz dissolution, Geochim. Cosmochim. Acta. 167 (2015) 195–204. https://doi.org/10.1016/j.gca.2015.07.030.

[203] F.K. Crundwell, On the Mechanism of the Dissolution of Quartz and Silica in Aqueous Solutions, ACS Omega. 2 (2017) 1116–1127. https://doi.org/10.1021/acsomega.7b00019.

[204] S.J.T. Pollard, P.G. Kibblewhite, Soils and Land Contamination, in: Introd. to Pollut. Sci., 2007: pp. 122–153. https://doi.org/10.1039/9781847555410-00122.

[205] H.F. Burstall, 34. Optical Activity dependent on Co-ordinated Bivalent Ruthenium., J. Chem. Soc. (1936) 173–175. https://doi.org/10.1039/JR9360000173.

[206] J. Steigman, N. Birnbaum, S.M. Edmonds, Ruthenium Dipyridyl-A New Oxidimetric Indicator, Ind. Eng. Chem. - Anal. Ed. 14 (1942) 30. https://doi.org/10.1021/i560101a010.

[207] W.W. Brandt, G.F. Smith, Polysubstituted 1,10-Phenanthrolines and Bipyridines as Multiple Range Redox Indicators, Anal. Chem. 21 (1949) 1313–1319. https://doi.org/10.1021/ac60035a003.

[208] T. Saji, S. Aoyagui, Polarographic studies on bipyridine complexes. I. Correlation between reduction potentials of iron(II), ruthenium(II) and osmium(II) complexes and those of free ligands, J. Electroanal. Chem. Interfacial Electrochem. 58 (1975) 401–410. https://doi.org/10.1016/S0022-0728(75)80098-2.

[209] K. Kalyanasundaram, Photophysics, photochemistry and solar energy conversion with tris(bipyridyl)ruthenium(II) and its analogues, Coord. Chem. Rev. 46 (1982) 159–244. https://doi.org/10.1016/0010-8545(82)85003-0.

[210] F.E. Lytle, D.M. Hercules, The Luminescence of Tris (2,2′-bipyridine) ruthenium (II) Dichloride, J. Am. Chem. Soc. 91 (1969) 253–257. https://doi.org/10.1021/ja01030a006.

[211] B. Durham, J. V. Caspar, J.K. Nagle, T.J. Meyer, Photochemistry of Ru(bpy)32+, J. Am. Chem. Soc. 104 (1982) 4803–4810. https://doi.org/10.1021/ja00382a012.

[212] D.M. Arias-Rotondo, J.K. McCusker, An Overview of the Physical and Photophysical

Properties of [Ru(bpy) 3]2+, in: Visible Light Photocatal. Org. Chem., Wiley-VCH Verlag GmbH & Co. KGaA, Weinheim, Germany, 2018: pp. 1–24. https://doi.org/10.1002/9783527674145.ch1.

[213] J.P. Paris, W.W. Brandt, Charge Transfer Luminescence of A Ruthenium(II) Chelate, J. Am. Chem. Soc. 81 (1959) 5001–5002. https://doi.org/10.1021/ja01527a064.

[214] A.. Juris, V. Balzani, Ru(II) POLYPYRIDINE COMPLEXES: PHOTOPHYSICS, PHOTOCHEMISTRY, ELECTROCHEMISTRY, AND CHEMILUMINESCENCE, Coord. Chem. Rev. 84 (1988) 85–277. https://doi.org/10.1016/0010-8545(88)80032-8.

[215] G.A.. Crosby, W.G.. Perkins, D.M. Klassen, Luminescence from Transition-Metal Complexes: Tris(2,2'-bipyridine)- and Tris(1,10-phenanthroline)Ruthenium(II), J. Chem. Phys. 43 (1965) 1498–1503.

[216] D.M. Klassen, G.A. Crosby, Spectroscopic studies of Ruthenium(II) complexes. Assignment of the luminescence, J. Chem. Phys. 48 (1968) 1867–1868. https://doi.org/10.1063/1.1668922.

[217] I.M. Dixon, E. Lebon, P. Sutra, A. Igau, Luminescent ruthenium–polypyridine complexes and phosphorus ligands: Anything but a simple story, Chem. Soc. Rev. 38 (2009) 1621–1634. https://doi.org/10.1039/b804763b.

[218] D.M. Hercules, F.E. Lytle, Chemiluminescence from Reduction Reactions, J. Am. Chem. Soc. 88 (1966) 4745–4746. https://doi.org/10.1021/ja00972a052.

[219] M.M. Chang, T. Saji, A.J. Bard, Electrogenerated Chemiluminescence. 30. Electrochemical Oxidation of Oxalate Ion in the Presence of Luminescers in Acetonitrile Solutions, J. Am. Chem. Soc. 99 (1977) 5399–5403. https://doi.org/10.1021/ja00458a028.

[220] N.E. Tokel, A.J. Bard, Electrogenerated Chemiluminescence. IX. Electrochemistry and Emission from Systems Containing Tris(2,2′-bipyridine)ruthenium(II) Dichloride, J. Am. Chem. Soc. 94 (1972) 2862–2863. https://doi.org/10.1021/ja00763a056.

[221] M.M. Richter, Electrochemiluminescence (ECL), Chem. Rev. 104 (2004) 3003–3036. https://doi.org/10.1021/cr020373d.

[222] I. Rubinstein, A.J. Bard, Electrogenerated Chemiluminescence. 37. Aqueous Ecl Systems Based on Ru(2,2'-bipyridine)32+ and Oxalate or Organic Acids, J. Am. Chem. Soc. 103 (1981) 512–516. https://doi.org/10.1021/ja00393a006.

[223] T. Kai, M. Zhou, S. Johnson, H.S. Ahn, A.J. Bard, Direct Observation of C2O4•- and CO2•- by Oxidation of Oxalate within Nanogap of Scanning Electrochemical Microscope, J. Am. Chem. Soc. 140 (2018) 16178–16183. https://doi.org/10.1021/jacs.8b08900.

[224] L. Bouffier, N. Sojic, Chapter 1: Introduction and Overview of Electrogenerated Chemiluminescence, in: RSC Detect. Sci., 2020: pp. 1–28. https://doi.org/10.1039/9781788015776-00001.

[225] Y. Zhang, R. Zhang, X. Yang, H. Qi, C. Zhang, Recent advances in electrogenerated chemiluminescence biosensing methods for pharmaceuticals, J. Pharm. Anal. 9 (2019) 9–19. https://doi.org/10.1016/j.jpha.2018.11.004.

[226] W. Miao, J. Choi, A.J. Bard, Electrogenerated Chemiluminescence 69 : The Tris(2,2′-bipyridine)ruthenium(II), (Ru(bpy)32+) / Tri-n-propylamine (TPrA) System Revisited - A New Route Involving TPrA•+ Cation Radicals, J. Am. Chem. Soc. 124 (2002) 14478–14485.

[227] Y. Zu, A.J. Bard, Electrogenerated Chemiluminescence. 66. The Role of Direct Coreactant Oxidation in the Ruthenium Tris(2,2′)bipyridyl/Tripropylamine System and the Effect of Halide Ions on the Emission Intensity, Anal. Chem. 72 (2000) 3223–3232.

[228] A.W. Knight, G.M. Greenway, Relationship between structural attributes and observed electrogenerated chemiluminescence (ECL) activity of tertiary amines as potential analytes for the tris(2,2-bipyridine)ruthenium(II) ECL reaction: A review, Analyst. 121 (1996). https://doi.org/10.1039/an996210101r.

[229] J.B. Noffsinger, N.D. Danielson, Generation of Chemiluminescence upon Reaction of Aliphatic Amines with Tr¡s(2,2'-b¡pyrid¡ne) ruthenium (III), Anal. Chem. 59 (1987) 865–868. https://doi.org/10.1021/ac00133a017.

[230] K. Uchikura, M. Kirisawa, A. Sugii, Electrochemiluminescence Detection of Primary Amines Using Tris(bipyridine)ruthenium (III) after Derivatization with Divinylsulfone, Anal. Sci. 9 (1993) 121–123.

[231] L. He, K.A.. Cox, N.D. Danielson, Chemiluminescence detection of amino acids, peptides, and proteins using tris-2,2'-bipyridine ruthenium (III), Anal. Lett. 23 (1990) 195–210. https://doi.org/10.1080/00032719008052438.

[232] S.N. Brune, D.R. Bobbitt, EFFECT OF pH ON THE REACTION OF TRIS(2,2'-BIPYRIDIL)RUTHENIUM(III) WITH AMINO-ACIDS : IMPLICATIONS FOR THEIR DETECTION, Talanta. 38 (1991) 419–424.

[233] W.-Y. Lee, Tris(2,2'-bipyridyl)ruthenium(II) Electrogenerated Chemiluminescence in Analytical Science, Mikrochim. Acta. 127 (1997) 19–39.

[234] M. Pravda, G.G. Guilbault, K.A. Fahnrich, Recent applications of electrogenerated chemiluminescence in chemical analysis, Talanta. 54 (2001) 531–559.

[235] Y.S. Obeng, A.J. Bard, Electrogenerated Chemiluminescence. 53. Electrochemistry and Emission from Adsorbed Monolayers of a Tris(bipyridyl)ruthenium(II)-Based Surfactant on Gold and Tin Oxide Electrodes, Langmuir. 7 (1991) 195–201. https://doi.org/10.1021/la00049a035.

[236] Y. Sato, K. Uosaki, Electrochemical and electrogenerated chemiluminescence properties of tris(2,2′-bipyridine)ruthenium(II)-tridecanethiol derivative on ITO and gold electrodes, J. Electroanal. Chem. 384 (1995) 57–66. https://doi.org/10.1016/0022-0728(94)03731-H.

[237] H. Wang, G. Xu, S. Dong, Electrochemistry and electrochemiluminescence of stable tris(2,2′-bipyridyl)ruthenium(II) monolayer assembled on benzene sulfonic acid modified glassy carbon electrode, Talanta. 55 (2001) 61–67. https://doi.org/10.1016/S0039-9140(01)00406-4.

[238] J. Premkumar, S.B. Khoo, Immobilization of ruthenium(II)bipyridyl complex at highly oxidized glassy carbon electrodes, Electrochem. Commun. 6 (2004) 984–989.

https://doi.org/10.1016/j.elecom.2004.07.013.

[239] X. Zhang, A.J. Bard, Electrogenerated chemiluminescent emission from an organized (L-B) monolayer of a Ru(bpy)32+-based surfactant on semiconductor and metal electrodes, J. Phys. Chem. 92 (1988) 5566–5569.

[240] C.J. Miller, A.J. Bard, Horizontal Touch Voltammetric Analysis-Determination of Insoluble Electroactive Species in Films at the Air/Water Interface, Anal. Chem. 63 (1991) 1707–1714. https://doi.org/10.1021/ac00017a011.

[241] I. Rubinstein, A.J. Bard, Polymer Films on Electrodes. 5. Electrochemistry and Chemiluminescence at Nafion-Coated Electrodes, J. Am. Chem. Soc. 103 (1981) 5007–5013. https://doi.org/10.1021/ja00407a006.

[242] T.M. Downey, T.A. Nieman, Chemiluminescence Detection Using Regenerable Tris(2,2'-bipyridyl)ruthenium(II) Immobilized in Nafion, Anal. Chem. 64 (1992) 261–268. https://doi.org/10.1021/ac00027a005.

[243] L.L. Shultz, J.S. Stoyanoff, T.A. Nieman, Temporal and spatial analysis of electrogenerated Ru(bpy)33+ chemiluminescent reactions in flowing streams, Anal. Chem. 68 (1996) 349–354. https://doi.org/10.1021/ac9507909.

[244] Z. Xu, Z. Guo, S. Dong, Electrogenerated chemiluminescence biosensor with alcohol dehydrogenase and tris(2,2′-bipyridyl)ruthenium (II) immobilized in sol-gel hybrid material, Biosens. Bioelectron. 21 (2005) 455–461. https://doi.org/10.1016/j.bios.2004.10.032.

[245] H. Wang, G. Xu, S. Dong, Electrochemiluminescence sensor using tris(2,2′-bipyridyl)ruthenium(II) immobilized in Eastman-AQ55D-silica composite thin-films, Anal. Chim. Acta. 480 (2003) 285–290. https://doi.org/10.1016/S0003-2670(03)00049-7.

[246] N.C. Han, S.H. Cho, Y.J. Park, D.W. Lee, W.Y. Lee, Sol-gel-immobilized Tris(2,2′-bipyridyl)ruthenium(II) electrogenerated chemiluminescence sensor for high-performance liquid chromatography, Anal. Chim. Acta. 541 (2005) 49–56. https://doi.org/10.1016/j.aca.2004.06.076.

[247] H.N. Choi, S.H. Cho, W.Y. Lee, Electrogenerated chemiluminescence from tris(2,2′-bipyridyl)ruthenium(II) immobilized in titania-perfluorosulfonated ionomer composite films, Anal. Chem. 75 (2003) 4250–4256. https://doi.org/10.1021/ac0206014.

[248] S.N. Ding, J.J. Xu, H.Y. Chen, Tris(2,2′-bipyridyl)ruthenium(II)-zirconia-Nafion composite films applied as solid-state electrochemiluminescence detector for capillary electrophoresis, Electrophoresis. 26 (2005) 1737–1744. https://doi.org/10.1002/elps.200410324.

[249] A.N. Khramov, M.M. Collinson, Electrogenerated chemiluminescence of tris(2,2'-bipyridyl)ruthenium(II) ion-exchanged in Nafion-silica composite films, Anal. Chem. 72 (2000) 2943–2948. https://doi.org/10.1021/ac9914519.

[250] H. Wang, G. Xu, S. Dong, Electrochemiluminescence of tris(2,2′-bipyridine)ruthenium(II) immobilized in poly(p-styrenesulfonate)-silica-Triton X-100 composite thin-films, Analyst. 126 (2001) 1095–1099. https://doi.org/10.1039/b100376n.

[251] H. Wang, G. Xu, S. Dong, Electrochemiluminescence of Tris(2,2′-bipyridyl)ruthenium(II) Ion-Exchanged in Polyelectrolyte-Silica Composite Thin-Films, Electroanalysis. 14 (2002) 853–857. https://doi.org/10.1002/1521-4109(200206)14:12<853::AID-ELAN853>3.0.CO;2-D.

[252] M. Ogawa, T. Nakamura, J. Mori, K. Kuroda, Luminescence of Tris(2,2‘-bipyridine)ruthenium(II) Cations ([Ru(bpy)3]2+) Adsorbed in Mesoporous Silica, J. Phys. Chem. B. 104 (2000) 8554–8556. https://doi.org/10.1021/jp0015123.

[253] G. Villemure, T.J. Pinnavaia, Cyclic voltammetry of tris(2,2′-bipyridyl)ruthenium(II) cations adsorbed in electrodes modified with mesoporous molecular sieve silicas, Chem. Mater. 11 (1999) 789–794. https://doi.org/10.1021/cm980659s.

[254] W. Yun, P. Dong, Y. Xu, L. Yang, P. He, Y. Fang, Selective immobilization of tris(2,2′-bipyridyl)ruthenium (II) onto array electrode for solid-state electrochemiluminescene sensor fabrication, Sensors Actuators, B Chem. 141 (2009) 244–248. https://doi.org/10.1016/j.snb.2009.04.063.

[255] L. Qian, X. Yang, One-step synthesis of Ru(2,2′-Bipyridine)3Cl2-immobilized silica nanoparticles for use in electrogenerated chemiluminescence detection, Adv. Funct. Mater. 17 (2007) 1353–1358. https://doi.org/10.1002/adfm.200600253.

[256] L. Zhang, S. Dong, Electrogenerated chemiluminescence sensors using Ru(bpy)32+ doped in silica nanoparticles, Anal. Chem. 78 (2006) 5119–5123. https://doi.org/10.1021/ac060451n.

[257] M. Sykora, T.J. Meyer, Electrogenerated chemiluminescence in SiO2 sol-gel polymer composites, Chem. Mater. 11 (1999) 1186–1189. https://doi.org/10.1021/cm9900148.

[258] E. Holder, D. Oelkrug, H.J. Egelhaaf, H.A. Mayer, E. Lindner, Synthesis, Characterization, and Luminescence Spectroscopic Accessibility Studies of Tris(2,2′-Bipyridine)Ruthenium(II)-Labeled Inorganic-Organic Hybrid Polymers, J. Fluoresc. 12 (2002) 383–395. https://doi.org/10.1023/A:1021309925702.

[259] J.K. Lee, S.H. Lee, M. Kim, H. Kim, D.H. Kim, W.Y. Lee, Organosilicate thin film containing Ru(bpy)32+ for an electrogenerated chemiluminescence (ECL) sensor, Chem. Commun. 9 (2003) 1602–1603.

[260] H. Takeda, M. Ohashi, Y. Goto, T. Ohsuna, T. Tani, S. Inagaki, A Versatile Solid Photosensitizer: Periodic Mesoporous Organosilicas with Ruthenium Tris(bipyridine) Complexes Embedded in the Pore Walls, Adv. Funct. Mater. 26 (2016) 5068–5077. https://doi.org/10.1002/adfm.201601587.

[261] S.M. Carlise, J.T. Trevors, Glyphosate in the environment, Water. Air. Soil Pollut. 39 (1988) 409–420. https://doi.org/10.1007/BF00118893.

[262] H. Zhan, Y. Feng, X. Fan, S. Chen, Recent advances in glyphosate biodegradation, Appl. Microbiol. Biotechnol. 102 (2018) 5033–5043. https://doi.org/10.1007/s00253-018-9035-0.

[263] G. Andreotti, S. Koutros, J.N. Hofmann, D.P. Sandler, J.H. Lubin, C.F. Lynch, C.C. Lerro, A.J. De Roos, C.G. Parks, M. Alavanja, D.T. Silverman, L.E.. Freeman, Glyphosate Use

and Cancer Incidence in the Agricultural Health Study, J. Natl. Cancer Inst. 110 (2018) 509–516. https://doi.org/10.1093/jnci/djy200.

[264] C.M. Benbrook, Trends in glyphosate herbicide use in the United States and globally, Environ. Sci. Eur. 28 (2016) 1–15. https://doi.org/10.1186/s12302-016-0070-0.

[265] V. Silva, L. Montanarella, A. Jones, O. Fernández-Ugalde, H.G.J. Mol, C.J. Ritsema, V. Geissen, Distribution of glyphosate and aminomethylphosphonic acid (AMPA) in agricultural topsoils of the European Union, Sci. Total Environ. 621 (2018) 1352–1359. https://doi.org/10.1016/j.scitotenv.2017.10.093.

[266] G.M. Dill, R.D. Sammons, P.C.C. Feng, F. Kohn, K. Kretzmer, A. Mehrsheikh, M. Bleeke, J.L. Honegger, D. Farmer, D. Wright, E.A. Haupfear, Glyphosate Resistance in Crops and Weeds, in: Glyphosate Resist. Crop. Weeds, 2010: pp. 1–34. https://doi.org/10.1002/9780470634394.

[267] A. Samsel, S. Seneff, Glyphosate, pathways to modern diseases IV: cancer and related pathologies, J. Biol. Phys. Chem. 15 (2015) 121–159. https://doi.org/10.4024/11sa15r.jbpc.15.03.

[268] C. Berry, Glyphosate and cancer: the importance of the whole picture, Pest Manag. Sci. 76 (2020) 2874–2877. https://doi.org/10.1002/ps.5834.

[269] R.E. Tarone, On the International Agency for Research on Cancer classification of glyphosate as a probable human carcinogen, Eur. J. Cancer Prev. 27 (2018) 82–87. https://doi.org/10.1097/CEJ.0000000000000289.

[270] O.P. de Amarante Junior, T.C.R. dos Santos, N.M. Brito, M.L. Ribeiro, Glifosato: propriedades, toxicidade, usos e legislação, Quim. Nova. 25 (2002) 589–593. https://doi.org/10.1590/s0100-40422002000400014.

[271] M.P. García De Llasera, L. Gómez-Almaraz, L.E. Vera-Avila, A. Peña-Alvarez, Matrix solid-phase dispersion extraction and determination by high-performance liquid chromatography with fluorescence detection of residues of glyphosate and aminomethylphosphonic acid in tomato fruit, J. Chromatogr. A. 1093 (2005) 139–146. https://doi.org/10.1016/j.chroma.2005.07.063.

[272] M. Ibáñez, Ó.J. Pozo, J. V. Sancho, F.J. López, F. Hernández, Re-evaluation of glyphosate determination in water by liquid chromatography coupled to electrospray tandem mass spectrometry, J. Chromatogr. A. 1134 (2006) 51–55. https://doi.org/10.1016/j.chroma.2006.07.093.

[273] V. Subramaniam, P.E. Hoggard, Metal Complexes of Glyphosate, J. Agric. Food Chem. 36 (1988) 1326–1329. https://doi.org/10.1021/jf00084a050.

[274] R.L. Glass, Metal Complex Formation by Glyphosate, J. Agric. Food Chem. 32 (1984) 1249–1253. https://doi.org/10.1021/jf00126a010.

[275] A.L. Valle, F.C.C. Mello, R.P. Alves-Balvedi, L.P. Rodrigues, L.R. Goulart, Glyphosate detection: methods, needs and challenges, Environ. Chem. Lett. 17 (2019) 291–317. https://doi.org/10.1007/s10311-018-0789-5.

[276] W.C. Koskinen, L.J. Marek, K.E. Hall, Analysis of glyphosate and aminomethylphosphonic acid in water, plant materials and soil, Pest Manag. Sci. 72 (2016) 423–432. https://doi.org/10.1002/ps.4172.

[277] S. Görög, Derivatization of Analytes, in: Encycl. Anal. Sci. (Second Ed., 2005: pp. 263–273. https://doi.org/10.1016/B0-12-369397-7/00739-1.

[278] J.S. Ridlen, G.J. Klopf, T.A. Nieman, Determination of glyphosate and related compounds using HPLC with tris(2,2'-bipyridyl)ruthenium(II) electrogenerated chemiluminescence detection, Anal. Chim. Acta. 341 (1997) 195–204.

[279] H.Y. Chiu, Z.Y. Lin, H.L. Tu, C.W. Whang, Analysis of glyphosate and aminomethylphosphonic acid by capillary electrophoresis with electrochemiluminescence detection, J. Chromatogr. A. 1177 (2008) 195–198. https://doi.org/10.1016/j.chroma.2007.11.042.

[280] J. Jin, F. Takahashi, T. Kaneko, T. Nakamura, Characterization of electrochemiluminescence of tris(2,2′-bipyridine)ruthenium(II) with glyphosate as coreactant in aqueous solution, Electrochim. Acta. 55 (2010) 5532–5537. https://doi.org/10.1016/j.electacta.2010.04.031.

[281] C. Quiong, C. Xiaoping, Q. Bin, L. Zhenyu, Electrochemiluminescent Detection Method for Glyphosate in Soybean on Carbon Fiber-ionic Liquid Paste Electrode, Chin. J. Chem. 29 (2011) 581–586.

[282] H. Chuang, T. Hong, C. Whang, A simple and rapid screening method for glyphosate in water using flow-injection with electrochemiluminescence detection, Anal. Methods. 5 (2013) 6186–6191. https://doi.org/10.1039/c3ay41059e.

[283] G. Marzari, M. V. Cappellari, G.M. Morales, F. Fungo, Electrochemiluminescent detection of glyphosate using electrodes modified with self-assembled monolayers, Anal. Methods. 9 (2017) 2452–2457. https://doi.org/10.1039/c7ay00506g.

[284] A. Habekost, Rapid and sensitive spectroelectrochemical and electrochemical detection of glyphosate and AMPA with screen-printed electrodes, Talanta. 162 (2017) 583–588. https://doi.org/10.1016/j.talanta.2016.10.074.

[285] J. Leland, M.J. Powell, Electrogenerated Chemiluminescence : An Oxidative-Reduction Type ECL Reaction Sequence Using Tripropyl Amine, J. Electrochem. Soc. 137 (1990) 3127–3131. https://doi.org/10.1149/1.2086171.

[286] Y. He, L. Ding, B. Su, Vertically ordered silica mesochannels as preconcentration materials for the electrochemical detection of methylene blue, Sci. China Chem. 58 (2015) 1593–1599. https://doi.org/10.1007/s11426-015-5365-2.

[287] M.R. Assalin, S.G. De Moraes, S.C.N. Queiroz, V.L. Ferracini, N. Duran, Studies on degradation of glyphosate by several oxidative chemical processes: Ozonation, photolysis and heterogeneous photocatalysis, J. Environ. Sci. Heal. Part B. 45 (2009) 89–94. https://doi.org/10.1080/03601230903404598.

[288] S.A. Neto, A.R. De Andrade, Electrooxidation of glyphosate herbicide at different DSA® compositions: pH , concentration and supporting electrolyte effect, 54 (2009) 2039–2045.

https://doi.org/10.1016/j.electacta.2008.07.019.

[289] A. Walcarius, R. Nasraoui, Z. Wang, F. Qu, V. Urbanova, M. Etienne, M. Göllü, A.S. Demir, J. Gajdzik, R. Hempelmann, Factors affecting the electrochemical regeneration of NADH by (2,2'-bipyridyl) (pentamethylcyclopentadienyl)-rhodium complexes: Impact on their immobilization onto electrode surfaces, Bioelectrochemistry. 82 (2011) 46–54. https://doi.org/10.1016/j.bioelechem.2011.05.002.

[290] P.A. Anderson, G.B. Deacon, K.H. Haarmann, F.R. Keene, T.J. Meyer, D.A. Reitsma, B.W. Skelton, G.F. Strouse, N.C. Thomas, Designed Synthesis of Mononuclear Tris(heteroleptic) Ruthenium Complexes Containing Bidentate Polypyridyl Ligands, Inorg. Chem. 34 (1995) 6145–6157. https://doi.org/10.1021/ic00128a028.

[291] Hua-Wei Liu, K.Y. Zhang, W.H.T. Law, K.K.W. Lo, Cyclometalated iridium(III) bipyridine complexes functionalized with an N-methylamino-oxy group as novel phosphorescent labeling reagents for reducing sugars, Organometallics. 29 (2010) 3474–3476. https://doi.org/10.1021/om100597g.

[292] Z. Jia, Q. Zhu, "Click" assembly of selective inhibitors for MAO-A, Bioorganic Med. Chem. Lett. 20 (2010) 6222–6225. https://doi.org/10.1016/j.bmcl.2010.08.104.

[293] K. Musilek, R. Pavlikova, J. Marek, M. Komloova, O. Holas, M. Hrabinova, M. Pohanka, V. Dohnal, M. Dolezal, F. Gunn-Moore, K. Kuca, The preparation, in vitro screening and molecular docking of symmetrical bisquaternary cholinesterase inhibitors containing a but-(2E)-en-1,4-diyl connecting linkage, J. Enzyme Inhib. Med. Chem. 26 (2011) 245–253. https://doi.org/10.3109/14756366.2010.496362.

[294] M. Li, Q. Liang, M. Zheng, C. Fang, S. Peng, M. Zhao, An efficient ruthenium tris(bipyridine)-based luminescent chemosensor for recognition of Cu(ii) and sulfide anion in water, Dalt. Trans. 42 (2013) 13509–13515. https://doi.org/10.1039/c3dt51047f.

[295] J.S. Strukl, J.L. Walter, Infrared and Raman spectra of heterocyclic compounds-III. The infrared studies and normal vibrations of 2,2'-bipyridine, Spectrochim. Acta. 27 (1971) 209–221. https://doi.org/10.1016/0584-8539(71)80027-2.

[296] J. Huang, W. Qu, J. Zhu, H. Liu, W. Wen, X. Zhang, S. Wang, Electrochemiluminescent sensor based on Ru(bpy)32+-doped silica nanoprobe by incorporating a new co-reactant NBD-amine for selective detection of hydrogen sulfide, Sensors Actuators, B Chem. 284 (2019) 451–455. https://doi.org/10.1016/j.snb.2019.01.006.

[297] J. Font, P. De March, F. Busqué, E. Casas, M. Benitez, L. Teruel, H. García, Periodic mesoporous silica having covalently attached tris(bipyridine)ruthenium complex: Synthesis, photovoltaic and electrochemiluminescent properties, J. Mater. Chem. 17 (2007) 2336–2343. https://doi.org/10.1039/b618773k.

[298] B. Paschkes, B. Bernas, A Rapid Method for the Determination of Ammonia (Combined) and Phosphate in the System of Diammonium Phosphate and Dipotassium Phosphate, Anal. Chim. Acta. 24 (1961) 5–10.

[299] A. Gutiérrez-Becerra, M. Barcena-Soto, V. Soto, J. Arellano-Ceja, N. Casillas, S. Prévost, L. Noirez, M. Gradzielski, J.I. Escalante, Structure of reverse microemulsion-templated

metal hexacyanoferrate nanoparticles, Nanoscale Res. Lett. 7 (2012) 1–12. https://doi.org/10.1186/1556-276X-7-83.

[300] K.H.S. Kung, K.F. Hayes, Fourier Transform Infrared Spectroscopic Study of the Adsorption of Cetyltrimethylammonium Bromide and Cetylpyridinium Chloride on Silica, Langmuir. 9 (1993) 263–267. https://doi.org/10.1021/la00025a050.

[301] D.J. Macquarrie, Direct preparation of organically modified MCM-type materials. Preparation and characterisation of arninopropyl-MCM and 2-cyanoethyl-MCM, Chem. Commun. (1996) 1961–1962. https://doi.org/10.1039/CC9960001961.

Abstract

The combination of rich surface chemistry of silica and ordered perpendicularly-standing hexagonal mesostructure of films generated by EASA makes this material a perfect choice for use as the electrode coatings. In this light, improvement of film design is a constant challenge in order to benefit from porous layer and to increase the efficiency of electrochemical sensors.

The first part of project was centred around the optimisation of the film thickness towards the thinnest with preservation of the beneficial hexagonal structure. The mesoporous silica film (MSF) thickness is a parameter that can affect the mass transport through the silica coating to the electrode specifically because of the reactivity of surface silanol groups. Thinning of the MSF can facilitate the diffusion of species, while keeping the presence of the beneficial silica layer can increase the electrochemical response, hence, the sensitivity of analysis. Two approaches were used in order to decrease thickness. The first was a study of the effect of the deposition time during the modification of the electrode (EASA process). The second one was the wet etching of film after its deposition. The thinnest uniform MSFs, which can be generated on indium tin oxide (ITO) surface, require minimum 10 seconds deposition with an applied potential equal to -1.3 V and a 100 mM silane-containing sol. This gave rise to 80 ± 9 nm coating. Post-synthesis etching with the soft fluoride solution of ammonium fluoride, NH_4F, allowed to control the decrease of the MSF thickness. By keeping the surfactant inside the silica pores, template agent for the synthesis, the kinetic of the etching reaction was faster, but with a more homogeneous dissolution. It was possible to obtain the thinnest ordered MSF in comparison with an etching procedure conducted on MSF after the extraction of the template. The profilometry determined thickness of well-structured film with vertical pore orientation was respectively of 28 ± 9 nm for the templated silica films and 57 ± 11 nm for films without surfactant inside their pores.

In the second part of the study, MSFs were applied to modify ITO electrodes for the development of electrochemiluminescence platform for detection of amine-containing herbicide glyphosate using co-reactant system with $Ru(bpy)_3^{2+}$. Comparison between physical and chemical immobilisation of the organometallic agent was studied. Covalent functionalisation was achievable due to introduction of azide functions on co-condensation step with their further coupling with propargyl-functionalised derivative of $Ru(bpy)_3^{2+}$ complex by Huisgen 1,3-cycloaddition reaction. The effect of the herbicide addition was investigated using electrodes with immobilised by two approaches $Ru(bpy)_3^{2+}$ complex as well as in solution of $Ru(bpy)_3^{2+}$, operating bare ITO electrode and ITO electrode covered with unmodified MSF. The evolution of electrochemical signal was used to conclude on the possibility to detect glyphosate.

Keywords: mesoporous silica films, EASA, thickness control, $Ru(bpy)_3^{2+}$, glyphosate, electrochemiluminescence.

Résumé abrégé

La modification d'électrodes par des films de silice mésoporeuse (FSM) ouvre des perspectives intéressantes dans le développement de capteurs électrochimiques. En particulier, la combinaison de la méthode électrochimique EASA (electrochemically-assisted self-assembly) permet d'obtenir des films fins et réguliers de silice mésoporeuse, de structure hexagonale et des pores perpendiculaire à la surface du support. Ces caractéristiques singulières contribuent à des transports de matière extrêmement rapides et indispensables aux applications type capteurs.

La première partie du projet est centrée sur la réduction de l'épaisseur du FSM pour obtenir le plus fin tout en préservant sa structure hexagonale organisée et minimiser les effets négatifs du dépôt tout en ne gardant que ses bénéfices. Nous avons tout d'abord déterminé que, par la méthode de déposition EASA, l'épaisseur minimale d'un film homogène et sans défaut pouvant être atteinte dans nos conditions opératoires ([Si] = 100 mM, 32 mM CTAB) est de 80 ± 9 nm pour 10 s du potentiel -1.3$V_{/Ag}$ appliqué. Notre approche pour obtenir des couches plus fines que cela a consisté à dissoudre le FSM par voie humide, en utilisant le fluorure d'ammonium, NH_4F, comme réactif «doux». La dissolution la plus contrôlée a été observée pour les FSMs dont le tensioactif est conservé dans la structure poreuse. La présence du CTAB favorise le transport et l'accumulation des ions fluorure dans le film accélérant ainsi la réaction (1.1 nm/min avec NH_4F 0.05 M). L'épaisseur du FSM le plus fin obtenu dans ces conditions est de 28 ± 9 nm. Lorsque le traitement est mené sur des FSMs pour lesquels le tensioactif a été extrait par voie humide ou par calcination, l'épaisseur la plus petite atteinte sans créer de défaut dans le film est seulement de 57 ± 11 nm.

Dans la deuxième partie de l'étude, les FSMs ont été fonctionnalisés par un complexe organométallique de ruthénium(II) dans le but d'essayer de développer une plateforme d'électrochimiluminescence pour la détection du glyphosate. L'originalité de l'approche est le choix d'immobiliser de manière covalente le complexe ruthénium(II) tris(bipyridine), $Ru(bpy)_3^{2+}$, au sein du FSM. L'approche par chimie «click» a été privilégiée et réalisée sur un FSM modifiée par des groupements azoture préparé par co-condensation. Les premiers résultats électrochimiques obtenus en présence de glyphosate ont montré que la présence du pesticide conduit à une modification du signal électrochimique quelle que soit la nature de l'électrode utilisée. La détection de l'herbicide est ainsi possible. On remarque cependant que la nature du signal enregistré avec une électrode modifiée par un FSM où le complexe organométallique a été préalablement greffé est différent de celui obtenu avec les autres électrodes et pas encore totalement expliqué.

Mots clés: film de silice mésoporeuse, EASA, contrôle de l'épaisseur, $Ru(bpy)_3^{2+}$, glyphosate, électrochimiluminescence.